UNIVERSITY OF SOUTHAMPTON

FACULTY OF SCIENCE, ENGINEERING AND MATHEMATICS
School of Chemistry

High Throughput and Traditional Routes Towards Functional Oxide and Oxide-Nitride Materials

by

Stuart James Henderson

Thesis for the degree of Doctor of Philosophy

May 2006

UNIVERSITY OF SOUTHAMPTON

ABSTRACT

FACULTY OF SCIENCE, ENGINEERING AND MATHEMATICS

SCHOOL OF CHEMISTRY

Doctor of Philosophy

HIGH THROUGHPUT AND TRADITIONAL ROUTES TOWARDS FUNCTIONAL OXIDE AND OXIDE-NITRIDE MATERIALS

by Stuart James Henderson

High-throughput methods have been used for the synthesis and preliminary characterisation of optically functional ceramic oxide and oxide-nitride materials on an alumina substrate. Gel routes have been investigated for their viability when used with a Teflon masking system. Three different systems and deposition methodologies have been studied. The first system uses a polymer complex method based on citric acid and ethylene glycol in aqueous media to create arrays of the formula $Ca_{1-x}Sr_xZr_{1-y}Cr_yO_3$ ($0 \leq x \leq 1$; $0 \leq y \leq 0.24$). Secondly a metal alkoxide sol-gel method using an acetic acid, acetic anhydride solvent has been employed to produce arrays of oxides and oxide-nitrides with the general formulae $SrZr_{1-x}Ta_xO_3$ and $SrZr_{1-x}Ta_xO_{2+x}N_{1-x}$ ($0 \leq x \leq 1$). Finally, compounds with the spinel structure in the series $Cu_{1-x}Zn_xAl_{2-y}Cr_yO_4$ ($0 \leq x \leq 1$; $0 \leq y \leq 2$) were prepared by co-evaporation. The materials were analysed by rapid sequential X-ray diffraction, scanning electron microscopy and a simple colour measurement technique.

The viability of applying this high throughput methodology to the synthesis and screening of phosphor materials has also been investigated. Arrays of europium doped lanthanum phosphate have been prepared and have revealed that the maximum intensity of the $^5D_0 \rightarrow {}^7F_2$ red transition is achieved at a composition of $(La_{0.8}Eu_{0.2})PO_4$. However, increasing the europium content also reduces the ratio of red:orange luminescence, reducing the usefulness of the material as a red phosphor. The compound $(Gd_{0.75}Tb_{0.25})P_{1.14}O_\delta$ was found to be the best green phosphor material from arrays of the type $(Gd_{1-x}Tb_x)P_{1.14}O_\delta$ ($0.11 \leq x \leq 0.27$); this replicated previous studies, where the optimum composition, from slightly different conditions, was reported as $(Gd_{0.83}Tb_{0.17})P_{1.14}O_\delta$.

The structural behaviour of the pyrochlore $Bi_2Hf_2O_7$ with varying temperature has been studied by powder neutron and X-ray diffraction. The unit cell transforms from monoclinic (a = 15.3536(4) Å, b = 15.3320(4) Å, c = 21.8253(3) Å and β = 90.051(5)°) at room temperature (α-phase) to cubic (a = 21.733(2) Å) at 400 °C (β-phase) then to tetragonal (a = 7.68964(3), c = 10.85171(9) Å) at 550 °C (γ-phase) and finally to cubic (a = 10.87791(2) Å) at 900 °C (δ-phase). The transformations represent a gradual increase in disorder and symmetry with temperature, driven by the need to accommodate the active bismuth lone pair. The four polymorphs characterised are compared to those seen in the related $Bi_2Sn_2O_7$ system.

A similar variation in disorder and symmetry has also been determined in the solid solution series $Bi_2Hf_{2-x}Ti_xO_7$ ($0 \leq x \leq 2$). The α-$Bi_2Hf_2O_7$ structure is adopted by samples in the range $0 \leq x \leq 0.4$; those in the range $0.6 \leq x \leq 1.8$ crystallise in the tetragonal γ-$Bi_2Hf_2O_7$ structure; while $Bi_2Ti_2O_7$ is isostructural to δ-$Bi_2Hf_2O_7$. This increase in structural disorder with increasing Ti^{4+} content is also supported by Raman spectroscopy.

A series of samples of Ta_3N_5 (*Cmcm*, a = 3.89 Å, b = 10.22 Å, c = 10.28 Å) have been produced by high temperature ammonolysis of amorphous tantalum oxide under various temperature and heating time regimes. These have been characterised by powder diffraction (X-ray and neutron), combustion microanalysis, thermogravimetric analysis and transmission electron microscopy. All samples were found to contain oxide in the 3-coordinate anion site. Samples heated for longer times at higher temperatures were anion deficient. The compositions of the samples have been related to their optical band gap UV-visible spectra.

TABLE OF CONTENTS

PREFACE

CHAPTER 1: INTRODUCTION

CHAPTER 2: EXPERIMENTAL TECHNIQUES

CHAPTER 3: DEVELOPMENT OF HIGH THROUGHPUT METHODOLOGY

CHAPTER 3A: HIGH THROUGHPUT STUDY OF CHROMIUM DOPED PEROVSKITES

CHAPTER 3B: HIGH THROUGHPUT STUDY OF OXIDE-NITRIDE PEROVSKITES

CHAPTER 3C: HIGH THROUGHPUT STUDY OF CHROMITE SPINELS

CHAPTER 4: HIGH THROUGHPUT STUDY OF PHOSPHOR MATERIALS

CHAPTER 5: VARIABLE TEMPERATURE STUDY OF PYROCHLORE BISMUTH HAFNATE, $Bi_2Hf_2O_7$

CHAPTER 6: SYNTHESIS, STUCTURE AND PHYSICAL PROPERTIES OF THE PYROCHLORE SERIES $Bi_2Hf_{2-X}Ti_XO_7$

CHAPTER 7: STRUCTURAL AND COMPOSITIONAL VARIATIONS IN Ta_3N_5 PRODUCED BY AMMONOLYSIS OF TANTALUM OXIDE

CHAPTER 8: CONCLUSIONS

DECLARATION

The material contained herein has not been submitted by the author for a degree at any other institution. The work was performed exclusively by the author, with the following exceptions. Neutron diffraction data for $Bi_2Hf_2O_7$ obtained using the HRPD instrument (Chapter 5) were collected by Dr. R. Ibberson (ISIS). Raman spectroscopy data for bismuth pyrochlores (Chapter 6) were collected by Dr. O. Shebanova (UCL).

ACKNOWLEDGEMENTS

Firstly I would like to thank my supervisors, Prof. Mark Weller and Dr. Andrew Hector for their excellent guidance and support over the course of my studies. I would also like to thank the following people for making the last few years both memorable and enjoyable. The Weller and Hector group members past and present, encompassing Vince, Jo, Fatty, Lee, Chris, Jenny, Alia (for comedy value), Nicola, Marianne, Tom, Seth, Andrew, Rina, Florian and Rosa. All members of the inorganic floor, particularly Bav, Tony, Colin, Robin and many others who have been good company along the way.

Particular thanks must go to Bob Hughes for all his help and for diligently proof reading this work and pretty much everything I have written during my PhD. A special mention is reserved for Mark 'Humanzee' Hogben and Peter Hickey for providing endless banter and generally being thoroughly good blokes. I doubt my pool or poker skills will ever be as refined again.

Finally, and most importantly, I must thank the people who mean the most to me. My family, Mum, Dad and Helen, for their love and support and for providing me with the opportunities to get me here and Laura, whose boundless optimism and encouragement was crucial in the completion of this work.

LIST OF ABBREVIATIONS USED

DTA	Differential Thermal Analysis
EDAX	Energy Dispersive Analysis of X-rays
esd	Estimated Standard Deviation
GSAS	General Structure Analysis System
HRPD	High Resolution Powder Diffractometer
JCPDS	Joint Committee on Powder Diffraction Standards
PND	Powder Neutron Diffraction
PSD	Position Sensitive Detector
PXD	Powder X-ray Diffraction
SEM	Scanning Electron Microscopy
TGA	Thermogravimetric Analysis
TOF	Time of Flight
UV-Vis.	Ultraviolet-Visible
VT-PXD	Variable Temperature Powder X-ray Diffraction

Chapter 1

Introduction

1.1 Introduction

Complex metal oxides and the related mixed anion oxide-nitride compounds have many industrial applications which result from the chemical and physical properties of the materials.[1] Consequently both the structural chemistry and physical properties of such compounds have been the focus of numerous studies in the last fifty years. These materials display a variety of characteristics that are exploited, including their optical, electrical and magnetic properties. Examples of the applications of these complexes include pigments, phosphors, solid state devices such as capacitors or magnets, catalysts, heating elements (due to their good thermal stability and shock resistance) and rechargeable batteries. The properties of these materials are greatly influenced by the preparative conditions, which can vary crystallite morphology and anion content and also by their stoichiometry.

Considering the number of possible combinations of elements and processing conditions, there are a staggering number of permutations for complex materials. With the ever increasing demand for new materials there is a need for techniques that can search these numerous possibilities for compounds optimised for specific industrial applications. High throughput methods provide a means of creating and testing large numbers of compounds rapidly and, when used in combination with traditional laboratory techniques, can provide an economically viable solution to the pursuit of novel materials

Having identified novel phases, structural and physical characterisation is paramount in the understanding of their chemistry and potential industrial viability. Many different experimental techniques exist for the characterisation of materials, giving information on their optical and electronic behaviour, the metal and anion composition and their location within an extended lattice.

Such techniques are utilised in this study in combination with high throughput and standard solid state preparation techniques to study potential optical and dielectric materials.

1.2 High Throughput Materials Chemistry

Combinatorial and high throughput methods have been utilised in the pharmaceutical industry for many years. The process allows the simultaneous synthesis of libraries containing thousands of compounds, which can then be screened for desirable properties. Libraries are created using automated liquid handling equipment for parallel, multi-step syntheses. Rapid screening for biological activity, usually the ability of the drug to bind to a receptor, is then carried out. More recently the concepts of parallel synthesis and high throughput screening have emerged as effective strategies in the search for novel inorganic materials.[2] This approach has been successful in developing new optical and magnetic materials and in areas such as polymers and catalysts.

1.2.1 Background

The primary aim of combinatorial chemistry for organic synthesis especially in pharmaceutical research is to find single compounds which are effective as drugs. The total number of drug-like molecules that are candidates is estimated to exceed 10^{63} compounds. If 1 mg of each were prepared the total mass would be 100 times that of the universe. Hence, strategies were developed to determine which small portion of these possibilities should be given the greatest chance of progressing through the development process.[3] Many different strategies have been developed such as the split-pool method and parallel synthesis (Figure 1.2.1).[4] The most common current strategy is one of diversity, where a subset of compounds is selected which represents the chemical space under investigation. Metrics are thus required to describe this space. These can be derived from properties that can be easily calculated from the structure of the compounds. Similarity coefficients are calculated and compounds selected for libraries using cluster, dissimilarity or partition-based methods. Although many new drugs have been developed from such strategies there is still debate as to whether they are any more efficient than purely random screening.

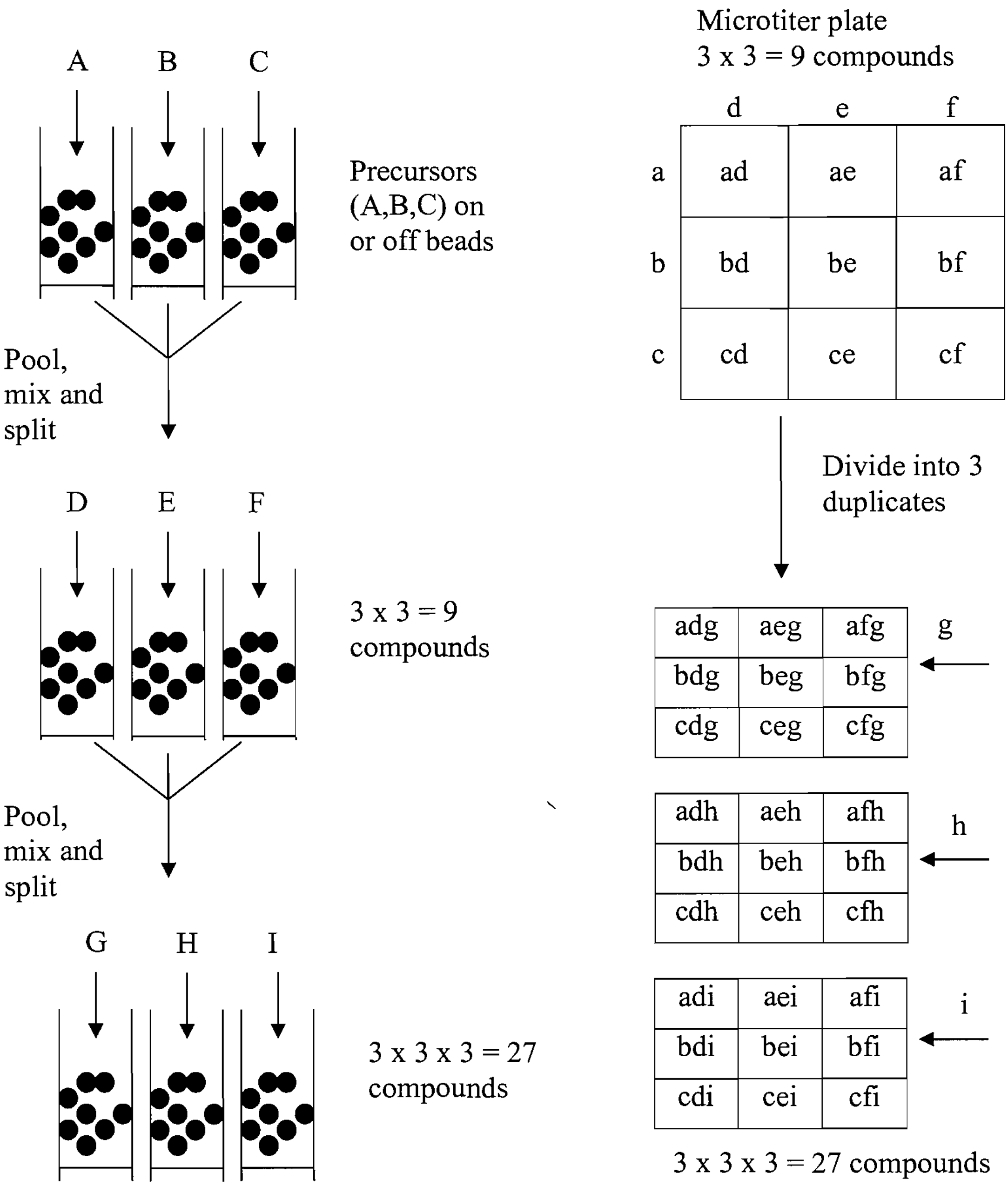

Figure 1.2.1 Split-pool (left) and parallel (right) library synthesis.

Combinatorial methods for materials development face challenges which are different to those in the pharmaceutical field; Table 1.2.1 compares the two fields. The properties for which the material needs to be screened are much more varied and are often unique for each system. There are no systematic methods for predicting structures and it is often the case that physical treatments are very significant in determining which phase forms. The strategies which have been developed are also different from the organic model. Split pool and parallel synthesis are typically replaced by high throughput array strategies such as gradient arrays or quaternary mask arrays.[3] The systems in this study are analogous to high speed versions of conventional experiments and hence are more appropriately termed high throughput rather than combinatorial.

Table 1.2.1. Comparison of pharmaceutical and materials development approaches to high throughput chemistry.

Pharmaceuticals	Materials development
• Focused on chemical synthesis • Emphasis on diversity • Easy sample evaluation on nanogram scale	• Synthesis, mixtures and process variables • Emphasis on broad coverage • Evaluation difficult and individual for each system

1.2.2 Thin Films

The first reports of the use of high throughput materials chemistry were in the 1960s where Kennedy[5] used combinatorial electron-beam co-evaporation to produce a ternary-alloy phase library. However, it was not until Xiang and Shultz[6] described the preparation of 128 member thin film libraries in 1995, that the technique saw a resurgence of interest. Since then the majority of inorganic combinatorial experiments have been based around thin film arrays.

The libraries are prepared by various deposition methods such as pulsed laser deposition (PLD)[7] or molecular beam epitaxy (MBE)[8] and generally fall into two categories. Either discrete samples are made by deposition through masking systems or continuous composition/thickness gradient films are produced. Xiang *et al.* began by using an RF magnetron sputtering gun in conjunction with a binary masking system (see Figure 1.2.2). They successfully created libraries of copper-based superconductors[6] and cobalt oxide magnetoresistance materials[9] with samples as small as 200 μm^2. Layers of precursors were deposited sequentially through the masks and the resulting films annealed to give the desired phases.

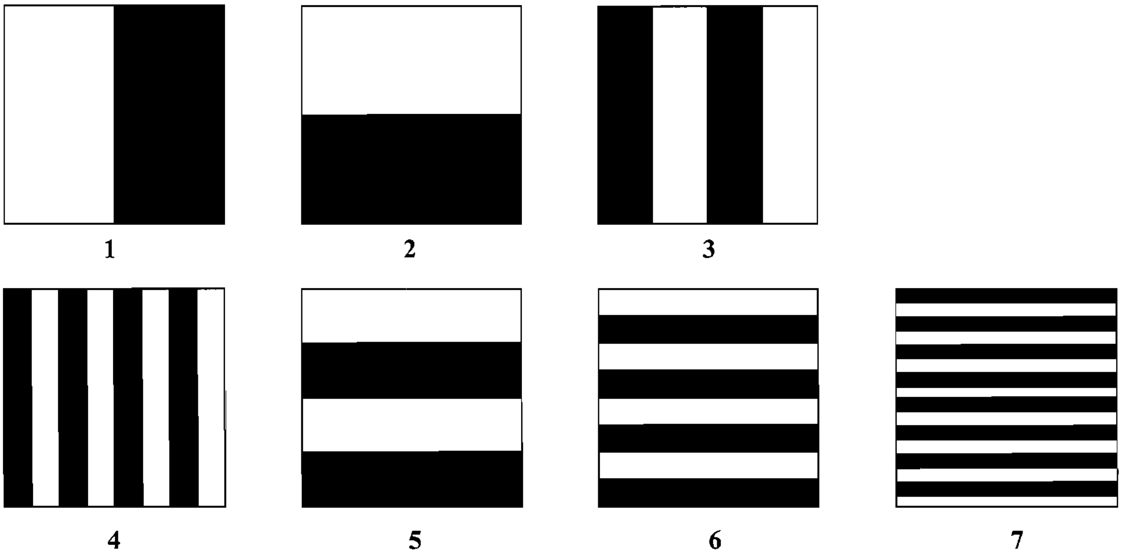

Figure 1.2.2 Binary shadow masks used for library synthesis.[10]

Gradient libraries use similar techniques except they apply a thickness gradient as well as composition. The properties of films can be greatly affected by their thickness so this technique can be extremely useful. Gradient arrays were used to prepare libraries of potential phosphor materials eventually leading to the discovery of Sr_2CeO_4.[11] Initial discovery gradient libraries were followed by more focused arrays and eventually bulk synthesis and characterisation. The libraries were screened at each stage for UV photoluminescence behaviour. This case study highlights some of the benefits and disadvantages of thin films. The main issue is that unless arrays can be screened rapidly for a particular property there is little point in rapid synthesis. Phosphorescence is easily measured over the whole array whereas more subtle properties such as superconductivity may be difficult to measure on such small samples. The second and most crucial point is that many thin film materials may not be reproducible as bulk powders as required by industry. Therefore intermediate methods must be developed for producing arrays of powdered samples, whose properties are representative of their bulk behaviour.

1.2.3 Hydrothermal Methods

The area of hydrothermal synthesis has many possible composition and process variables. Akporiaye realised the potential benefit of combinatorial hydrothermal methods for synthesising zeolites.[12] They produced phase diagrams mapping the structures formed in ternary and quaternary systems. They designed a Teflon block with a hundred reaction wells sealed with Teflon coated septa (Figure 1.2.3). Stacking of plates led to around a thousand combinations possible in one experiment which could then be characterised by conventional X-ray diffraction. These methods have been further developed by Maier[13] and Bein.[14] Maier introduced silicon wafers as reaction substrates, which eliminates the need for processing samples individually. The wafers were screened using automated X-ray diffraction. The continued improvements to the method enable wells of just 6 μl with reaction volumes as small as 2 μl in each of the 347 wells.

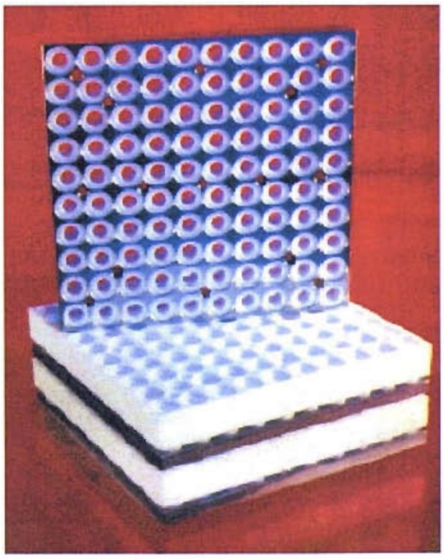

Figure 1.2.3 Multiautoclave design used by Akporiaye.[12]

However, there are still a number of problems associated with the technique, some of which are also applicable to this study. These include inhomogeneities of precursor mixtures; dispensing small volumes of fluids with varying viscosities; mixing of well contents under reaction conditions; and contamination from debris, dirt or chemical attack on multiclave components.[15] There are also challenges in designing systems that maintain a constant reaction temperature across the array and that do not leak.

1.2.4 Ceramic and Ink Jet Methods

As mentioned in section 1.2.1 it is necessary to develop ways of scaling up potential target materials from thin film discovery libraries to give more focused powdered arrays. Libraries of powdered materials will be a powerful discovery tool as some screening methods may only be viable on larger samples. Some compositions are only be accessible through solution methods as mixing occurs at the molecular level, reducing the need for high temperature interdiffusion in solid state reactions. These methods also provide a more viable option to most research groups than thin film arrays, requiring equipment which is available in many organic chemistry groups.

Sun and Jabbour described the use of both an ink-jet system and a conventional automated liquid dispenser for preparing high density powder phosphor libraries.[16] The ink-jet system produced libraries of phosphors with up to 100 samples per square inch. However, this system proved not to be as reliable as the commercially available liquid handler. Up to eight different metal precursors were dispensed into an alumina plate with 128 machined wells. After heat treatment, the library was screened for activity under UV excitation and characterised by X-ray diffraction and X-ray fluorescence using a synchrotron X-ray source. The starting precursors are not described in detail but it is likely that they are ink solutions of some kind.

Inks and nano-particle slurries as well as sol-gel routes have also been investigated by Yanase who produced sixteen member arrays on platinum pallets.[17] They have looked at battery materials such as $LiCo_{1-x}Mn_xO_2$ $(0 \leq x \leq 0.2)$[18] and doping of metal oxides in to the maghemite structure.[19] Here the screening is based more on traditional structure and composition analysis by thermal analysis, X-ray diffraction that described in this study and provides a useful comparison. However, with only sixteen samples being produced at once this may not be considered as a truly high throughput experiment. Measurement of electrochemical properties of ink derived materials on a 64 member electrode array has also been demonstrated at Southampton.[21] The electrode arrays were prepared using the same equipment as this work so comparable accuracy of composition and characterisation may be expected.

The largest effort towards high throughput ink-jet produced arrays is the London University Search Instrument (LUSI) at Queen Mary, University of London.[22] The integrated system comprises an eight head ink-jet printer with 20 nl dispensing capability (Figure 1.2.4), a four zone atmosphere controlled furnace, and a three-axis measurement table. Around 100 alumina slides can have up to 50 different precursor inks printed on them in any combination. Slides can be analysed by a luminescence spectrometer, superconductivity detector, an impedance/gain phase analyser and by high performance liquid chromatography (HPLC). All the components can be controlled by one interface and can be accessed by many different groups. The eventual aim is for the system to steer the search itself by identifying critical parts of parameter space.

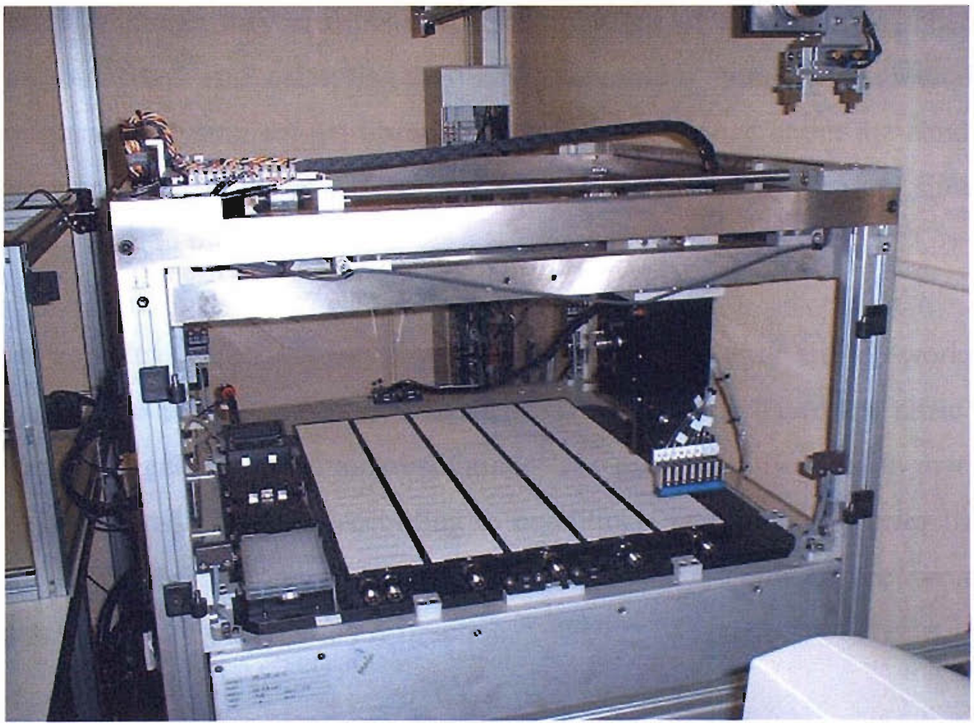

Figure 1.2.4 The ink-jet module of the LUSI instrument.[23]

1.2.5 Sol-gel and Polymer Complex Methods

Sol-gel techniques should be useful in array deposition because precursors may be mixed at the molecular level. Their properties are also greatly affected by processing conditions which can be explored by combinatorial methods. Conventional equipment available for organic liquid dispensing should be appropriate for handling precursors. There are, however, few reports describing high throughput sol-gel synthesis.

Rantala assessed the potential of combinatorial sol-gel methods, mainly focusing on the processing variables that can influence the materials performance.[24] Sol-gel derived antimony-doped tin dioxide films were treated by argon RF-plasma by varying amounts on a single spot. Segments were measured for resistance, thickness and refractive index. This is a different approach to the majority of combinatorial materials development, which have concentrated on varying composition rather than processing conditions.

The main group currently developing sol-gel techniques is at Symyx Technologies in California. Although they are involved in many areas of combinatorial chemistry such as thin films and catalysis, they have patented a number of methods for preparing and analysing sol-gel libraries.[25] Little is mentioned about the conditions or equipment used, however the reagents and solvents listed for use are similar to those being used in this study.

Polymer complex methods have been used extensively by Park and co-workers in Korea to create phosphor libraries.[26-28] Their methods are based on citric acid/ ethylene glycol gels of mixed metal solutions. The arrays are prepared in machined alumina plates and processed according to conditions determined by prior thermal analysis. Libraries are screened for UV and VUV excitation before promising candidates are analysed by X-ray diffraction.[29]

The overall aim of this study is to develop high throughput methods for preparing and undertaking preliminary characterisation of complex oxides and oxide nitrides. Methods of synthesising such materials in arrays using ceramic sol gel type methods are described together with results on three material classes (Chapters 3A-C). Methods of and problems in investigating the key optical properties of these compounds are also discussed (Chapter 3).

1.3 Inorganic Pigments

1.3.1 Background

A pigment can be defined as '...a coloured, black, white or fluorescent particulate organic or inorganic solid, which is usually insoluble in and essentially physically and chemically unaffected by the vehicle or substrate into which it is incorporated. A pigment will alter appearance by selective absorption and/or scattering of light. The pigment is usually dispersed in a vehicle for application in, for example, the manufacture of paints, plastics or other polymeric materials and inks. The pigment will retain its own unique crystalline or particulate structure throughout the incorporation period.[30]

Inorganic pigments account for around 96% of all the pigments synthesised world-wide. They therefore form a very important class of inorganic materials with applications ranging from ceramics and building materials, to artists colours and cosmetics. Total world production of white, black and coloured pigments reached 5.7 million tons in 1999, with titanium dioxide accounting for around 68% of the total.[31]

There are a multitude of inorganic pigments, some derived from coloured transition metal oxides *i.e.* α-Fe_2O_3 (red to violet), Cr_2O_3 (green) and $CoAl_2O_4$ (blue), with others based on charge transfer compounds such as cadmium sulphide. The different types of pigment can be grouped together into the five categories as shown in Table 1.3.1. There has been growing concern about the use of heavy metals such as lead and cadmium in materials. This has resulted in tighter health and safety regulations and hence an increased effort to produce industrial inorganic pigments with less toxic elements.[32]

Table 1.3.1 Classification of pigments.

Type	Definition
White	Optical effect caused by non-selective light scattering (e.g. TiO_2).
Coloured	Optical effect caused by selective light absorption and selective light scattering (e.g. Fe oxides and Cd, Cr, Co pigments).
Black	Optical effect caused by non-selective light absorption (e.g. Carbon black, Fe oxide black)
Lustre	Optical effect caused by regular reflection or interference (e.g. Al flakes, mica)
Luminescent	Optical effect caused by capacity to absorb radiation and emit it as light of longer wavelength (e.g. Ag doped ZnS (fluorescent), Cu doped ZnS (phosphorescent)).

This study focuses on the investigation of coloured and luminescent materials using high throughput and standard methods. The two main types of coloured pigment studied are mixed metal oxide pigments and mixed anion oxide-nitride pigments. Luminescent materials are discussed in Section 1.4.

1.3.2 Mixed Metal Oxide Pigments

A mixed metal pigment is one that has crystallised in a stable oxide lattice. The colour is often a result of the incorporation of 'coloured' cations within the structure. These cations have partially filled d or f shells, permitting transitions between levels within those shells, with the absorption of energy at optical frequencies. The most common colouring ions are those of the first transition series, vanadium through to copper.

The excellent stability of these oxide materials allows these pigments to be used for applications where resistance to chemicals and weathering is important; for example when incorporated in exterior paints and masonry coatings. This stability also renders metal oxide pigments relatively inert; toxicological investigations for spinel and rutile-type pigments have shown that they can be classified as non-toxic despite containing heavy metals.[33,34]

Examples of mixed metal oxide pigments include *Nickel Rutile Yellow* which has the composition $(Ti_{0.85}Sb_{0.10}Ni_{0.05})O_2$ and *Spinel Black* with the composition $CuFe_{0.5}Cr_{1.5}O_4$.

1.3.3 Mixed Anion Oxide-Nitride Pigments

Generally oxide-nitride compounds can be thought of as oxides in which oxygen has partially been replaced by nitrogen. Therefore their structure types and properties can be easily compared with those of the parent oxide.[35] The most common route to oxide-nitrides is the reaction of an oxide precursor with flowing ammonia gas at elevated temperatures. Above 550 °C NH_3 decomposes into active species that can act as both nitriding (oxidising) and reducing agents towards starting materials. Therefore nitrogen can be incorporated while hydrogen combines with oxygen atoms, eliminating them as water vapour.

$$\text{oxide} + NH_3(g) \rightarrow \text{oxide-nitride} + H_2O^{\uparrow}(g)$$

There are however no systematic rules regarding ammonolysis. Each system reacts differently as a function of several intrinsic (reacting components) or extrinsic (temperature, reaction time, gas flow rate) parameters. It is this non-systematic behaviour which makes high throughput techniques particularly suitable for oxide-nitride systems. Both the intrinsic and extrinsic properties can be investigated using composition gradients at different temperatures, flow rates etc.

Oxide-nitrides have an ionocovalent character; the ionic character is more significant when the metal elements associated with nitrogen are more electropositive.[36] The electroneutrality of the compound can be maintained in two ways. The first applies a cross-substitution principle which allows the same stoichiometry to be kept. This generally involves replacing divalent alkaline earth or monovalent alkali cations with trivalent rare-earth elements which form strong bonds with nitrogen:

$$R^{3+} + N^{3-} = Ca^{2+} + O^{2-}$$

$$R^{3+} + 2N^{3-} = Na^{1+} + 2O^{2-}$$

The second case compensates by replacing three oxygens with two nitrogens and is particularly favourable if the lattice is flexible enough to accept the resulting anion vacancies.[37]

The colour of solids arises from the selective absorption of light. Electronic interband transitions occur, leading to a steep absorption edge in the visible region of the electromagnetic spectrum. The width of the bandgap between the conduction band and the valence band is determined by the extent to which valence orbitals overlap. The distance between the bands also alters according to the differences in electronegativity of the cations and anions involved. The majority of metal oxides have very wide bandgaps which do not allow absorption in the visible spectrum. The bandgap energy can be reduced by up to ~1 eV through nitridation of oxides, as nitrogen has a lower electronegativity than oxygen.

The replacement of oxygen by nitrogen often results in a highly coloured compound and for this reason oxide-nitrides have been investigated by a number of groups as potential pigments.[38] Jansen and Letschert investigated solid solutions of the $CaTaO_2N$ and $LaTaON_2$ perovskite systems as potential replacements for cadmium based red and yellow pigments.[39] The colour can be tuned from bright yellow to deep red depending on the O to N ratio in the $Ca_{(1-x)}La_xTaO_{(2-x)}N_{(1-x)}$ system. Typically oxide-nitrides are thermally stable to 400 °C after which they begin to release nitrogen and take up oxygen.[40,41] Therefore they may find uses as non-toxic pigments for plastics, make-up and other medium temperature applications.

1.4 Luminescent Materials

Luminescence is an emission of ultraviolet, visible or infrared photons from an electronically excited species. The word luminescence derives from the Latin, *lumen* meaning light and was first introduced as *luminescenz* by the physicist Eilhardt Wiedermann in 1888, to describe 'all those phenomena of light which are not solely conditioned by the rise in temperature', as opposed to incandescence.[42] The various types of luminescence can be classified according to the mode of excitation (Table 1.4.1)

Table 1.4.1 Classification of various types of luminescence.

Phenomenon	Mode of excitation
Photoluminescence (fluorescence, phosphorescence/delayed fluorescence)	Absorption of light (photons)
Radioluminescence	Ionizing radiation (X-rays, α, β, γ)
Cathodoluminescence	Cathode rays (electron beams)
Electroluminescence	Electric field
Thermoluminescence	Heating after prior storage of energy (e.g. radioactive irradiation)
Chemiluminescence	Chemical process (e.g. oxidation)
Bioluminescence	Biochemical process
Triboluminescence	Frictional and electrostatic forces
Sonoluminescence	Ultrasounds

There are numerous different kinds of luminescent compounds such as organic compounds (*e.g.* aromatic hydrocarbons or fluorescein), inorganic compounds (*e.g.* uranyl ion, UO_2^+ or lanthanide ions) or organometallic compounds (*e.g.* $Ru(biPy)_3$). This study focuses on applying high throughput methods to investigate photoluminescent inorganic solids, frequently referred to as phosphors.

Two main categories of photoluminescence exist: fluorescence, for which the period between the absorption and emission of a photon is less than 10^{-8} s, and phosphorescence, for which the delay times are much longer.[43] Phosphor materials typically consist of a host structure into which an activator ion is introduced by doping. The host may be any inorganic extended lattice structure such as ZnS, $CaWO_4$ or Y_2O_3 and are usually colourless. The activator ion is generally a lanthanoid ion (Eu^{3+}, Tb^{3+} *etc.*) or certain *d*-block metals (Mn^{2+}, Cu^{2+} *etc.*) although other ions also have the ability to absorb and emit light at appropriate wavelengths, such as Bi^{3+}.[44] A second dopant may also be added to aid the absorption of light of the desired wavelength (sensitiser) or to extend the period of luminescence (*e.g.* $SrAl_2O_4$:Eu^{2+}, Dy^{3+}).[45]

Phosphor materials find applications in fluorescent lamps and television screens, where there is a need for materials that fluoresce in specific regions of the visible spectrum. For example, in many fluorescent lamps a mercury discharge produces UV radiation at 254 and 185 nm. A coating consisting of ZnS doped with various activators then produces fluorescences at several wavelengths that combine to give an effective white light.

1.5 Dielectric Materials

Band theory is used to understand the way in which electrons are held in metals, semiconductors and insulators whereby the electron energy levels are broadened into energy bands. It is derived from molecular orbital theory and the bonding within an infinitely large molecule, *i.e.* a solid.

The overlap of a large number of atomic orbitals in a solid leads to a large number of molecular orbitals that are closely spaced in energy and so form an almost continuous band of energy levels (Figure 1.5.1). These bands are separated by band gaps, which are values of the energy for which there is no molecular orbital.[43] The nature of these bands determines the electronic properties of the solid. For example, if these materials are coloured it is due to electronic transitions within and between these bands.

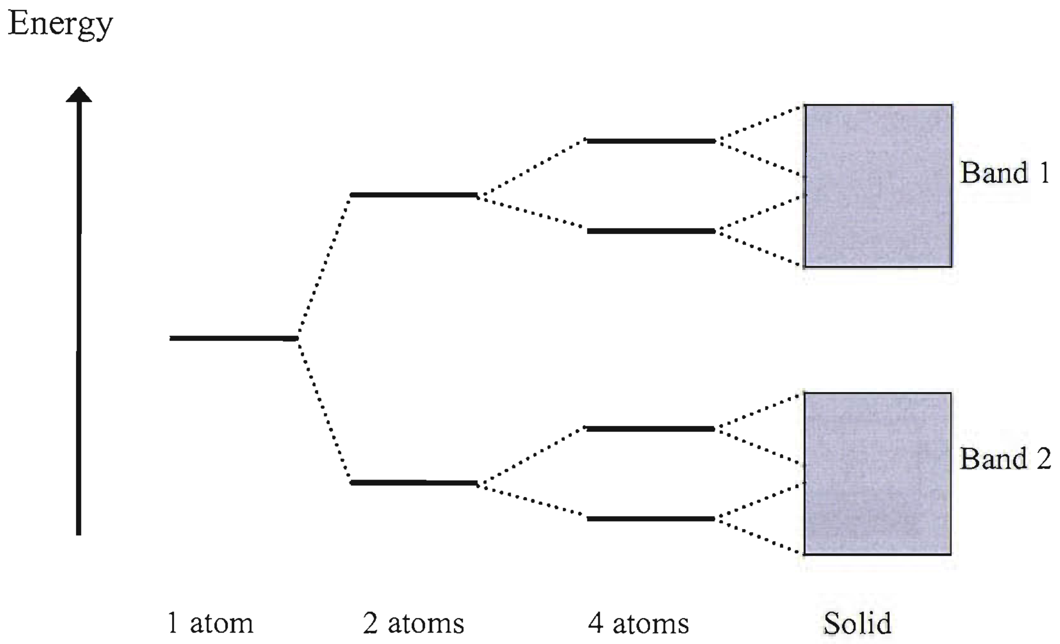

Figure 1.5.1 The formation of energy bands within a solid from the constituent atomic orbitals.

The uppermost of these two bands, *i.e.* that of higher energy, is called the conduction band. Conversely the lower energy band is named the valence band. In each orbital it is possible to have two electrons in opposing spin directions. In a completely filled band the net motion of electrons is zero and the conductivity is therefore also zero. Metals are materials in which the valence band is full and the conduction band partially filled. The highest energy attained by the electrons in the conduction band is known as the *Fermi level* (Figure 1.5.2). When an electric field is applied, the electrons at the top of the valence band can move into other orbitals, resulting in a net movement of charge within the solid, hence metals are conducting solids.

For semiconductors and insulators, also known as dielectrics, the conduction band contains no electrons and the valence band is completely filled. Intrinsic semiconductors have a band gap of around 0.1- 3 eV, which means it is possible for some electrons of sufficient energy, gained through thermal excitation *etc.*, to transfer from the top of the valence band to the bottom of the conduction band at room temperature leaving behind a vacancy in the valence band. These vacancies behave as positively charged particles and are labelled as positive *holes*. Hence with each transition two mobile charge carriers are created, an electron and a hole.

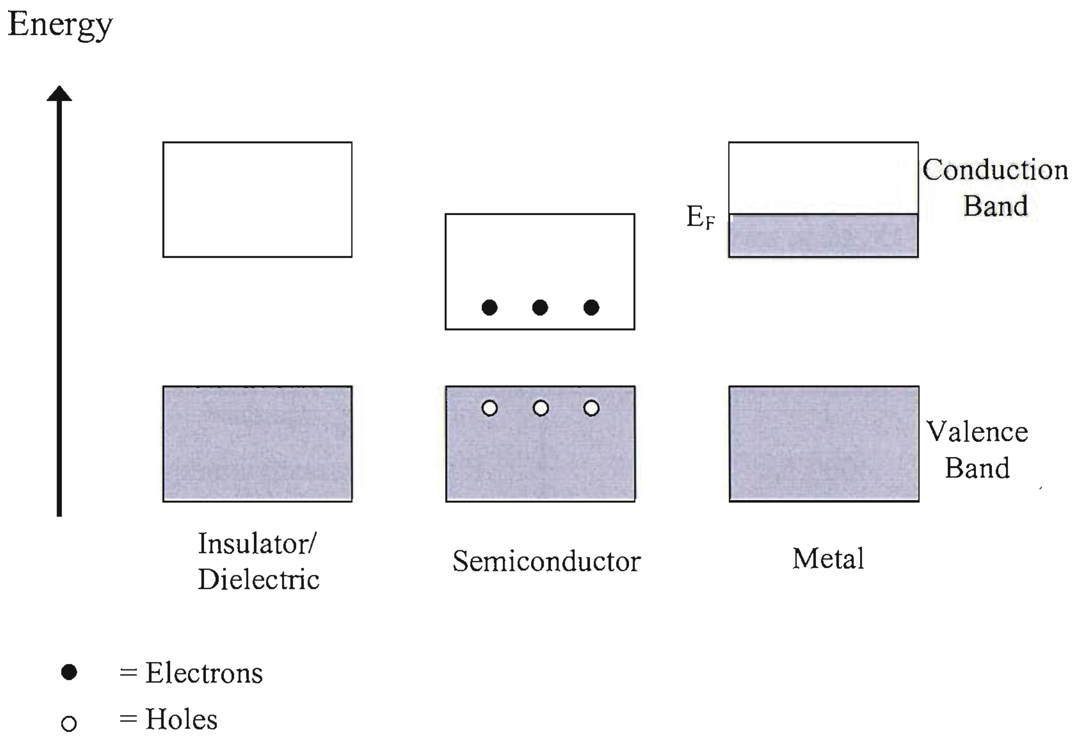

Figure 1.5.2 Schematic illustration of the energy bands in an insulator (left), a semiconductor (middle) and a metal (right), where E_F represents the Fermi level.

The energy gap for an insulator is typically much larger than for semiconductors, >12 eV for some ionic solids and it is this property that enables dielectric materials to be used as capacitors.

The capacitance of a condenser is increased if the space between the conductors is filled with a dielectric material. If C_0 is the capacitance of the condenser with the region between the conductors evacuated and C its capacitance when this region is filled with a dielectric, then the ratio

$$\frac{C}{C_0} = \varepsilon_r$$

is found to be solely a characteristic of the particular dielectric medium used. ε_r is called the relative permittivity or dielectric constant of the medium (Table 1.5.1). The relative permittivity of a material is a directly measurable quantity, which observed on a macroscopic scale between an externally applied field and the atoms or molecules of the material. This interaction is referred to as polarisation.

Table 1.5.1 The relative permittivity of some solid dielectrics at 25 °C.[46]

Dielectric	ε_r
Vacuum	1
Air (atmospheric pressure & 0 °C)	1.0006
Borosilicate glass	4.0
Diamond	5.5
Marble	~10-15
Rubber	~3-4
PVC	6
Mica	~6-11
Paraffin wax	2.3
Barium titanate	1200

Dielectric ceramics are widely used in microelectronic and microwave communication technologies.[47] Materials with high dielectric constants are particularly important in reducing the size of microelectronic circuits, where high permittivity and low dielectric loss are required for many applications.[48]

1.6 Crystal Structures

1.6.1 The Perovskite Structure

The mineral $CaTiO_3$ (perovskite) was first identified by the Russian mineralogist L. A. Perovski. Perovskite is the most abundant mineral on earth and its structure is adopted by several hundred materials with the stoichiometry ABO_3.[49]

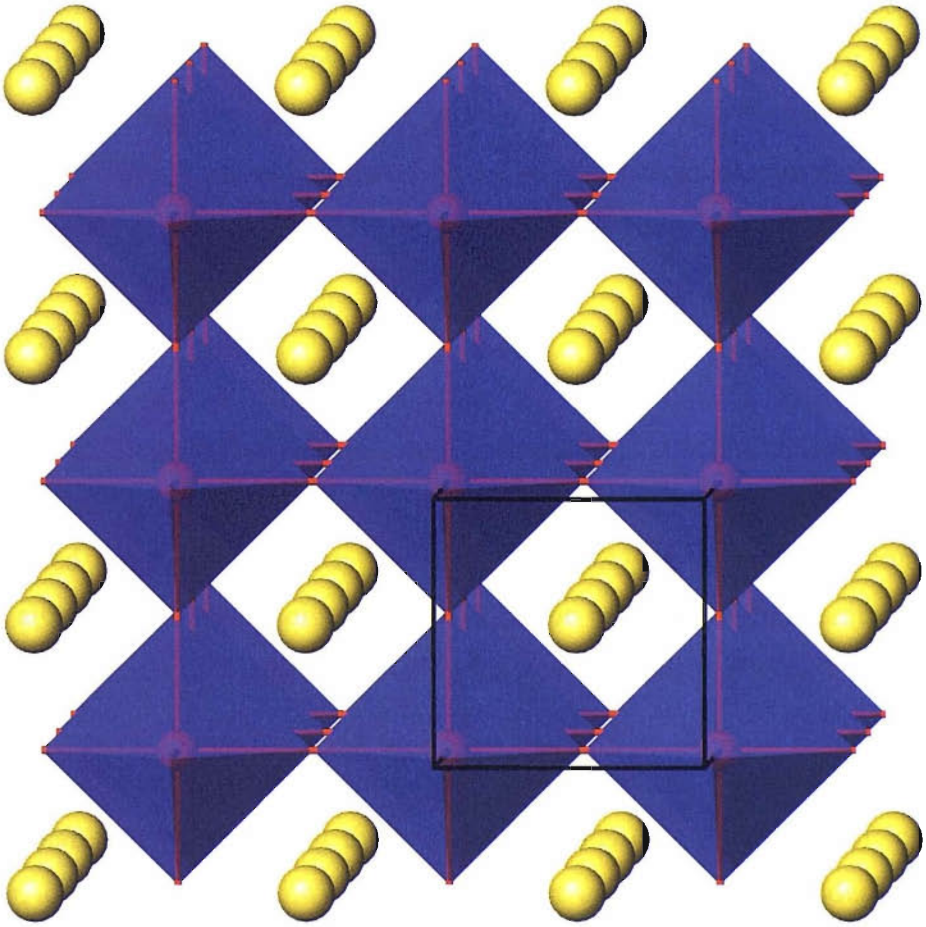

Figure 1.6.1 Representation of the perovskite structure showing the BO_6 octahdra network (purple) and the 12-coordinate A cation (yellow). The unit cell is shown as black lines.

The structure of a perovskite is based on a face centred cubic (*fcc*) lattice. The A and B atoms typically represent +2 and +4 cations respectively in the ABO_3 notation, however different cation types can also be incorporated (e.g. $La^{3+}Cr^{3+}O_3$). The corners of the unit cell are occupied by the six co-ordinate B cation with the twelve co-ordinate A atoms in the centre (Figure 1.6.1). The dimensions of the sites accommodating the A and B cations means that the structure is frequently adopted for ternary oxides with one large and one small cation; conventionally the larger is denoted as A. Shifting of the B atom due to applied electric fields will cause structural alterations, creating electric dipoles. This is often thought of as Jahn-Teller distortion due to the similarities with molecular species' behaviour.

The perovskite structure is highly stable and can vary in several ways according to the different cation types present. Distortion from ideal geometry towards a rhombohedral or orthorhombic geometry is a typical example. The structure can also incorporate defects or vacancies readily where oxygen anions are missing.

1.6.2 The Spinel Structure

Materials with the spinel crystal structure owe their name to the naturally occurring mineral magnesium aluminate ($MgAl_2O_4$). Their structure is based around a cubic close packed arrangement of oxygen ions.[43] In $MgAl_2O_4$ the unit cell contains 32 oxygen atoms, magnesium ions occupy 1/8 of the possible 64 tetrahedral sites and aluminium ions occupy 1/2 of the possible 32 octahedral sites (Figure 1.6.2).[50]

Magnesium aluminate itself is colourless, but colour can be introduced to form pigment materials by replacing the 'colourless' ions (Mg^{2+}, Al^{3+}) with 'coloured' ones *e.g.* cobalt, chromium, nickel, copper, iron *etc.* One of the oldest and most studied of these pigments is Cobalt Blue ($CoAl_2O_4$), a cobalt-aluminium spinel.

When one type of cation occupies the tetrahedral and half of the octahedral sites in the lattice and the remaining octahedral sites are occupied by the other cation the compound is known as an inverse spinel *e.g.* Zn_2TiO_4. The normal and inverse spinels are ideal limiting structures and in practice the structure obtained is often a mixture of the two with random distribution of the cations over the tetrahedral and octahedral sites. The distribution of the cations is influenced by their size, oxidation state and ligand field stabilisation energies.

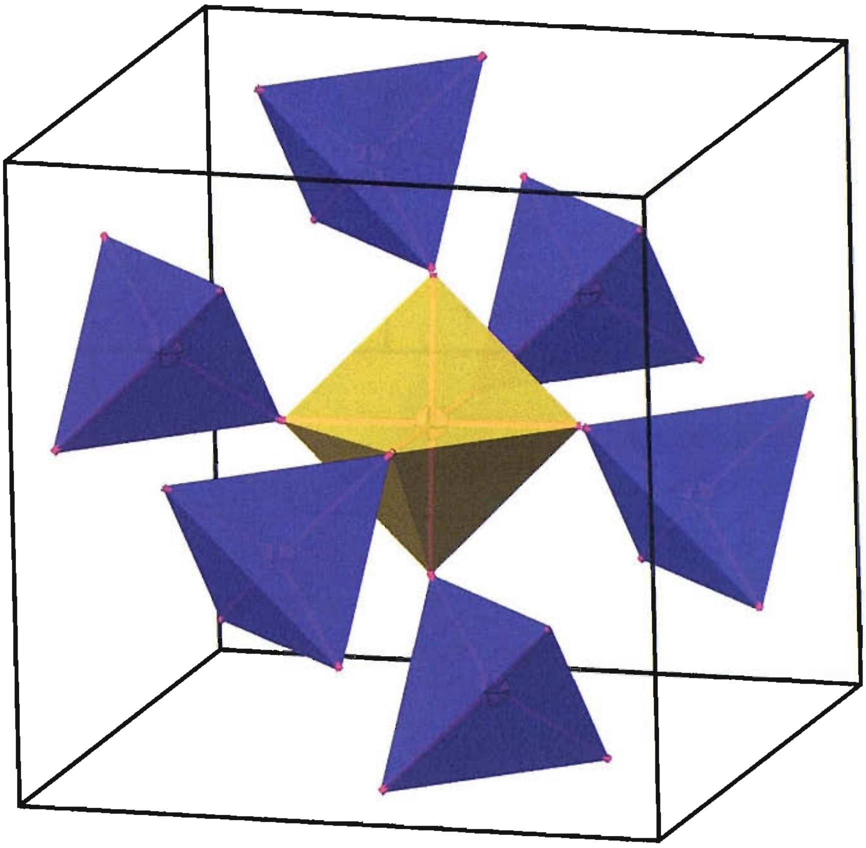

Figure 1.6.2 Representation of the spinel structure showing the tetrahedral AO_4 sites (purple) surrounding an octahedral BO_6 site (yellow).

There are numerous commercially available spinel pigments, making it the most common structure for inorganic pigments. Table 1.6.1 shows some examples of spinel pigments.

Table 1.6.1 Some pigments with the spinel structure.

Composition	Manufacturer	Colour
$CoCr_2O_4$	Ferro	Turquoise
$(Co,Ni,Zn)_2(Ti,Al)O_4$	Bayer	Green
Co_2TiO_4	Ferro	Green
$Co(Al,Cr)_2O_4$	Bayer	Blue/Green
$CoAl_2O_4$	Bayer	Blue
$(Zn,Fe)Fe_2O_4$	Ferro	Brown
$Cu(Cr,Fe)_2O_4$	Bayer	Black
$(Fe,Mn)(Fe,Mn)_2O_4$	Ferro	Black

1.6.3 The Pyrochlore Structure

Pyrochlore materials are complex oxides which are isostructural to the mineral pyrochlore, $(NaCa)(NbTa)O_6F/(OH)$. The mineral derives its name from the Greek nomenclature, *pyros* – a fire and *chloros* – green, as it turns green upon ignition. The compounds are predominantly cubic and have the general formula, $A_2B_2O_7$, where 'A' and 'B' are metals.[51] As with perovskite compounds, pyrochlore materials lend themselves to a variety of chemical substitutions at the 'A', 'B' and 'O' sites providing the ionic radius and charge neutrality criteria are satisfied. Considering only integral compositions there are two groups of cation combinations; (A^{3+}, B^{4+}) pyrochlores and (A^{2+}, B^{5+}) pyrochlores. Further compounds are accessible due to the ability of the crystal structure to tolerate vacancies at the 'A' and 'O' sites. This flexibility provokes interest in pyrochlore materials because they exhibit a wide range of interesting physical properties. Materials with electronic properties ranging from highly insulating to semi-conducting to metallic can be produced depending on the cation composition. Pyrochlore compounds have also shown properties such as superconductivity ($Cd_2Re_2O_7$ at ~1 K)[52] and potential as dielectric ($Bi_{1.5}ZnNb_{1.5}O_7$),[53] piezoelectric, ferroelectric ($Cd_2Nb_2O_7$)[54] and magnetic materials.

The pyrochlore formula $A_2B_2O_7$ can also be expressed as $A_2B_2O_6O'$ to distinguish the four crystallographically non-equivalent types of atom. The ideal form of pyrochlore crystallises in the cubic space group, $Fd\overline{3}m$. The structure consists of an 8 co-ordinate 'A' cation that usually has a radius of ~1 Å and a smaller (~0.6 Å), 6 co-ordinate 'B' cation. The 'B' cation arrangements are commonly referred to as BO_6 octahedra although this is not technically correct as due to the space group symmetry requirements the BO_6 units are not symmetrical octahedral.

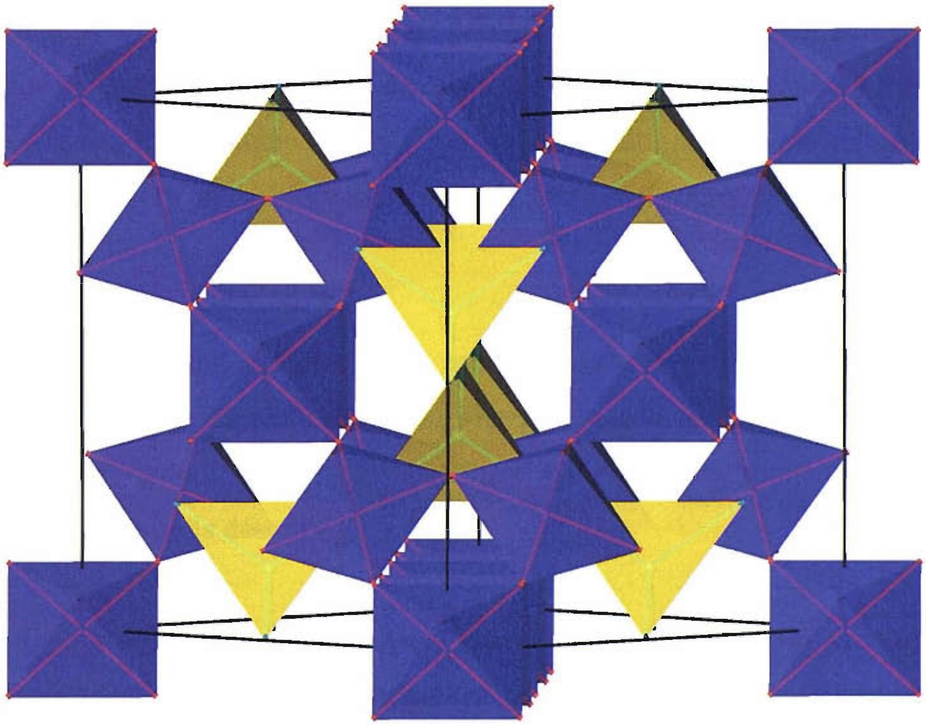

Figure 1.6.3 The pyrochlore structure highlighting the interpenetrating tetrahedral A_4O' (yellow) and octahedral BO_6 (purple) networks.

The structure can be considered as a 3D network of corner linked BO_6 units with the 'A' atoms in the resulting channels.[55] The eight co-ordinate 'A' cation is at the centre of a puckered hexagonal ring due to the (6+2) surrounding arrangement. The A-O' bond distance is shorter than the A-O distance. Therefore, by neglecting the A-O interaction the structure can be regarded as B_2O_6 and A_2O' units. The A_2O' linkages form zig-zag chains and two such chains intersect at O'. The structure can therefore also be viewed as interpenetrating networks of BO_6 octahdra and A_4O' tetrahedral (Figure 1.6.3).

1.7 Scope of the Work

The aim of this work is to investigate the use of both high throughput and standard methods for the synthesis and screening of materials with useful optical or dielectric properties. The systems studied range from metal oxide, nitride and oxide-nitride pigments to complex pyrochlore oxides with interesting structural and physical properties.

The work presented in Chapters Three and Four concerns the development and application of high throughput methods. The preparation and analysis of optical materials using automated liquid handling, X-ray diffraction, colour and fluorescence screening is described.

Chapters Five and Six present the synthesis, structure and physical properties of bismuth pyrochlore oxides. These materials have been investigated by a combination of high-resolution neutron diffraction, X-ray diffraction, Raman spectroscopy and dielectric measurement to probe their structure-property relationships.

In addition, the effect of synthetic conditions on the properties of the red pigment tantalum nitride is investigated in Chapter Seven. Powder neutron diffraction and UV-visible spectroscopy along with various compositional analysis techniques have been utilised to gain an insight into the optimum preparative method.

The findings of these investigations are summarised in Chapter Eight.

1.8 References

[1] M. A. Subramanian, G. Aravamundan and G. V. Subba Rao, *J. Solid State Chem.* **31** 329 (1980).

[2] R. Malhotra (Editor), '*Combinatorial Materials Development' (ACS Symposium Series 814)*, American Chemical Society, USA (2002).

[3] J. N. Cawse, *Acc. Chem. Res.* **34** 213 (2001).

[4] E. W. McFarland and W. H. Weinberg, *Trends Biotechnol.* **17** 107 (1999).

[5] E. J. Amis, X. D. Xiang and J. C. Zhao, *MRS Bull.* **27** 295 (2002).

[6] X. D. Xiang, X. Sun, G. Briceno, Y. Lou, K. A. Wang, H. Chang, W. G. Wallace-Freedman, S. W. Chen and P. G. Schultz, *Science* **268** 1738 (1995).

[7] I. Takeuchi, H. Chang, C. Gao, P. G. Schultz, X. D. Xiang, R. P. Sharma, M. J. Downes, and T. Venkatesan, *Appl. Phys. Lett.* **73** 894 (1998).

[8] K.Y. Yoo and F. Tsui, *MRS Bull.* **27** 316 (2002).

[9] G. Briceno, H. Chang, X. Sun, P. G. Schultz and X. D. Xiang, *Science* **270** 273 (1995).

[10] Y. K. Yoo and X. D. Xiang, *J. Phys.: Condens. Matter* **14** R49 (2002).

[11] E. Danielson, J. H. Golden, E. W. McFarland, C. M. Reaves, W. H. Weinberg and X. D. Wu, *Nature* **389** 944 (1997).

[12] D. E. Akporiaye, I. M. Dahl, A. Karlsson and R. Wendelbo, *Angew. Chem. Int. Ed.* **37** 609 (1998).

[13] J. Klein, C. W. Lehmann, H. W. Schmidt and W. F. Maier, *Angew. Chem. Int. Ed.*, **37** 3369 (1998).

[14] K. Choi, D. Gardener, N. Hilbrandt and T. Bein, *Angew. Chem. Int. Ed.* **38** 2891 (1999).

[15] J. M. Newsam, T. Bein, J. Klein W. F. Maier and W. Stichert, *Micropor. Mesopor. Mat.* **48** 355 (2001).

[16] T. X. Sun and G. E. Jabbour, *MRS Bull.* **27** 309 (2002).

[17] I. Yanase, T. Ohtaki and M. Watanabe, *Appl. Surf. Sci.* **189** 292 (2002).

[18] I. Yanase, T. Ohtaki and M. Watanabe, *Solid State Ionics* **151** 189 (2002).

[19] I. Yanase, T. Ohtaki and M Watanabe, *Solid State Ionics* **154** 419 (2002).

[20] I. Yanase, K. Fujimoto, K. Takada, T. Ohtaki and M. Watanabe, *Mat. Res. Soc. Symp. Proc.* **700** S5.1.1 (2002).

[21] A. D. Spong, G. Vitins, S. Guerin, B. E. Hayden, A. E. Russell and J. R. Owen, *J. Power Sources* **119** 778 (2003).

[22] J. Eames, M. J. Edirisinghe, J. R. G. Evans and P. V. Coveney, *J. Eur. Ceram. Soc.* **21** 2291 (2001).

[23] www.realitygrid.org/lusi/LUSI.html (2004).

[24] L. Kivimäki, T. Kololuoma and J. T. Rantala, *Proceedings of SPIE (Combinatorial and Composition Spread Techniques in Materials and Device Development)* **3941** 11 (2000).

[25] D. Giaquinta, M. Devenney, K. A. Hall, I. Goldwasser, P. G. Schultz, X. D. Xiang, E. McFarland and L. Matsiev, *Worldwide Patent Nos. WO0017413, WO9611878, WO9815501,* United States Patent Office (2000).

[26] H. D. Park, S. Y. Seo and K. S Sohn, *Electrochem. Solid-State Lett.* **4** H26 (2001).

[27] K. S. Sohn, I. W. Jeon, H. Chang, S. K. Lee and H. D. Park, *Chem. Mate*r. **14** 2140 (2002).

[28] K. S. Sohn, J. M. Lee, I. W. Jeon and H. D. Park, *J. Electrochem. Soc.* **150,** H182 (2003).

[29] S. Y. Seo, K. S. Sohn, H. D. Park and S. Lee, *J. Electrochem. Soc.* **149** H183 (2002).

[30] G. Buxbaum, *'Industrial Inorganic Pigments'* (*Second Edition*), Wiley-VCH, Germany (1998).

[31] Market Report, SRI Consulting, Menlo Park, CA, USA (2001).

[32] European Economic Community Guideline No. 91/338/ EWG (1991).

[33] E. Bomhard, *Toxicol. Lett.* **14** 189 (1982).

[34] D. Steinhoff and U. Mohr, *Exp. Pathol.* **41** 169 (1991).

[35] F. Tessier and R. Marchand, *J. Solid State Chem.* **171** 143 (2003).

[36] R. Marchand, *C.R. Acad. Sci.II C* **2** 669 (1999).

[37] N. Diot, O. Larcher, R. Marchand, J. Y. Kempf and P. Macaudière, *J. Alloy. Compd.* **323** 45 (2001).

[38] E. Guenther, R. Hagenmayer and M. Jansen, *Z. Anorg. Allg. Chem.* **626** 1519 (2000).

[39] M. Jansen and H. Letschert, *Nature*, **404** 980 (2000).

[40] J. C. Rooke and M. T. Weller, *Sol. St. Phen.* **90-91** 417 (2003).

[41] L. L. Gendre, R. Marchand and Y. Laurent, *J. Eur. Ceram. Soc.* **17** 1813 (1997).

[42] B. Valeur, *'Molecular Fluorescence: Principles and Applications'*, Wiley-VCH, Germany (2002).

[43] D. F. Shriver, P. W. Atkins, T. L. Overton, J. P. Rourke, M. T. Weller and F. A. Armstrong, *'Inorganic Chemistry' (Fourth Edition)*, Oxford University Press, UK (2006).

[44] A. M. Srivastava and W. W. Beers, *J. Luminesc.* **81** 293 (1999).

[45] C. Chang, D. Mao, J. Shen and C. Feng, *J. Alloy. Compd.* **348** 224 (2003).

[46] A. A. Zaky and R. Hawley, *'Dielectric Solids', Routledge and Kegan Paul Ltd., UK (1970).*

[47] H. Du and X. Yao, *Mater. Res. Bull.*, **40** 1527 (2005).

[48] H. C. Ling, M. F. Yan and W. W. Rhodes, *J. Mater. Res.* **5** 1752 (1990).

[49] M. T. Weller, *'Inorganic Materials Chemistry'*, Oxford University Press, UK (1994).

[50] A. R. West, *'Solid State Chemistry and its Applications'*, John Wiley & Sons Ltd., UK (1984).

[51] M. A. Subramanian, G. Aravamudan and G. V. Subba Rao, *Prog. Solid State Chem.* **15** 55 (1983).

[52] M. Hanawa, Y. Muraoka, T. Tayama, T. Sakakibara, J. Yamaura and Z. Hiroi, *Phys. Rev. Lett.* **87** 187001 (2001).

[53] I. Levin, T. G. Amos, J. C. Nino, T. A. Vanderah, C. A. Randall and M. T. Lanagan, *J. Solid State Chem.* **168** 69 (2002).

[54] W. R. Cook and H. Jaffe, *Phys. Rev.* **88** 1426 (1952).

[55] A. Byström, *Ark. Kemi min. Geol.* **18A** 1 (1945).

Chapter 2

Experimental Techniques

2.1 Introduction

The preparation and analysis of materials carried out in this study can be divided into two categories: high throughput and standard solid state methods. This chapter describes the theory of the general techniques used for both categories, as well as specific instrumentation used for analysing bulk samples. Detailed descriptions of the specific high throughput methods developed to prepare and analyse arrays in this study can be found in Chapter 3.

The main technique used for this work is powder X-ray diffraction (PXD). This provided the means for both initial phase identification and detailed structural characterisation. Powder neutron diffraction (PND) has also been employed to provide accurate structural information, especially on oxygen and nitrogen environments, which are readily resolved using this technique. The physical properties of the materials have been investigated by combinations of ultraviolet-visible (UV-Vis.) spectroscopy, electron microscopy and thermal analysis.

2.2 Synthetic Techniques

Reactions carried out in the solid state have very high activation energies so both thermodynamics and kinetics are taken into account. Reasonably high temperatures are therefore required for the synthesis to obtain an appreciable rate of reaction.[1] The rate of reaction is governed by ion diffusion between the component ionic lattices. This rate of diffusion is increased by elevated temperature but the stability of the target product at the reaction temperature must also be taken into account. A balance between temperature and reaction rate must therefore be maintained.

For traditional solid state reactions the components or their precursors, typically oxides or carbonates, are mixed by grinding with a pestle and mortar before heating. However, due to the small level of surface area contact between the reactants, the reaction time can be increased. This problem may be overcome by pressing the samples into pellets for firing. Regrinding during the course of the reaction also helps to increase the interfacial contact of the reactants, increasing the rate of reaction.

2.2.1 Precipitation Method

The large particle sizes of the reactants in solid-solid reaction often requires the use of high reaction temperatures and repeated milling to generate a material. This process is also difficult to automate for the purpose of high throughput experimentation. To overcome these problems reactive precursors can be synthesised from solutions, where the reactant ions are dispersed on the atomic scale.[2] Precipitation from mixed ion solutions will produce a solid containing the ratio of ions required to achieve the desired stoichiometry. For example metal nitrates dissolved in dilute nitric acid can be precipitated simultaneously by the addition of a basic solution such as ammonium hydroxide. The resulting intimate mixture of ions gives improved solid state diffusion and typically requires significantly lower reaction temperatures and shorter reaction times.

2.2.2 Gel Routes

Precipitation methods have many advantages but it can be difficult to ensure the precipitate has the desired stoichiometry and thus control the morphology of the product. Materials can be produced in a more controlled manner from a solution of molecules, which can be linked by condensation reactions. This leads to a viscous, polymeric material which can be strengthened by ageing then dried. As condensation reactions proceed a stable suspension of amorphous or crystalline particles forms (sol). A 3-dimensional solid network eventually forms around a continuous liquid phase (wet gel). Sol particles can be connected by covalent bonds, H-bonds, Van der Waals forces or entanglement of polymer chains. In materials synthesis the gel formation is usually through covalent bonds and is irreversible. The resulting gels can then be processed to give a number of useful forms. For example evaporating the solvent from gels gives a xerogel, which can then be dried to form a dense glass or ceramic.[3]

Silicon alkoxides are often used to form silica gels through hydrolysis reactions followed by condensation. These reactions require nucleophilic attack on the silicon but as silicon is not particularly electropositive, acid or base catalysis is required. In contrast metal alkoxides are less electronegative leading to much faster hydrolysis rates than for $Si(OR)_4$ ($Ti(OR)_4$ ~10^5 times faster). As gel formation is promoted by slower reaction, metal alkoxide sol-gels require control of the reactivity. This may include the correct choice of solvent to control oligomer formation or the use of chemical moderators to block vacant coordination sites with slow-hydrolysing bidentate ligands. For example, a sol-gel process described by Guenther and Jansen used metal alkoxides, $Ta(OEt)_5$ and $Zr(OPr)_4$, with acetic acid as solvent and acetic anhydride as a moderator.[4] This method was used as the basis for library preparation (Chapter 3B).

Gels can also be formed by polymer complex methods such as the Pechinni process.[5] In this case, rather than organometallic species reacting directly together, a separate complexing agent is added to aqueous metal salt solutions. The most commonly used agent is citric acid as it is soluble in water and its solution is stable in air. This is often combined with a gelling agent such as ethylene glycol to speed up the formation of a viscous gel. Arrays were prepared using this technique as outlined in Chapter 3A. These gels allow crystalline products to be formed at much lower temperatures than via solid state routes and can provide more control over the stoichiometry of the final product.

2.3 Powder X-ray Diffraction (PXD)

2.3.1 Theory

X-ray diffraction is a technique used to measure the atomic arrangement of materials. When a monochromatic beam of electromagnetic radiation, such as X-rays, interacts with a sample it can be scattered or deflected away from its original direction of propagation. Coherent scattering results if the wavelength is unchanged from that of the incident beam, if the wavelength is altered scattering is incoherent. The coherent scattering of X-rays from a sample is not evenly distributed but is a function of the electron distribution in the sample. Scattering from ordered materials can therefore form a specific diffraction pattern which is the 'fingerprint' of the sample. Radiation with comparable wavelength to interatomic distances (~1 Å) is required for such diffraction, hence copper $K_{\alpha 1}$ emission (λ = 1.5406 Å) is commonly used.

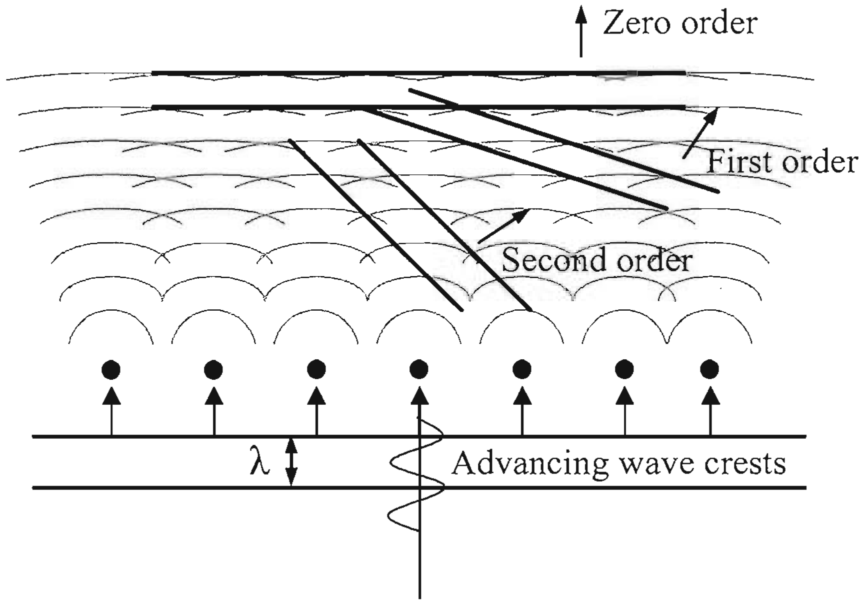

Figure 2.3.1 Schematic representation of the diffraction of X-rays from atoms in a plane.

Diffraction can be described using Bragg's Law for which the crystal can be thought of as containing planes of atoms which are semi-transparent to X-rays. Some X-rays are scattered and others pass through to scatter from other planes. If an X-ray beam is directed at a row of equally spaced atoms, as represented in Figure 2.3.1, each atom becomes a source of scattered waves. These waves spread spherically and reinforce in certain directions to produce the zero-, first-, second-, and higher order diffracted beams. Constructive interference between the beams will only occur if the pathlength difference for X-rays scattered from adjacent planes is equal to an integer number of wavelengths. Simple trigonometry leads to the Bragg Equation:[6]

$$n\lambda = 2d\sin\theta \qquad \text{Equation 2.3.1}$$

where λ is the X-ray wavelength,

n is an integer (1, 2, 3...),

d is the inter-planar separation,

θ is the angle of incidence (Bragg angle).

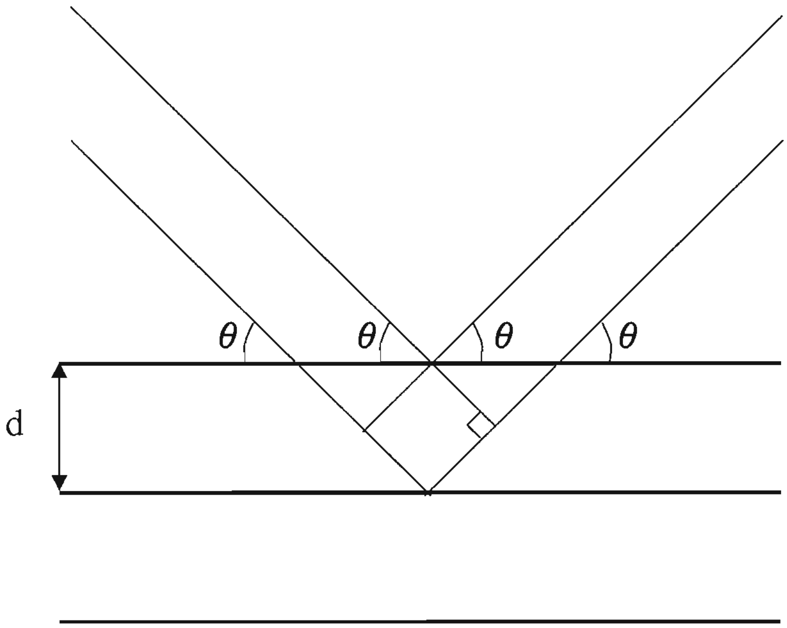

Figure 2.3.2 Schematic representation of scattering from parallel planes of point scatterers, which can be used to derive the Bragg equation.

It is this constructive interference which gives intensity to a diffraction pattern. The beams will interact destructively at θ values which do not satisfy the Bragg equation and hence not contribute to the pattern. Examination of diffraction maxima, or reflections, allows the plane separation (d-spacing) to be calculated. The crystal system is derived from these d values by identification of the planes involved (Table 2.3.1). These planes are defined by Miller indices, h, k, and l to distinguish them from one another, where hkl are the reciprocal of the a, b, c values in which the planes intercept along the crystal axes *a*, *b* and *c*. In theory, diffraction maxima should be seen for all planes in a structure, but in practise this is not the case. Reflection conditions or systematic absences arise from the symmetry of the structure as well as space symmetry elements such as glide planes and screw axes.[7,8]

Table 2.3.1 Equations for d-spacings in the different crystal systems.

Crystal System	**Expression for d_{hkl}**
Cubic	$\frac{1}{d_{hkl}^2} = \frac{h^2+k^2+l^2}{a}$
Tetragonal	$\frac{1}{d_{hkl}^2} = \frac{h^2+k^2}{a^2} + \frac{l^2}{c^2}$
Orthorhombic	$\frac{1}{d_{hkl}^2} = \frac{h^2}{a^2} + \frac{k^2}{b^2} + \frac{l^2}{c^2}$
Hexagonal	$\frac{1}{d_{hkl}^2} = \frac{4}{3}\left(\frac{h^2+hk+k^2}{a^2}\right) + \frac{l^2}{c^2}$
Monoclinic	$\frac{1}{d_{hkl}^2} = \frac{1}{\sin^2\beta}\left(\frac{h^2}{a^2} + \frac{k^2\sin^2\beta}{b^2} + \frac{l^2}{c^2} - \frac{2hl\cos\beta}{ac}\right)$
Triclinic	$\frac{1}{d_{hkl}^2} = \frac{1}{V^2}\left[h^2b^2c^2\sin^2\alpha + k^2a^2c^2\sin^2\beta + l^2a^2b^2\sin^2\gamma\right.$ $+ 2hkabc^2(\cos\alpha\cos\beta - \cos\gamma) + 2kla^2bc(\cos\beta\cos\gamma - \cos\alpha)$ $\left.+ 2hlab^2c(\cos\alpha\cos\gamma - \cos\beta)\right]$ where $V = abc\left(1 - \cos^2\alpha - \cos^2\beta - \cos^2\gamma + 2\cos\alpha\cos\beta\cos\gamma\right)^{1/2}$

Originally X-ray diffraction was applied to the analysis of single crystals of compounds. It is often difficult to obtain single crystals, particularly from the direct reaction of oxides. An alternative method is powder X-ray diffraction (PXD). A powdered sample contains a random orientation of numerous crystallites, many of which satisfy the Bragg equation for each set of their Miller indices. The result is that each lattice spacing in the crystal will give rise to a cone of diffraction at an angle, 2*θ*. Measuring these 2*θ* values therefore allows the d-spacings and other structural information to be calculated.

2.3.2 PXD Instrumentation

The majority of PXD data collection for this study was carried out using a Siemens D5000 diffractometer. X-rays are generated by firing an electron beam at a copper target. X-rays of wavelength, $\lambda = 1.54056$ Å (copper $K_{\alpha 1}$) are selected using a single crystal monochromator. The monochromated beam is collimated by aperture slits and directed onto the sample which is mounted in a recessed aluminium or plastic sample holder. The diffracted beam passes through a further set of slits before reaching a standard scintillation detector. The incident beam, sample stage and detector are positioned according to the Bragg Brentano geometry. The sample is rotated at a constant angular velocity, with the detector rotating at precisely double this velocity. This maintains a fixed relationship between the incident angle (*θ*) and the diffraction angle (2*θ*) through the angular range to be studied. The instrument is controlled by a PC, which also collects and stores the diffraction data.

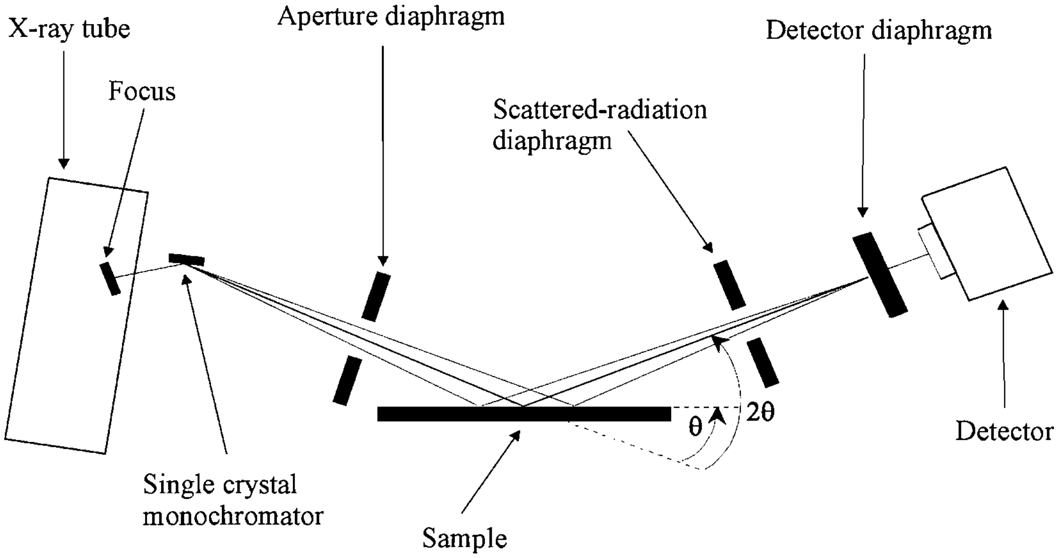

Figure 2.3.2 Schematic representation of the D5000 diffractometer.

The remaining data were collected using a Bruker D8 Advance diffractometer. The main components and geometry are the same as for the D5000 instrument except that different types of detector and sample environments can be fitted. For diffraction experiments in this study the instrument was fitted with a position sensitive detector (PSD). This is comprised of an anode (at which an intense electric field is applied) and a cathode. These are separated by a work gas (methane: argon) which is ionised by the diffracted X-ray photons. This in turn induces a charge which travels to the cathode. The position of the charge can be calculated by the time taken to reach each end of the detector wire. The main advantage of the PSD compared to the scintillation detector is that the detector wire covers approximately 8 degrees in 2θ. Therefore data can be collected much more rapidly with the PSD. However the resolution is not as good as the scintillation detector, giving a broader peak shape in the diffraction pattern.

The D8 diffractometer can be fitted with several different sample stages. In this study a Paar HTK-1200 furnace stage was used (Figure 2.3.3). The sample is mounted on a recessed alumina holder which is loaded inside a sealed chamber. Kapton windows allow the incident and diffracted X-ray beams to pass into and out of the chamber. The furnace can be controlled by PC to reach any temperature between 25 and 1200 °C and can be placed under vacuum or gas flow.

The data collected from both instruments was initially analysed using the Diffrac$^{\text{plus}}$ evaluation program[9] (*EVA*) for phase identification and indexing. The diffraction pattern can also be matched against *Powder Diffraction Files* (PDF) of known compounds. These PDFs are stored in a database maintained by the Joint Committee on Powder Diffraction Standards (JCPDS)[10] and contain information on the positions and intensities of diffraction lines.

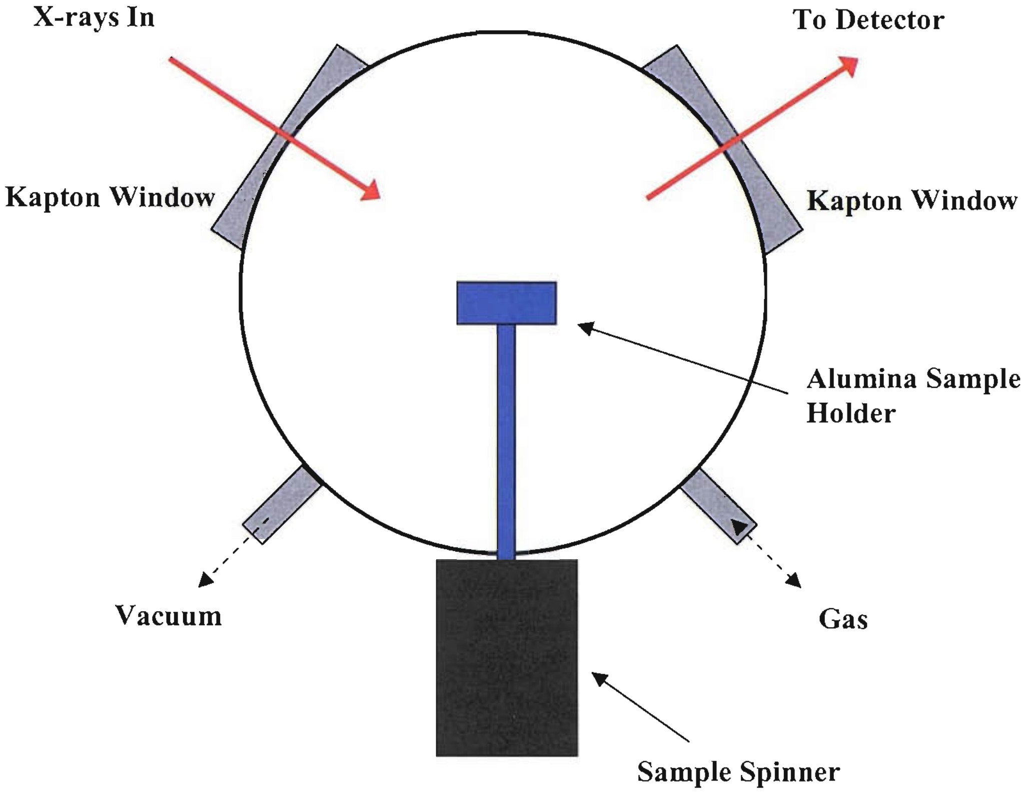

Figure 2.3.3 Schematic representation of the Paar HTK-1200 sample stage.

The program CELREF[11] was used to extract lattice parameter values from the PXD data obtained for crystalline materials. The software uses an iterative least squares refinement method to minimise the following expression:

$$M = \sum_i W_i \left(\sin_i^2 \theta^{obs} - \sin_i^2 \theta^{calc} \right)^2 \qquad \textit{Equation 2.3.2}$$

where W_i is a weighting factor,

M is a weighted minimised difference for observed 2θ data.

The observed reflections from a raw data file can be selected for refinement against the theoretical values of expected reflections. These expected values are calculated based upon the cell parameters of similar, known compounds. The refined unit cell parameters are attributed estimated standard deviations (ESDs) but these only reflect the goodness of fit between the observed and calculated 2θ positions. The program provides no indication of systematic experimental errors or sample impurities. Following these initial analyses, full structure determination can be carried out using the Rietveld refinement method (Section 2.5).

2.4 Powder Neutron Diffraction (PND)

2.4.1 Theory

Powder neutron diffraction is another useful technique for the analysis of solid state materials. Following the realisation that neutron motion is governed by wave mechanics, the first neutron diffraction experiments were carried out in 1936.[12] The wavelength of a neutron is governed by the de Broglie equation:[13]

$$\lambda = \frac{h}{mv} \qquad \textit{Equation 2.4.1}$$

where λ is the wavelength,
h is Planck's constant,
m is the mass of a neutron,
v is the velocity of a neutron.

The root mean square of a Boltzmann distribution of neutron velocities is 2200 ms^{-1} at 273 K, corresponding to a wavelength of approximately 1.55 Å, which is comparable to interatomic spacings. Moderate velocity neutrons are therefore suitable for diffraction experiments and have several advantages over X-rays for this purpose. While X-rays are diffracted by the electron cloud of an atom, neutrons are scattered by the nuclei. The X-ray scattering power of an atom increases as a function of atomic number, whereas there is no simple dependence for neutron scattering power. The neutron scattering power of a nucleus is dependant on both the potential and resonant scattering, which varies across the periodic table giving neighbouring elements and isotopes markedly different scattering lengths. Neutron diffraction is therefore advantageous for locating light elements in solids containing heavier atoms, although samples containing hydrogen require deuteration due to the incoherent scattering of the ^{1}H isotope. Neutron diffraction is also useful for distinguishing atoms of similar atomic number such as silicon and aluminium or oxygen and nitrogen. PND probes the bulk of the solid sample as the interaction between a neutron and an atomic nucleus is weak, whereas PXD is essentially a surface technique. The main disadvantages of PND are the cost of both the generation of neutrons and the complex instrumental set up, as well as the low flux of neutrons that can be produced resulting in long experiment times.

2.4.2 Time of Flight (TOF) PND

PND experiments were carried out at the ISIS facility at the Rutherford Appleton Laboratory (RAL) in Oxfordshire. This is a pulsed neutron spallation source where neutrons are generated by bombarding a heavy metal target, typically a mixture of tantalum and tungsten, with high energy protons from an accelerator. Initially H^- ions are produced from an ion source; a pulse of 70 MeV H^- ions is injected into an 800 MeV synchrotron ring by a linear accelerator. Stripping of the electrons results in a stream of H^+ ions which can be accelerated by a series of magnets before being extracted by a 'kicker' magnet and sent to the target. The pulses of neutron produced have wavelengths too short for diffraction experiments so must be slowed by hydrogenous moderators placed around the target.

Although the principle of PND is similar to PXD, a pulsed neutron source diffractometer operates in a fundamentally different way from a conventional diffractometer. As described in section 2.3 for a conventional PXD set-up the variables within the Bragg equation are the angle of detection (θ) and d, while the wavelength (λ) is fixed. In TOF experiments θ is fixed and the variables are d and the wavelength of the neutron (λ). The relationship between d-spacing and TOF is linear and can be derived from de Broglie's relationship (Equation 2.4.1) and Bragg's law (Equation 2.3.1):

$$\lambda = \frac{h}{m_n v_n} = 2d\sin\theta \qquad \textit{Equation 2.4.2}$$

The distance from the moderator to the sample, L_1 can be considered as a primary flight path and the distance from the sample to the detector, L_2 a secondary flight path with their respective flight times being t_1 and t_2. As velocity is distance over time these variables can be substituted to give:

$$\frac{h}{m_n}\left[\frac{t_1+t_2}{L_1+L_2}\right] = 2d\sin\theta \qquad \textit{Equation 2.4.3}$$

Therefore for a total neutron flight path $L_1 + L_2 = L$ and a total time of flight $t_1 + t_2 = t$ then:

$$t = 2dL\left(\frac{m_n}{h}\right)\sin\theta \qquad \textit{Equation 2.4.4}$$

Therefore the relationship is such that $t \propto d$. For an instrument at 12m from the neutron source such as POLARIS a 1 Å d-spacing reflection will be detected in a backscattering bank at a TOF of ~ 5000 μs.

2.4.3 PND Instrumentation

For this work two different instruments at the ISIS facility were used. These were the High Resolution Powder Diffractometer (HRPD) and the POLARIS diffractometer. With a resolution of $\Delta d/d = 4\text{-}5 \times 10^{-4}$ in backscattering mode, HRPD is the highest resolution powder neutron diffractometer in the world. The backscattering bank consists of an array of zinc sulphide scintillation detectors at fixed scattering angles of $160° \leq 2\theta \leq 176°$. The highest resolution is therefore available in the d-spacing range of ~ 0.6- 4.6 Å. The high resolution is a result of the instruments path length of 95 m which gives long times of flight. However long collection times are required (8-12 hours) as the beam line only uses one in five of the pulses from the source to avoid overlap.

HRPD was designed to handle materials with large cell volumes with up to 400 structural parameters making it ideal for studying complicated structures. In this work the instrument was required to study accurately the atomic positions, particularly of oxygen, for the complex pyrochlore related compound $Bi_2Hf_2O_7$.

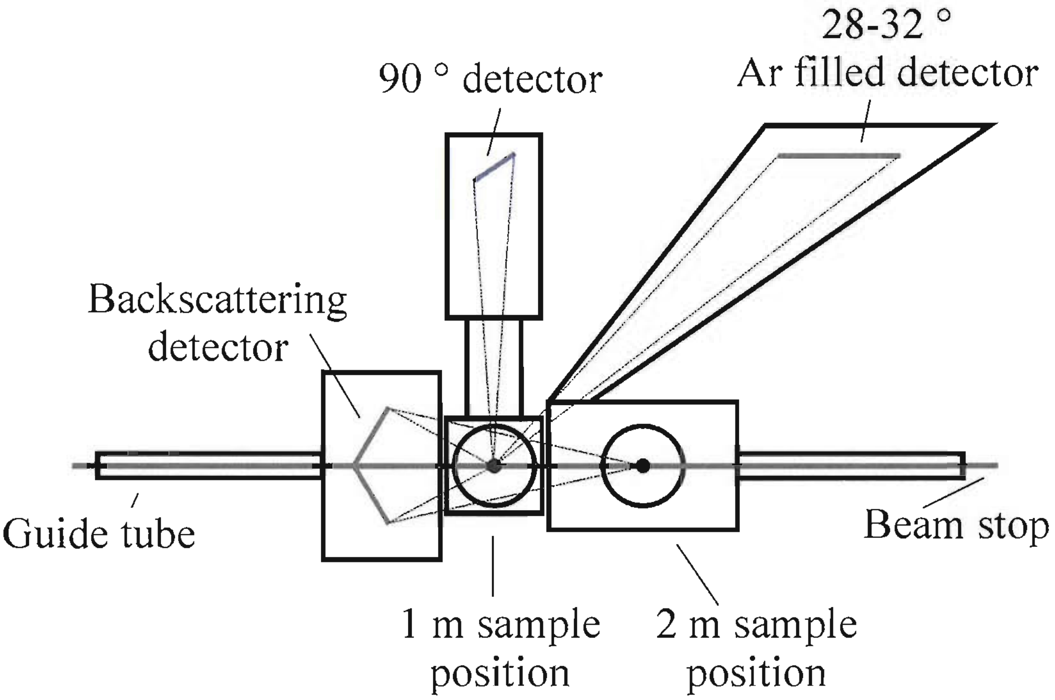

Figure 2.4.1 Schematic of the HRPD instrument.

Samples were sealed inside silica tubes (to reduce decomposition) and placed into vanadium cans. Vanadium cans are typically used to hold PND samples as the metal is largely transparent to neutrons due to incoherent scattering. The can is mounted within a sample tank which must be evacuated before the sample can be exposed to the neutron beam. Specialist sample environments can also be mounted in the sample tank. In this study a furnace capable of operating up to 1000 °C was used.

The POLARIS instrument is a high flux, medium resolution diffractometer. The instrument receives short pulses (< 90 μs) of a polychromatic or white beam of neutrons from an ambient temperature, gadolinium-poisoned water moderator. With a flight path of 12 m from the target and good detector coverage the counting times are much lower than for HRPD. Backscattered neutrons are detected by 38 ^{3}He detectors fixed at angles in the range $135° \leq 2\theta \leq 160°$, giving a resolution of $\Delta d/d \sim 5 \times 10^{-3}$ and a d-spacing range of 0.2- 3.2 Å. The diffractometer is ideal for small samples, typically in the range 1-2 g (~0.7 g for this study) with collection times of ~2 hours. The dimensions of the beam can be altered by using collimators to in order to match the sample size or reduce background noise from sample environment equipment.

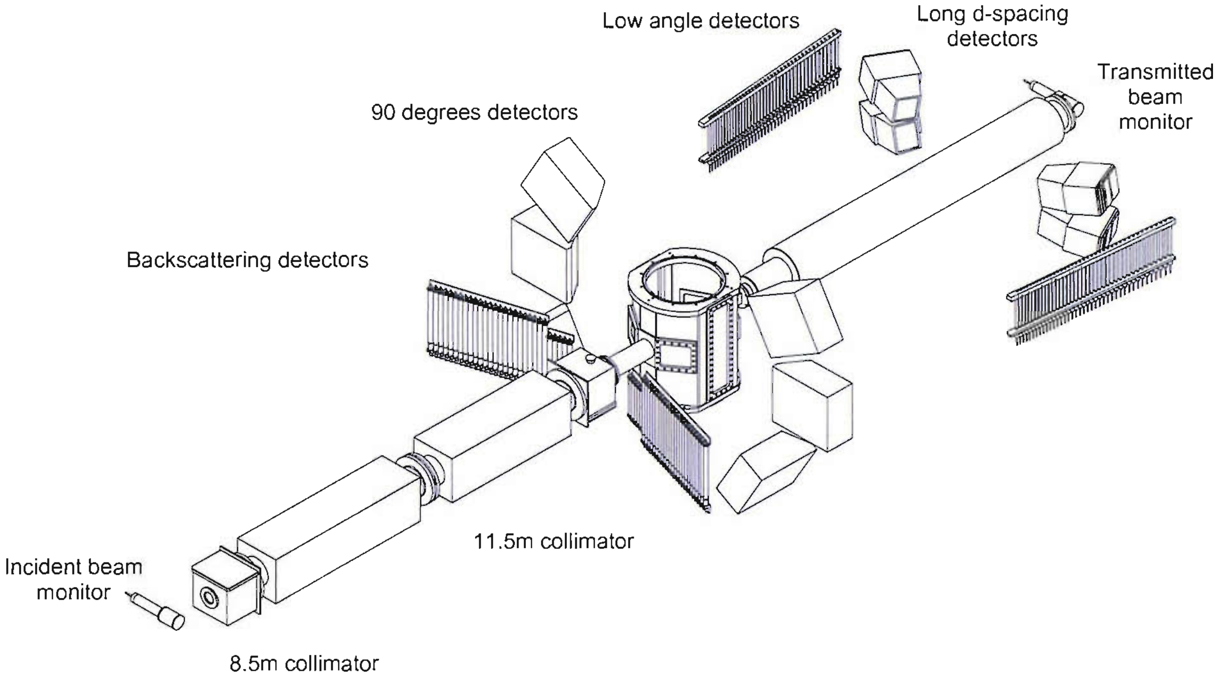

Figure 2.4.2 Schematic of the POLARIS diffractometer.[14]

2.5 Structural Refinement

2.5.1 Theoretical considerations

For a regular array of stationary atoms the structure factor, F, can be described as the sum of the contributions of the scattering amplitudes, f, and the phases, ϕ, of each atom in the expression:

$$F = \sum_{j=1}^{N} f_j \exp[i\phi_j] \qquad \textit{Equation 2.5.1}$$

The total phase shift of an atom, j, in a unit cell at a point (x_j, y_j, z_j) from the origin, is the sum of the phase shifts in each direction. When the phase shift is evaluated the structure factor for one unit cell becomes:

$$F_{hkl} = \sum_{j=1}^{N} f_j \exp[2\pi i(hx_j + kx_j + lz_j)] \qquad \textit{Equation 2.5.2}$$

with *h*, *k* and *l* representing the Miller indices defining the plane from which the reflection occurs. For very small crystals it may be shown that the intensity of the scattered beam is proportional to the square of the structure factor:

$$I_{hkl} = kL^2 |F_{hkl}|^2 \qquad \textit{Equation 2.5.3}$$

where *k* is a scaling constant and *L* is the Lorentz factor, a geometric function of the method of data collection and hence the instrument used.[15]

The scattered intensity is modified for real crystals due to imperfections in the lattice structure. Substitutional disorder and defects, particularly in non-stoichiometric materials, can cause local structural irregularities. Thermal motion also reduces the scattered intensity because of time dependent vibrations of the atoms about their mean positions, which disrupts the in-plane behaviour of their combined scattering. The correction of the structure factor, reflected by a plane *hkl* is shown below.

$$T_{hkl} = \exp\left[-B_{hkl}\frac{\sin^2\theta}{\lambda^2}\right] \qquad \textit{Equation 2.5.4}$$

Where T_{hkl} represents the thermal motion correction and B is equal to $8\pi^2U$, U being the root mean square thermal displacement. The structure factor for a unit cell thus becomes:

$$F_{hkl} = \sum_{j=1}^{N} f_j n_j \exp\left[-B_j\frac{\sin^2\theta}{\lambda^2}\right]\exp\left[2\pi i\left(hx_j + kx_j + lz_j\right)\right] \qquad \textit{Equation 2.5.5}$$

where n_j is the occupation of the j^{th} atom, equal to one in a structure free from defects. This assumes that the thermal motion displacements are equal in all directions (isotropic), which is rarely the case except for some highly symmetric positions of cubic space groups.[16] Anisotropic thermal motion can be described in the form of an ellipsoid so T_{hkl} can now be expressed as:

Equation 2.5.6

$$T_{hkl} = \exp\left[-\tfrac{1}{4}\left(B_{11}h^2a*^2 + B_{22}k^2b*^2 + B_{33}l^2c*^2 + 2B_{12}hka*b* + 2B_{23}klb*c* + 2B_{13}hla*c*\right)\right]$$

The intensities of the diffracted beams are also governed by the multiplicity of an *hkl* reflection. Therefore in a particular crystal symmetry class for a specific hkl reflection, there can be a series of equivalent planes diffracting at the same angle resulting in an increased intensity.

Using this theory a simulated diffraction pattern can be calculated from an initial structural model using cell parameters, atomic positions and symmetry elements. This is the basis of the Rietveld method for diffraction data analysis.

2.5.2 The Rietveld Method

The early methods of data analysis of diffraction data were carried out using the principles developed for single crystal diffraction patterns. These were least squares refinements using $|F|$ values based on the structure factors extracted from the pattern. However, as powder diffraction data often contains many overlapping peaks, structure factor extraction is often difficult and sometimes impossible. In order to increase the amount of information that could be extracted from powder data, H. M. Rietveld devised a new analysis technique.[17,18] Rietveld realised that although many reflections did overlap and thus could not be modelled as single entities, the total intensity and peak shape of a cluster of reflections could be determined by using simple peak shape parameter. This method was developed further with the advent of computers allowing increasingly complex structural problems to be solved. There are numerous parameters which can be varied when undertaking a refinement though not all of them are necessary for every refinement. A typical refinement procedure is outlined below.

i) Determine an approximate model of the structure by comparison with reference materials.
ii) Refine the overall scale factor and background parameters.
iii) Refine lattice parameters, zero-point correction and sample displacement to accurately locate Bragg reflections.
iv) Preliminary refinement of peak shape parameters.
v) Locate and refine atom positions in the structure thus altering the peak intensities.
vi) Refine the isotropic temperature factors accounting for atomic vibrations.
vii) Fully refine peak shape parameters to account for sample broadening effects.
viii) Refine the anisotropic temperature factors if possible.

The method is the same for both PXD and PND data, although the preparation of data is different. The instrument parameters that can be varied also depend on the particular experiment carried out. The refinement is a least squares best fit process which aims to minimise the function M.

$$M = \sum_i w_i \left(y_i^{obs} - y_i^{calc}\right)^2 \qquad \textit{Equation 2.5.7}$$

where w_i is a weighting factor given by $1/y_i^{obs}$,

y_i^{obs} is the observed intensity at each step/point i (2θ for PXD),

y_i^{calc} is the calculated intensity at each step.

For PXD these calculated intensities are determined from the $|F_k|^2$ values calculated from the structural model by summing the calculated contributions from neighbouring Bragg reflections (k) plus a background b_i:

$$y_i^{calc} = s \sum_k L_k |F_k|^2 \phi(2\theta_i - 2\theta_k) P_k A + y_{bi} \qquad \textit{Equation 2.5.8}$$

where s is the scale factor,

L_k contains Lorentz, polarisation and multiplicity factors,

ϕ is the reflection profile function,

F_k is the structure factor for the k^{th} Bragg reflection,

P_k is the preferred orientation function,

A is an absorption factor,

y_{bi} is the background intensity at the i^{th} step.

The background intensity can be modelled using a variety of functions. A common example of such a function is a cosine Fourier series with a leading constant term:

$$y_{bi} = B_i + \sum_{j=2}^{N} B_j \cos[P*(j-l)]$$ Equation 2.5.9

where P is the position of the step in 2θ (for PXD) or times scaled by 180/TMAX (for TOF). TMAX is the maximum allowed by the incident spectrum,

B_i and B_j are determined by least squares during the refinement.

A comparison of intensities is performed at every point so it is essential for the calculation of the calculated profile to accurately describe the peak shape of the Bragg reflections. The peak shape is generally dictated by the instrument. For both the Siemens D5000 and the Bruker D8 the peak shape is pseudo-Voigt as described by the expression:

$$\eta L + (1-\eta)G$$ Equation 2.5.10

where L and G are the Lorentzian and Gaussian contributions to the peak shape and η is the mixing parameter which can be refined as a linear function of 2θ.

The Gaussian (G) and Lorentzian (L) contributions to the peak shape are described by the equations:

$$G = \frac{(4\ln 2)^{1/2}}{H_k\sqrt{\pi}} \exp\left[\frac{-4\ln 2(2\theta_i - 2\theta_k)^2}{H_k^2}\right]$$ Equation 2.5.11

and

$$L = \frac{2}{\pi H_k} 1 \Big/ \left[1 + 4\frac{(2\theta_i - 2\theta_k)^2}{H_k^2}\right]$$ Equation 2.5.12

where $2\theta_k$ is the calculated position for the k^{th} Bragg reflection corrected for the counter zero-point,

H_k is the full-width-at-half-maximum (FWHM) of the k^{th} Bragg reflection.

The FWHM, H_k of a peak varies with the scattering angle $2\theta_k$ and is modelled as:

$$H_k^2 = U \tan^2 \theta + V \tan \theta + W \qquad \textit{Equation 2.5.13}$$

where U, V and W are refineable and are instrument and sample dependent.

This formula can be used to account for peak broadening effects resulting from particle size. More complex expression can be applied for the same purpose depending on the experimental set up. These are described in section 2.5.5.

The least squares parameters fall into two distinct groups. The first defines the structural parameters. These describe the contents of the unit cell and include the overall temperature factors, atomic co-ordinates and fractional occupancies of each site. The second contains the profile parameters, which describe the position, shape and FWHM of each peak. This includes the scale factor, unit cell parameters, U, V, W and zeropoint correction. In order to make a quantitative assessment of the agreement between the observed and calculated profiles, a number of reliability factors are defined. These are labelled R_{profile} (R_p), R_{expected} (R_{exp}) and $R_{\text{weightedprofile}}$ (R_{wp}) and are given by:

$$R_{profile} = R_p = 100 \left[\frac{\sum_i \left| y_i^{obs} - y_i^{calc} \right|}{\sum_i y_i^{obs}} \right] \qquad \textit{Equation 2.5.14}$$

$$R_{expected} = R_{exp} = 100 \left[\frac{(N - P + C)}{\sum_i w_i \left(y_i^{obs} \right)^2} \right]^{½} \qquad \textit{Equation 2.5.15}$$

where R_{exp} is defined from the statistics of the refinement,
N is the number of observations,
P is the number of refineable parameters,
C is the number of constraints.

From a mathematical standpoint, $R_{weightedprofile}$ (R_{wp}) is the most significant of the R factors because the numerator is the residual being minimised. By the same reasoning it is also the factor that best reflects the progress of the refinement and is given by:

$$R_{weightedprofile} = R_{wp} = 100\left[\frac{\sum_i \left(y_i^{obs} - y_i^{calc}\right)^2}{\sum_i w_i \left(y_i^{obs}\right)^2}\right]^{1/2} \qquad \textit{Equation 2.5.16}$$

The final measure of the whole fit that is minimised during the refinement is the chi-squared parameter and is defined by:

$$\chi^2 = \left[\frac{R_{wp}}{R_{\exp}}\right]^2 \qquad \textit{Equation 2.5.17}$$

For a good fit, the R_{wp} should approach the statistically expected R factor, R_{exp}. The goodness of fit should also be observed by examining a plot of the profile fit. For a good fit the difference between the calculated and observed patterns should be as flat as possible. All Rietveld refinements carried out for this study were performed using the General Structure Analysis Suite (GSAS) developed by von Dreele and Larson.[19]

2.5.3 Particle Size Estimation from GSAS Refinement

As mentioned in Section 2.5.2, particle size can be related to peak shape for a diffraction pattern. Information on particle size can therefore be extrapolated from the complex expressions derived to model the Gaussian and Lorentzian components of the peak shape. These functions can also yield information on particle strain.

For PXD the particle size broadening can be obtained from the expression:

$$\Delta d / d^2 = \frac{\Delta 2\theta \cot\theta}{d} = constant \qquad \textit{Equation 2.5.18}$$

From Bragg's law this becomes:

$$\Delta d/_{d^2} = \frac{2\Delta 2\theta \cot\theta \sin\theta}{\lambda} \qquad \textit{Equation 2.5.19}$$

The broadening is then:

$$\Delta 2\theta = \frac{\lambda \,\Delta d/_{d}}{2\cos\theta} \qquad \textit{Equation 2.5.20}$$

For PXD the Lorentzian coefficient, γ, of the peak shape is composed of two functions, X and Y (denoted LX and LY in the GSAS program) in the expression:[19]

$$\gamma = \frac{X + X_s \cos\phi}{\cos\theta} + (Y + Y_e \cos\phi)\tan\theta \qquad \textit{Equation 2.5.21}$$

where X_s and Y_e are anisotropy coefficients.

The first term in the expression for the Lorentzian broadening, X, is of this form where:

$$X = \frac{\Delta d}{d^2} \qquad \textit{Equation 2.5.22}$$

Rearranging this expression and converting from centideg to radians gives the particle size, *p*:

$$p = \frac{18000K\lambda}{\pi X} \qquad \textit{Equation 2.5.23}$$

where K is the Scherrer constant and the units are Å.

Similarly strain broadening in real space is related to *2θ* broadening from the expression below, where Δ2θ is in radians:

$$\Delta 2\theta = \left(\Delta d/_{d}\right)\tan\theta \qquad \textit{Equation 2.5.24}$$

The strain term from Equation 2.5.21 varies with tan*θ* so the strain, *S*, can be expressed as a percentage by:

$$S = \frac{\pi}{18000}(Y - Y_i)100\% \qquad \text{Equation 2.5.25}$$

where Y$_i$ is the instrumental contribution to the broadening.

For TOF PND data the isotropic particle size broadening makes all points the same size in reciprocal space, independent of the distance from the origin, so:

$$\Delta d^* = constant \qquad \text{Equation 2.5.26}$$

The reciprocal of this quantity is then the average particle size, therefore in real space,

$$\Delta d / d^2 = constant \qquad \text{Equation 2.5.27}$$

The Gaussian variance of the peak shape from a TOF pattern can be described by,

$$\sigma^2 = \sigma_0^2 + \sigma_1^2 d^2 + \sigma_2^2 d^4 + \left(\sigma_{1e}^2 d^2 + \sigma_{2e}^2 d^4\right)\cos^2\phi \qquad \text{Equation 2.5.28}$$

The particle size affects the third term (σ_2^2) in the expression. The term generally has no instrument contribution and is used to directly calculate the particle size, p, from the expression:

$$p = \frac{CK}{\sqrt{(8\ln 2)\sigma_2^2}} \qquad \text{Equation 2.5.29}$$

where C is the diffractometer constant (DIFC) that relates TOF to d-spacing, K is the Scherrer constant and the units are Å.

The expression in Equation 2.5.28 implies the second term contains an isotropic contribution from strain broadening. The other major contribution to σ_1^2 is from the instrument, which can be subtracted because it is expressed as a variance. The remainder can then be converted to give the strain, S, as a percentage:

$$S = \frac{1}{C}\sqrt{(8\ln 2)(\sigma_1^2 - \sigma_{1i}^2)}100\%$$ *Equation 2.5.30*

where σ_{1i}^2 is the instrumental contribution.

The particle size and strain can therefore be directly calculated from the profile coefficients denoted σ_2 and σ_1 respectively in the GSAS program.

2.6 Solid State Ultraviolet-Visible Spectroscopy

Ultraviolet-Visible (UV-Vis.) spectroscopy data was collected using a Perkin Elmer UV-Vis. Lambda 35 spectrometer in diffuse reflectance mode. Spectra were recorded in the visible range 380-780 nm

The instrument contains two radiation sources, a halogen lamp and a deuterium lamp, which cover the working range of the spectrometer. A holographic concave grating with 1053 lines/ mm acts as a monochromator. When collecting data in the visible region, a series of mirrors within the instrument align to allow radiation from the halogen lamp to reach the sample, while the ultra violet radiation from the deuterium lamp is blocked. After interaction with the sample the radiation passes through a convex lens onto a photodiode detector.

Samples were mounted in a recessed aluminium holder with a quartz window. A barium sulphate block was used as a reference to obtain a background correction before collecting data. Colour measurements were carried out on the data recorded as detailed in Section 2.7.

2.7 Colour Measurement

Perceived colour arises from the observation of different wavelengths of visible light. Different coloured pigments can be unambiguously characterised by their spectral reflectance curves, $\rho(\lambda)$, which is measured over the visible region of the electromagnetic spectrum (380 to 780 nm).

There are several factors that affect the observed colour of an object. These are the spectral reflectance (if opaque) or spectral transmittance (if translucent) of the material; the spectral composition of the light present and the spectral sensitivity of the eye of the observer.

The human eye is receptive to three fundamental colour components, the primary colours, red green and blue. The observation of these components is transmitted to the brain where the perceived colour is computed from the information. The response to colour is psychological, hence colourimetry has been developed to provide a standardised physical measurement that can equate to perceived colour.

All colours can be simulated by additively mixing the three primary colours (red, green and blue) or *colour stimuli* in the correct ratios.[20] A colour can therefore be defined by a set of three values. This is known as the trichromatic principle where the three reference stimuli are pre-defined enabling a three-dimensional colour space to be constructed. The tristimulus values are interpreted as components of a vector within this space based on the *Commission Internationale de l'Eclairage* (CIE) system.[21]

For colourimetry a sample is illuminated with three separate light sources, red, green and blue, in order to determine colour measurements. It is also possible to extract some colour measurements from uncoloured illumination of a sample. For example UV-Vis. spectroscopic data can be used to ascertain the colour of a sample and thus its suitability as a pigment. In the case of uncoloured illumination, the tristimulus values depend on the spectral reflectance:

$$X = \int \bar{x}(\lambda)\rho(\lambda)\cdot d\lambda \qquad \text{Equation 2.7.1}$$

$$Y = \int \bar{y}(\lambda)\rho(\lambda)\cdot d\lambda \qquad \text{Equation 2.7.2}$$

$$Z = \int \bar{z}(\lambda)\rho(\lambda)\cdot d\lambda \qquad \text{Equation 2.7.3}$$

where $\bar{x}(\lambda)$, $\bar{y}(\lambda)$ and $\bar{z}(\lambda)$ are the CIE spectral tristimulus values.

However this does not allow for pigment testing between the sample and a reference, *i.e.* colour differences, hence an absolute colour space is required. The three co-ordinates of this space are denoted as L^*, a^* and b^*. The L^* value or lightness axis represents the lightness of an object; zero being black and one hundred being white. The a^* value is a measure of redness when positive or a measure of greenness when negative, the red-green axis. Similarly the b^* value represents a measure of yellowness when positive or blueness when negative, the yellow-blue axis. When L^*, a^* and b^* are represented as axes (z, x, and y respectively) in a Cartesian co-ordinate system, any colour can be described by the location of its unique $L^*a^*b^*$ values within the three-dimensional space. These values are calculated by computer based on the equations:

$$L* = 116\left(\frac{Y}{Y_0}\right)^{1/3} - 16 \qquad \text{Equation 2.7.4}$$

$$a* = 500\left[\left(\frac{X}{X_0}\right)^{1/3} - \left(\frac{Y}{Y_0}\right)^{1/3}\right] \qquad \text{Equation 2.7.5}$$

$$b* = 200\left[\left(\frac{Y}{Y_0}\right)^{1/3} - \left(\frac{Z}{Z_0}\right)^{1/3}\right] \qquad \text{Equation 2.7.6}$$

where X, Y and Z are tristimulus values,

X_0, Y_0 and Z_0 are illuminant values (standard/reference).

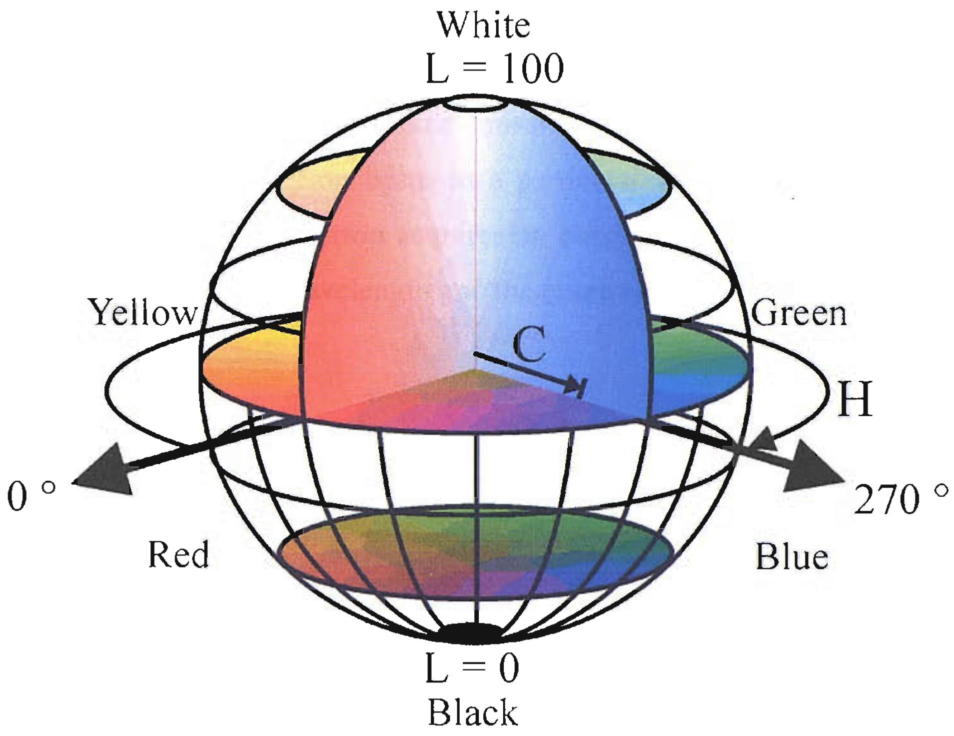

Figure 2.7.1 CIELCH colour space diagram, where lightness is represented as the axis of the sphere.

An alternative system is based on polar co-ordinates as in Figure 2.7.1 where the H axis corresponds to the hue angle and the C axis the chroma (intensity). The L value again represents lightness as in the CIELAB system.

2.8 Electron Microscopy

Electron microscopy has many applications ranging from electron diffraction to high-resolution imaging. In this study scanning electron microscopy (SEM) has been used to examine morphology and energy dispersive analysis of X-rays (EDAX) employed to study the composition of samples.

In many ways electron optics are identical to light optics as light can be considered as both a wave and a particle. Visible light can be conceived as photons or as radiation of wavelength 380-780 nm whilst electrons can be considered as radiation with wavelengths typically between 0.001 and 0.01 nm.

Electrons are generated by thermionic emission then accelerated through a potential, monochromating the electron beam to a particular wavelength. When accelerated through a voltage V an electron acquires an energy, eV. Equation 2.8.1 shows the relationship between the wavelength and the energy of the electron beam.

$$\lambda = \left[\frac{1.5}{(V + 10^{-6} V^2)} \right]^{1/2} nm \qquad \textit{Equation 2.8.1}$$

where λ is the wavelength in nm,

V is the potential difference.

The electron beam then hits sample leading to two main types of interaction. Elastic scattering occurs if the direction of the primary electrons is altered but not its energy. If the primary electrons loose energy (>0.1 eV) this is known as inelastic scattering. While elastic scattering can be used for techniques such as electron diffraction, it is the inelastically scattered electrons combined with secondary effects which are useful for imaging (SEM) and analysis.[22]

Electron-specimen interactions result in many different types of electron. The most useful for imaging and analysis are secondary, Auger and backscattered electrons. Single valence electron excitation gives rise to electrons which escape from the surface of the specimen with energy below 50 eV; these are the main secondary electrons. The most commonly used imaging mode in SEM is secondary electron detection.

Backscattered electrons are primary electrons that have undergone elastic collisions with the nuclei of atoms in the sample. Backscattered electron detection can be used to give topographic images with better contrast than those using secondary electrons.

Bombardment of an atom by the primary beam results in the expulsion of an excited electron from the atom after it has absorbed energy. Relaxation of the atom results in emission of energy in the form of X-rays. The energies of the emitted X-rays are characteristic of particular atomic species so can be used for quantitative elemental analysis of the sample. This technique is known as Energy Dispersive Analysis of X-rays (EDAX).

SEM data were collected using either a Philips XL30ESEM or JEOL JSM-5910 microscope. In both cases samples were mounted on an aluminium stub using carbon tape and coated with a thin film of carbon. A schematic of a scanning electron microscope is shown in Figure 2.8.1. The system is operated under vacuum. The electron beam is focussed by a series of electromagnetic lenses and the resulting spot scanned across the sample by a set of scan coils. Detectors count the secondary or backscattered electrons to form images, which can then be transferred to a computer for manipulation.

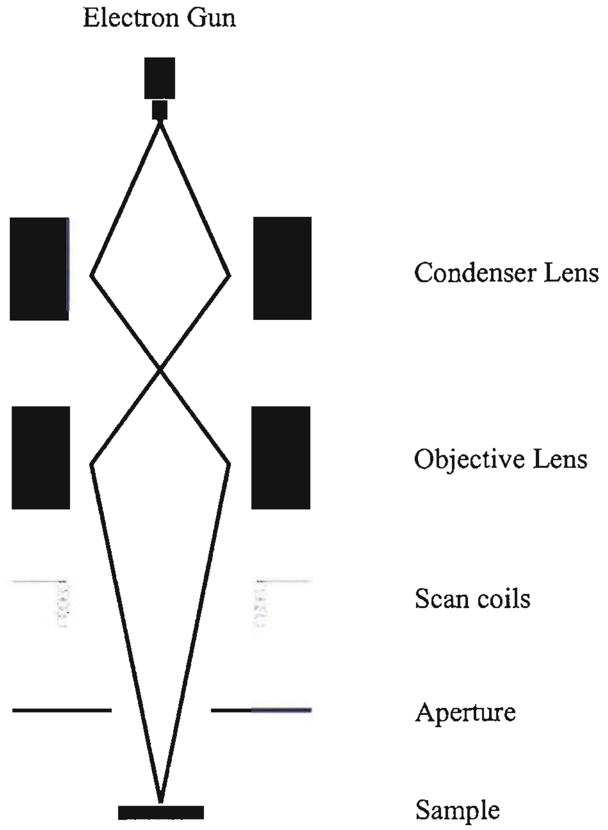

Figure 2.8.1 Schematic of a scanning electron microscope.

For the EDAX experiment the same equipment is used with the addition of an EDAX analyser to obtain information about the characteristic X-rays emitted. The software outputs a spectrum showing the intensities of the various energy X-rays. This provides a qualitative description of the composition of the sample. Quantitative analysis is also carried out by the software but care must be taken in interpretation as the errors on light elements are large and the energies from different shells of different elements may overlap.

2.9 Thermal Analysis

Thermal analysis can be described in general as the measurement of physical or chemical change with respect to temperature. The main thermal analysis techniques used for solid state chemistry are thermogravimetric analysis (TGA) and differential thermal analysis (DTA). The properties examined are usually limited to mass, enthalpy or heat capacity for solid compounds.

TGA curves follow the change in weight of a sample upon heating. Typically a few milligrams of sample are heated at a rate of 1-20 °C per minute in a controlled atmosphere. Changes in sample weight will be recorded if a decomposition event occurs, for example the loss of water from a hydrated species.

Comparison of the sample temperature with an inert reference material yields a DTA trace. The reference will undergo no phase changes or decompositions in the temperature range of the experiment. Hence, if no thermal events occur both materials will be at the same temperature, but if a decomposition or phase change takes place the temperatures will differ. An exothermic process will give the sample a higher temperature than the reference, whereas for an endothermic event it will be lower.

Comparison of the DTA and TGA traces reveals which thermal events are accompanied by mass loss. Studying the curves during cooling can indicate if a reversible event is occurring; if there is an opposing thermal change on cooling the process is reversible. If there is no change on cooling, an irreversible change has occurred.

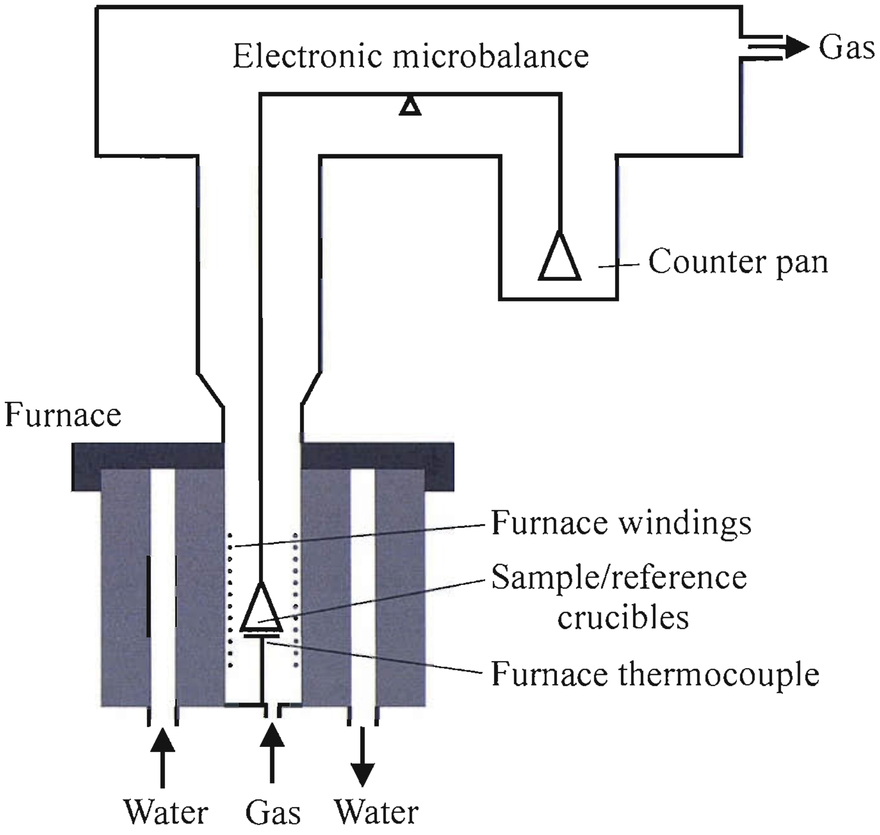

Figure 2.9.1 Schematic representation of the STA-1500 instrument

Data were collected using a either a Mettler Toledo TGA/SDTA851e fitted with a TSO801RO Universal Sample Robot, or a Polymer Laboratories STA-1500 thermal analysis system. The Mettler instrument has a horizontal furnace and a parallel guided balance to minimise disturbing influences such as gas flow perturbations. The automated loading of pans from a carousel allows runs of up to 34 samples to be analysed sequentially. A well defined mathematical model allows DTA and TGA data to be collected concurrently, even with only one sample crucible. The model calculates the reference temperature from that of the sample using the SDTA (Single

Differential Thermal Analysis) operation. The STA-1500 is comprised of an electronic microbalance with a platinum wire hang-down (Figure 2.9.1). DTA measurements are recorded by comparison with an alumina standard placed next to the sample crucible.

Two methods were used in this study; one to determine tantalum content of tantalum nitride materials and the other to assess the decomposition of either hydrated starting materials or bismuth containing pyrochlores. A typical tantalum content experiment involved heating under oxygen (50 ml/min) at 10 °C per minute to 1000 °C and holding for 30 minutes before cooling to room temperature. Decomposition events were recorded by heating samples to various temperatures under flowing air.

2.10 References

[1] A. R. West, '*Solid State Chemistry and its Applications*', John Wiley & Sons, UK (1984).

[2] M. T. Weller, '*Inorganic Materials Chemistry*', Oxford University Press, UK (1994).

[3] J. D. Wright and N. Sommerdijk, '*Sol-gel Materials: Chemistry and Applications*', Taylor and Francis (2000).

[4] E. Guenther and M. Jansen, *Mater. Res. Bull.* **36** 1399 (2001).

[5] M. P. Pechinni, U.S. Pat. No. 3330697 (1967).

[6] W. L. Bragg, *Proc. Camb. Phil. Soc.* **17** 43 (1913).

[7] A. K. Cheetham and P. Day, '*Solid State Chemistry: Techniques*', Oxford Science Publications, Clarendon Press, UK (1988).

[8] T. Hahn, '*International Tables For Crystallography Vol. A*', D. Reidel (1983).

[9] Bruker Advanced X-Ray Solutions; *EVA*, **V10.1** (2004).

[10] International Centre for Diffraction Data, 12 Campus Boulevard, Newton Square, Pennsylvania 19073-3273, U.S.A.

[11] J. Laugier, B. Bochu, *CELREF*, Laboratoire des Matériaux et du Génie Physique, Ecole Nationale Supérieure de Physique de Grenoble INPG, France, (2000).

[12] D. P. Mitchell and P. N. Powers, *Phys. Rev.* **50** 486 (1936).

[13] D. E. Shriver, P. W. Atkins and C. H. Langford, '*Inorganic Chemistry*', Oxford University Press, UK (1990).

[14] http://www.isis.rl.ac.uk (2005).

[15] M. J. Buerger, '*Contemporary Crystallography*', McGraw-Hill, USA (1970).

[16] B. T. M. Willis and A. W. Pryor, '*Thermal Vibrations in Crystallography*', Cambridge University Press, UK (1975).

[17] H. M. Rietveld, *Acta Cryst.* **22** 151 (1967).

[18] H. M. Rietveld, *J. Appl. Cryst.* **2** 65 (1969).

[19] A. C. Larson and R. B. Von Dreele, *General Structure Analysis System (GSAS)*, Los Alamos National Laboratory Report LAUR 86-748, (2004).

[20] R. Tilley, '*Colour and the Optical Properties of Materials*', Wiley, UK (2000).

[21] Commission Internationale de l'Eclairage, *CIE Technical Report*, **116** (1995).

[22] R. Beanland, P. J. Goodhew and J. Humphreys, '*Electron Microscopy and Analysis*', Taylor & Francis (2001).

Chapter 3

Development of High Throughput Methodology

3.1 Introduction

The application of high throughput methods for the synthesis and screening of inorganic materials is an area of growing interest.[1,2] The ability to assess rapidly the properties of large numbers of discrete compounds, prepared using small quantities of reagents make, these techniques attractive for both industrial and academic research. Much of the literature focuses on the preparation of thin film arrays by vapour deposition.[3,4] However, such samples may not give a true indication of the material's properties when prepared as a bulk powder. Libraries of powdered catalysts and phosphor materials prepared from solutions have been shown to be an effective lower cost route to novel inorganic materials.[5,6] The preparation of pigment materials using high throughput methods has however received little attention.

Inorganic pigments are widely used to colour materials that are exposed to elevated temperatures during processing or application. However, most inorganic pigments contain heavy metals that can adversely affect the environment and human health if critical levels are exceeded. Red and yellow cadmium-based pigments are a particular concern as although they are not toxic themselves, toxic cadmium metal may enter the environment through incineration or waste disposal. Therefore there is a strong demand for inherently safer substitutes with comparable colour properties.[7]

This chapter describes the development of high throughput methods for preparing arrays of pigments by solution methods, which can subsequently be screened for their colour properties. The generic method of synthesis may then be applied to materials with different properties.

3.2 Considerations for Method Development

Developing high throughput techniques as with any other experiment requires consideration of the scope and aims of the study. The equipment available for both synthesis and screening, software capabilities and the range of materials to be studied all influence the design of the methodology. Even with a limited number of compositional variants, the vast number possibilities lead to numerous dimensions of parameter space. The number of useful, stable elements (*i.e.* chemically reactive and non-radioactive) in the periodic table can be assumed to be around 50. Based on this assumption and using a combinatorial formula as in Equation 3.2.1 it can be shown that there will be 1,225 binary, 19,600 ternary, 230,000 quaternary and 10^{10} decanary combinations of these elements.[8]

$$N(n_E/n_r) = n_E!/[n_r!(n_E - n_r)!] \qquad \text{Equation 3.2.1}$$

Where N is the total number of combinations,
n_E is the number of elements
n_r is the specific group i.e. binary, ternary etc.

This parameter space becomes significantly larger if structural and compositional diversities are introduced. For example a library having 10 elements and 25 composition increments in the binary axes leads to 38,567,100 discrete combinations. If synthetic variables are also considered such as temperature, reaction time or reaction atmosphere the parameter space again increases immensely. It is clearly not possible to investigate all these possibilities, therefore, strategies for probing this space for new materials would be required. The design of experiments and the analysis of the results require specialised statistical software to be developed, which is not included in the scope of this work. Therefore the aim of this study is to develop general high throughput methods to provide a step change in productivity compared to traditional experiments, within the limitations of the equipment available. These methods could be applied to prepare a wide range of materials in an array format that could potentially be analysed by various instruments.

3.3 High Throughput Synthesis Methods

3.3.1 Array System

An array system suitable for preparing libraries of solid state compounds from solution methods has two main requirements. It must be able to receive and contain liquids but also be capable of withstanding elevated temperatures without reaction. Various groups have utilised substrates with wells machined into the surface. Yanase used platinum pallets with 16 wells,[9] while the groups of Park,[10,11] Luo[12] and Liu[13] opted for machined alumina substrates. The main drawback of these systems is the cost. A machined alumina well plate may cost up to £300 so has to be re-useable to be cost efficient. As the reaction plate must be re-used a second problem is that of cleaning between experiments. Substrates may be slightly porous or have some reactivity with samples, which can lead to cross contamination. Thorough cleaning of the plate would require several steps including the use of concentrated acids. This clearly is not desirable for a high throughput experiment. Such a plate may also require manual removal of the samples or a probe to enter the wells for analysis.[12] To avoid these problems a flat alumina tile (100 × 70 × 1mm) was chosen for this study. The relatively low cost (~ £1.50 each) allows these tiles to be treated as disposable. A flat substrate also provides more flexibility for characterisation and screening processes as the samples can be analysed *in situ*. The use of such tiles is less common in the literature but has been applied to produce n-type semiconducting oxides[14] and dielectric materials,[15] both in conjunction with ink-jet printing.

For this work a masking system was required to contain the liquid reagents on the tile such that the component elements could be mixed. The system developed comprises a Teflon mask, with a 6 × 9 grid of 5 mm holes, pressed on to the alumina tile by stainless steel plates (Figures 3.3.1 and 3.3.2). Beneath the substrate is a layer of rubber to allow even pressure across the tile and a PTFE sheet to prevent the tile sticking to the rubber during heating steps. This system creates discrete wells in to which solutions can be dispensed, but can be removed once the solvent has evaporated.

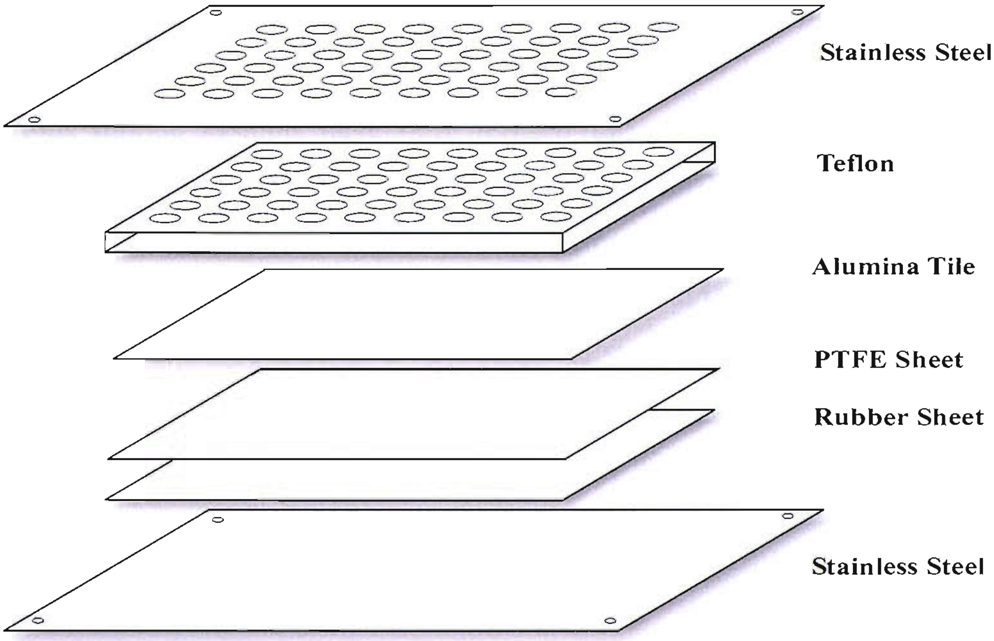

Figure 3.3.1 Components of the masking system based around an alumina substrate.

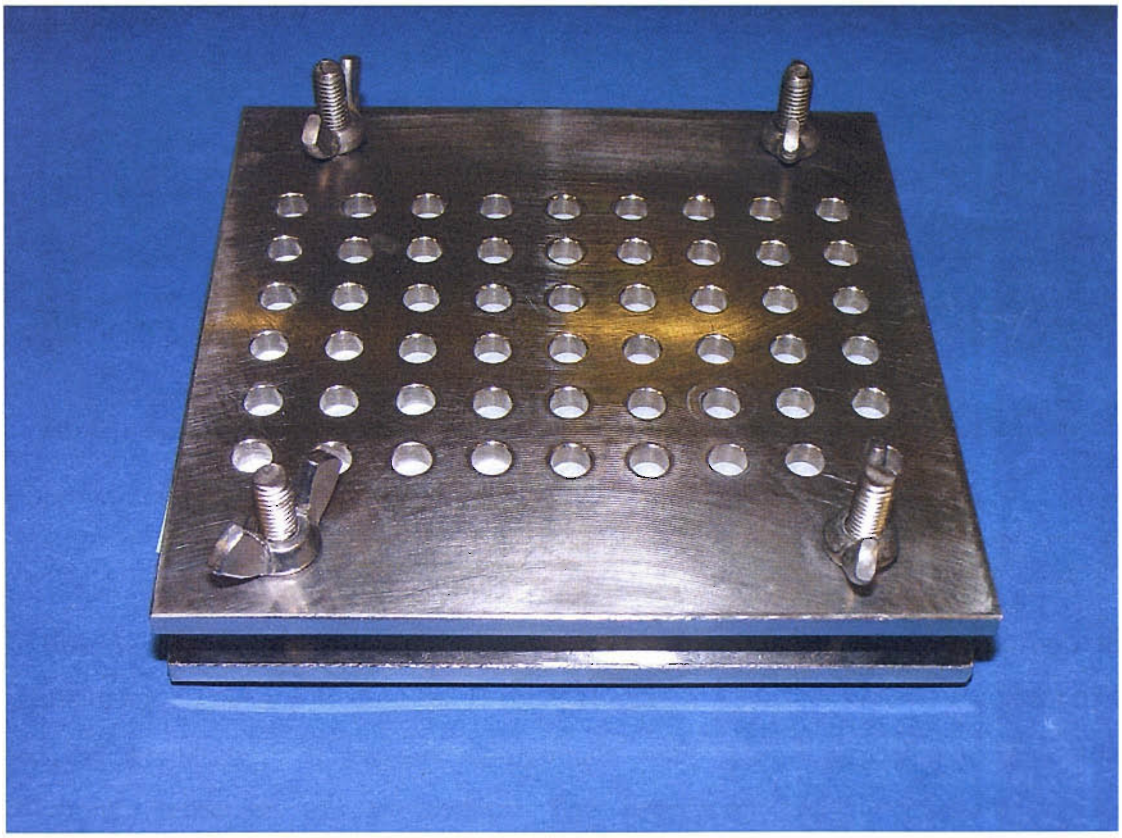

Figure 3.3.2 Photograph of the complete masking system.

3.3.2 Liquid Handling System

Various robotic systems have been utilised for preparing arrays from solutions. These range from purpose built pipetting systems capable of transferring liquids or nanoparticle slurries[16] to modified ink-jet printing systems.[15,17] Research groups have also used technology developed for the pharmaceutical industry.[18,19] These platforms are designed to accommodate a wide range of standard well plates but can also be programmed for custom designed systems. This affords a level of flexibility not available with systems designed around a specific well format.

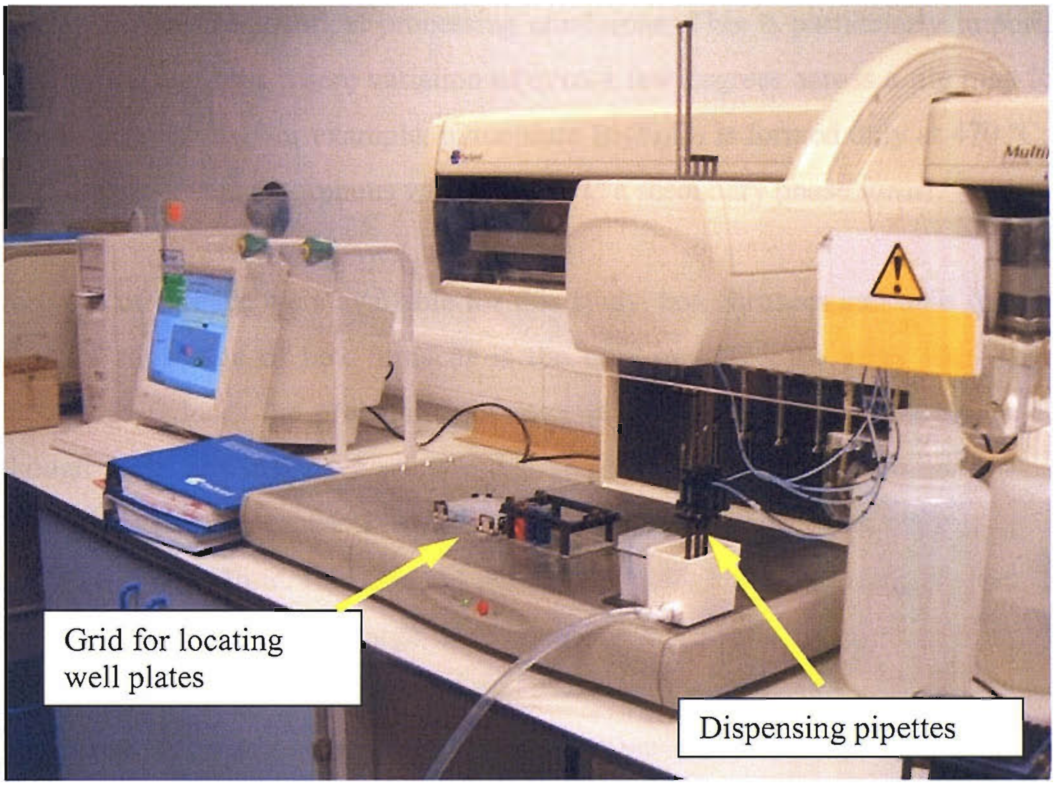

Figure 3.3.3 The Multiprobe II instrument with controlling computer.

In this investigation stock solutions were dispensed in to the array in the appropriate ratios using a Packard Multiprobe II robot (Figure 3.3.3). The system was designed for the preparation of organic compounds with typical procedures including dilutions, genomics and proteomics. The instrument has 4 channels, whose separation can be varied to match distances between wells, on a 3-axis dispensing head. Each channel has liquid level sensing capability and can be controlled independently. Depending on the set-up used, volumes from 0.1 μl to greater than 1 ml can be dispensed. The set-up used for this study allows an accuracy of 1±0.1 μl. It is also possible to switch between fixed and disposable tips within one assay. The system is controlled through WinPREP software,[20] which works on a visual drag and drop basis that can accommodate standard and custom well plates.

3.3.3 Furnaces

A major factor for high throughput materials synthesis is ensuring that all samples on the array experience identical processing conditions. This is particularly important for the annealing steps where variation of even a few degrees across a tile may lead to misleading results. For example, pyrochlore $Bi_2Ti_2O_7$ is formed only at 470 °C; at 460 °C the product is amorphous while at 480 °C a secondary phase forms.[21]

Two types of furnace were available for this study, box furnaces and tube furnaces. The main advantage of box furnaces is the ease in which the array tiles can be loaded. This reduces the probability of material becoming detached from the tile. Although these furnaces have relatively large chambers they are designed to focus their heat towards the centre. Therefore the heated zone is only large enough for one tile to be fired at a time. It is also not possible to change the annealing environment by introducing gases. The large bore (internal diameter 75 mm) tube furnace available has a heated zone of around 400 mm allowing up to four array plates to be fired at once. The use of stainless steel end plates sealed to the recrystallised alumina tube with rubber gaskets also allows reactive gases to be introduced. Therefore this type of furnace is more suited for use in high throughput methodology. The only disadvantage of this equipment is that much more care is required during loading to ensure samples do not become detached from the tile as it is pushed along the tube length.

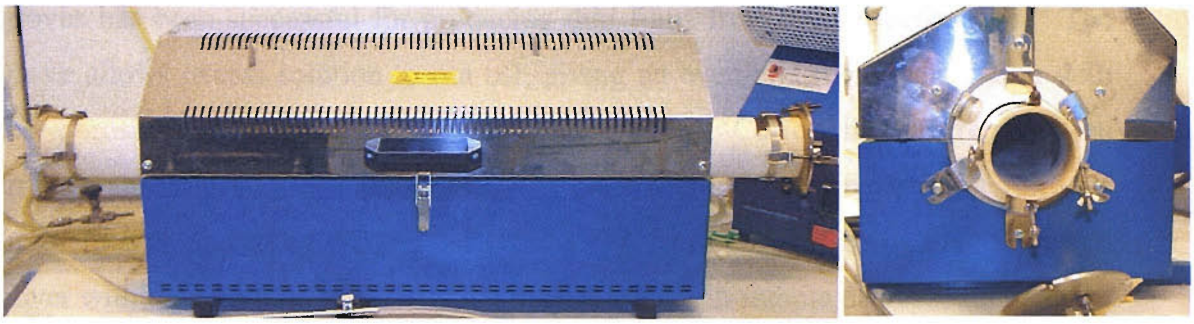

Figure 3.3.4 The large bore tube furnace used for firing alumina tile arrays.

3.3.4 Problems and Modifications

During the development of the synthesis methods various issues arose which required modification of the design or work flow.

Initial tests of the masking system revealed that the pressure provided by the steel plates was not sufficient to form a tight seal between the Teflon and the alumina tile. Liquids dispensed in to the wells simply seeped and mixed under the mask. To overcome this various sealants were trialled. Silicon grease was not suitable for this purpose as it could lead to silica impurities in the final fired samples. The use of eicosaine sealing wax, a purely organic wax, also proved problematic. The low melting point wax was applied to the Teflon mask as a liquid then allowed to set against the alumina tile. This resulted in a reasonable seal in places, but even distribution of wax across the array was difficult and would not be consistent between experiments. The most useful sealant was apiezon grease which reproducibly provided a good seal and could be completely burnt off during the firing processes.

The second issue arose from the evaporation of solvent during the ageing step. In many cases rings of sample formed instead of spots (Figure 3.3.5). The surface tension of the liquid causes a meniscus to form, which results in material being deposited at the edge of the well as the solvent is removed. This effect has been described in several high throughput studies and was overcome with various modifications. Photolithographic etching of a silicon wafer substrate to form circular groves has been successful for producing thin films from sol-gel deposition.[22] The grove allows excess solution to run off, giving an even and reproducible film with low porosity and little crack formation (Figure 3.3.6). 'Coffee rings' were also seen in the combinatorial preparation of organic clear coatings by spin casting.[23] Here the problem was caused by differential evaporation from the surface of the sample. A cover with a 4 mm hole in the middle, placed over each sample decreased the rate of evaporation at the edge of the well to give more uniform coatings. The addition of a larger than expected amount (10 wt%) of an organic dispersant agent was needed to reduce a similar effect for ink-jet printed ceramic samples.[24] In many cases the effect is not a major concern as the physical properties can simply be measured from the sample edge. However, it is desirable to produce uniform samples for some analyses.

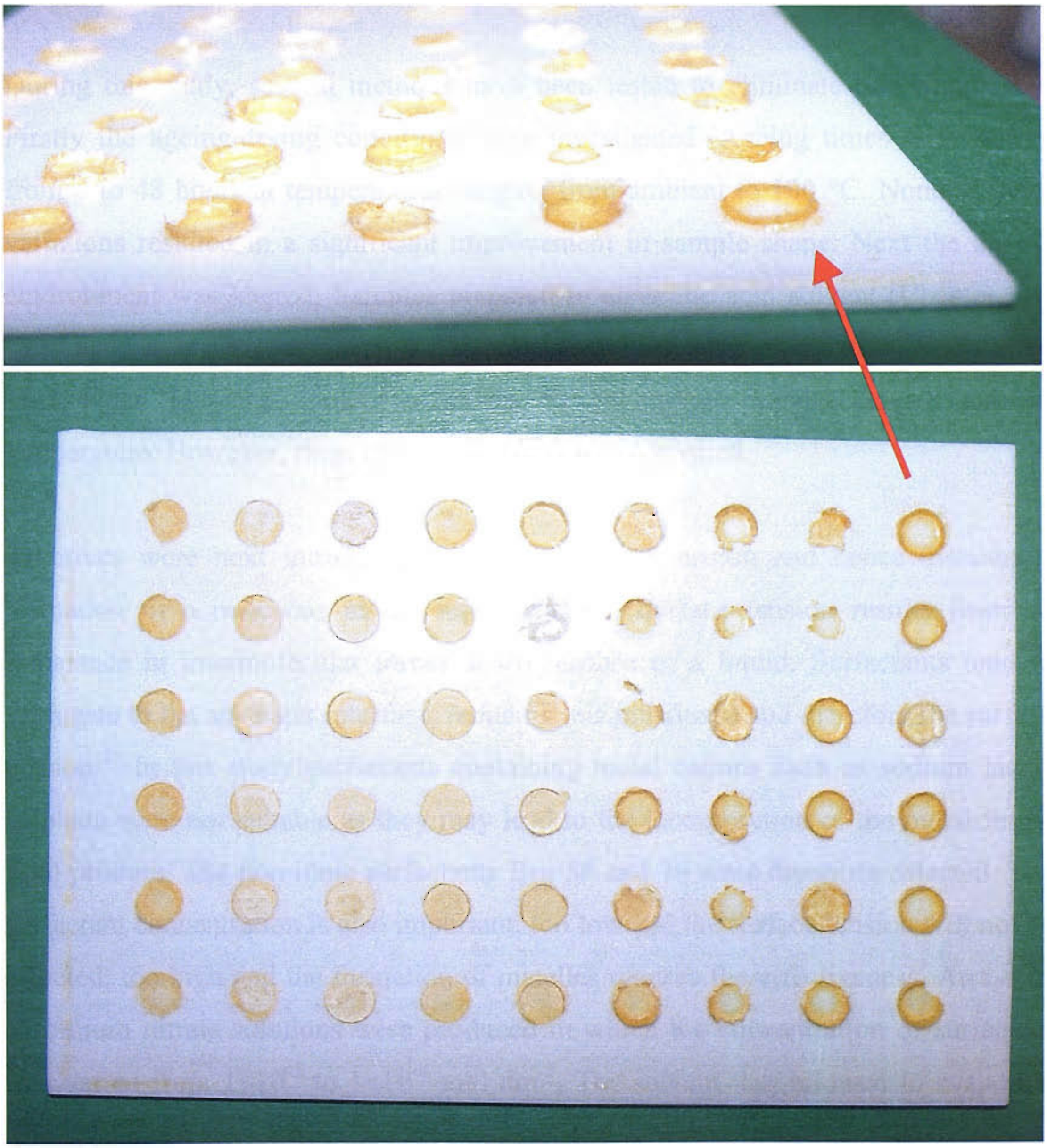

Figure 3.3.5 Array of unfired samples demonstrating the ring forming effect.

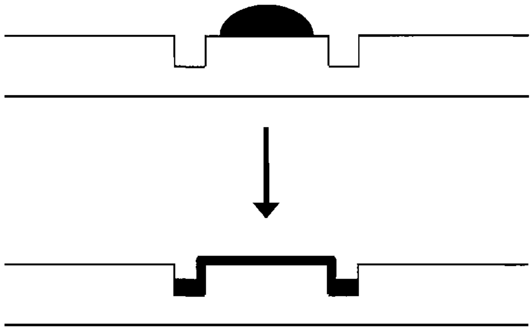

Figure 3.3.6 Schematic view of the spread of liquid on a photolithographically structured substrate.[22]

During this study, several methods have been tested to eliminate this ring effect. Firstly the ageing/drying conditions were investigated. Ageing times were varied from 4 to 48 hours at temperatures ranging from ambient to 100 °C. None of these variations resulted in a significant improvement in sample shape. Next the ageing environment was altered. Samples prepared in an acetic acid solvent (Chapter 3B) were aged in a desiccator over KOH pellets whereas aqueous solutions were dried over silica gel and molecular sieves to encourage evaporation at ambient temperature. However, rings of material were still deposited.

Additives were next introduced to reduce surface tension and hence discourage formation of a meniscus at the liquid surface. Surface tension results from an imbalance in intermolecular forces at the surface of a liquid. Surfactants tend to segregate to the air-water interface, reducing this imbalance and therefore the surface tension.[25] In this study surfactants containing metal cations such as sodium lauryl sulphate were not suitable as they may lead to the incorporation of the metal in the final product. The non-ionic surfactants Brij 58 and 76 were therefore selected. The surfactant concentration is also important; too low and the surface tension will not be affected, too high and the formation of micelles reduces the effectiveness. Arrays of chromium nitrate solutions were produced in which the concentration of surfactant was varied from 1×10^{-5} to 1×10^{-4} mol dm^{-3}. The solvent was allowed to evaporate slowly at room temperature. This too proved unsuccessful in reducing ring formation.

Reducing differential evaporation by using a mask with different sized holes (1- 4 mm) above each sample also proved unsuccessful. The most effective way to produce uniform samples was simply to remove the Teflon mask while a small amount of solvent remained. Removal of the mask released the surface tension while the samples were kept from mixing by residual apiezon grease. Increasing the well diameter from 5 to 7 mm also helped alleviate the problem.

The initial heating steps often resulted in foaming of samples giving a dome effect (Figure 3.3.7), especially for the polymer complexation methods or when reactions contained nitrate groups. As the array is heated above 90 °C gaseous NO_x, CO_2 and organic groups evolve from the sample. The increasingly dense gel prevents these gases from escaping easily and so the material expands.

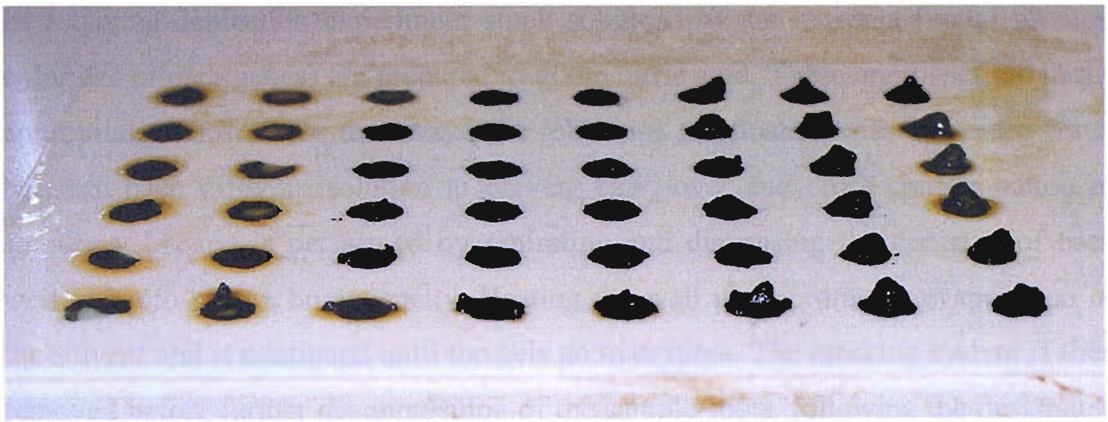

Figure 3.3.7 The foaming effect on array of aged $Cr(NO_3)_3.9H_2O$ solutions, with initial volumes ranging from 10 µl (left column) to 80 µl (right column).

This is a common problem for sol-gel type processes and in some cases can be managed by slowing the rate of heating, allowing gases to evolve over a longer period. However, the presence of both nitrate and organic groups as in Pechini type reactions often leads to an uncontrolled exothermic reaction approximately between 250 °C and 370 °C,[26] negating the benefit of low ramp rates. This effect was exploited by McGinn who created arrays of $Cu_{1-x}Ce_xO_3$ catalysts for the oxidation of CO.[27] The foaming gave high surface area 'caps' of material within a well plate, and these 'caps' could be analysed for catalytic activity by infrared thermal imaging. This effect however is not desirable for most screening techniques. Powder X-ray diffraction requires a flat surface to reduce zero point errors while the accuracy of compositional analysis using EDAX is also affected by sample topography.[28]

In this study the problem arose even when the reactions were simply co-evaporation from nitrate solutions, likely due to interaction with the apiezon grease. In these cases, reducing the initial volume of liquid and applying a rapid heating rate reduced the doming effect significantly (Figure 3.3.7). In cases where no processing variables improved the situation, the samples were carefully flattened after firing.

3.3.5 Outline of the General Synthesis Method

In a typical deposition experiment stock solutions of the reagents (metal nitrates, chlorides or carbonates) are prepared in dilute nitric acid. These are dispensed in the appropriate ratios across the array. The robot tips are flushed with deionised water between each different solution to prevent carry-over and cross contamination of solutions. Mixing is performed by aspirating and dispensing the contents of each well twice to ensure homogeneity. Heating the well plate promotes evaporation of the solvent and is continued until the gels go to dryness. The masking system is then removed before further decomposition of the sample spots, following the designated heating regime, to burn out solvent and organic residues. The alumina tile is then annealed at the desired temperature to give 54 discrete powdered spots.

3.4 High Throughput Screening Methods

3.4.1 X-ray Diffraction using 2-dimensional PXD

As discussed in Section 2.3, the diffracted beams from a single crystal point to discrete directions, each corresponding to a family of diffraction planes. Polycrystalline (powder) samples yield a series of diffraction cones if a large number of crystallites of random orientation are covered by the incident X-ray beam. Each cone corresponds to the diffraction from the same family of crystalline planes in all the participating grains. This is represented schematically in Figure 3.4.1.

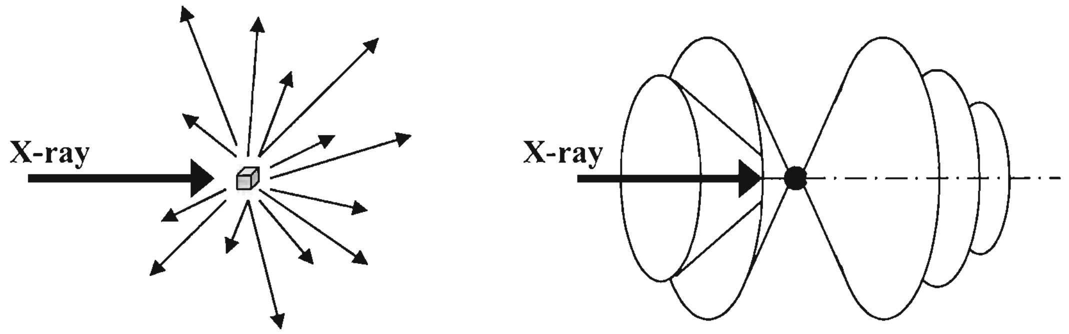

Figure 3.4.1 Diffraction of X-rays a) from a single crystal and b) from a polycrystalline sample.

In conventional PXD experiments the diffraction measurement is confined within a plane. If a point detector or a one-dimensional position-sensitive detector (PSD) is used, a 2θ scan is taken along a detection circle also known as the diffractometer plane. The variation of diffraction pattern in the direction (Z) perpendicular to the diffractometer plane is not considered. Therefore the actual pattern measured is an average over a range defined by beam size in the Z-direction. The missing diffraction data will either be ignored, losing potential structural information, or will require sample rotation to complete the measurement.

Diffraction patterns measured by instruments fitted with two-dimensional detectors are not limited to the diffractometer plane. Whole or large portions of the diffraction rings can thus be measured simultaneously, depending on the detector size, position and distance to sample. Figure 3.4.2 shows how the diffraction cones are sampled with three types of detector.

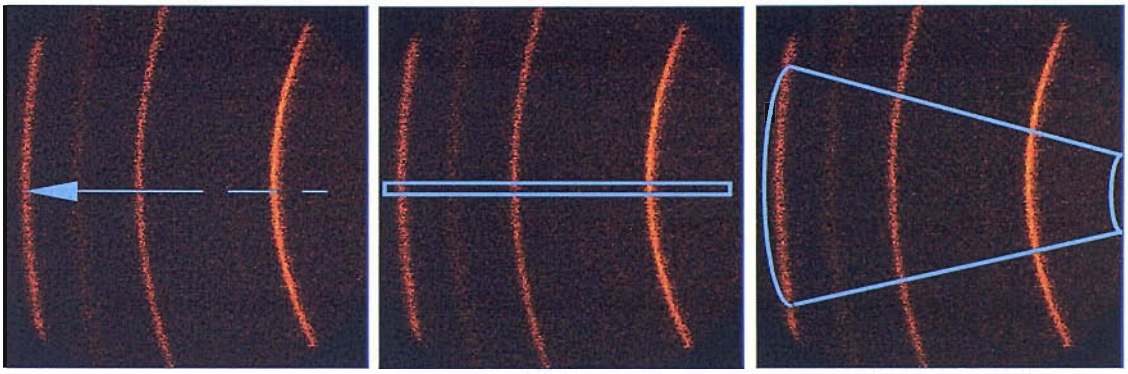

Scintillation Detector	PSD	2-D Detector
- Small spot measured	- Large 2θ range measured simultaneously	- Large 2θ and chi range measured simultaneously
- Long measuring time	- Medium measuring time	- Very short measuring time
- High resolution	- Medium resolution	- Low resolution
- Scan necessary		- Measurement of orientated samples

Figure 3.4.2 Comparison of detector sampling of diffraction cones.

The ability to look at large sections of diffraction cones makes 2-dimensional PXD a powerful tool, enabling structural and mechanical properties to be analysed which would otherwise not be possible. The system allows rapid phase identification making it ideal for high throughput screening. It also enables texture, residual stress, crystal size and percentage crystallinity analyses. Preferred orientation effects, which can alter relative intensities of peaks in a diffraction pattern, can also be easily measured.

Diffraction patterns were measured using a Bruker D8 Discover with General Area Detector Diffraction System (GADDS) for Combinatorial Screening. The instrument uses CuK_α radiation ($\lambda = 1.5418$ Å) with other emission wavelengths being excluded by use of cross-coupled Göbel mirrors. These are parabolic shaped multilayer mirrors which reflect X-rays in the same way as Bragg diffraction from crystals. In contrast to conventional single crystal monochromators, Göbel mirrors have controlled variations in the d-spacing between layers. If two mirrors are used with the second turned 90 degrees a highly parallel beam is produced which is much more intense than can be obtained with a standard pinhole collimator with graphite monochromator. This intensity is useful for high throughput experiments as it allows rapid scans using a small spot size. The low divergence of the beam incident on the sample also decreases the width of crystalline peaks which improves resolution.

The diffractometer is also fitted with an XYZ stage and laser video sample alignment system allowing multiple samples to be accurately positioned in the beam. Hence arrays of crystalline samples can be analysed sequentially according to pre-set target lists. The HI-STAR area detector facilitates rapid collection of data, which for most applications is 100 times faster than a linear PSD. The detector consists of an X-ray proportional chamber with a 2-dimensional multiwire grid. The chamber contains a high-pressure xenon gas mixture behind a beryllium window. Each X-ray photon is converted into a charge pulse and is collected on the grid. The X-Y position of the photon is then calculated by a Position Decoding Circuit (PDC). These factors make the instrument highly suited for high throughput X-ray diffraction. Figure 3.4.3 illustrates the configuration of the diffractometer.

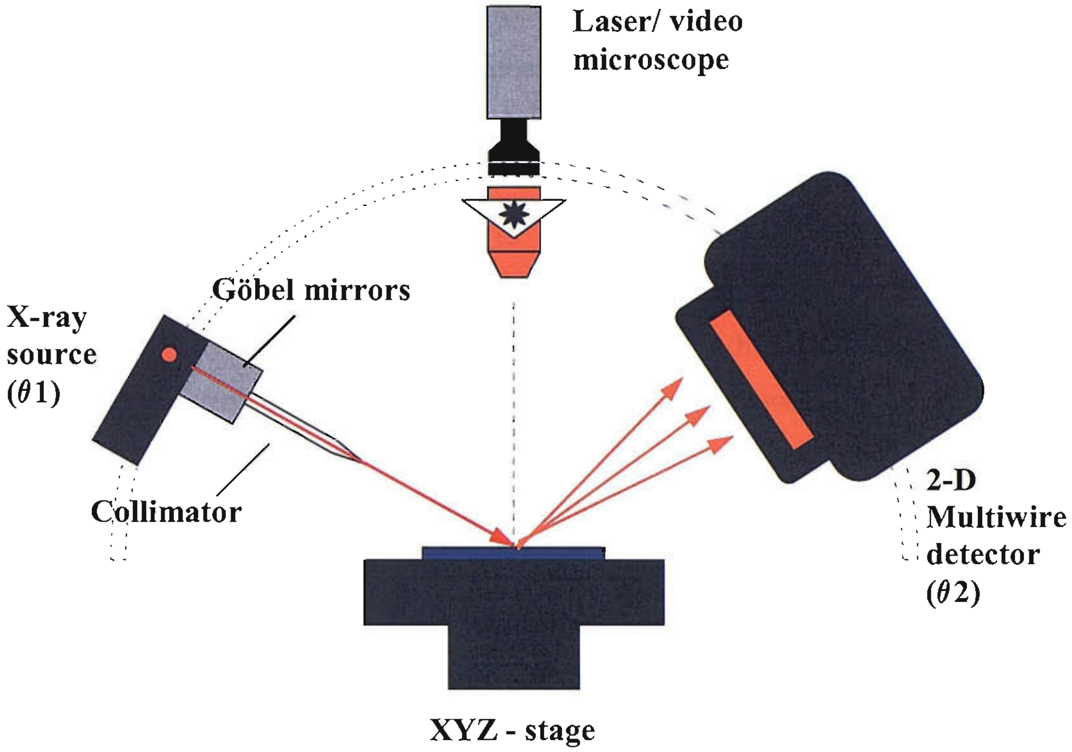

Figure 3.4.3 Configuration of the diffractometer used for high throughput analysis.

Integration of the diffraction data yields an intensity versus 2θ plot analogous to a standard diffraction plot. For phase identification the pattern can be matched against known compounds on the Powder Diffraction File (PDF) database maintained by the Joint Committee on Powder Diffraction Standards (JCPDS).[29] In some cases the diffraction patterns were analysed with the GSAS package as described in Section 2.5.

3.4.2 Colour Measurement

All high throughput experiments require a screening process to determine which materials are potentially useful. To determine the suitability of compounds as pigments it is clear that the colour/optical properties of the samples must be assessed in a rapid manner. Few high throughput studies have investigated the measurement of colour properties. Colour space measurements of metal nitride coatings have previously been carried out by Perkins using simultaneous optical reflection and transmission spectrum mapping.[30] A multichannel fibre optically coupled CCD array-based spectrometer was used to collect data in the UV-Vis-NIR region. Calculations from the combined spectra produced CIELab values for colour quantification. However, this is only possible for thin films deposited on a transparent substrate so is not suitable for the arrays in this work.

The colour measurement technique used in this study simply used a digital image of each array. To maintain consistency between experiments the array is mounted on a photographers copy stand with two lamps providing even illumination (Figure 3.4.4). The values for the red, green and blue (RGB) colour components of each sample can then be extracted using a standard graphics package (CorelDRAW version 10). These values are normalised and corrected for brightness by subtracting values from a standard photographers grey card.

Samples displaying promising colour properties can be scaled up to produce approximately a gram of sample. This is studied in more detail by analysis using a Perkin Elmer Lambda 35 UV-Vis spectrometer as described in Section 2.6.

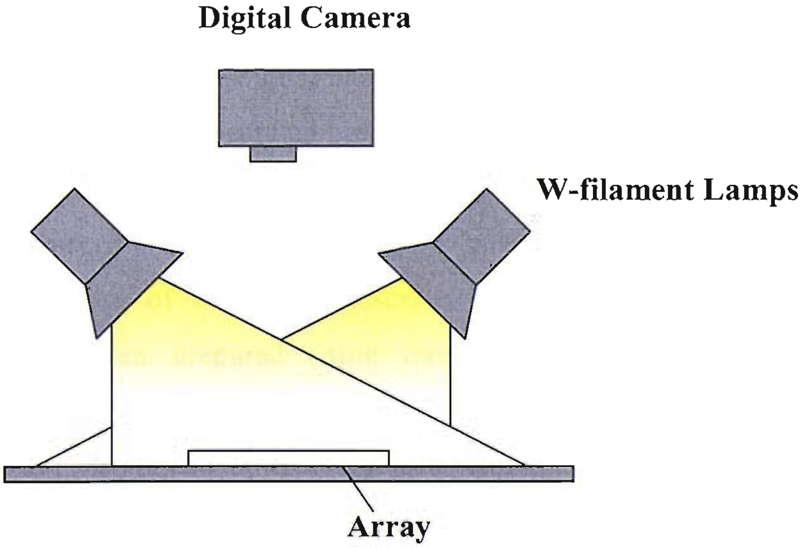

Figure 3.4.4 Schematic of the set up used to acquire digital images for colour measurement.

3.4.3 Electron Microscopy/ Elemental Analysis

To ensure the desired composition is achieved across an array some form of elemental analysis is necessary. In some studies this has been in the form of X-ray fluorescence (XRF).[31,32] However, this requires non-standard equipment and is not suitable in all cases. As described in Section 2.8 it is possible to obtain compositional information from samples mounted in an electron microscope using the EDAX technique. Selected arrays in this study were analysed in this way using a microscope fitted with a large sample chamber. The entire array is placed on the positionally addressable XYZ stage contained within the vacuum chamber. Point readings across a sample are used to assess their homogeneity, while area scans over each material in turn yield the compositional trend across the array. This process however is fairly time consuming and so would not be carried out for all arrays. The sample compositions should derive from the stoichiometric ratio of the reactants so the elemental analysis is simply a confirmatory technique.

3.5 Conclusions

A general method for creating arrays of solid materials on an alumina substrate by solution deposition has been developed. In order to carry out numerous reactions in parallel on the substrate, a re-usable Teflon/stainless steel masking system was constructed. This creates discrete wells into which solutions can be dispensed, but can be removed once the solvent has been evaporated. High temperature annealing then transforms these amorphous precursors into crystalline materials. The samples produced can be analysed *in situ* by X-ray diffraction, colour measurement and electron microscopy. In this study arrays of pigment materials have been prepared, the initial findings of which are described in subchapters 3A-C. Three pigment systems have been prepared using three distinct solution methods; polymer complexation, alkoxide based sol-gel and co-evaporation techniques. Luminescent materials have also been studied using these techniques and are described in Chapter 4.

These high throughput synthesis methods may be applied to a wide range of materials providing that suitably stable, soluble reagents are available. The format of the libraries should allow further properties to be screened with the development of suitable instrumentation. Variants of this methodology have been already been applied to produce potential transparent conducting oxide[33] and battery materials.[34]

3.6 References

[1] B. Jandeleit, T. S. Powers, D. J. Schaefer, H. W. Turner, and W. H. Weinberg, *Angew. Chem. Int. Ed.* **38** 2494 (1999).

[2] X. D. Xiang and Y. K. Yoo, *J. Phys.: Condens. Matter.* **14** R49 (2002).

[3] T. X. Sun, *Biotechnol. Bioeng.* **61** 193 (1999).

[4] H. Koinuma, I. Takeuchi and R. B. Van Dover, *MRS Bull.* **27** 301 (2002).

[5] P. J. Mcginn and H. M. Reichenbach, *J. Mater. Res.* **16** 967 (2001).

[6] H. D. Park, S. Y. Seo and K. S. Sohn, *Electrochem. Solid-State Lett.* **4** H26 (2001).

[7] M. Jansen and H. P. Letschert, *Nature* **404** 980 (2000).

[8] S. Senkan, *Angew. Chem. Int. Ed.* **40** 312 (2001).

[9] I. Yanase, T. Ohtaki and M. Watanabe, *Appl. Surf. Sci.* **189** 292 (2002).

[10] S. Y. Seo, K.-S. Sohn, H. D. Park and S. Lee, *J. Electrochem. Soc.* **149** H12 (2002).

[11] K.-S. Sohn, J. M. Lee, I. W. Jeon and H. D. Park, *J. Electrochem. Soc.* **150** H182 (2003).

[12] Z.-L. Luo, B. Geng, J. Bao and C. Gao, *J. Comb. Chem.* **7** 942 (2005).

[13] X.-N. Liu, H.-B. Cui, Y. Tang, S.-X. Huang, W.-H. Liu and C. Gao, *Appl. Surf. Sci.* **223** 144 (2004).

[14] R. Funahashi, S. Urata and M. Kitawaki, *Appl. Surf. Sci.* **223** 44 (2004).

[15] J. R. G. Evans, M. J. Edirisinghe, P. V. Coveney and J. Eames, *J. Eur. Ceram. Soc.* **21** 2291 (2001).

[16] I. Yanase, *Mat. Res. Soc. Symp. Proc.* **700** S5.1.1 (2002).

[17] B-J. de Gans and U. S. Schubert, *Macromol. Rapid Commun.* **24** 659 (2003).

[18] T. Bein, *Angew. Chem. Int. Ed.* **38** 323 (1999).

[19] C. J. Vess, J. Gilmore, N. Kohrt and P. J. McGinn, *J. Comb. Chem.* **6** 86 (2004).

[20] Winprep software, Version 1.14.0187, (2001).

[21] A. L. Hector and S. B. Wiggin, *J. Solid State Chem.* **177** 139 (2004).

[22] B. Wessler, V. Jéhanno, W. Rossner and W. F. Maier, *Appl. Surf. Sci.* **223** 30 (2004).

[23] J. N. Cawse, D. Olsen, B. J. Chisholm, M. Brennan, T. Sun, W. Flanagan, J. Akhave, A. Mehrabi and D. Saunders, *Prog. Org. Coat.* **47** 128 (2003).

[24] J. Wang and J. R. G. Evans, *J. Comb. Chem.* **7** 665 (2005).

[25] I. W. Hamley, *'Introduction to Soft Matter'*, John Wiley & Sons, UK (2002).

[26] L.-W. Tai and P. A. Lessing, *J. Mater. Res.* **7** 502 (1992).

[27] H. M. Reichenbach and P. J. McGinn, *J. Mater. Res.* **16** 967 (2001).

[28] R. Beanland, P. J. Goodhew and J. Humphreys, *'Electron Microscopy and Analysis' (Third Edition)*, Taylor & Francis, UK (2001).

[29] PCPDFWIN Version 2.4, Powder Diffraction File, International Centre for Diffraction Data, Swarthmore, PA, USA (2003).

[30] J. D. Perkins, C. W. Teplin, M. F. A. M van Hest, J. L. Alleman, X. Li, M. S. Dabney, B. M. Keyes, L. M. Gedvilas, D. S. Ginley, Y. Lin and Y. Lu, *Appl. Surf. Sci.* **223** 124 (2004).

[31] D. G. Duff, A. Ohrenberg, S. Voelkening and M. Boll, *Macromol. Rapid Commun.* **25** 169 (2004).

[32] E. D. Isaacs, M. Marcus, G. Aeppli, X. D. Xiang, X. D. Sun, P. Schultz, H. K. Kao, G. S. Cargill and R. Haushalter, *Appl. Phys. Lett.* **73** 1820 (1998).

[33] S. J. Henderson, J. A. Armstrong, A. L. Hector and M. T. Weller, *J. Mat. Chem.* **15** 1528 (2005).

[34] A. D. Spong, G. Vitins, S. Guerin, B. E. Hayden, A. E. Russell and J. R. Owen, *J. Power Sources* **119** 778 (2003).

Chapter 3A

High Throughput Study of Chromium Doped Perovskites

3A.1 Introduction

Doping into the ABO_3 perovskite structure can allow tailoring of properties to specific applications. Subtle changes in chemical doping at the A or B cation sites are therefore of considerable importance. Zirconates have been investigated previously as high temperature proton conductors with potential applications as fuel cells and hydrogen sensors.[1] However, there have been few reports on the doping of first row transition metals, specifically chromium, into zirconates.

Blasse and co-workers explored the possibility of such doping for solar energy applications.[2,3] The aim was to produce visible light photocatalysts for the decomposition of water to hydrogen and oxygen. This followed from reports of successful electrode systems consisting of chromium-doped titanates. The colouration of the white titanates reduces their bandgap to allow absorption of a greater range of energy from solar radiation. However, these studies only involved doping on a very small level (1000 ppm) and neither the colours produced nor the X-ray data were reported.

The addition of Cr_2O_3 to ABO_3 compounds (A = Ca, Sr, Ba; B = Ti, Sn, Zr, Hf) to form ceramic pigments has also been investigated.[4] The report suggests that addition of Cr_2O_3 to $SrZrO_3$ leads to a rose-red colour, but little X-ray data were reported. Hence there is a need to study the system further and is an ideal opportunity to investigate pigments it in a rapid fashion.

3A.2 Synthesis and Characterisation

Doped perovskite zirconates were prepared by the citrate gel method outlined in Section 2.2.2. Stock solutions (0.3 M) of the metal reagents ($CaCO_3$, $SrCO_3$, $ZrO(NO_3)_2.3H_2O$ and $Cr(NO_3)_3.9H_2O$) were prepared in dilute nitric acid. These were dispensed across the array in the appropriate ratios to give a total volume of 60 μl in each well. An aqueous citric acid/ ethylene glycol solution (1.2 M) was then added to each mixture (15 μl/well) before mixing was performed (2 cycles of 60 μl aspiration/dispensing). Various heating regimes were tested; a typical scheme involving heating to 90 °C for 10 minutes followed by evaporation/gelation overnight at 40 °C. The mask was then removed and the tile treated at 350 °C (24 hours) and 550 °C (24 hours) before annealing at 600, 800, 1000 or 1200 °C.

Phase identification of the sample spots was carried using the Bruker D8 Discover with General Area Detector Diffraction System (GADDS). The diffractometer was set up with the X-ray source (theta-1) at 20 ° and the area detector (theta-2) at 25 ° combined with the 0.3 mm collimator. This produced diffraction patterns with a 2θ range from 27.5 ° to 62 °. The scan time was ten minutes per spot.

Selected samples were analysed by SEM/EDAX to study morphology and elemental composition using a Philips XL30ESEM. Images of each spot were taken at 100x and 500x magnification using the secondary electron detector with the instrument in wet mode. EDAX measurements were taken at 50x magnification with a spot size of 6.0, accelerating voltage of 15 kV and water pressure of 0.4 torr.

3A.3 Results and Discussion

Arrays were prepared such that chromium was doped into replace zirconium by up to 24%. The doping was increased in 3% steps across the nine wells in the x direction. In the y direction the A cation was varied from calcium to strontium in 20% steps giving an overall formula for the array of $Ca_{1-x}Sr_xZr_{1-y}Cr_yO_3$ (x = 0, 0.2, 0.4, 0.6, 0.8, 1; y = 0, 0.03…0.24). Colour gradients from white (undoped) to dark yellow-brown ($SrZr_{0.76}Cr_{0.24}O_3$) to rose-red ($CaZr_{0.76}Cr_{0.24}O_3$) were observed. The rose-red colour compares to that described previously with chromium in the +3 oxidation state.[4] Examination of the X-ray data revealed that a perovskite phase was present in all samples for most of the arrays, even at 600°C. The only exceptions were the arrays fired at slow ramping rates. The idea behind the slow increase in temperature was to reduce the possibility of samples foaming as vapours escaped during the initial decomposition steps. The later firings were also carried out in this manner to prevent cracking of the spots as the remaining carboniferous material was burned out. Arrays fired in this manner were visibly inhomogeneous and the diffraction patterns revealed that calcium and strontium carbonates were present along with other phases such as zirconium oxide. This indicates that the slow increase in temperature favoured formation of the carbonates, as the organic material was not burnt off quickly enough.

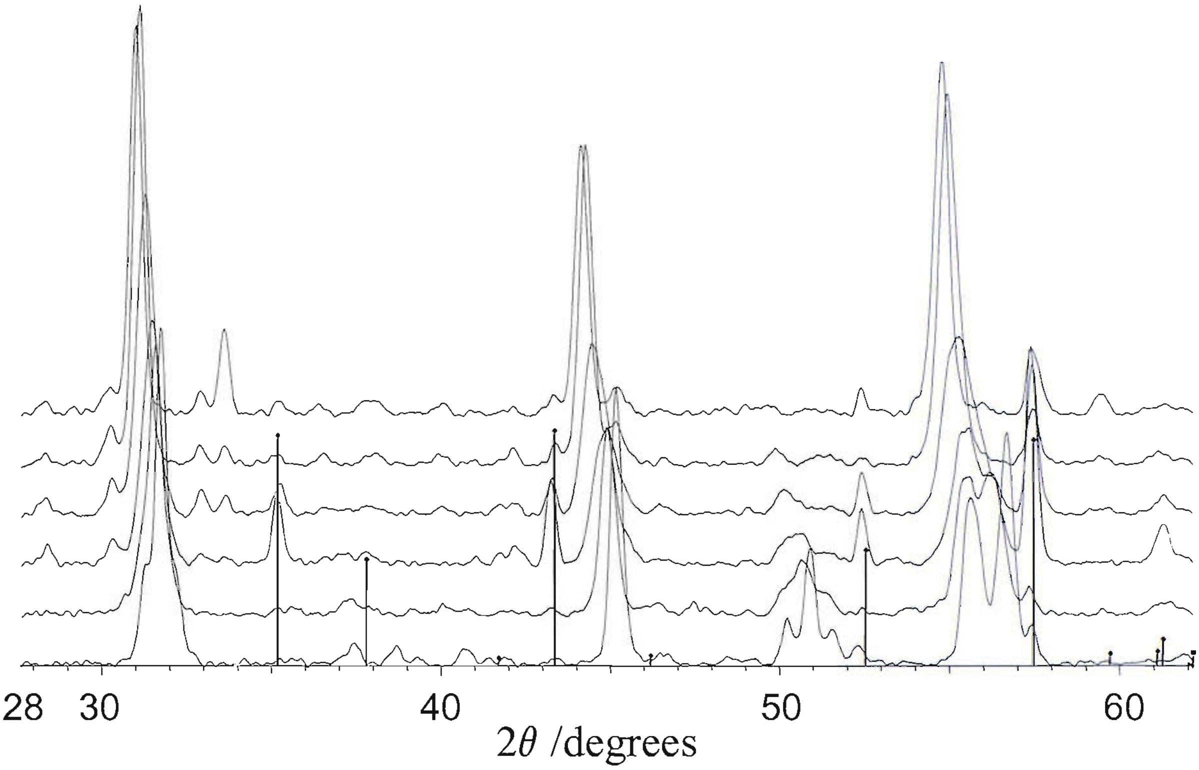

Figure 3A.3.1 Diffraction patterns of the undoped perovskite samples showing the variation from $CaZrO_3$ (front) to $SrZrO_3$ (back). Black lines indicate the main reflections arising from the alumina substrate.

Homogeneous samples were formed when arrays were heated more quickly; however in all cases as the gels decomposed they formed dome shapes as vapours escaped. Various heating schemes were tried to overcome this but none succeeded. The main problem with this behaviour is that diffraction measurements require a flat sample for accurate extraction of lattice parameters though phase identification is unaffected. To overcome this problem each sample was to be crushed flat using a glass slide prior to being analysed with care taken to avoid cross contamination between samples.

The perovskite phases present corresponded with the JCPDS cards for calcium zirconate and strontium zirconate as expected (Figure 3A.3.1). The CELREF[5] programme was used initially to attempt to determine whether the lattice parameters were varying with the addition of chromium. Note that only three or four peaks could be used to extract the lattice parameter due to the small angular range of the detector and the pattern simplicity. Although there were slight deviations in the parameters, there was no clear pattern to suggest systematic variation with doping. A further issue is that peaks from the alumina substrate were visible in many of the patterns when the sample had cracked revealing the tile below. Although these did not interfere with the main perovskite reflections, they may have obscured other trends such as the growing of impurity phases.

Refinements were also attempted using the GSAS[6] suite of programs. A fit was obtained for an undoped sample, then the histogram replaced by subsequent doped versions and the lattice parameters refined for each. This method also came up against a number of problems. Refinements were very unstable due to the quality of the data and so became a lengthy process to refine significant numbers of samples. The broadness of the peaks due to the small particle size and the inherent properties of patterns obtained using an area detector made the task more challenging. However, refining the peakshape profiles of a standard sample such as alumina and retaining these values for profile coefficients of array samples proved a useful tool. The data was of significant quality to allow lattice parameter values to be calculated, but more detailed refinement of thermal parameters or atom positions was not possible. The results show a clear increase in lattice parameter with increasing strontium content (Table 3A.3.1). There is also some indication of decreasing values as the chromium doping level increases.

Table 3A.3.1 Lattice parameters (Å) obtained using GSAS. Calcium rich phases refined with the orthorhombic Pcmn space group (pdf 76-2401); strontium rich phases with the cubic Pm3m space group (pdf 76-0167) (estimated standard deviations in parentheses).

Nominal composition		Chromium doping level(x)/ % of B site					
		0	3	6	9	12	15
$CaZr_{1-x}O_3$	*a*	5.578(5)	5.584(5)	5.588(4)	5.597(5)	5.584(4)	5.592(5)
	b	8.032(7)	8.038(6)	8.029(7)	8.038(7)	8.039(7)	8.036(7)
	c	5.762(5)	5.762(5)	5.755(5)	5.762(5)	5.764(4)	5.757(5)
$Ca_{0.8}Sr_{0.2}Zr_{1-x}O_3$	*a*	5.604(5)	5.604(4)	5.607(5)	5.606(5)	5.605(5)	5.605(4)
	b	8.066(6)	8.060(7)	8.061(7)	8.061(7)	8.061(7)	8.056(6)
	c	5.784(5)	5.756(4)	5.763(5)	5.761(5)	5.752(5)	5.767(4)
$Ca_{0.6}Sr_{0.4}Zr_{1-x}O_3$	*a*	5.622(4)	5.623(5)	5.622(5)	5.620(5)	-	5.597(5)
	b	8.045(7)	8.054(7)	8.046(7)	8.053(6)	-	8.030(7)
	c	5.811(4)	5.781(5)	5.800(5)	5.778(5)	-	5.805(5)
$Ca_{0.4}Sr_{0.6}Zr_{1-x}O_3$	*a*	4.064(2)	4.074(1)	4.049(1)	4.065(1)	4.059(2)	4.045(1)
$Ca_{0.2}Sr_{0.8}Zr_{1-x}O_3$	*a*	4.086(1)	4.076(1)	4.074(1)	4.074(1)	4.073(2)	4.071(1)
$SrZr_{1-x}O_3$	*a*	4.095(1)	4.094(2)	4.097(1)	4.098(1)	4.094(1)	4.094(2)

Colour gradients from white (undoped) to dark yellow-brown ($SrZr_{0.76}Cr_{0.24}O_3$) to rose-red ($CaZr_{0.76}Cr_{0.24}O_3$) were observed. Results obtained from the colour screening for a $Ca_{1-x}Sr_xZr_{1-y}Cr_yO_3$ array are shown in Figure 3A.3.2. The 0 and 20 % Sr rows showed a pale red colour from 3 % Cr increasing in intensity up to 24 % doping. The 40-80 % Sr samples varied from pale yellow at 3 % Cr to a yellow-orange at higher levels. A yellow-brown shade was observed for 100 % Sr that became darker as the level of chromium increased. Although coloured material was produced, none of the compositions achieved suitable qualities for use as a pigment so more detailed colour measurements on bulk samples were not carried out.

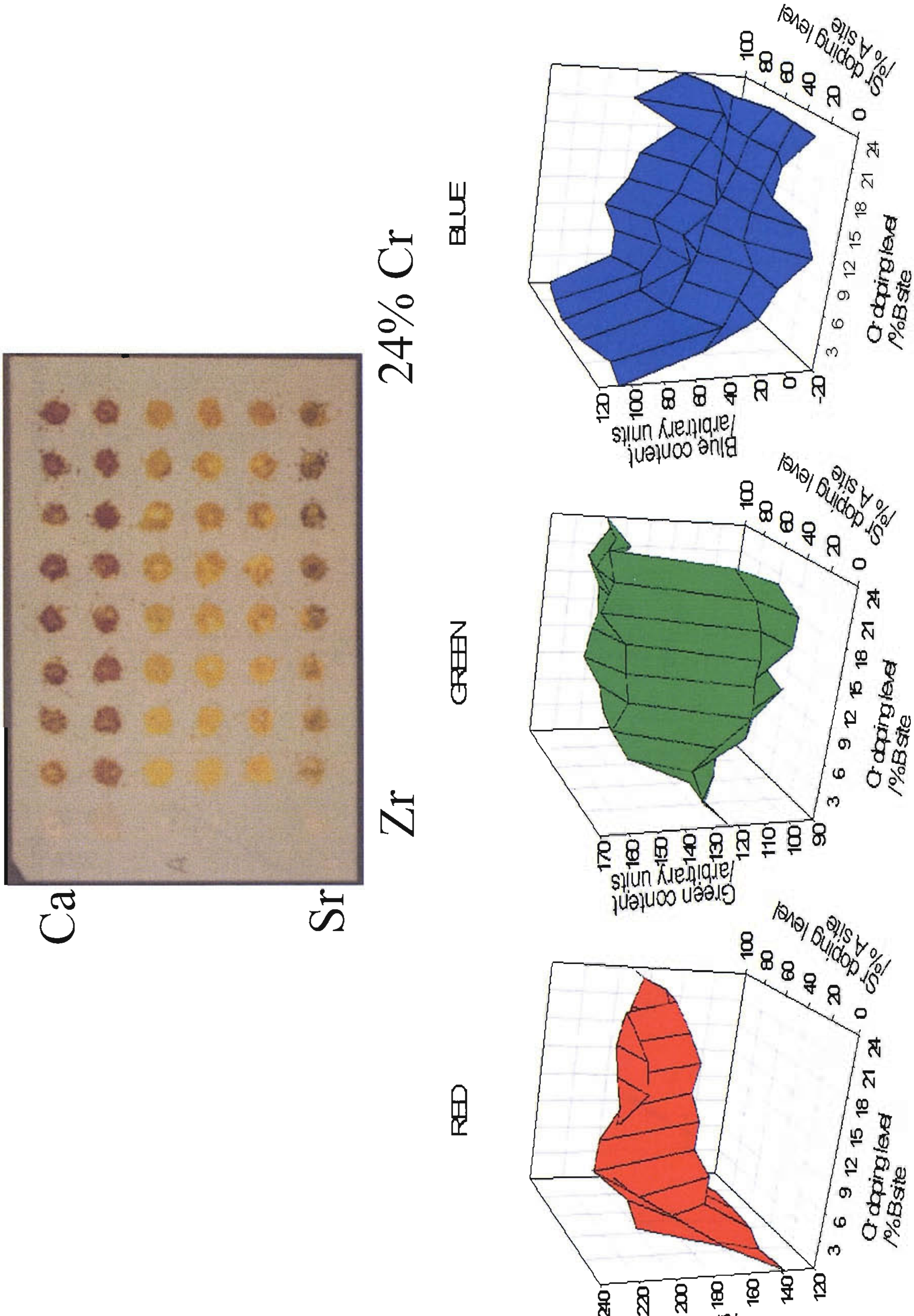

Figure 3A.3.2 Digital image and colour measurement results from an array of the composition $Ca_{1-x}Sr_xZr_{1-y}Cr_yO_3$ fired at 1000 °C.

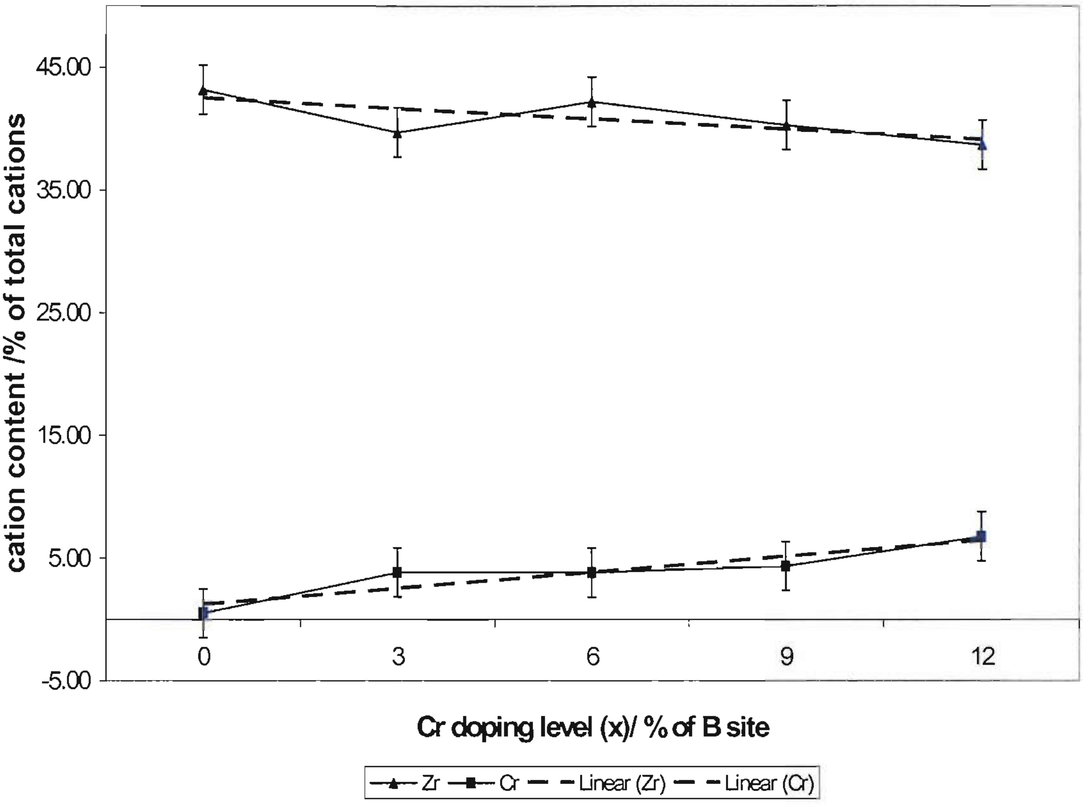

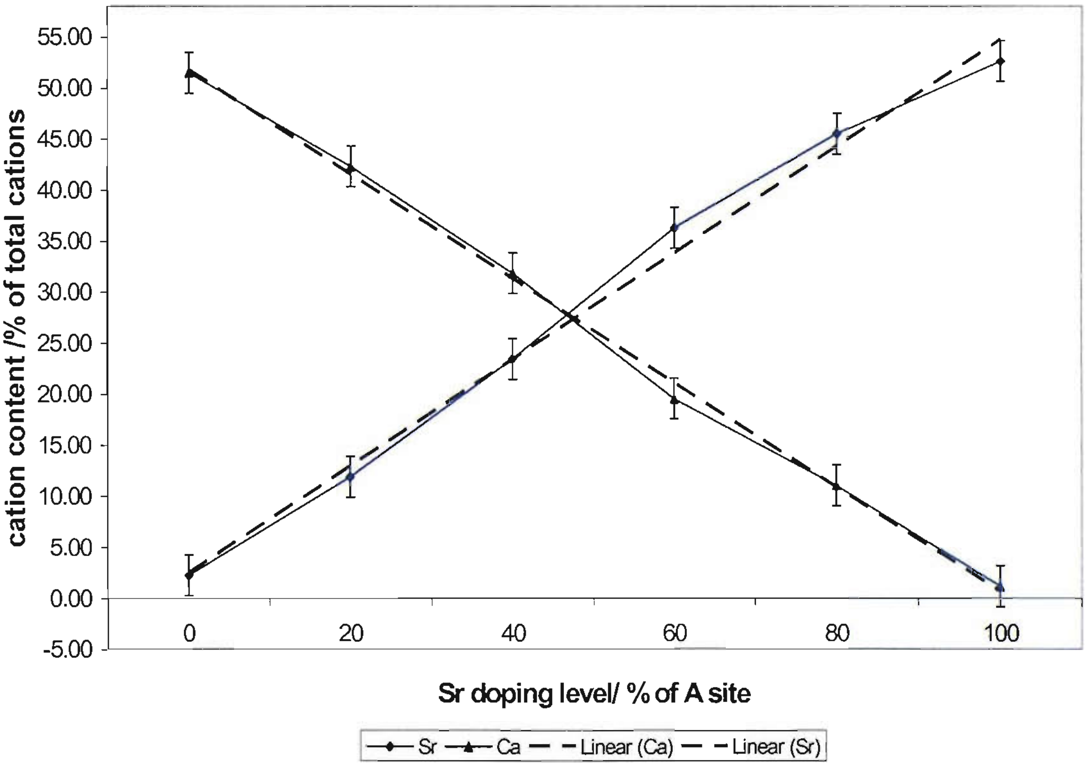

Figure 3A.3.3 Graphical representation of EDAX results from array fired at 1000°C. The top graph shows the variation of Zr and Cr across a row; the lower graph shows the change on the A cation site down a column of the array.

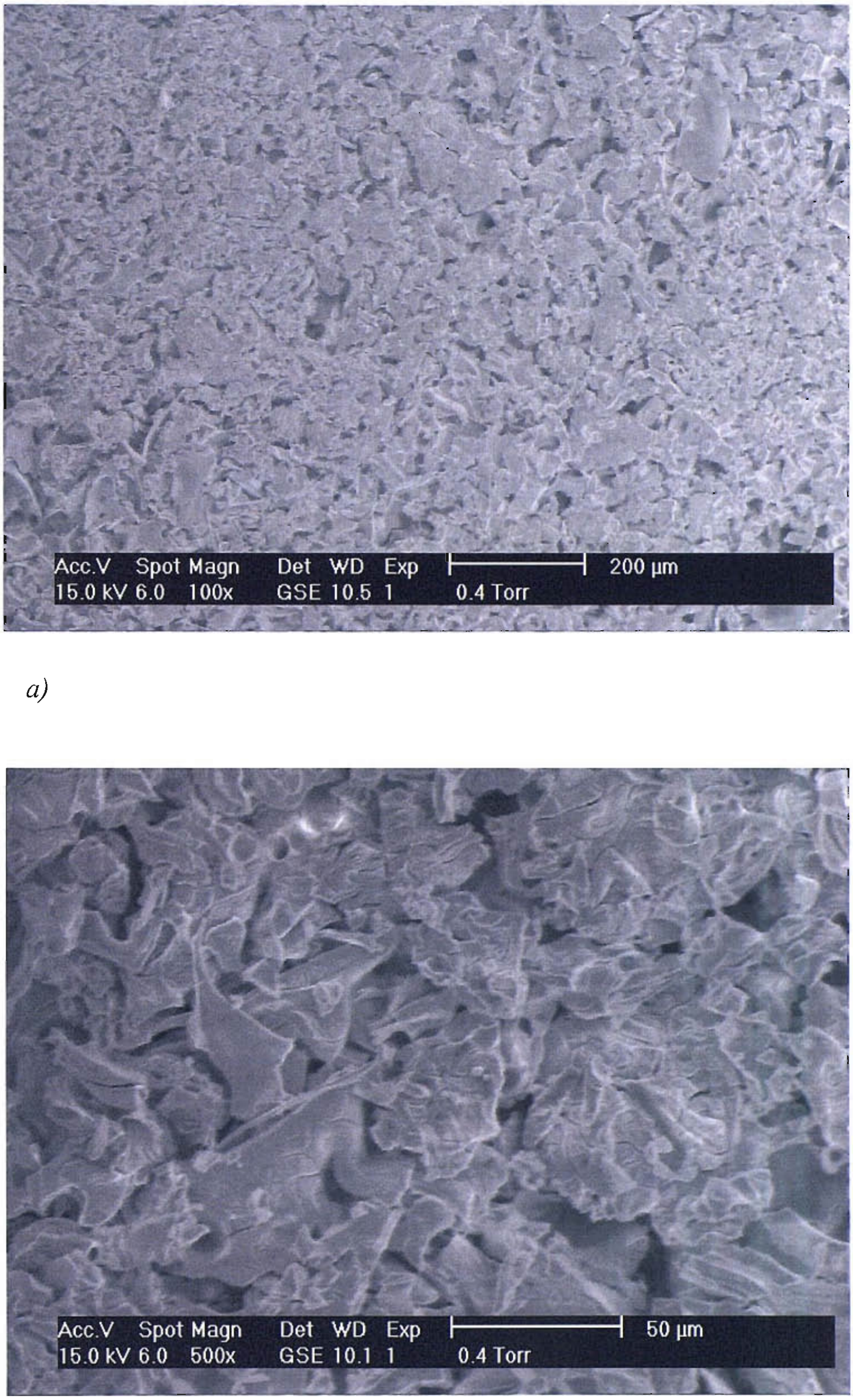

a)

b)

Figure 3A.3.4 Scanning electron micrographs of $Ca_{0.8}Sr_{0.2}Zr_{0.91}Cr_{0.09}O_3$ *spot fired at 1000 °C; a) at 100× magnification and b) at 500× magnification.*

Electron microscopy studies of the samples of an array fired at 1000 °C revealed the spots to be porous materials as expected using the citrate method (Figure 3A.3.4). The results from the compositional analysis studies follow the anticipated trends. The chromium doping increases gradually to 6.8 % of total cations equating to 13.6 % of the B site with a concurrent decrease in zirconium (Figure 3A.3.3). The 13.6 % value falls within the error limits of the expected 12 % Cr for that sample. The calcium and strontium contents remain constant across the row and vary in approximately 20 % steps down the column. Hence arrays can be analysed successfully by SEM and EDAX in a viable timescale (~3 hrs for EDAX measurement of 54 samples) and have shown that the desired stoichiometries can be achieved.

It is unclear from the structural information whether successful doping into the perovskite lattice has been achieved. From the radii of the Cr^{4+} and Zr^{4+} cations (r = 69 and 86 pm respectively)[7] one would expect a more significant variation in lattice parameter by 24 % doping. However, this is only 24 % of the B site and it is the larger A cation which has more influence on the size of the unit cell. A lack of dopant incorporation may be because the +4 chromium oxidation state is required and the synthesis here favours the more stable +3 state. Previous studies indicate that a low level of doping Cr^{3+} (1000 ppm) is readily achieved using standard solid state methods.[2,3] It is also possible that the formation the purely zirconium perovskite phase is thermodynamically favourable. Hence, even at temperatures as low as 600 °C this is the phase that crystallises first and that the chromium forms an amorphous impurity phase. However, the variation in colour in the presence of different A cations does suggest some level of incorporation of chromium onto the B site.

3A.4 Conclusions

Arrays of chromium doped zirconate perovskites have been prepared and screened using high throughput methods. Doping produces materials ranging in colour from yellow to rose-red depending on the A cation content. Homogeneous material can be produced from citrate-gel amorphous precursors in the desired ratios if appropriate processing conditions are established. These arrays can successfully be analysed for their structural, compositional and colour properties in a rapid manner providing an increase in efficiency compared to one-at-a-time experiments.

3A.5 References

[1] R. A. Davies, M. S. Islam and J. D. Gale, *Solid State Ionics* **126** 323 (1999).

[2] G. Blasse and P. H. M. De Korte, *J. Inorg. Nucl. Chem.* **43** 1499 (1981).

[3] G. Blasse and P. H. M. De Korte, *J. Inorg. Nucl. Chem.* **43** 1505 (1981).

[4] L. Tcheichvili, *Bol. Soc. Espan. Ceram.* **10** 3 (1971).

[5] J. Laugier and B. Bochu, *CELREF*, Laboratoire des Matériaux et du Génie Physique, Ecole Nationale Supérieure de Physique de Grenoble INPG, France (2000).

[6] A. C. Larson and R. B. Von Dreele, *General Structure Analysis System (GSAS)*, Los Alamos National Laboratory Report LAUR 86-748, (2004).

[7] R. D. Shannon, *Acta Cryst.* **A32** 751 (1976).

Chapter 3B

High Throughput Study of Oxide-Nitride Perovskites

3B.1 Introduction

The replacement of oxygen by nitrogen often results in a highly coloured compound and for this reason oxide-nitrides have been investigated by a number of groups as potential pigments.[1] Jansen used standard methods to investigate solid solutions of the $CaTaO_2N$ and $LaTaON_2$ perovskite systems as potential replacements for cadmium based red and yellow pigments.[2] The colour can be tuned from bright yellow to deep red depending on the O to N ratio in the $Ca_{(1-x)}La_xTaO_{(2-x)}N_{(1-x)}$ system. This tuning of colour with compositional variation makes such systems highly suited to high throughput investigation.

Typically oxide-nitrides are thermally stable to 400 °C after which they begin to release nitrogen and take up oxygen.[3,4] Therefore they may find uses as non-toxic pigments for plastics and cosmetics.

Amorphous precursors, which can be fired under ammonia to form oxide-nitrides or in air to give oxide phases, can be prepared by sol-gel methods. In this study a procedure based on work by Guenther and Jansen was modified to produce arrays. A mixed solvent of acetic acid and acetic anhydride (9:1) is used in conjunction with metal alkoxides or metal salts to yield a highly reactive gel.[5] The solvent allows for a slow gelation process that ensures optimal distribution of metal atoms in the resulting gel. The acetic acid acts as a chelating agent to suppress premature coagulation of the evolving sol particles while the acetic anhydride buffer binds the water produced by esterification. Water is thus kept at a low and constant level so as to promote co-condensation reactions rather than hydrolysis of individual alkoxides. Applying this sol-gel technique to high throughput experiments should allow arrays of coloured material with varying nitrogen contents to be prepared.

3B.2 Synthesis and Characterisation

Oxide-nitride arrays were prepared by the modified sol-gel method from stock solutions (0.25 M) of the metal reagents ($Sr(OPr^i)_2$, $La(NO_3).6H_2O$, $Zr(OEt)_4$ and $Ta(OEt)_5$) in 90:10 acetic acid: acetic anhydride. These were dispensed across the array in the appropriate ratios to give a total volume of 80 μl in each well before mixing was performed (2 cycles of 60 μl aspiration/dispensing). Disposable conductive tips were used to prevent blockages as the solutions hydrolyse. Typical processing regimes involved leaving the array in a dessicator over KOH overnight, allowing the gel to form slowly as the solvent evaporated. The mask was then removed and the tile treated at 250 °C under N_2 (16 hours) and 550 °C in air (16 hours) before annealing at 650, 750, 850 or 950 °C under high purity ammonia at very high flow rates (4 hours).

Phase identification of the sample spots was carried using the Bruker D8 Discover with General Area Detector Diffraction System (GADDS). The diffractometer was set up with $\theta 1$ (the X-ray source) at 20 ° and $\theta 2$ (the area detector) at 25 ° combined with the 0.3 mm collimator. This produced diffraction patterns with a 2θ range from 27.5 ° to 62 °. The scan time was ten minutes per spot. Selected samples were analysed by SEM/EDAX to study morphology and elemental composition using a JEOL JSM5910.

3B.3 Results and Discussion

Arrays were prepared such that the B cation was varied from zirconium to tantalum in 12.5 % steps and the A cation was strontium throughout. Six identical rows of this composition were produced to provide comparison. This gave an overall formula for the array of $SrZr_{1-x}Ta_xO_{2+x}N_{1-x}$, analogous to that reported by Grins.[6] Arrays incorporating lanthanum failed as the solutions hydrolysed too quickly in the presence of the hydrated nitrate. In order to obtain the oxide-nitride arrays it was necessary to fire the array in air at 1000 °C first then heat in ammonia at 950 °C. Oxide-nitride arrays could not be obtained directly from the amorphous precursors due to apparent carbon contamination of the products. Diffraction patterns indicated the expected phases but materials were black.

Arrays of white crystalline solids were formed after the initial firing, which when analysed by PXD depicted a change from perovskite $SrZrO_3$ to the pyrochlore $Sr_2Ta_2O_7$ (Figure 3B.3.1). Closer inspection revealed splitting of the peaks at a doping level of 25 % Ta into the system, with a shift to higher 2*θ* values as the Ta content increases. The indication is that there is a maximum uptake of Ta into the zirconate phase, after which two separate phases form, one being tantalum rich the other zirconium rich. This was supported by a bulk sample of $SrZr_{0.5}Ta_{0.5}O_3$, prepared using identical conditions to those of array samples, which was also biphasic (Figure 3B.3.2).

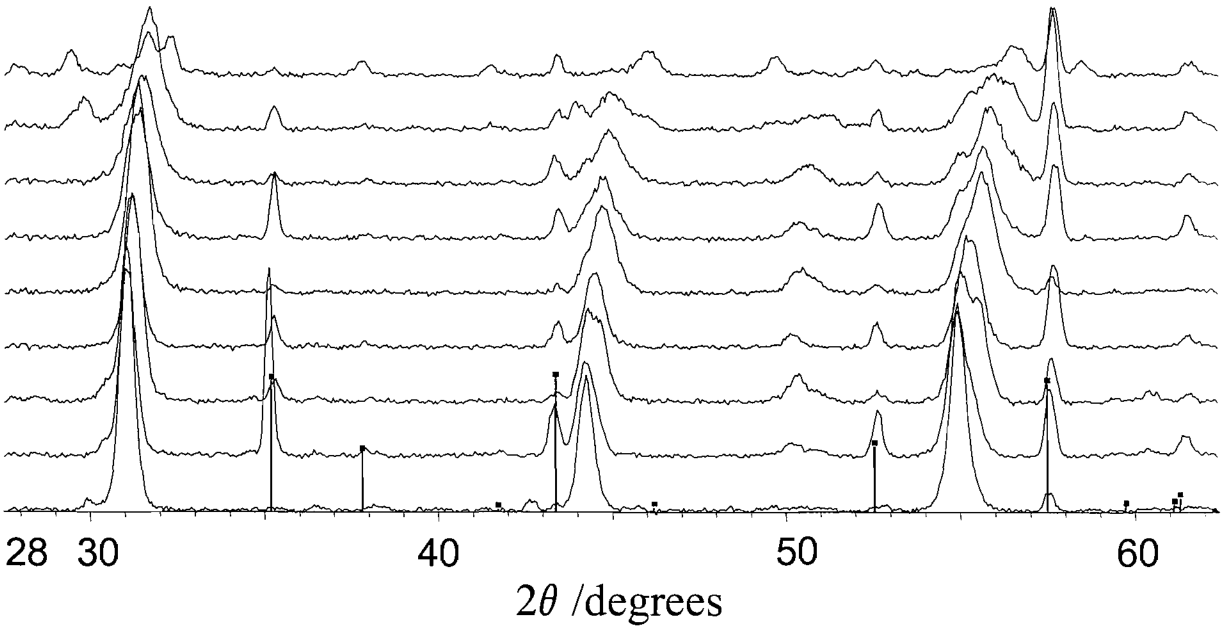

Figure 3B.3.1 Diffraction patterns showing the variation from $SrZrO_3$ *(front) to* $Sr_2Ta_2O_7$ *(back). Black lines indicate the main peaks arising from the alumina substrate.*

The refinement of the bulk sample was carried out using two phases based on the standard perovskite model (Sr (0, 0, 0), Zr/Ta (½, ½, ½), O (½, ½, 0). The first phase was attributed a nominal fractional occupancy of 10 % Zr and 90 % Ta on the ‘B’ site while the reverse was applied to the second phase. Initially lattice parameters, zero point, background and profile coefficients were refined, followed by the relative phase fractions. Attempts to then refine the fractional ‘B’ site occupancies resulted in an unstable refinement.

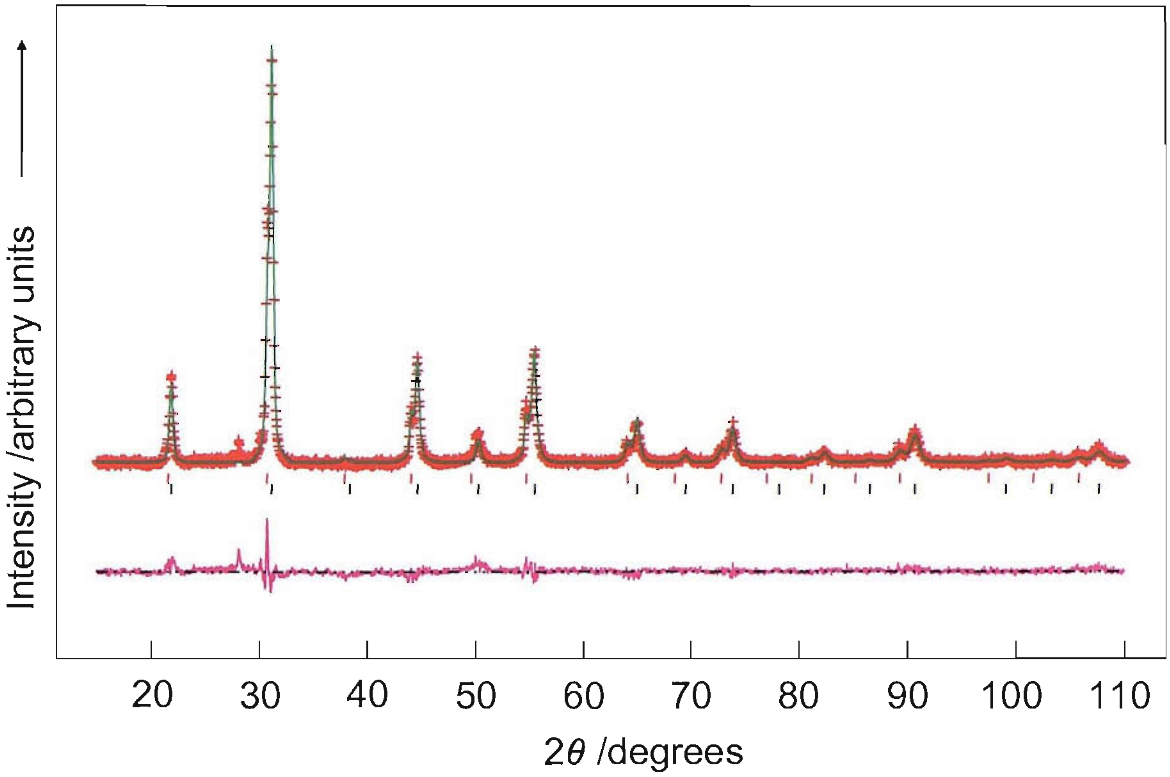

Figure 3B.3.2 Rietveld refinement of $SrZr_{0.5}Ta_{0.5}O_3$ *bulk sample. The black tickmarks represent the tantalum rich phase; the red is the zirconium rich phase.* ($\chi^2 = 2.23$ $R_{wp} = 15.13\%$, R_p *11.42%)*

After ammonolysis the samples were coloured and matched the previous observations for the same system.[9] Increasing tantalum content across the array gave a colour gradient from white (0 % Ta) to green (12.5-50 % Ta) to yellow (62.5-75 % Ta) to orange (87.5-100 % Ta). Colour measurements demonstrated that a reasonable consistency was retained between the rows of identical composition (Figure 3B.3.3). The RGB plots show a gradual increase in the red value and a decrease in blue content with increasing tantalum content. The green value reaches a maximum at $SrZr_{0.375}Ta_{0.625}(O,N)_3$.

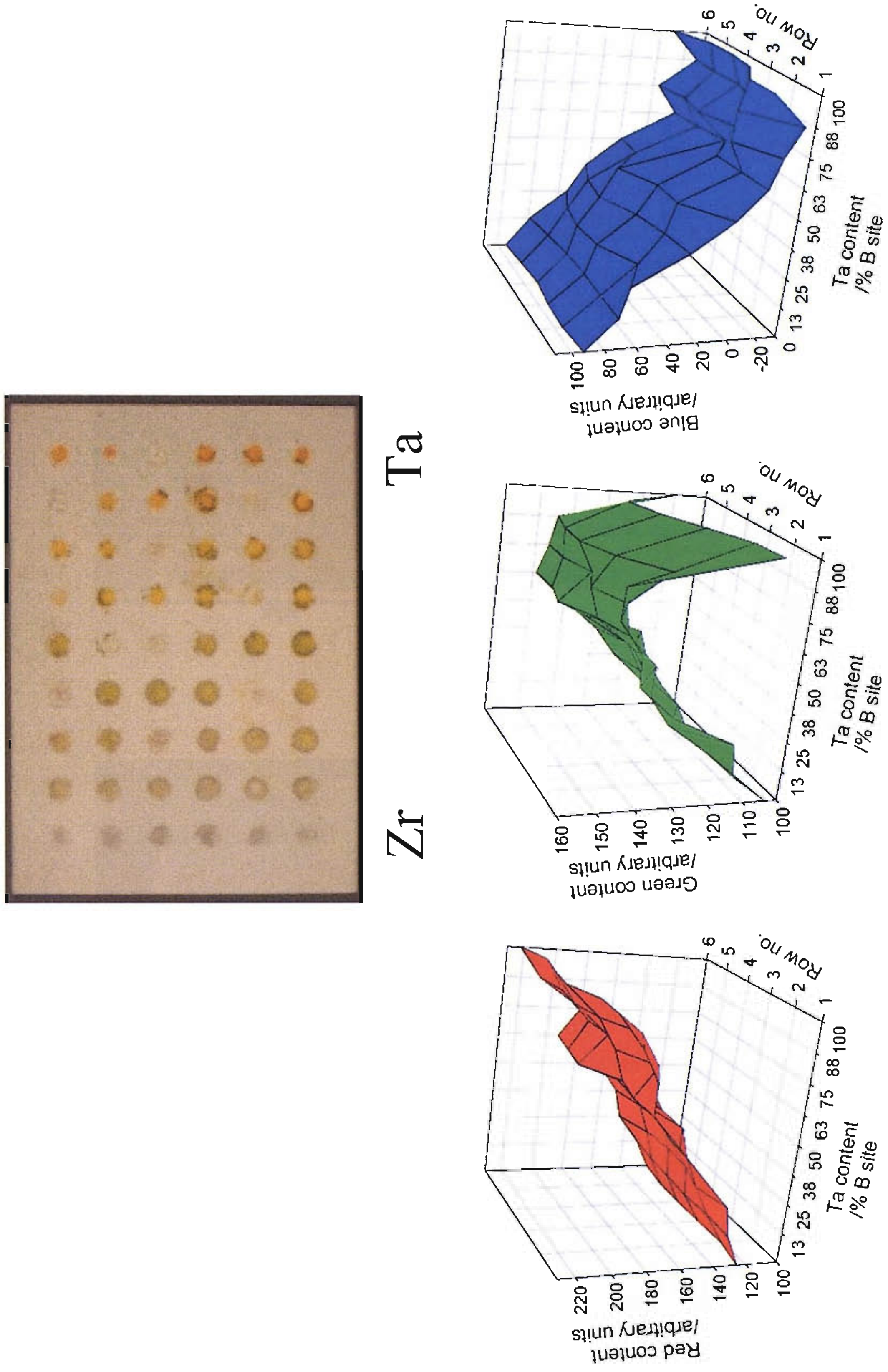

Figure 3B.3.3 Digital image and colour measurement results from an array of the composition $SrZr_{1-x}Ta_xO_{2+x}N_{1-x}$.

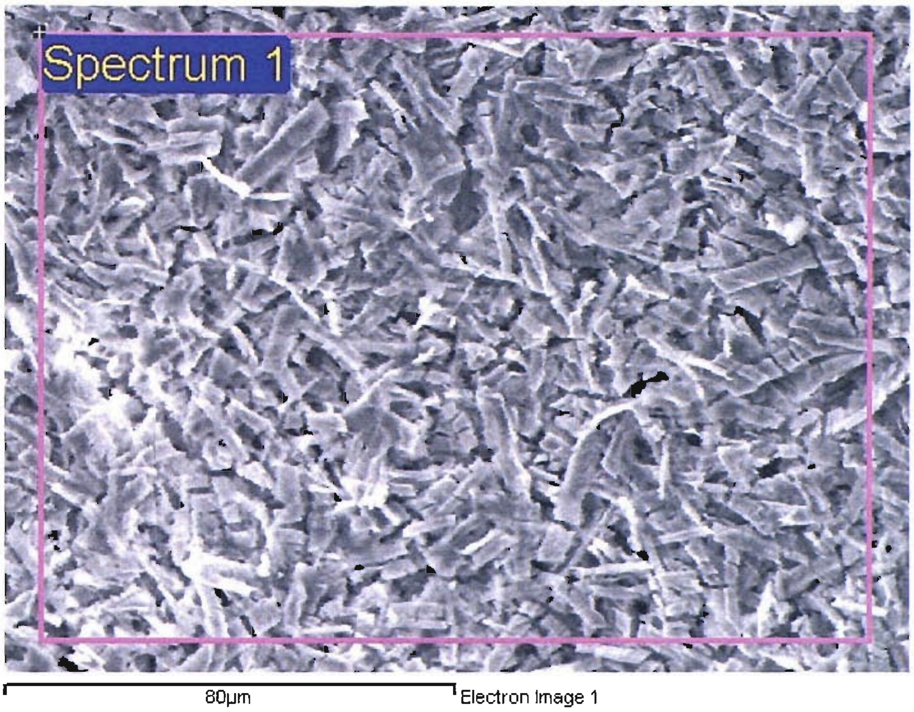

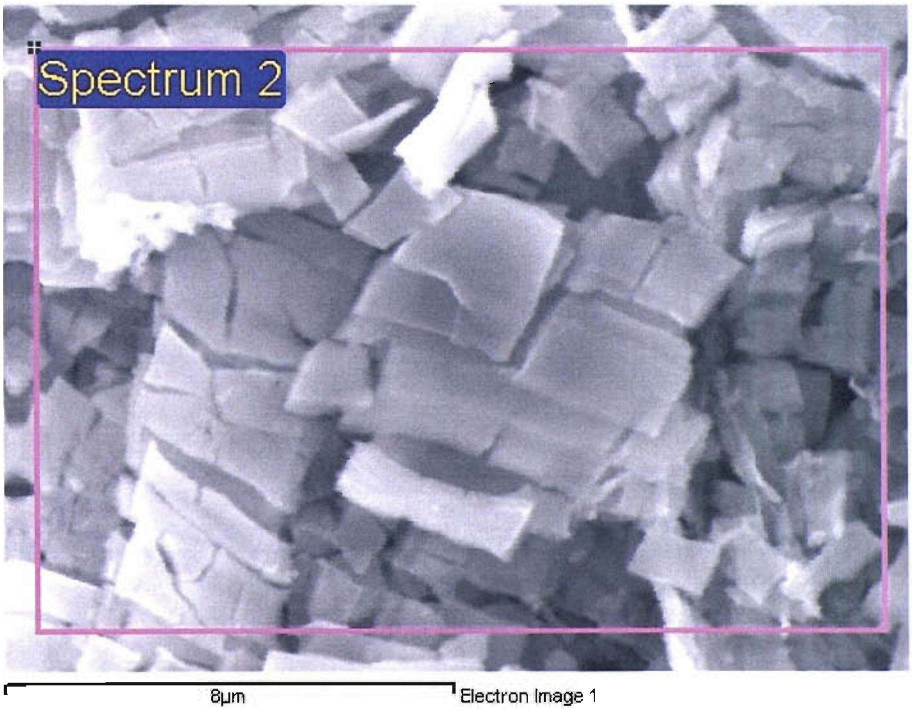

Figure 3B.3.4 Scanning electron micrographs of the $SrZrO_3$ spot fired at 1000 °C.

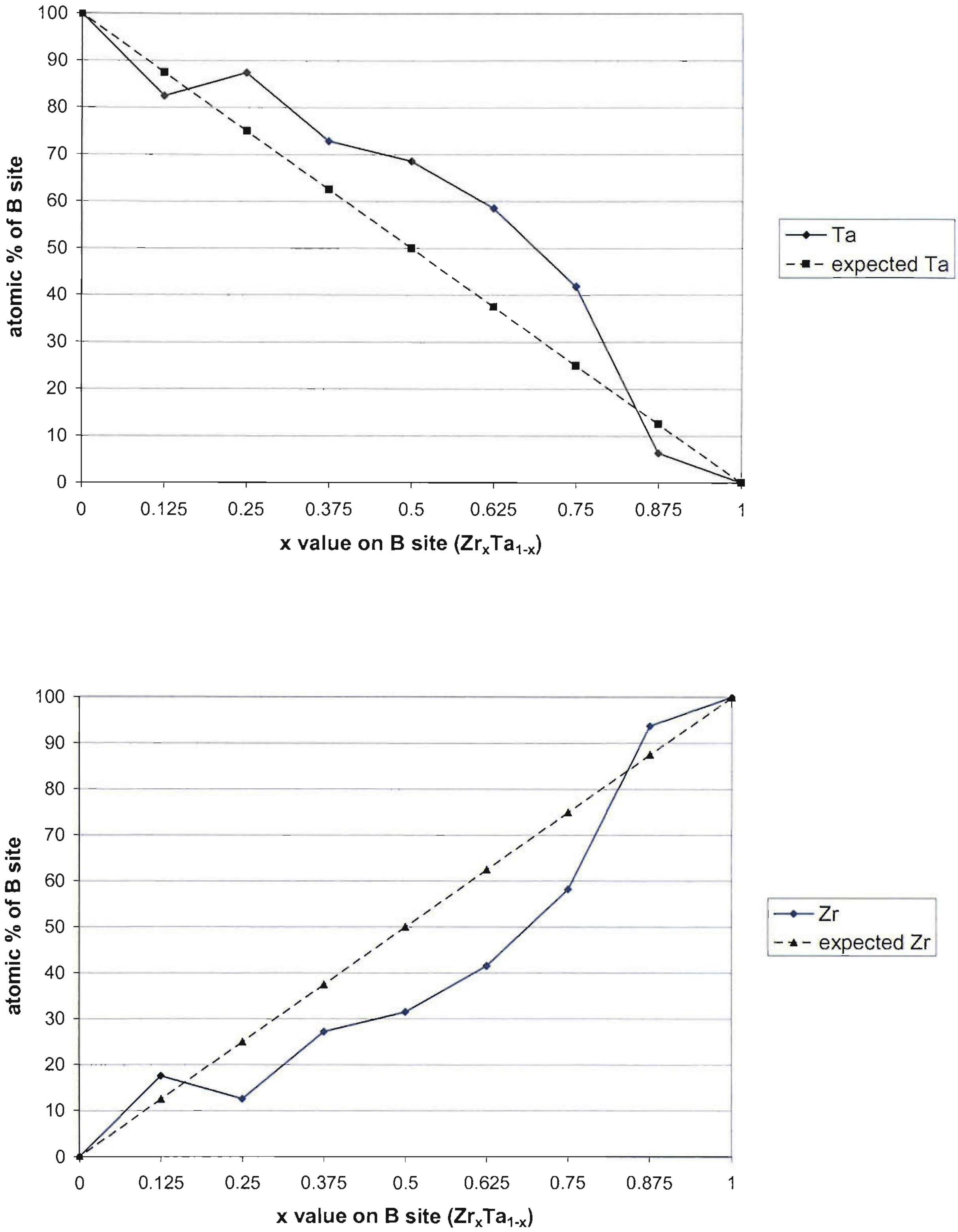

Figure 3B.3.5 Compositional analysis data for one row of the $SrZr_xTa_{1-x}O_{2+x}N_{1-x}$ *array.*

SEM micrographs revealed that the samples were composed of well defined crystallites (Figure 3B.3.4). The elemental composition of the array samples follows the general trend expected (Figure 3B.3.5). However some results are as much as twenty percent different to the expected value. This is probably due to the topology of the samples which can greatly affect the accuracy of the EDAX measurements. For this technique to be improved flatter, crack free samples must be produced.

3B.4 Conclusions

Arrays of oxide-nitride materials with the general formula $SrZr_xTa_{1-x}O_{2+x}N_{1-x}$ have been produced, which vary in colour from white to green to orange with increasing tantalum content. The addition of different cations to the system may allow further tuning of the optical properties. The arrays have been prepared using an alkoxide sol-gel route however the process needs to be optimised for each new system studied. The main problems which arise are the stability of the stock solutions and cracking of sample spots.

3B.5 References

[1] E. Guenther, R. Hagenmayer and M. Jansen, *Z. Anorg. Allg. Chem.* **626** 1519 (2000).

[2] M. Jansen and H. Letschert, *Nature* **404** 980 (2000).

[3] J. C. Rooke and M. T. Weller, *Sol. St. Phen.* **90** 417 (2003).

[4] L. L. Gendre, R. Marchand and Y. Laurent, *J. Eur. Ceram. Soc.* **17** 1813 (1997).

[5] E. Guenther and M. Jansen, *Mater. Res. Bull.* **36** 1399 (2001).

[6] J. Grins and G. Svensson, *Mater. Res. Bull.* **29** 801 (1994).

Chapter 3C

High Throughput Study of Chromite Spinels

3C.1 Introduction

Spinel-type systems, as described in Section 1.2, are extremely useful as inorganic pigments due to their high chemical and thermal stability. The ability of this structure type to incorporate a wide variety of metal cations allows a diverse array of colours to be produced. Numerous studies have investigated the effect that structure[1,2] and/or the substitution of 'coloured' and 'colourless' cations[3,4] have on pigment properties.

Compounds with the spinel structure (AB_2O_4) nominally varying Cu/Zn on the A site and Al/Cr on the B site have previously been investigated as catalysts for the decomposition of ammonium nitrate.[5] The end members in this series have also been investigated for pigment applications ($ZnCr_2O_4$ brown, $CuCr_2O_4$ black, $CuAl_2O_4$ red-brown, $ZnAl_2O_4$ white).[6,7] This quaternary system was therefore suitable for the purpose of further developing the high throughput methodology.

3C.2 Synthesis and Characterisation

Arrays of samples in the $Cu_{1-x}Zn_xAl_{2-y}Cr_yO_4$ series were prepared from solutions of the metal nitrates and acetates (0.5 M) in dilute nitric acid. The stock solutions were dispensed into a standard 96 well plate (total volume = 180 μl) in the appropriate ratios and mixed using a Packard Multiprobe II EX robot. Aliquots of the mixtures (30 μl) were then transferred to separate alumina/Teflon plates giving three duplicate arrays. Water was evaporated by heating at 60 °C overnight before the tiles were fired at the desired temperature (600-1200 °C) for 4 hours.

Colour screening was carried out by measuring red, green and blue (RGB) values for each sample from a digital image, taken under controlled lighting conditions. These were normalised and corrected for colour balance by comparison with a standard grey card. Colour measurements of bulk samples were taken using a Perkin Elmer Lambda 35 UV-Vis spectrometer in the range of 380 nm to 780 nm with $BaSO_4$ used as a reference. Diffraction patterns were measured using a Bruker D8 Discover with General Area Detector Diffraction System (GADDS) for Combinatorial Screening.

Phase identification of sample spots was carried out with a 0.5 mm collimated beam, $\theta 1$ at 25 ° and the area detector, $\theta 2$ at 25 °. This produced diffraction patterns with a 2θ range of 33.8 ° to 67.0 °. The scan time was two minutes per sample, allowing data for each 54 member array to be collected in under two hours. Higher resolution diffraction data were collected for bulk samples using a Siemens D5000 diffractometer. Phases present were identified by comparison with the PDF2 database.[8]

3C.3 Results and Discussion

Initially arrays over the entire quaternary series $Cu_{1-x}Zn_xAl_{2-y}Cr_yO_4$ ($0 \leq x \leq 1$ in 0.2 steps, $0 \leq y \leq 2$ in 0.25 steps) were prepared at 600, 800 and 1000 °C. Although the samples were not completely uniform and in some cases formed as rings due to surface tension effects, their optical and structural properties could still be measured. X-ray diffraction revealed formation of the expected spinel phases in all cases. Samples were more crystalline and contained fewer impurities with increasing temperature. The majority could be identified as crystallising in the cubic $Fd\bar{3}m$ space group, however in the Cu/Cr rich region the tetragonal $I4_1/amd$ structure could be assigned (Figure 3C.3.1-2).

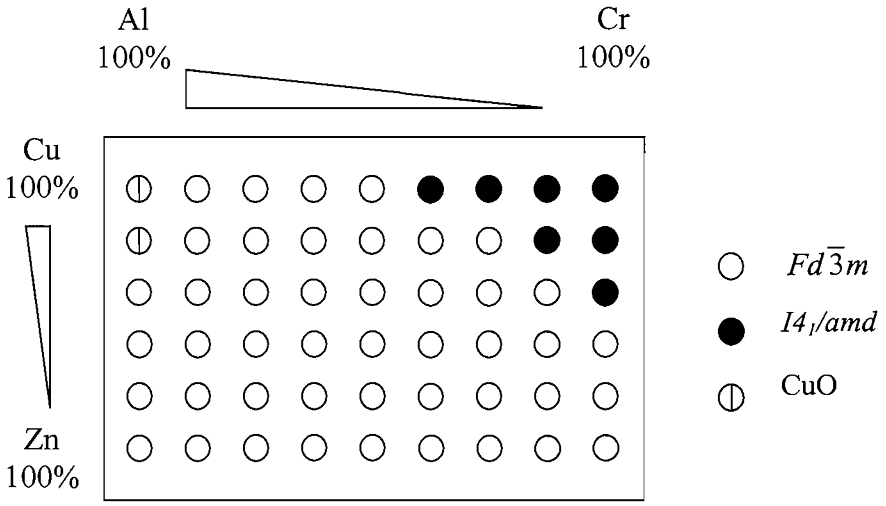

Figure 3C.3.1 The space groups and impurities present in each sample for the array $Cu_{1-x}Zn_xAl_{2-y}Cr_yO_4$ *(*$0 \leq x \leq 1$, $0 \leq y \leq 2$*) fired at 1000 °C (the first row representing* $CuAl_{2-y}Cr_yO_4$ *(*$0 \leq y \leq 2$*)).*

For selected samples from the 1000 °C array, lattice parameters were calculated using the GSAS[9] suite of programs. An initial refinement of the end member $ZnAl_2O_4$ was used as a template for the other samples across the series. Each refinement could then be carried out in the minimum number of steps: replacing the histogram then refining the zero point and lattice parameters. The unit cell increases as expected (Figure 3C.3.3) as Al^{3+} is substituted by the larger Cr^{3+} cation (0.535 and 0.615 Å).[10] However, the values for the *a* parameters differ somewhat from those in the literature: $ZnAl_2O_4$ array = 8.061(3) Å, lit. = 8.087 Å; $ZnCr_2O_4$ array = 8.321(4) Å, lit.= 8.326 Å.

This may be attributed to the quality of the data used in the refinements. Peak broadening, both instrumental and from the small particle size as well as the limited 2θ range reduce the accuracy of the results. The smaller difference in radii between copper and zinc (0.57 and 0.60 Å respectively)[10] and the CuO impurity made distinguishing the increase in lattice parameter more difficult. The difference is comparable to the errors on the refined *a* parameter.

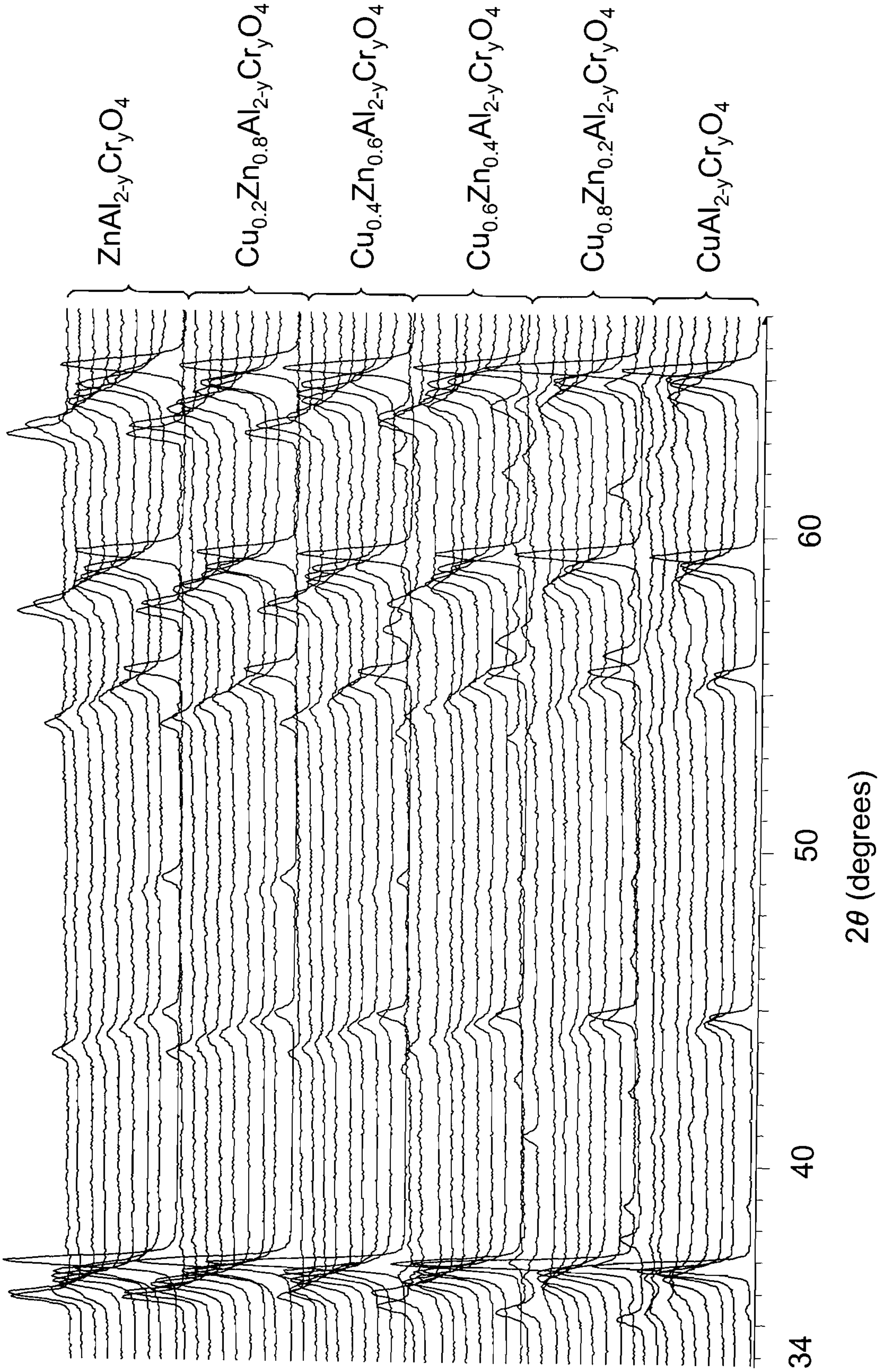

Figure 3C.3.2 X-ray diffraction patterns for the array $Cu_{1-x}Zn_xAl_{2-y}Cr_yO_4$ ($0 \leq x \leq 1$, $0 \leq y \leq 2$) fired at 1000 °C showing the 54 individual profiles.

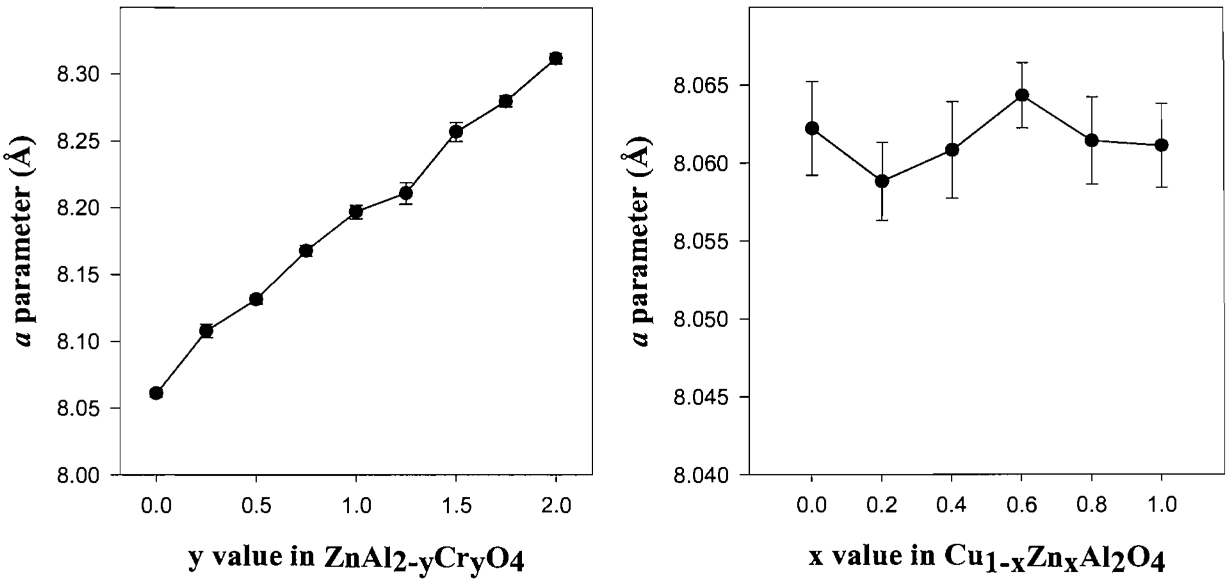

Figure 3C.3.3. Calculated lattice parameters for samples across a row (left) and down a column (right) of the $Cu_{1-x}Zn_xAl_{2-y}Cr_yO_4$ *(*$0 \leq x \leq 1$, $0 \leq y \leq 2$*) array fired at 1000 °C.*

Despite the problems with accuracy, the GADDS high throughput X-ray system is still a valuable tool for phase identification and with further optimisation should yield improved quantitative data. For the purpose of maintaining the high throughput workflow, refinements could only be undertaken for a limited number of samples. This provides a guide to the structural behaviour of the array samples, but more accurate refinements can be carried out from bulk versions of the most interesting compounds.

Visual inspection of the powders showed that increasing copper and chromium content led to darker colours. Samples where $x > 0.8$ and $y > 0.75$ were dark grey/black. Chromium doped into $ZnAl_2O_4$ gave a pink hue when $0.25 \leq y \leq 0.75$, becoming brown as y increased further. Substituting zinc with copper gave a red-brown colour becoming darker as the level of copper increased. Colour measurement results showed that the samples with the reddest hue were $Cu_{0.6}Zn_{0.4}Al_2O_4$ and $Cu_{0.4}Zn_{0.6}Al_2O_4$ (Figure 3C.3.4-5a) on the array fired at 1000 °C.

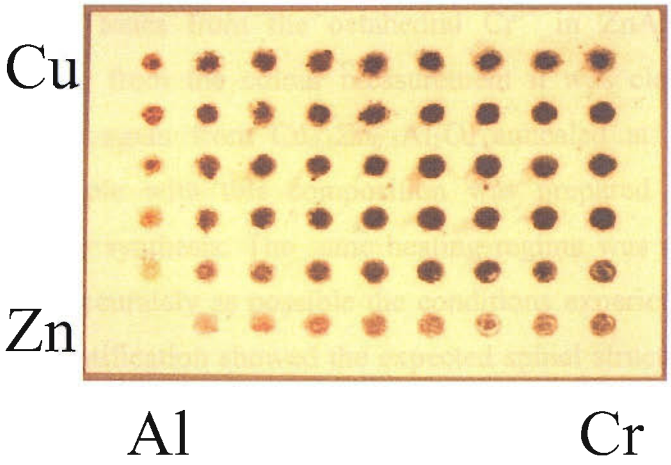

Figure 3C.3.4. Digital image of an array fired at 1000 °C.

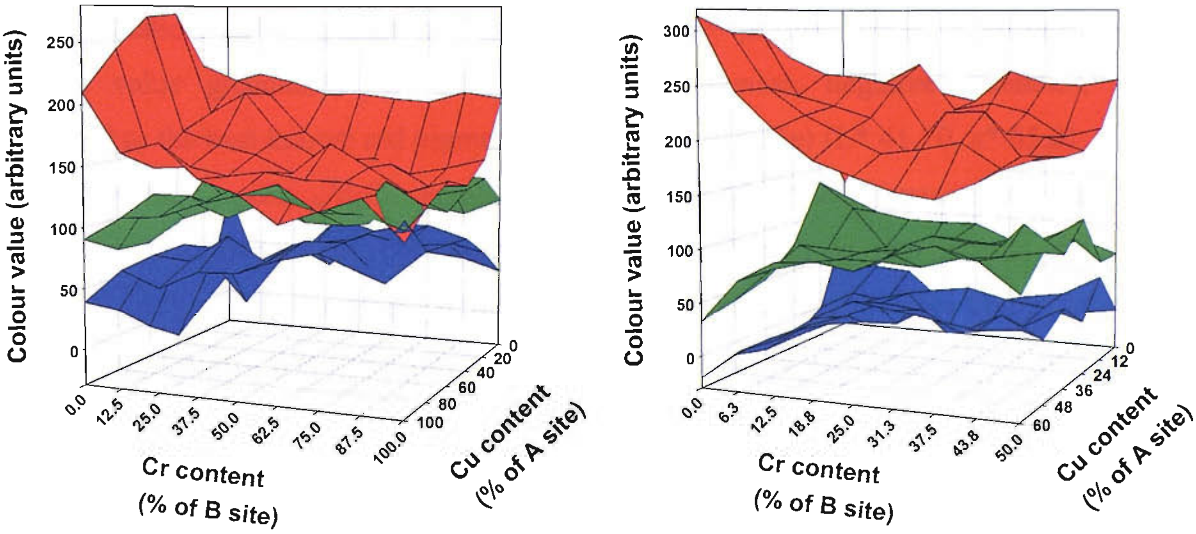

(b) *(c)*

Figure 3C.3.5. RGB values (Red top, Green middle, Blue bottom) for $Cu_{1-x}Zn_xAl_{2-y}Cr_yO_4$ arrays (a) the initial library where $0 \leq x \leq 1$, $0 \leq y \leq 2$ and (b) the focus library where $0.4 \leq x \leq 1$, $0 \leq y \leq 1$, both fired at 1000 °C.

A second series of arrays which focussed on the more promising region of the system was thus prepared. Three duplicates were synthesised at 800, 1000 and 1200 °C with the composition $Cu_{1-x}Zn_xAl_{2-y}Cr_yO_4$, where $0.4 \leq x \leq 1$ in 0.12 steps and $0 \leq y \leq 1$ in 0.125 steps. The samples all crystallised in the cubic $Fd\bar{3}m$ space group; those fired at 1200 °C were the most crystalline and homogeneous.

At 1200 °C the pink tones from the octahedral Cr^{3+} in $ZnAl_2O_4$ were more pronounced. However, from the colour measurement it was clear that the best relative red value was again from $Cu_{0.6}Zn_{0.4}Al_2O_4$ annealed at 1000°C (Figure 3C.3.5b). A bulk sample with this composition was prepared from the stock solutions used for array synthesis. The same heating regime was also followed in order to reproduce as accurately as possible the conditions experienced by samples on the array. Phase identification showed the expected spinel structure with the a = 8.076 Å compared to 8.061 Å from array data.

Visibly the sample appeared darker than its array analogue, most likely due to particle size effects. Colour measurement results were recorded using the CIE L*a*b* notation (L* = lightness, values 0-100; a* = positive value is redness, negative value greenness; b* = +v value is yellowness, negative blueness). Compared to the best known red pigment, Cadmium red (CdSe) (L* 41.10, a* 65.21, b* 56.84),[11] the $Cu_{0.6}Zn_{0.4}Al_2O_4$ sample (L* 35.25, a* 6.42, b*12.05) was not a good pigment. The drawback of the RGB measurement system is that results are essentially only relative to other samples on the array. With regard to searching for new pigment systems it is still a valid technique, which can be used to quickly assess which composition regions have potential. However, the discovery arrays must be followed up by obtaining more accurate data on bulk versions of the promising samples if useful comparisons to existing pigments are to be made.

3C.4 Conclusions

High throughput co-evaporation methods have been investigated as a potential way of searching for novel pigment materials. From developmental arrays of the composition $Cu_{1-x}Zn_xAl_{2-y}Cr_yO_4$ ($0 \leq x \leq 1$, $0 \leq y \leq 2$) it was shown that addition of low levels copper and chromium led to brick red and pink colouration respectively while increasing amounts produced black material. The best red value from RGB measurements was $Cu_{0.6}Zn_{0.4}Al_2O_4$, although this would not be of use as a commercial pigment. The spinel materials were shown to crystallise in the tetragonal $I4_1/amd$ space group at higher levels of chromium and copper incorporation rather than the cubic $Fd\bar{3}m$ structure.

3C.5 Overall Conclusions for Chapter 3

High throughput methods which utilise the deposition of solutions into a specially designed well plate, based around an alumina substrate have been developed. These methods have been applied to three pigment systems using three distinct sol-gel methods. All three solution deposition techniques proved successful in creating homogeneous pigment materials, which could be screened for their colour properties, structure and composition. Citrate gel methods have been used to prepare chromium doped zirconate perovskite materials giving colours varying from rose-red to yellow as the A cation varies from calcium to strontium. Tantalum based oxide-nitride perovskite pigments have been synthesised from metal alkoxides and shown to vary in colour from orange to green to white as the optical band gap increases with the incorporation of zirconium. Co-evaporation methods have been utilised to produce spinel compounds with colours varying from white to pink to brick-red with low levels of chromium and copper incorporation into zinc aluminate then to black as these levels increase.

Using this system 162 samples can be prepared and screened in a 2-3 day cycle. This presents a significant improvement on the standard one-at-a-time approach. These methods should be more applicable and accessible to most research groups than thin-film techniques as they only require equipment that is available in many organic research groups. The main drawback of the technique is in the analysis and interpretation of the large amounts of data created. Improvements in data handling would reduce this problem and allow more complex pigment systems to be studied. Further work to improve the uniformity of the array samples may also be required before the techniques can be applied to materials with more complex properties.

3C.6 References

[1] M. Zayat and D. Levy, *Chem. Mater.* **12** 2763 (2000).

[2] J. F. Marco, J. R. Gancedo, M. Gracia, J. L. Gautier, E. Rios and F. J. Berry, *J. Solid State Chem.* **153** 74 (2000).

[3] H. Kawai, M. Tabuchi, M. Nagata, H. Tukamoto and A. R. West, *J. Mater. Chem.* **8** 1273 (1998).

[4] G. J. Yan, J. J. Cheng, J. C. Zhang and S. L. Chun, *J. Inorg. Mater.* **15** 660 (2000).

[5] N. A. Belokonova, O. A. Antropova and E. A. Nikonenko, *Inorg. Mater.* **31** 995 (1995).

[6] I. V. Pishch, N. F. Popovskaya and E.V. Radion, *Glass Ceram.* **56** 320 (1999).

[7] V. Burghelea, C. Runcanu and C. Popa, *Mater. Constructii.* **30** 173 (2000).

[8] PCPDFWIN Version 2.4, Powder Diffraction File, International Centre for Diffraction Data, Swarthmore, PA, USA (2003).

[9] R. B. Von Dreele, A. C. Larson, GSAS General Structure Analysis System, Neutron Scattering Centre, MS-H805, Los Alamos National Laboratory, Los Alamos, NM, USA (2003).

[10] R. D. Shannon, *Acta. Cryst.* **A32** 751 (1976).

[11] M. Jansen and H. Letschert, *Nature* **404** 980 (2000).

Chapter 4

High Throughput Study of Phosphor Materials

4.1 Introduction

Photoluminescent materials, often known as phosphors generally consist of a host structure, such as Y_2O_3 or Zn_2SiO_4 into which an activator ion is introduced by doping.[1] The activator ions are typically lanthanoid ions such as Eu^{3+} or certain d-block metals such as Mn^{2+} that can absorb and emit light of the desired wavelengths. High throughput methods have been both used to optimise existing materials and discover novel luminescent compounds.[2,3] The early developments of such techniques focussed on these materials due to the relatively simple screening protocol required - *i.e.* the sample with the highest luminance is the best - compared to more complex properties such as superconductivity. Libraries of materials can be synthesised to study the effect of the host, activator ion, sensitisers or processing conditions, all of which contribute to the final efficiency of the phosphor.

Libraries of phosphor materials have been prepared by both thin film[4] and sol-gel type methods.[5] The high throughput methods developed in this work are more similar to the sol-gel techniques described by Park[6], Luo[7] and Liu.[8] These studies all use aqueous solutions of metal salts as precursors, deposited into machined alumina well plates for processing and analysis. The work encompasses compounds ranging from europium doped borophosphate red phosphors[8] to manganese doped $BaAl_{12}O_{19}$ green phosphors.[9] However, no previous study has applied similar methods to create arrays on flat alumina substrates. As alumina displays an inherent porosity, precursor solutions containing activating ions can be absorbed and may react with the substrate at high temperature. Even with significant, time-consuming cleaning efforts, small traces of the ions may remain and be leeched from the well plate into the next batch of samples during annealing steps. Using the essentially disposable flat substrates rather than re-using well plates should eliminate the possibility of carry-over of activating ions between experiments.

This chapter describes the application of the techniques developed for preparing arrays of pigment materials (Chapter 3) to luminescent compounds. Studying compounds with known behaviour or those which have already been investigated by high throughput methods should provide useful information about the effectiveness of the technique.

4.2 Synthesis

Arrays of europium doped lanthanum phosphate as well as terbium doped gadolinium phosphate were prepared from solutions of the metal nitrates and ammonium dihydrogen phosphate (0.01- 0.5 M) in dilute nitric acid. The stock solutions were dispensed into a standard 96 well plate (total volume = 300 μl) in the appropriate ratios and mixed using a Packard Multiprobe II EX robot. Aliquots of the mixtures (150 μl) were then transferred to separate alumina/Teflon plates giving duplicate arrays. Water was evaporated by heating at 60 °C overnight before the tiles were fired at the appropriate temperature for 16 hours.

4.3 Characterisation

Diffraction patterns were measured using a Bruker D8 Discover with General Area Detector Diffraction System (GADDS) for Combinatorial Screening. Phase identification of sample spots was carried out with a 0.5 mm collimated beam ($\theta 1$) at 20 ° and the area detector ($\theta 2$) at 20 °. This produced diffraction patterns with a 2θ range of 22 ° to 57 °. The scan time was two minutes per sample, allowing data for each 54 member array to be collected in under two hours. Phases present were identified by comparison with the PDF2 database.[10] Fluorescence spectra were collected using a Perkin Elmer LS55 spectrometer fitted with a well plate reader (Figure 4.3.1). The source for the spectrometer is a xenon flash tube and the red-sensitive photomultiplier allows detection in the range 200 – 900 nm. Using the well plate reader each sample on the array can be assessed automatically for emission or excitation intensity at a particular wavelength. Full emission or excitation spectra can also be collected manually for any sample on the array but this is more time consuming.

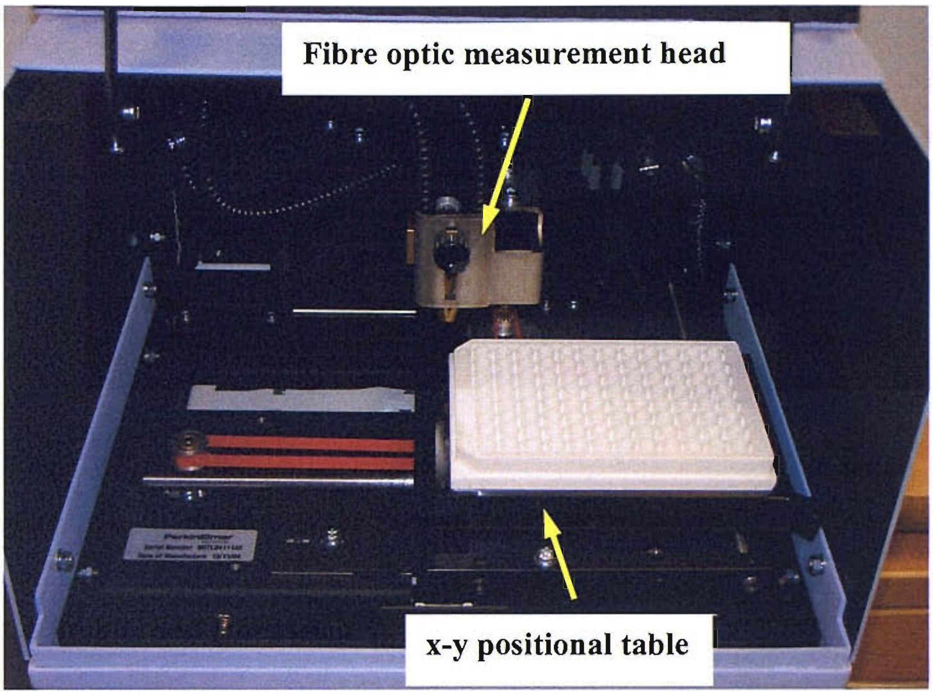

Figure 4.3.1 The well plate reader accessory, which allows rapid sequential analysis of an array is attached to the fluorescence spectrometer.

4.4 Results and Discussion

4.4.1 Europium Doped Lanthanum Phosphate

Initially arrays of europium doped lanthanum phosphate were prepared such that lanthanum was replaced by europium by up to 50 %. The level of substitution was increased on a logarithmic type scale to give six identical rows of compounds with the formula $LaPO_4$:Eu (0.1, 0.2, 0.5, 1, 2, 5, 10, 20, 50 %).

PXD phase identification revealed that all the samples crystallised with the monazite structure (space group $P2_1/n$) with no impurities. Rietveld refinements were undertaken for each sample in the array using the GSAS program.[11] Initially the 0.1 % sample of the first row was refined using a structural model for $LaPO_4$.[12] Background, zero point, lattice parameters and profile coefficient functions were sequentially refined to obtain a reasonable fit to the data. This was then used as a starting model for each sample in turn with the same functions being varied until convergence was achieved. The derived lattice parameters and cell volumes are graphically represented in Figures 4.4.1 and 4.4.2.

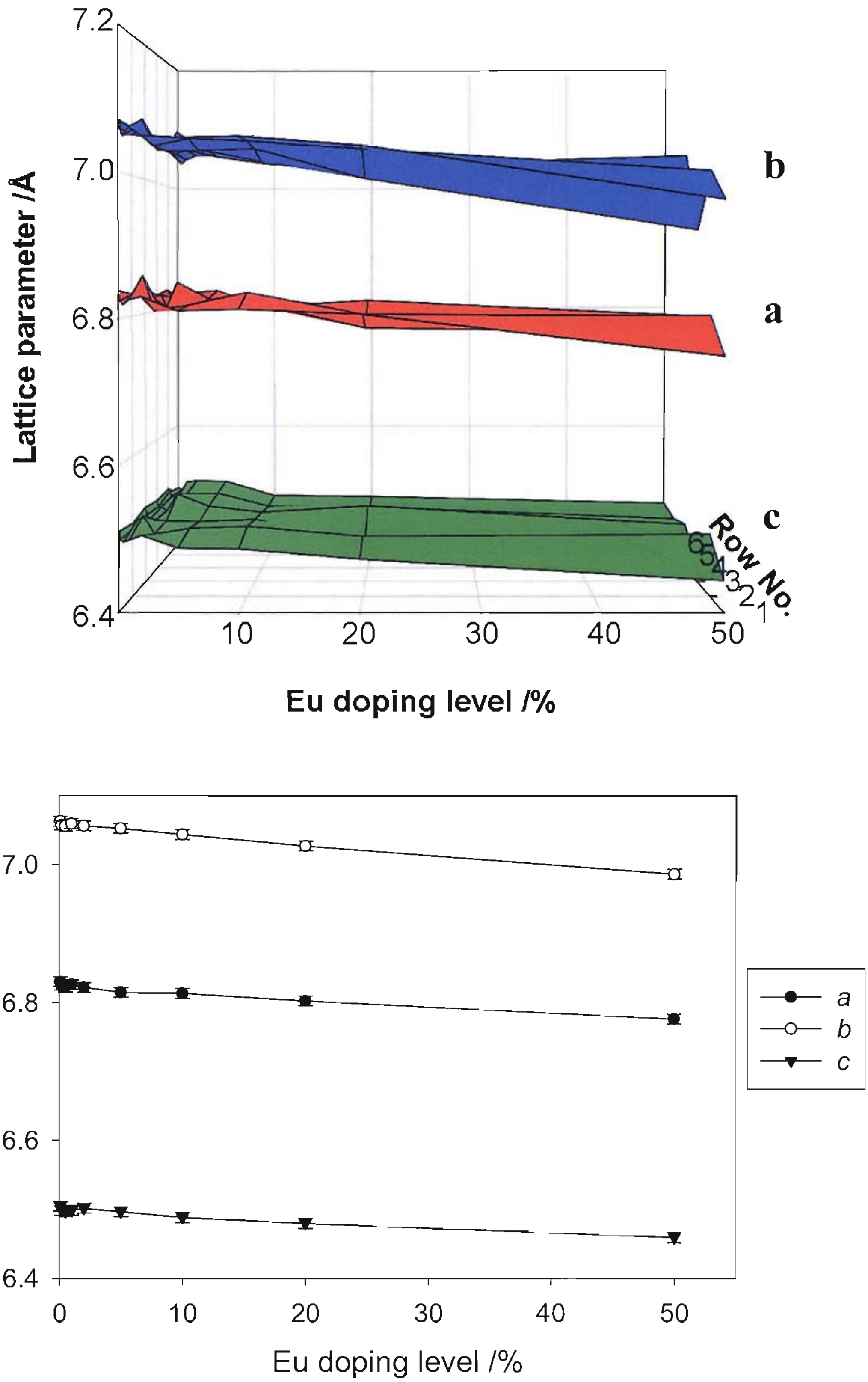

Figure 4.4.1 Derived lattice parameters for a LaPO$_4$:Eu array fired at 1000 °C showing the individual values (top) and the averaged values (bottom) (averaged error bars within data points).

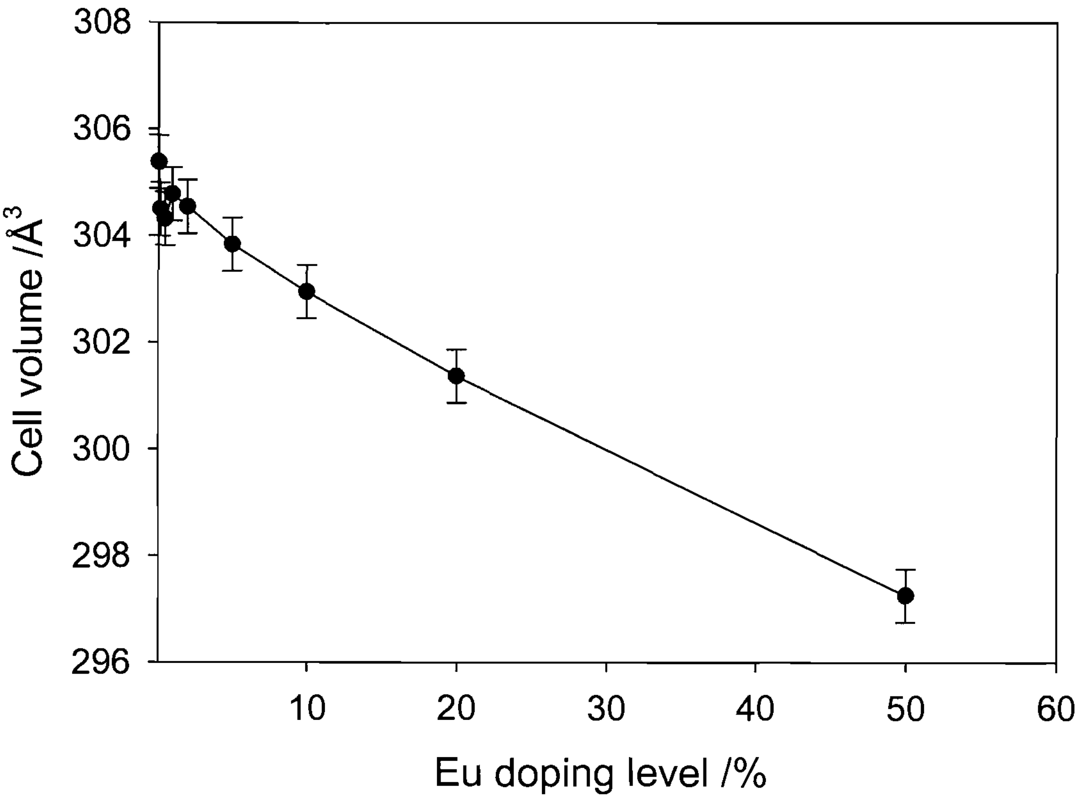

Figure 4.4.2 Averaged unit cell volumes for a $LaPO_4$:Eu array fired at 1000 °C.

The lattice parameters and cell volumes gradually decrease with increasing europium content. This is expected based on the relative size of the lanthanide ions (La^{3+} = 1.216 Å; Eu^{3+} = 1.062 Å).[13] The unit cell values obtained in this study are slightly larger than those found in the literature (Table 4.4.1) likely due to the limited range of 2θ measured and the broad peaks of the diffraction pattern.

Table 4.4.1 Comparison of averaged lattice parameters from $LaPO_4$:Eu array with literature values (averaged estimated standard deviations given in parentheses)

	a (Å)	*b (Å)*	*c (Å)*	Volume *(Å^3)*
$LaPO_4$[12]	6.825	7.057	6.482	303.9
$EuPO_4$[14]	6.639	6.823	6.318	277.7
$(La_{0.999}Eu_{0.001})PO_4$	6.830(7)	7.063(7)	6.504(7)	305.4(5)
$(La_{0.5}Eu_{0.5})PO_4$	6.776(7)	6.986(7)	6.459(7)	297.3(5)

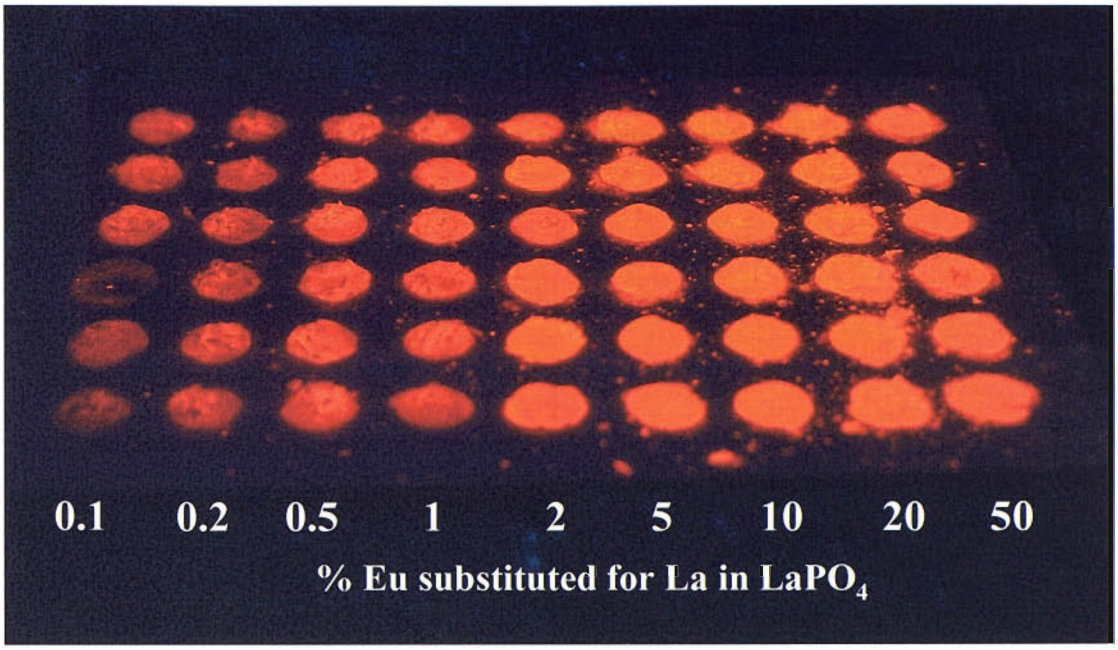

Figure 4.4.3 Photograph of a LaPO₄:Eu array fired at 1000 °C under 254 nm UV radiation.

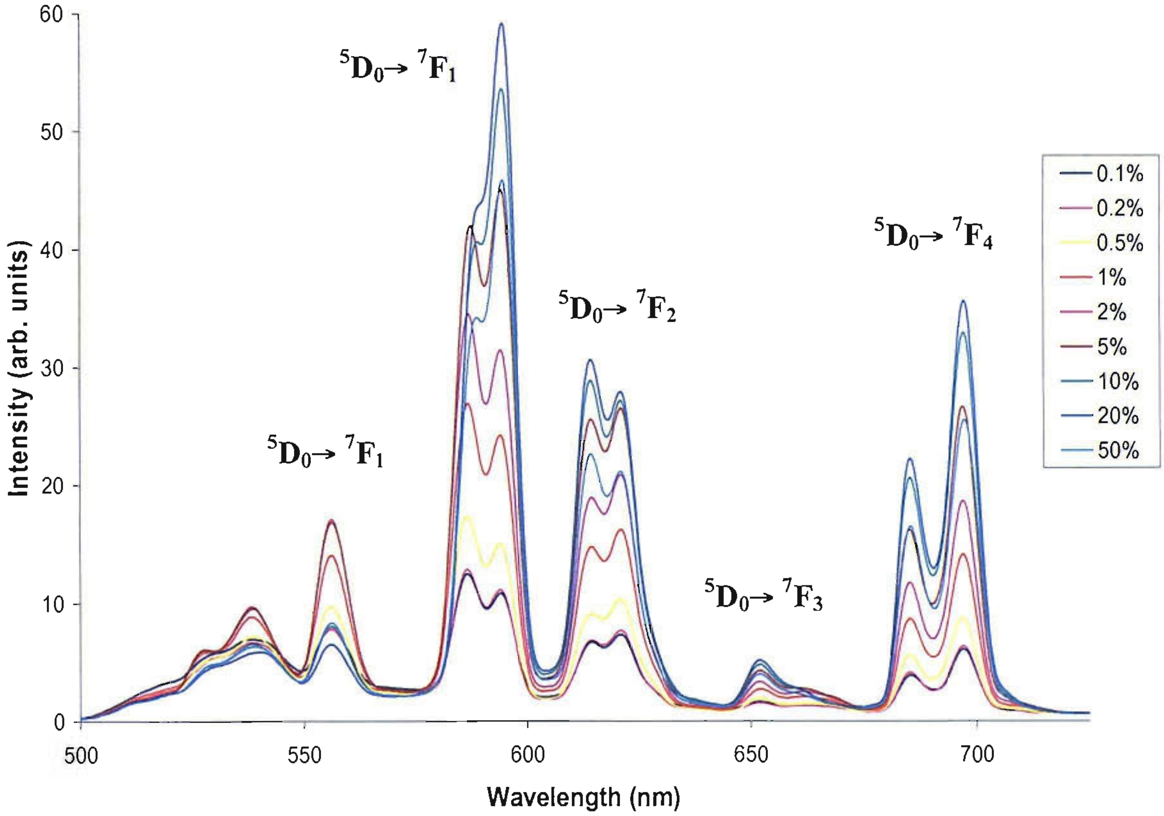

Figure 4.4.4 Emission spectra of row 2 of the Eu:LaPO₄ array recorded at an excitation wavelength of 254 nm.

The visual appearance of the array under UV light is shown in Figure 4.4.3. The spectra obtained for one row of an array annealed at 1000 °C (Figure 4.4.4) show an increase in intensity of all peaks with increasing levels of europium up to 20 % substitution. At 10 % Eu^{3+} the appearance of the spectra changes as the peak at 594 nm becomes more intense than that at 588 nm and the latter shifts towards the former. The ratio of the doublet between 610 and 622 nm also changes, with the peak at 614 nm becoming the more intense.

The orange-red fluorescence from Eu^{3+} doped materials is associated with the $^5D_0 \rightarrow {}^7F_1$ (magnetic dipole line) and $^5D_0 \rightarrow {}^7F_2$ (electric dipole line) emission transitions respectively.[15] The intensity of the peak at 614 nm is typically used as an indication of the most useful red phosphor.[16] The intensity of this peak was measured for each sample in turn, taking approximately one minute for the whole array. Figure 4.4.5a shows how the intensity of this peak varies with composition. The value for samples with identical composition varies somewhat but the general trend is an increase in intensity with increasing europium. Removing the highest and lowest values for each doping level and averaging the remaining four values should provide a more accurate reading (Figure 4.4.5b). The average intensity values indicate that the 20 % doping level is the optimum composition with a concentration quenching effect seen at 50 % doping. It is somewhat surprising that the maximum intensity is at such a high level of europium doping as typically much smaller levels of doping are used *e.g.* 6 % for the well known $Eu{:}Y_2O_3$.[17]

The quality of the material however should be gauged by the intensity of both of the $^5D_0 \rightarrow {}^7F_1$ and $^5D_0 \rightarrow {}^7F_2$ transitions. Ideally the higher the ratio of red to orange ($^5D_0 \rightarrow {}^7F_1 / {}^5D_0 \rightarrow {}^7F_2$) intensity the better as this will produce a more pure red colour.[15] Figure 4.4.6 shows the ratio of these peaks with increasing Eu^{3+} substitution. The ratio red:orange intensity decreases as the level of doping increases. Hence, although the overall luminescence of the materials increases with europium addition, their qualities as red phosphors diminish.

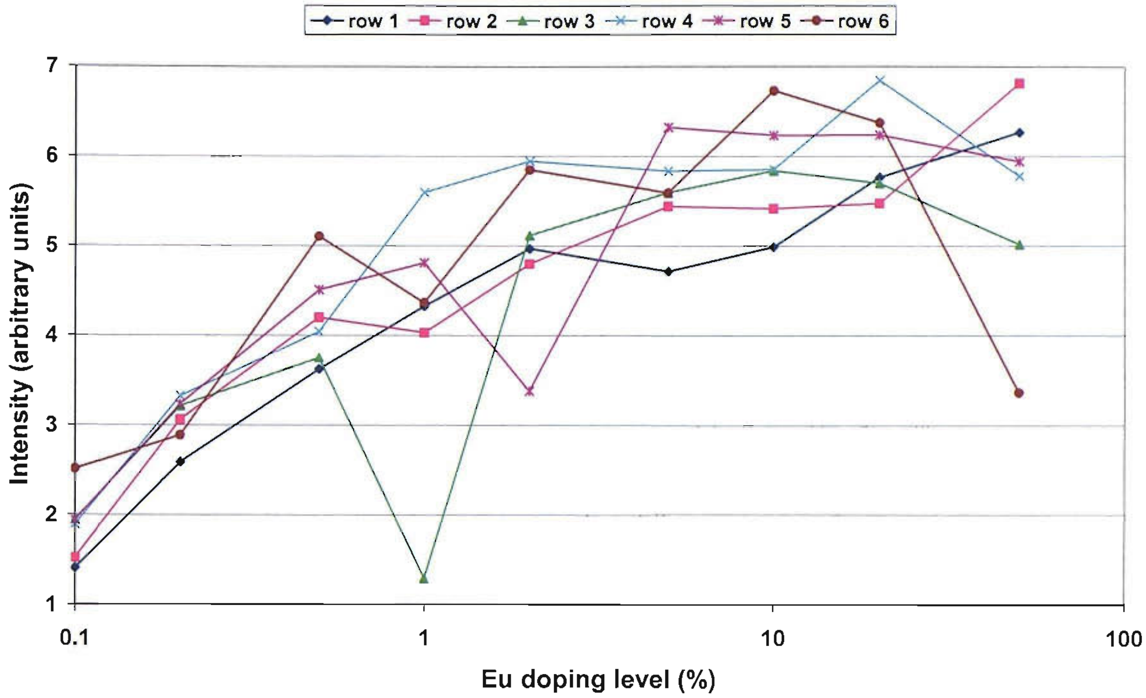

a)

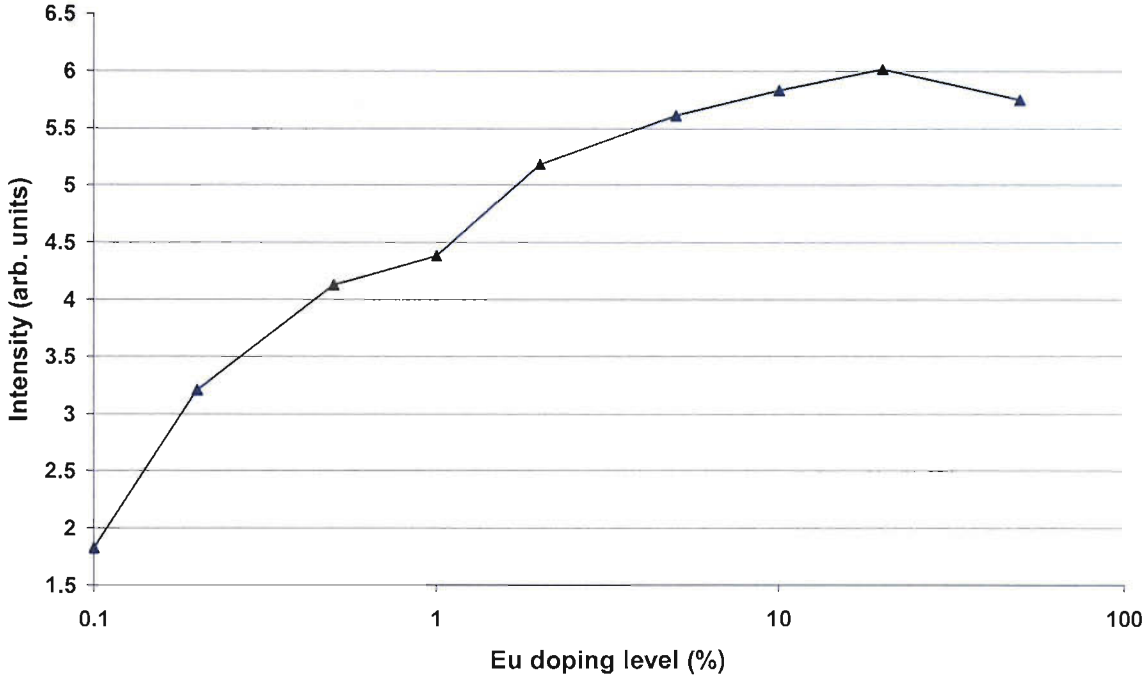

b)

Figure 4.4.5 The intensity of the emission peak at 614 nm, recorded at an excitation wavelength of 254 nm, for all samples (a) and the average (b). (Average values obtained from the intensity of the median four samples of each doping level).

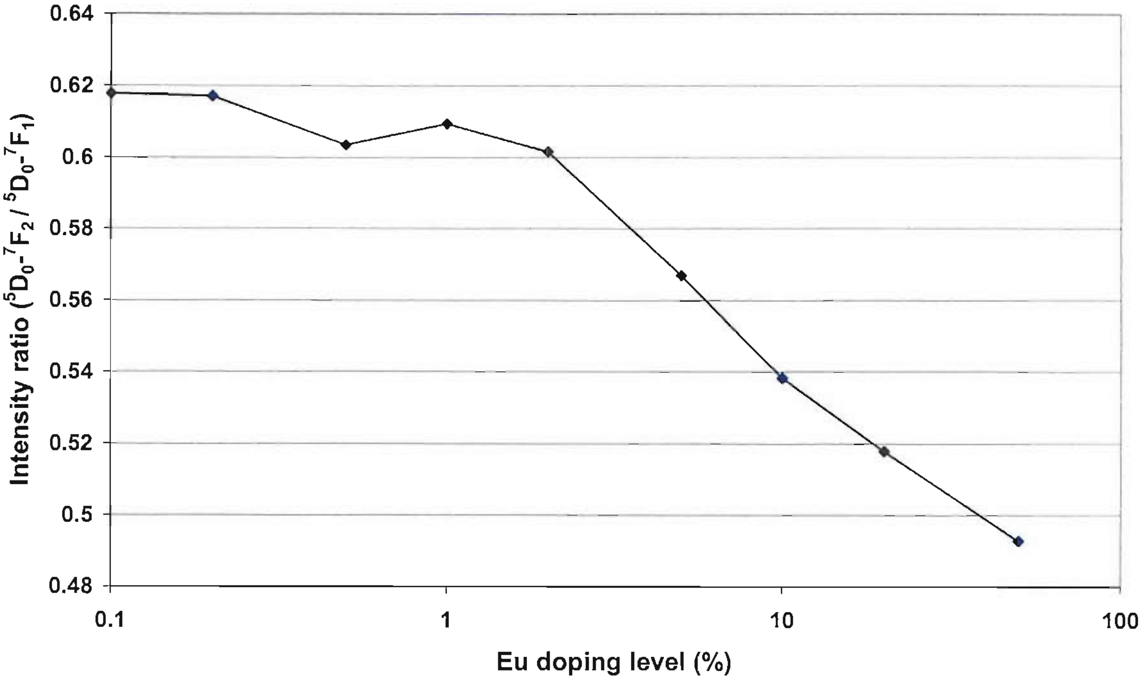

Figure 4.4.6 The intensity ratio of the red/orange transitions of $LaPO_4$:Eu taken from the and $^5D_0 \rightarrow {}^7F_2$ (614 nm, red) and $^5D_0 \rightarrow {}^7F_1$ (594 nm, orange) peaks.

The difference in intensity readings of nominally identical samples may be explained by the fact that the samples are not uniform. As described in Section 3.3 the synthesis methods used to prepare the arrays often result in cracked or domed samples. This can affect the fluorescence measurements as the closer the sample to the fibre optic read head the greater the measured intensity. The alumina substrate also produces a broad feature between ~ 450 and 600 nm under 254 nm radiation. If the sample does not completely fill the beam spot – *i.e.* due to cracking – a false reading may be taken. Subtracting a background spectrum would not improve the problem as more of the substrate may be visible for different samples.

To reduce these effects an array holder was developed. The holder consists of a Perspex base of the same dimensions as a standard 96 well plate with a recess to accommodate the alumina tile. A 2 mm thick quartz sheet can be carefully pressed against the array by Perspex clamps (Figure 4.4.7). The quartz window is transparent to the incoming beam and does not affect the luminescence measurement. The pane acts to hold the powders in place during the movement of the x-y stage while ensuring that the samples are compacted to the same height with respect to the fibre optic read head. However, it does not resolve the problems of cracked sample spots revealing the substrate below.

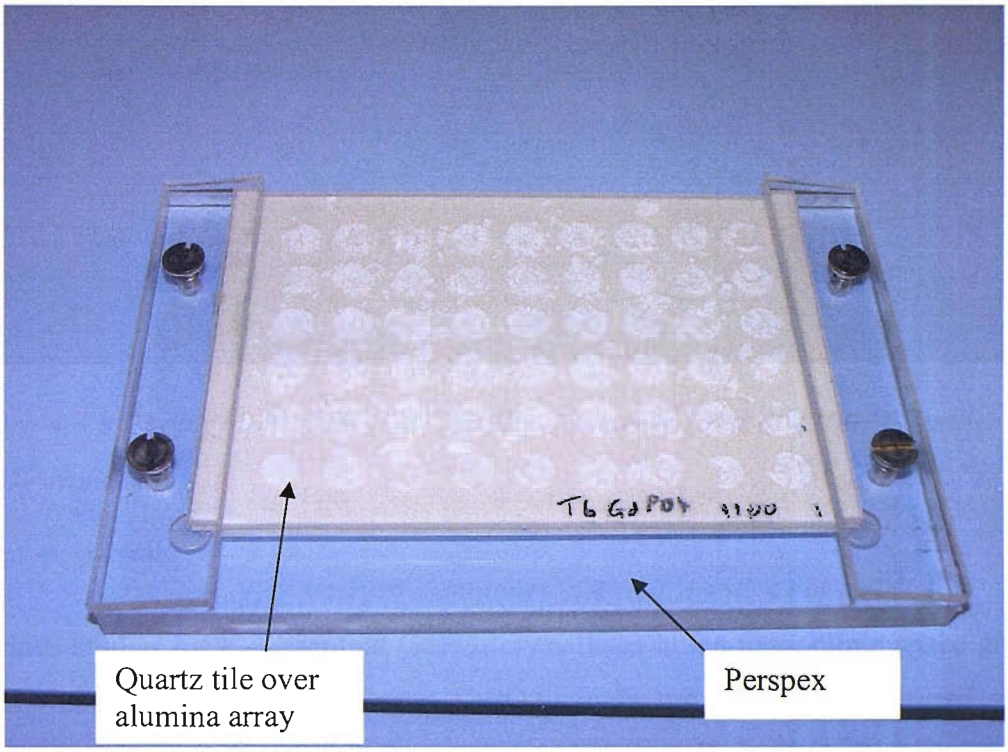

Figure 4.4.7 Photograph of the array holder designed for use with the fluorescence spectrometer plate reader.

4.4.2 Terbium Doped Gadolinium Phosphate

To assess the validity of the high throughput method further, arrays of materials were prepared that have previously been studied by similar methods and instrumentation. Arrays of terbium doped gadolinium phosphate were prepared in machined alumina well plates by Park and co-workers.[18] The optimum green fluorescence was obtained from the composition $Gd_{0.83}Tb_{0.17}P_{1.14}O_{\delta}$ (excess phosphorous having been shown to improve luminance; $\delta \sim 4$) from a series in the range $(Gd_{1-x}Tb_x)P_{1.14}O_{\delta}$ ($0.11 \leq x \leq 0.27$). To reproduce this study arrays were prepared with six identical rows of the composition $(Gd_{1-x}Tb_x)P_{1.14}O_{\delta}$ ($0.11 \leq x \leq 0.27$ in 0.02 steps) and annealed at 1100 °C in a nitrogen atmosphere (Figure 4.4.8). The materials all had a white body colour, indicating that all the terbium ions were in the trivalent state.

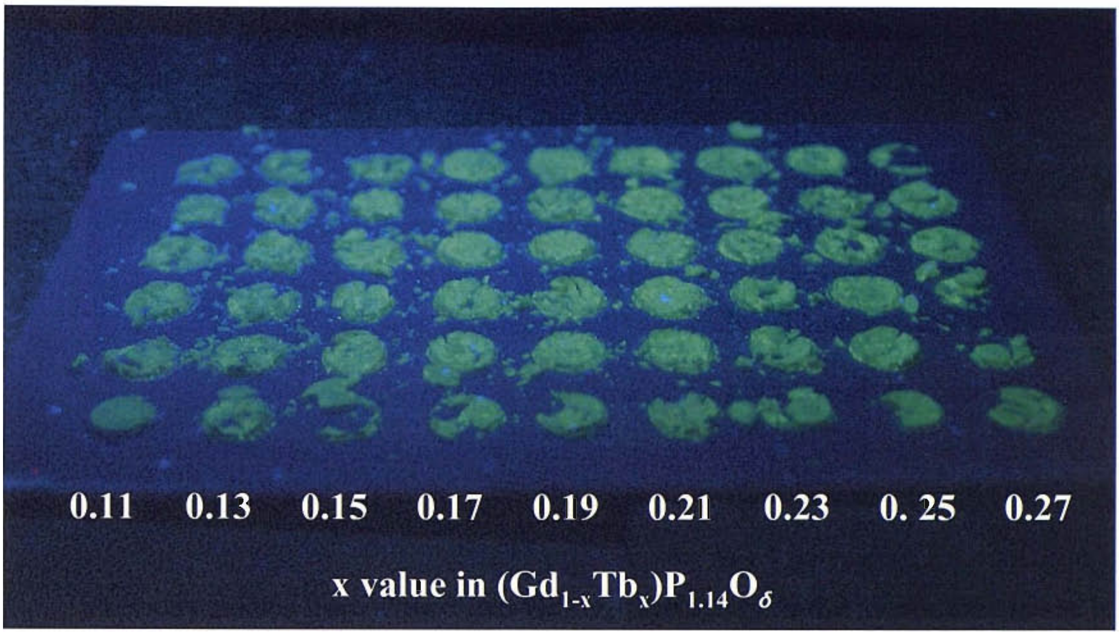

Figure 4.4.8 Photograph of an $(Gd_{1-x}Tb_x)P_{1.14}O_\delta$ *array fired at 1100 °C, under 254 nm UV radiation.*

Previous studies have shown that $GdPO_4$ crystallises in the monoclinic space group, $P2_1/n$ (monazite structure) whereas $TbPO_4$ adopts the tetragonal, $I4_1/amd$ space group (xenotime structure).[19] PXD scans revealed that all samples were phase pure and had the monazite type structure. Rietveld refinements were undertaken for selected samples only, as the time consuming process would be unlikely to yield significant information due to the small doping increments and the similar size of the lanthanide ions involved (Gd^{3+} = 1.107 Å; Tb^{3+} = 1.095 Å).[13] Initially the 0.11 sample of the first row was refined using a structural model for $GdPO_4$.[19] Background, zero point, lattice parameters and profile coefficient functions were sequentially refined to obtain a reasonable fit to the data. This was then used as a starting model for the each sample in turn with the same functions being varied until convergence was achieved. Figure 4.4.9 shows the lattice parameters for one row and one column repeats of the array. As expected there is little variation in the cell parameters. The only variation occurs where the PXD scans collected were of poorer quality due to the alumina substrate dominating the pattern.

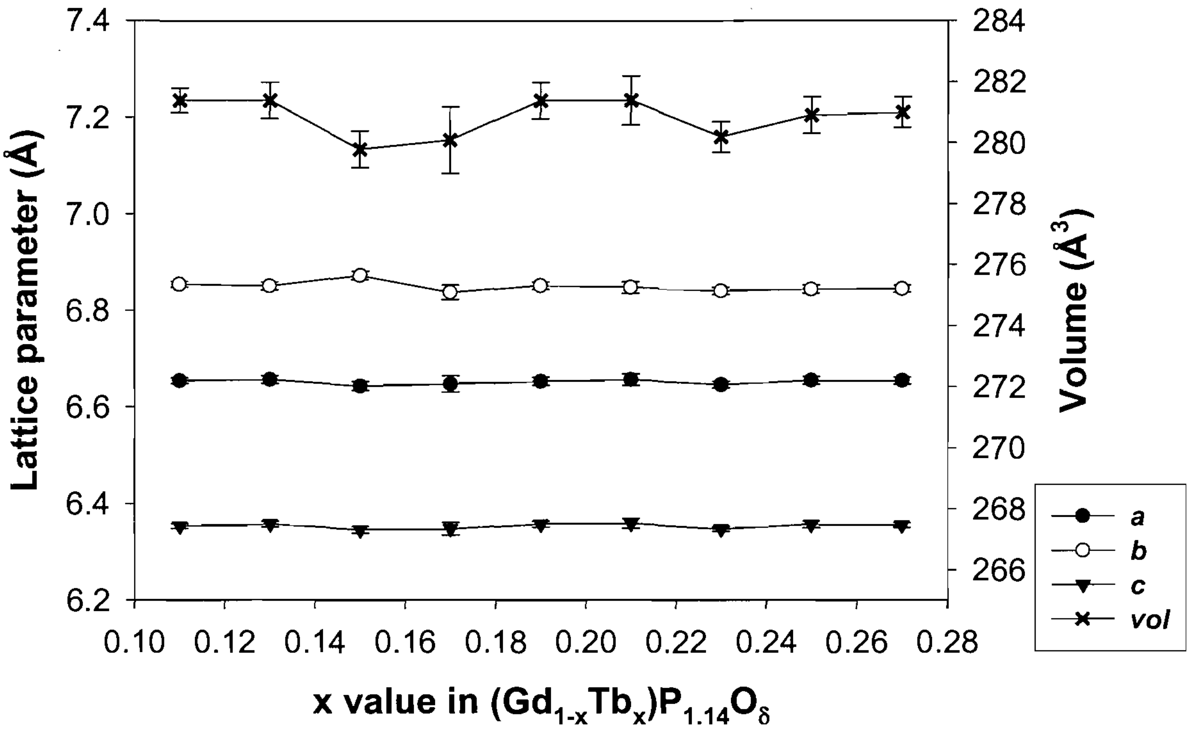

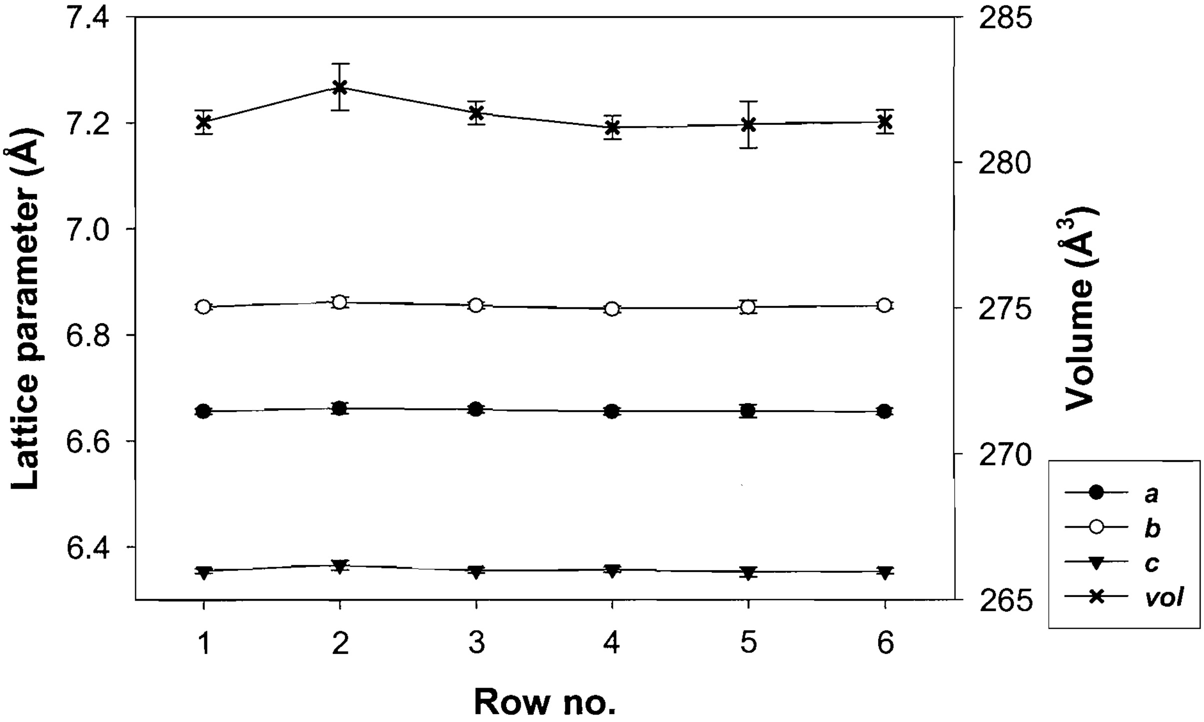

Figure 4.4.9 Derived lattice parameters and cell volumes of selected samples from a one row of the composition $(Gd_{1-x}Tb_x)P_{1.14}O_\delta$ (top) and repeats of the sample $Gd_{0.89}Tb_{0.11}P_{1.14}O_\delta$ (bottom).

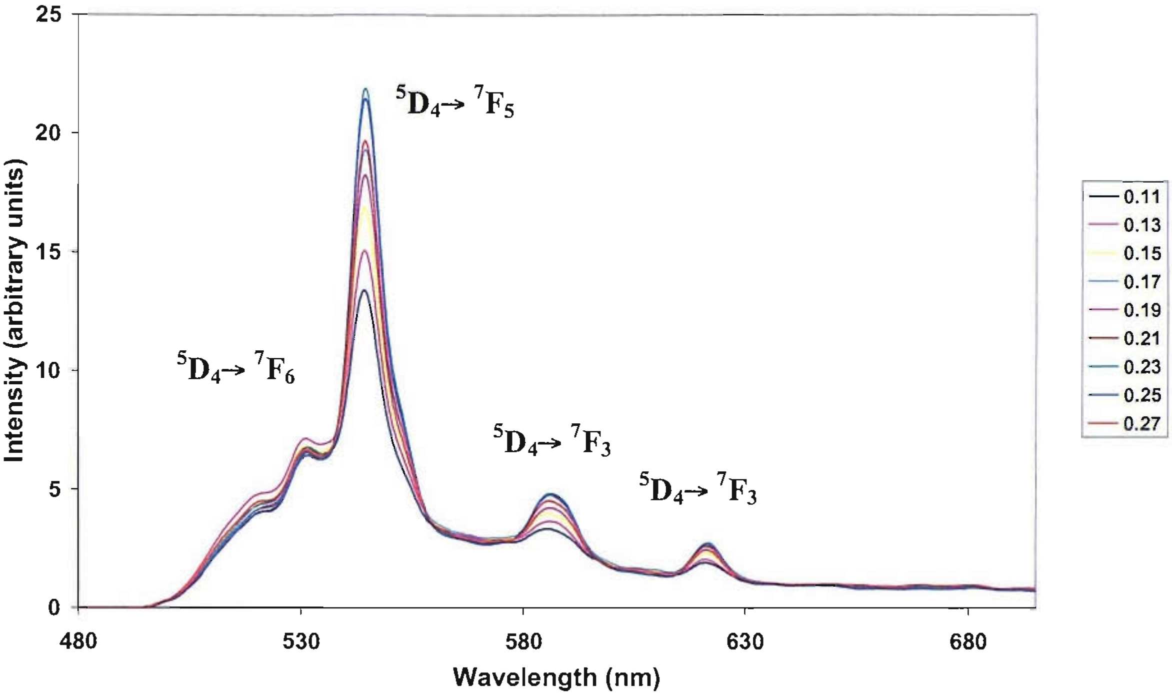

Figure 4.4.10 Emission spectra of one row from an $(Gd_{1-x}Tb_x)P_{1.14}O_\delta$ *array recorded at an excitation wavelength of 254 nm.*

Figure 4.4.10 shows the emission spectra of the samples in one row of the array. The spectra consist of a series of peaks that are characteristic of terbium fluorescence.[20] The intensity of the $^5D_4 \rightarrow {}^7F_5$ transition at 544 nm can be used as an indication of the most useful green material. The intensity of this transition peak was measured (at an excitation wavelength of 254 nm) for each sample in turn (Figure 4.4.11a) and the average of median four samples for each composition calculated (Figure 4.4.11b).

There is a degree of scatter among samples of the same composition but the general trend is an increase in intensity with increasing Tb^{3+} substitution. The averaged values reveal that a concentration quenching effect occurs above x = 0.25. The optimum composition is therefore at a higher level of doping than the previous study suggested (x = 0.17).[18] However, the samples in the previous study were prepared at a higher temperature (1300 °C) and the overall luminance was measured rather than just the intensity of the $^5D_4 \rightarrow {}^7F_5$ transition peak.

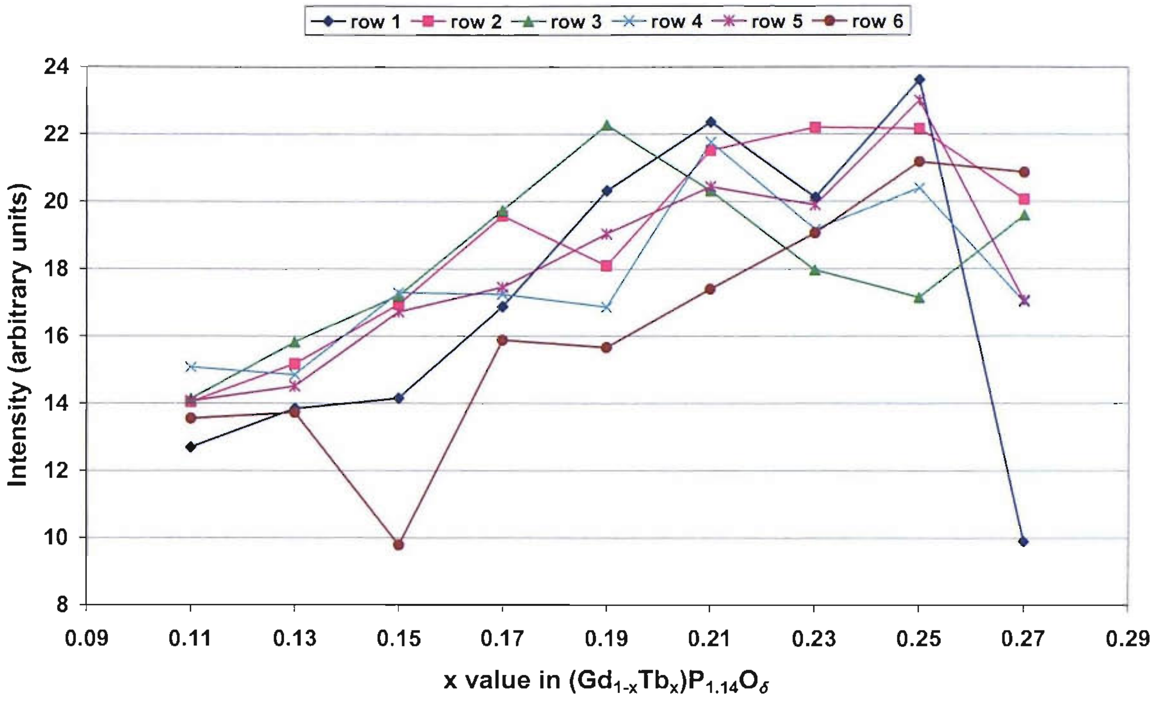

a)

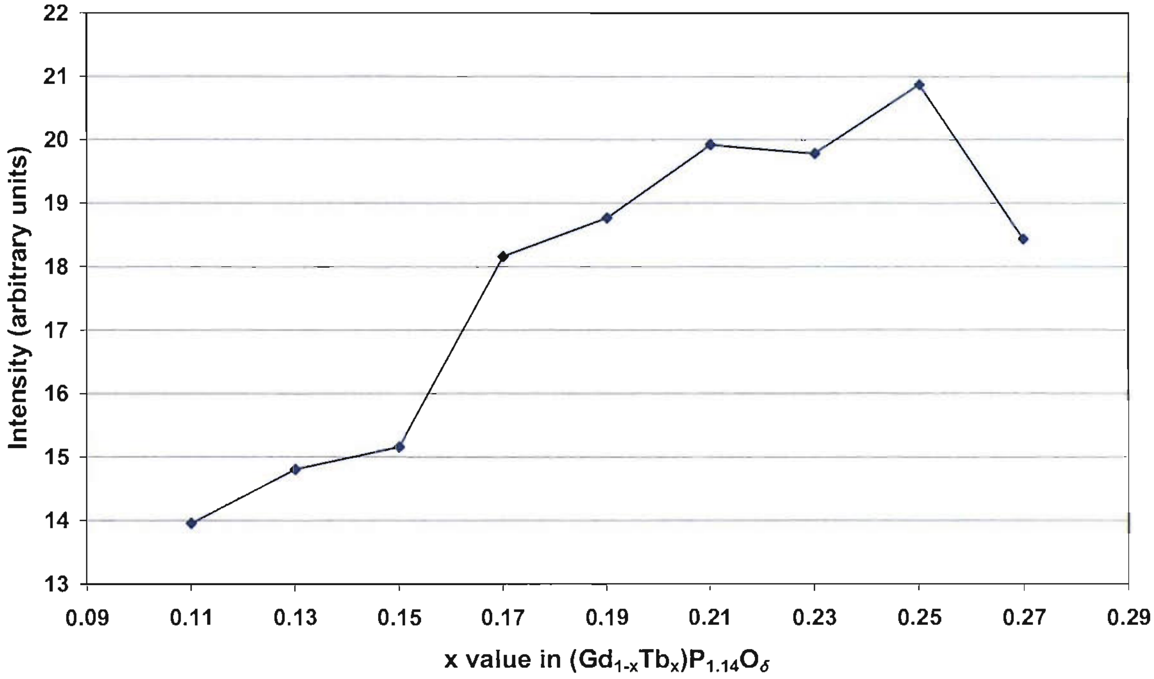

b)

Figure 4.4.11 The intensity of the emission peak at 544 nm, recorded at an excitation wavelength of 254 nm, for all samples (a) and the average (b). (Average values obtained from the intensity of the median four samples of each doping level).

The two sets of arrays in the study show that high throughput experiments carried out on flat alumina substrates can provide useful information about luminescent materials. The techniques are particularly effective in studying relationships between structure and the nature of the fluorescence spectra. Further improvements to the synthesis methods to provide uniform samples should reduce the need to produce repeats of the same compositions. This will allow more information to be attained from each array, improving the productivity of the experiments.

4.5 Conclusions

Arrays of europium doped lanthanum phosphate have been prepared and revealed that the maximum intensity of the $^5D_0 \rightarrow {}^7F_2$ red transition is achieved at a composition of $(La_{0.8}Eu_{0.2})PO_4$. This level of substitution is well above the normal level for optimised industrial phosphors. However, the increase in europium also reduces the ratio of red:orange luminescence, reducing the usefulness of the material as a red phosphor.

The compound $(Gd_{0.75}Tb_{0.25})P_{1.14}O_\delta$ was found to be the best green phosphor material from arrays replicating previous studies, where the optimum composition found in the literature and prepared via different conditions was $(Gd_{0.83}Tb_{0.17})P_{1.14}O_\delta$.

Arrays of luminescent materials can be synthesised on an alumina substrate and their structural and optical properties can be screened. This will provide a useful tool for examining the structure property relationships of potential phosphor materials. However, to achieve improved quantitative information, further refinements to the synthesis and fluorescence spectroscopy methods are required. This would enable array materials to be directly compared to current, industrially used luminescent materials.

4.6 References

[1] D. F. Shriver, P. W. Atkins, T. L. Overton, J. P. Rourke, M. T. Weller and F. A. Armstrong, *Inorganic Chemistry (Fourth Edition)*, Oxford University Press, UK (2006).

[2] E. Danielson, J. H. Golden, E. W. McFarland, C. M. Reaves, W. H. Weinberg and X. D. Wu, *Nature* **389** 944 (1997).

[3] T. X. Sun and G. E. Jabbour, *MRS Bull.* **27** 309 (2002).

[4] T. X Sun, *Biotech. Bioeng.* **61** 193 (1999).

[5] K.-S. Sohn, J. M. Lee and N. Shin, *Adv. Mater.* **15** 2081 (2003).

[6] S. Y. Seo, K.-S. Sohn, H. D. Park and S. Lee, *J. Electrochem. Soc.* **149** H12 (2002).

[7] Z.-L. Luo, B. Geng, J. Bao and C. Gao, *J. Comb. Chem.* **7** 942 (2005).

[8] X.-N. Liu, H.-B. Cui, Y. Tang, S.-X. Huang, W.-H. Liu and C. Gao, *Appl. Surf. Sci.* **223** 144 (2004).

[9] K.-S. Sohn, E. S. Park, C. H. Kim and H. D. Park, *J. Electrochem. Soc.* **147** 4368 (2000).

[10] PCPDFWIN Version 2.4, Powder Diffraction File, International Centre for Diffraction Data, Swarthmore, PA, USA (2003).

[11] A. C. Larson and R. B. Von Dreele, *General Structure Analysis System (GSAS)*, Los Alamos National Laboratory Report LAUR (2004).

[12] D. F. Mullica, W. O. Milligan, D. A. Grossie, G. W. Beall and L. A. Boatner, *Inorganica Chimica Acta* **95** 231 (1984).

[13] R. D. Shannon, *Acta Cryst.* **A32** 751 (1976).

[14] D. F. Mullica, D. A. Grossie and L. A. Boatner, *Inorganica Chimica Acta* **109** 105 (1985).

[15] U. Rambabu and S. Buddhudu, *Opt. Mater.* **17** 401 (2001).

[16] K. S. Sohn, I. W. Jeon, H. Chang, S. K. Lee and H. D. Park, *Chem. Mate*r. **14** 2140 (2002).

[17] Y. Shimomura and N. Kijima, *Electrochem. Solid-State Lett.* **7** H1 (2004).

[18] K. S. Sohn, J. M. Lee, I. W. Jeon and H. D. Park, *J. Electrochem. Soc.* **150** H182 (2003).

[19] Y. Ni, J. M. Hughes and A. N. Mariano, *Amer. Mineral.* **80** 21 (1995).

[20] Y.Y. Choi, K. S. Sohn, H. D. Park and S. Y. Choi, *J. Mater. Res.* **16** 881 (2001).

Chapter 5

Variable Temperature Study of Pyrochlore Bismuth Hafnate, $Bi_2Hf_2O_7$

5.1 Introduction

Compounds adopting the pyrochlore structure and containing polarisable A-cations have attracted interest as electroceramic materials for capacitor and high-frequency filter applications. The need to reduce the use of high toxicity ceramics such as lead titanate (PT) and lead zirconate titanate (PZT) perovskite has led to the development of bismuth based electroceramic materials.

The pyrochlore structure is widely adopted by oxide materials of the stoichiometry $A_2B_2O_7$; where A is a trivalent or divalent species and so B is tetravalent or pentavalent respectively. These compounds have numerous applications and have been reviewed extensively.[1] Their formula is often expressed as $A_2O'B_2O_6$ to emphasize the interpenetrating networks of cuprite-like A_2O' tetrahedral nets with hexagonal tungsten bronze sheets of corner sharing octahedra with B_2O_6 composition. The ideal cubic pyrochlore structure (Figure 5.1.1) crystallises in the $Fd\overline{3}m$ space group with A, B and O' on special positions. The position of the O (48*f*: x, $^1/_8$, $^1/_8$) varies according to the tilting of the BO_6 octahedra, the B-O distance and the coordination geometry around the A-cation.

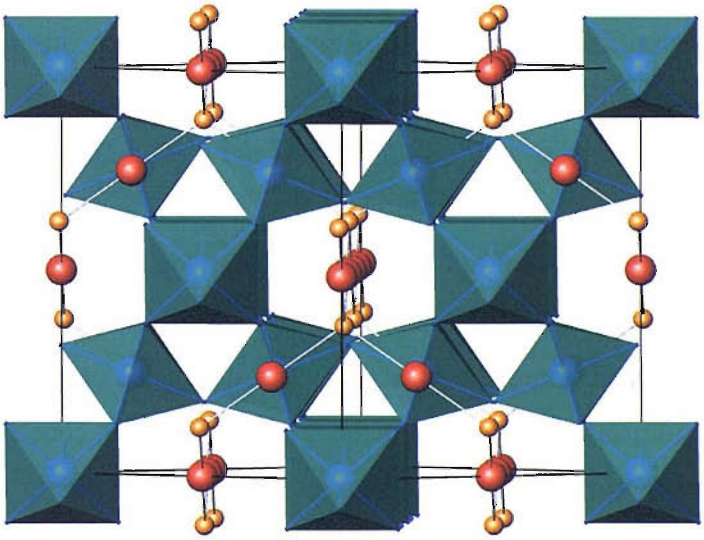

Figure 5.1.1. The ideal pyrochlore structure viewed along the [110] axis (A red, O' orange and BO_6 octahedra in green).

Disorder in the A_2O' network is often seen when the A cation of a pyrochlore compound has an active lone pair. In the standard pyrochlore model the *A*-cation is located at the centre of a puckered hexagonal ring of O atoms on a centre of $\bar{3}m$ symmetry. There are two short bonds of equal length to O' along the three-fold axis. A lone pair can not easily be accommodated in this space. Avdeev speculated that the disorder of *A* and O' ions is present due to static displacements in most pyrochlore compounds in which the *A* cation has an active s^2 lone pair.[2] This has been evidenced in detailed studies on such compounds: Investigations of tin niobate and tantalate pyrochlores by Mössbauer spectroscopy showed that the Sn^{2+} could not be located in the highly symmetric $\bar{3}m$ environment.[3] This was supported by the observation of the 442 reflection in the powder X-ray diffraction pattern. In ideal cubic pyrochlores this reflection has zero intensity but could be modelled by anisotropic thermal vibration or more successfully with a static displacement toward the ring of O atoms. This allows the lone pair to be accommodated with two or three of the Sn-O distances being shortened. Similarly far-infrared spectroscopy studies of bismuth zinc niobate (BZN) showed that disorder in the A_2O' network resulted in a glass like dielectric behaviour.[4] BZN exhibits high dielectric constants, low dielectric loss and has temperature coefficients of capacitance, which are tuneable with composition.[5] This tunability can also be varied for thin film samples according to the substrate used.[6] The variation in biaxial stresses and tensile strains caused by varying the substrate can significantly influence the dielectric relaxation behaviour of cubic BZN.[7] For bismuth containing pyrochlores this disorder has been described by various models for B = Ti,[8,9] Nb,[5] Ru [2] and Sn.[10-12]

The A_2O' network of spin frustrated pyrochlores has been compared with the crystal structure of ice-I_h. The Bernal-Fowler rules state that each O atom in the lattice is bonded tetrahedrally to four protons such that two are proximal (covalent) and two are distal (H-bonded).[13] In ice-I_h these rules can not be be satisfied by any unique arrangement so there is a residual zero-temperature entropy. Hence it can be considered a frustrated sytem.[14] Seshadri applied this analogy to compare the stereochemistry of the lone pairs of stoichiometric $Bi_2Ti_2O_7$ and the Aurivillius phase ferroelectric $SrBi_2Ta_2O_9$ using density functional calculations.[15] $SrBi_2Ta_2O_9$

undergoes a transition from a paraelectric to a ferroelectric phase at 608 K which is thought to be driven by the off-centering tendency of the Bi^{3+} ions along the *b* axis. In the room temperature phase of $Bi_2Sn_2O_7$ disorder in the structure is very pronounced. This highly complex structure has recently been solved by simulated annealing methods.[16] With a large unit cell of a = 15.050 Å, b = 15.054 Å, c = 21.511 Å and β = 90.038 ° the compound is essentially metrically tetragonal. The average displacements from the ideal pyrochlore sites for Bi, Sn, O and O' were calculated to be 0.389, 0.104, 0.189 and 0.312 Å respectively. This highlights the greater distortion of the Bi-O' subnetwork compared to that of the Sn-O. At 140 °C a transformation occurs to a face-centered cubic unit cell with dimensions double that of a standard pyrochlore (a = 21.4 Å). Kennedy suggested that this phase could be refined in the space group $F\bar{4}3c$ and that there was an ordered displacement of the Bi atoms.[10] However no model was provided and there have been no other models in the literature. Above 630 °C $Bi_2Sn_2O_7$ forms a more standard face-centred cubic pyrochlore structure (a = 10.75 Å) with disorder around the bismuth site similar to that found in $Bi_2Ti_2O_7$[9] and BZN.[5] The Bi is displaced to a 96 fold site with the O' having a large thermal parameter.[12]

The preparation of $Bi_2Hf_2O_7$ was first described by Sleight with diffraction experiments indicating the compound was isostructural with $Bi_2Sn_2O_7$.[17] However more comprehensive structural studies have not been published. This may be because the hafnate cannot be sintered at high temperature to produce single crystalline or high quality polycrystalline material. Hence observation of small reflections required for *ab initio* structure solution becomes problematic. The recent solution of the stannate structure, and recent findings within the research group of large Bi site displacements in $Bi_2Ti_2O_7$,[9] prompted the re-investigation of bismuth hafnate in this study. The fact that the pyrochlore structure is able to accommodate a wide variety of cations leads to the possibility of studying structure/property variations with doping. These pyrochlore systems were therefore of interest as potential candidates for high throughput studies similar to those described in Chapter 3.

5.2 Synthesis

The $Bi_2Hf_2O_7$ sample was prepared following the coprecipitation procedure outlined by Sleight.[17] Hafnium oxynitrate hydrate and bismuth nitrate pentahydrate were dissolved in dilute HNO_3 to form a solution of pH = 2, which was heated to ~50 °C. The $HfO(NO_3)_2.xH_2O$ was produced from $HfCl_4$[18] and the degree of hydration being determined by thermal analysis with x $\approx$1.7. An aqueous ammonia solution (35%) was added dropwise to the Bi-Hf mixture with continuous stirring until a white precipitate had formed at around pH = 11. Stirring was continued for a further 30 min to agglomerate particles and to ensure complete precipitation. The product was then filtered, washed with deionised water and dried at 90 °C overnight. To minimise bismuth loss through volatilisation, the sample was calcined as a pressed disk at 875 °C. Although Sleight reported that $Bi_2Hf_2O_7$ was formed at up to 950 °C, thermal analysis of samples used in this study indicated a large weight loss above 875 °C (Figure 5.2.1). Analysis of samples fired above this temperature revealed the presence of HfO_2 impurity.

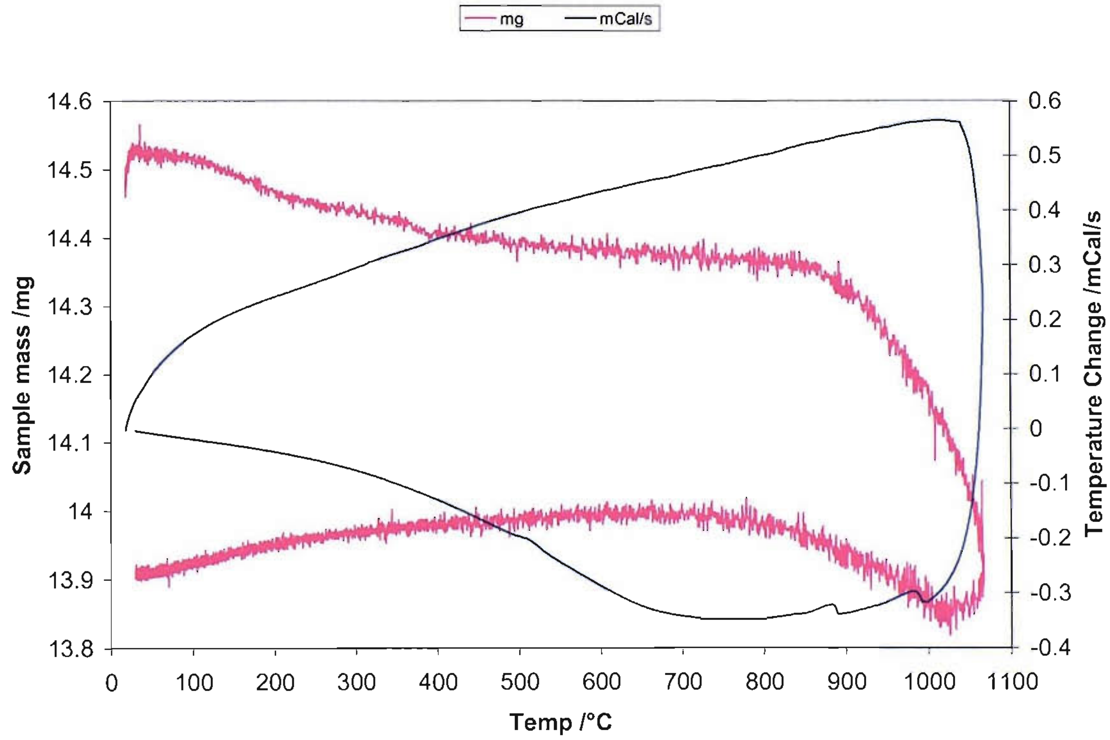

Figure 5.2.1 Thermal analysis data for $Bi_2Hf_2O_7$ as a pressed pellet.

5.3 Characterisation

Powder X-ray diffraction patterns were collected using a Siemens D5000 diffractometer over a 2θ range of 10-110 ° with a step size of 0.02 ° for a period of 15 hours. Variable temperature PXRD was carried out using a Bruker D8 Advance fitted with an Anton Paar HTK-1200 high temperature furnace. Scans were recorded at 50 °C intervals from room temperature to 950 °C over a 2θ range of 20 - 80 ° with a step size of 0.017 ° using the PSD. Both instruments use Cu$K_{\alpha 1}$ radiation. Powder neutron diffraction data were collected using the high-resolution time-of-flight HRPD diffractometer at the ISIS facility. Data were collected from a 3g sample sealed in a silica tube placed inside a vanadium can at 22 °C (300 μA), 600 °C (300 μA) and 900 °C (150 μA). Data from the backscattered bank (2θ = 168.33°) with a time of flight range of 40 - 120 μs (d = 0.828 - 2.484 Å) were refined using the GSAS package.[19] Thermal analyses were carried out using a Polymer Laboratories STA 1500 between 25 and 1000 °C under flowing air. The sample was analysed by EDX using a JEOL JSM-5910 with an Oxford Inca 300 detector. Several area scans on a pressed pellet showed a Bi:Hf ratio of 1:1 within experimental error.

5.4 X-ray Diffraction Data

Initial inspection of the room temperature X-ray diffraction data suggested that $Bi_2Hf_2O_7$ is indeed isostructural with $Bi_2Sn_2O_7$. The hafnate compound cannot be sintered at high temperature due to decomposition, hence broad reflections are recorded. As a result, symmetry peak splitting, due to a reduction from the ideal cubic cell, is not as well resolved as in the stannate, making direct *ab initio* structure solution problematic.

Variable temperature PXRD data sets were recorded in 50 °C steps up to 950 °C in order to compare the phase change behaviour of $Bi_2Hf_2O_7$ with $Bi_2Sn_2O_7$. Four distinct phases could be identified with transformations occurring at around 400, 550 and 900 °C (Figure 5.4.1). The respective transitions occur at significantly higher temperatures than the α-β (90 °C) and β-γ (680 °C) of the stannate. The phase above 550 °C phase did not appear to adopt a doubled cubic cell because exhibited more reflections than the standard $Fd\bar{3}m$ model allows. The data from the phase above 900 °C was consistent with a standard pyrochlore though no intensity was seen for the 311 reflection. To limit decomposition through bismuth loss, scans were collected over a short 2θ range, reducing the overall collection time at elevated temperature. High resolution neutron diffraction experiments, in sealed silica tubes to prevent bismuth loss, were undertaken to investigate these phases in more detail. Good quality data sets were recorded on heating for the α, γ and δ phases while shorter collections were used at 50 °C intervals on cooling. The difference between the α and β phases is small and was only observed after the neutron experiment, hence only a short collection was available.

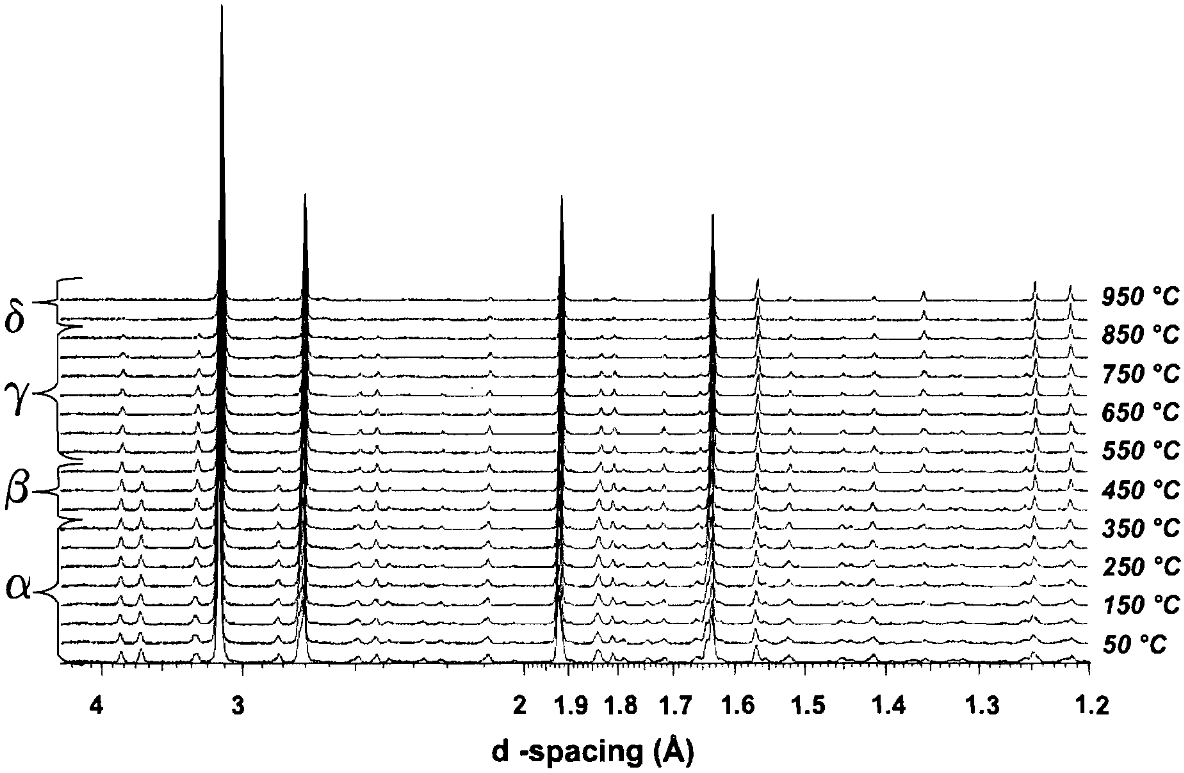

Fig. 5.4.1 Variable temperature PXRD data for $Bi_2Hf_2O_7$ from 25 °C to 950 °C.

5.5 Neutron Diffraction Data

α – Phase (22 °C)

The room temperature structure of $Bi_2Sn_2O_7$ was unknown for many years due to the complexity of its unit cell. Using simulated annealing methods the structure was solved in the monoclinic *Pc* space group with 176 crystallographically independent atoms.[16] The structure of $Bi_2Hf_2O_7$ was refined using this as a starting model. Initially lattice parameters and thermal parameters (with like atoms constrained together) were refined. Due to the low sintering temperature, peaks were broader than those used in refinements on $Bi_2Sn_2O_7$ and it was not possible to simultaneously refine all atom positions freely to convergence. However, using soft constraints on the Hf-O, O-O and Bi-O' bond lengths and a high level of damping on the atom positions produced a stable refinement. The soft constraint distances were obtained by an iterative process, the Hf-O (with an e.s.d. of 0.01 Å) and Bi-O' (e.s.d. of 0.02 Å; each Bi having one short and one long bond to O') distances were regularly reset to their average value and O-O was set as $\sqrt{2}\times$ the Hf-O distance (e.s.d. of 0.05 Å) to maintain a roughly octahedral geometry. With refinement of the peak shape profiles, background and a linear absorption correction, a good fit was achieved to the data (Figure 5.5.1) with acceptable bond lengths and angles (Table 5.5.1). The O' thermal parameter was slightly high and this may have indicated an oxygen deficiency; refining the O' occupancy gave a value of 0.95. However, there was no indication of Bi or Hf deficiency and lower oxidation states than Bi^{3+} and Hf^{4+} are unlikely considering the synthesis method so the occupancy of O' was retained as 1 in the final model. Refined atomic positions are shown in Table 5.5.2.

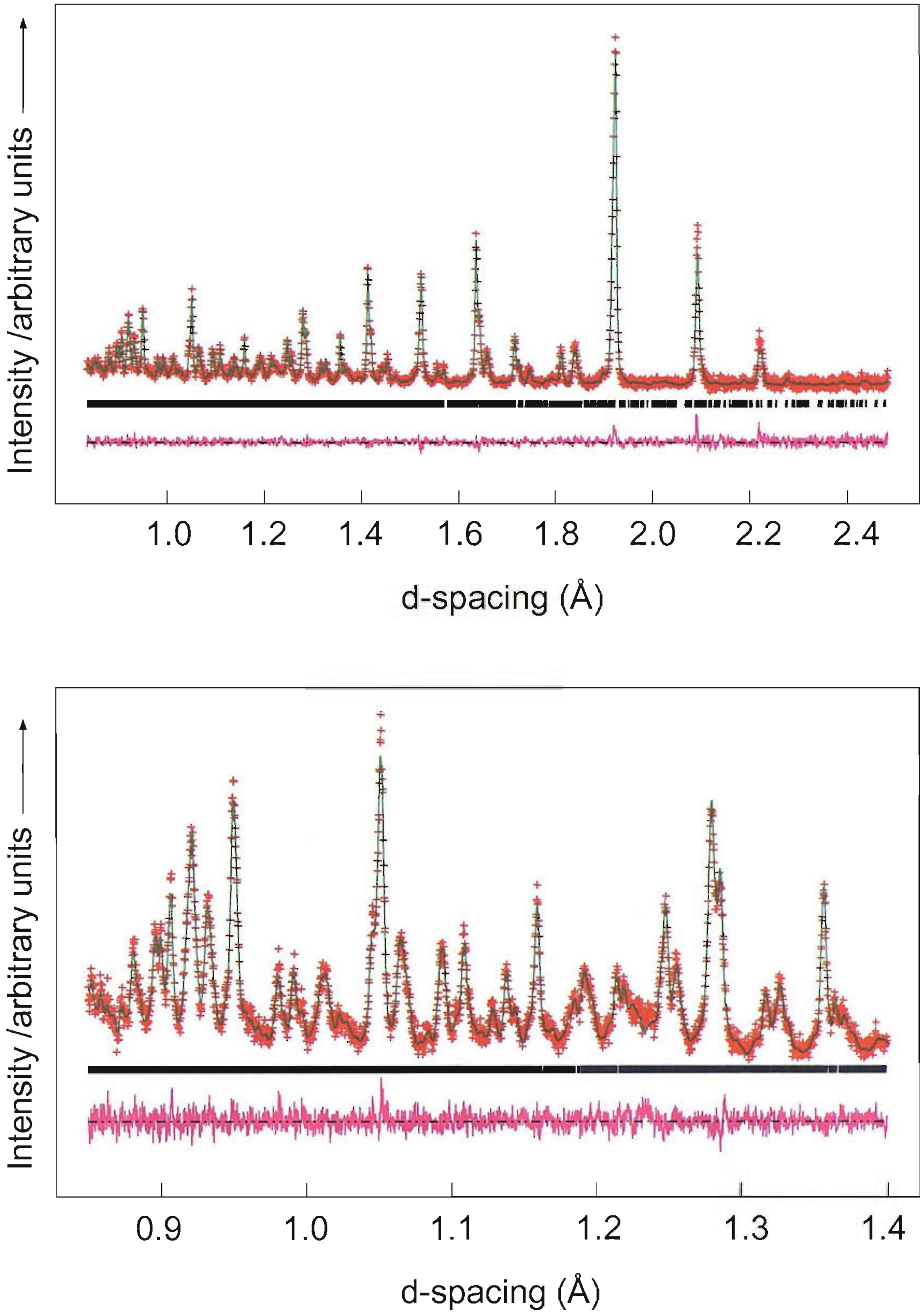

Figure 5.5.1 Final fit to the data collected for $Bi_2Hf_2O_7$ *at 22 °C. Crosses mark the data points, upper continuous line the calculated profile and lower continuous line the difference. Tick marks show the reflection positions.*

Table 5.5.1 Selected bond distances (Å) and angles (°) for $Bi_2Hf_2O_7$ at 22 °C (estimated standard deviations in parentheses).

Bond	Length (Å)			Angle	Angle (°)		
	Avg.	Min.	Max.		Avg.	Min.	Max
Bi-O'(i)	2.24	2.20(3)	2.29(3)	O'-Bi-O'	154.69	132.69(18)	177.28(26)
Bi-O'(ii)	2.63	2.57(3)	2.68(3)	Hf-O-Hf	134.0	120.0(19)	145.6(20)
Bi-O	2.75	1.51(7)	3.67(6)				
Hf-O	2.09	2.07(1)	2.11(1)				

Space group *Pc*; $a = 15.3536(4)$ Å, $b = 15.3320(4)$, $c = 21.8253(3)$ Å, $\beta = 90.051(5)°$ $R_p = 4.16$ %, $R_{wp} = 4.65$ % and $\chi^2 = 1.79$.

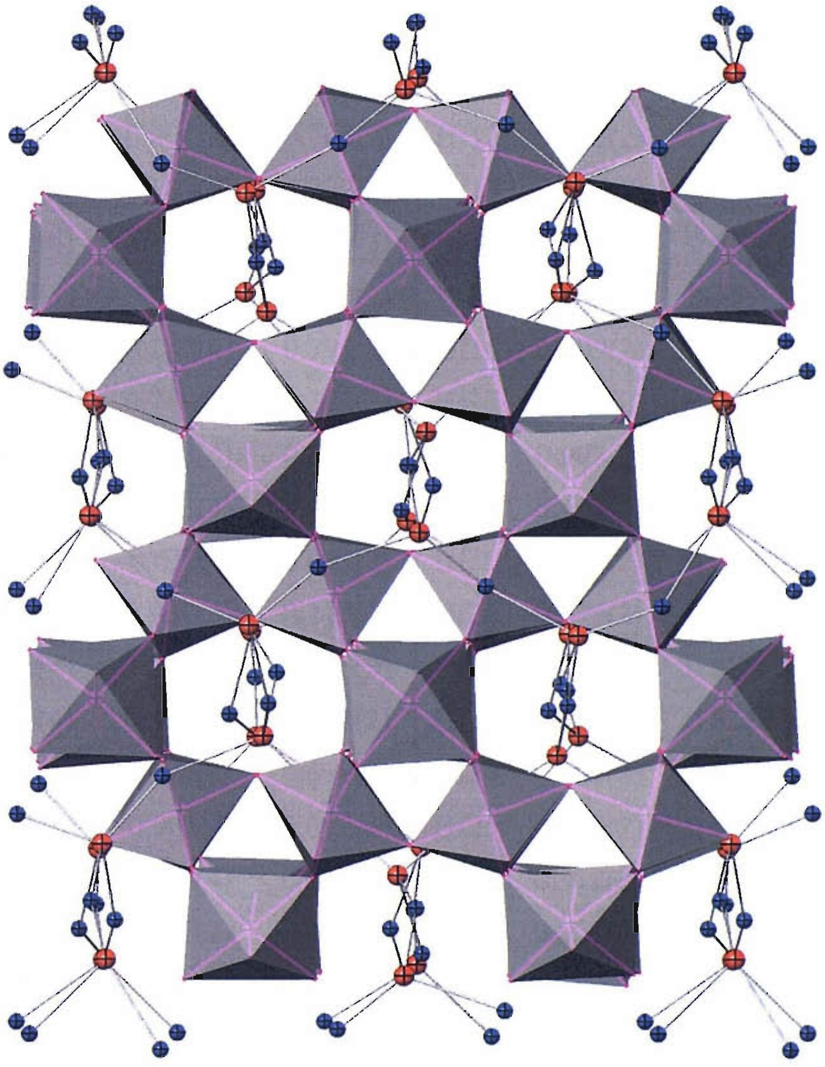

Figure 5.5.2 The room temperature structure of $Bi_2Hf_2O_7$. Bi in blue, O' in red and HfO_6 octahedra in grey.

Table 5.5.2 Refined atomic positions for $Bi_2Hf_2O_7$ at 22 °C (estimated standard deviations in parentheses).

	x	*y*	*z*		*x*	*y*	*z*
Bi1	0.168(4)	-0.028(4)	0.050(2)	Hf1	0.157(2)	0.497(2)	0.304(1)
Bi2	0.671(3)	0.517(3)	0.022(2)	Hf2	0.659(2)	-0.001(2)	0.300(1)
Bi3	0.169(3)	0.251(4)	0.334(2)	Hf3	0.159(2)	0.754(2)	0.060(1)
Bi4	0.171(3)	0.263(3)	0.826(3)	Hf4	0.158(2)	0.749(2)	0.559(1)
Bi5	0.674(4)	0.748(4)	0.319(2)	Hf5	0.658(2)	0.252(2)	0.059(1)
Bi6	0.665(3)	0.715(3)	0.839(2)	Hf6	0.660(2)	0.245(2)	0.556(1)
Bi7	-0.003(4)	0.617(3)	0.436(2)	Hf7	0.032(2)	0.136(2)	0.184(1)
Bi8	0.039(4)	0.649(3)	0.958(3)	Hf8	0.032(2)	0.123(2)	0.679(1)
Bi9	0.522(4)	0.128(3)	0.445(3)	Hf9	0.533(2)	0.626(2)	0.181(1)
Bi10	0.503(4)	0.128(3)	0.933(3)	Hf10	0.527(2)	0.624(2)	0.683(1)
Bi11	0.261(4)	0.654(3)	0.176(2)	Hf11	0.285(2)	0.125(2)	0.431(1)
Bi12	0.275(4)	0.601(3)	0.703(2)	Hf12	0.275(2)	0.126(2)	0.930(1)
Bi13	0.775(4)	0.104(3)	0.222(2)	Hf13	0.774(2)	0.619(2)	0.435(1)
Bi14	0.752(4)	0.127(3)	0.679(3)	Hf14	0.782(2)	0.623(2)	0.928(1)
Bi15	0.414(3)	0.210(4)	0.293(2)	Hf15	0.404(2)	0.759(2)	0.057(1)
Bi16	0.418(3)	0.282(4)	0.797(2)	Hf16	0.409(2)	0.751(2)	0.555(1)
Bi17	0.927(3)	0.749(4)	0.302(2)	Hf17	0.908(2)	0.243(2)	0.049(1)
Bi18	0.909(4)	0.728(4)	0.805(2)	Hf18	0.903(2)	0.247(2)	0.559(1)
Bi19	0.411(3)	0.503(4)	0.072(2)	Hf19	0.409(2)	-0.003(2)	0.309(1)
Bi20	0.925(3)	-0.010(4)	0.082(2)	Hf20	0.909(2)	0.499(2)	0.305(1)
Bi21	0.228(3)	0.907(3)	0.213(2)	Hf21	0.275(2)	0.381(2)	0.435(1)
Bi22	0.260(4)	0.864(3)	0.680(3)	Hf22	0.277(2)	0.378(2)	0.932(1)
Bi23	0.741(4)	0.380(3)	0.181(2)	Hf23	0.781(2)	0.871(2)	0.430(1)
Bi24	0.761(4)	0.394(3)	0.691(2)	Hf24	0.782(2)	0.883(2)	0.929(1)
Bi25	0.425(4)	-0.001(4)	0.077(3)	Hf25	0.413(2)	0.502(2)	0.308(1)
Bi26	0.918(3)	0.507(4)	0.073(3)	Hf26	0.912(2)	-0.001(2)	0.311(1)
Bi27	0.008(4)	0.107(3)	0.431(3)	Hf27	0.029(2)	0.624(2)	0.178(1)
Bi28	0.056(4)	0.101(3)	0.914(2)	Hf28	0.029(2)	0.628(2)	0.682(1)
Bi29	0.532(4)	0.638(3)	0.446(3)	Hf29	0.532(2)	0.132(2)	0.184(1)
Bi30	0.487(4)	0.628(3)	0.928(2)	Hf30	0.534(2)	0.119(2)	0.677(1)
Bi31	0.169(4)	0.467(4)	0.050(2)	Hf31	0.164(2)	0.005(2)	0.300(1)
Bi32	0.668(4)	0.028(4)	0.060(2)	Hf32	0.657(2)	0.497(2)	0.308(1)

	x	*y*	*z*		*x*	*y*	*z*
O1	0.289(2)	-0.008(3)	0.264(2)	O33	0.137(2)	0.344(3)	0.128(2)
O2	0.782(2)	0.518(3)	0.274(2)	O34	0.137(2)	0.343(3)	0.625(2)
O3	0.036(2)	0.244(3)	0.016(2)	O35	0.627(3)	0.867(2)	0.107(2)
O4	0.032(2)	0.244(3)	0.525(2)	O36	0.630(3)	0.851(3)	0.618(2)
O5	0.532(2)	0.758(3)	0.024(2)	O37	0.285(2)	0.254(3)	0.092(2)
O6	0.535(2)	0.753(3)	0.519(2)	O38	0.283(2)	0.258(3)	0.600(2)
O7	0.019(3)	0.751(2)	0.213(2)	O39	0.782(2)	0.762(3)	0.099(2)
O8	-0.003(3)	0.746(2)	0.725(2)	O40	0.787(2)	0.746(3)	0.590(2)
O9	0.515(3)	0.253(2)	0.224(2)	O41	0.041(2)	-0.001(3)	0.340(2)
O10	0.540(3)	0.245(2)	0.711(2)	O42	0.535(2)	0.484(3)	0.348(2)
O11	0.262(3)	0.502(2)	0.476(2)	O43	0.036(3)	0.497(2)	0.144(2)
O12	0.759(3)	-0.005(2)	0.467(2)	O44	0.515(3)	0.008(2)	0.146(2)
O13	0.423(2)	0.856(3)	0.124(2)	O45	0.273(3)	0.748(2)	0.395(2)
O14	0.432(3)	0.849(3)	0.620(2)	O46	0.285(3)	0.746(2)	0.900(2)
O15	0.946(3)	0.344(2)	0.108(2)	O47	0.786(3)	0.247(2)	0.399(2)
O16	0.934(3)	0.355(2)	0.611(2)	O48	0.775(3)	0.256(2)	0.897(2)
O17	0.437(3)	0.353(2)	0.114(2)	O49	0.427(3)	0.400(3)	0.246(2)
O18	0.441(3)	0.346(2)	0.614(2)	O50	0.438(3)	0.395(3)	0.748(2)
O19	0.933(3)	0.860(2)	0.113(2)	O51	0.942(3)	0.898(3)	0.249(2)
O20	0.940(3)	0.851(3)	0.614(2)	O52	0.934(3)	0.906(3)	0.744(2)
O21	0.385(2)	0.906(3)	0.378(2)	O53	0.449(3)	0.894(2)	0.252(2)
O22	0.384(3)	0.899(3)	0.868(2)	O54	0.439(3)	0.900(3)	0.750(2)
O23	0.883(3)	0.396(3)	0.365(2)	O55	0.922(2)	0.412(3)	0.232(2)
O24	0.876(2)	0.415(3)	0.876(2)	O56	0.932(3)	0.397(3)	0.744(2)
O25	0.377(3)	0.411(3)	0.375(2)	O57	0.379(3)	0.348(3)	-0.008(2)
O26	0.383(3)	0.402(3)	0.874(2)	O58	0.373(3)	0.343(3)	0.497(2)
O27	0.880(3)	0.892(3)	0.366(2)	O59	0.873(3)	0.856(3)	-0.002(2)
O28	0.896(2)	0.911(3)	0.881(2)	O60	0.884(3)	0.863(2)	0.492(2)
O29	0.188(3)	0.898(2)	0.358(2)	O61	0.380(3)	0.865(2)	-0.000(2)
O30	0.194(3)	0.894(3)	0.861(2)	O62	0.370(3)	0.851(3)	0.496(2)
O31	0.689(3)	0.386(2)	0.359(2)	O63	0.878(3)	0.350(3)	-0.007(2)
O32	0.672(3)	0.405(3)	0.873(2)	O64	0.881(3)	0.343(3)	0.490(2)

	x	*y*	*z*		*x*	*y*	*z*
O65	0.184(3)	0.357(2)	0.001(2)	O'1	0.276(3)	0.002(3)	0.140(2)
O66	0.175(3)	0.345(3)	0.494(2)	O'2	0.783(3)	0.478(3)	0.110(2)
O67	0.677(3)	0.844(3)	-0.016(2)	O'3	0.020(3)	0.241(3)	0.393(2)
O68	0.686(3)	0.846(3)	0.496(2)	O'4	0.020(3)	0.235(3)	0.881(2)
O69	0.136(3)	0.905(3)	0.238(2)	O'5	0.529(3)	0.750(3)	0.383(2)
O70	0.129(3)	0.885(2)	0.750(2)	O'6	0.515(3)	0.756(3)	0.886(2)
O71	0.634(2)	0.407(3)	0.238(2)	O'7	0.269(3)	0.515(3)	0.142(2)
O72	0.631(3)	0.404(3)	0.744(2)	O'8	0.781(3)	0.008(3)	0.146(2)
O73	0.286(2)	0.492(3)	0.273(2)	O'9	0.277(3)	0.254(3)	0.267(2)
O74	0.788(2)	0.006(3)	0.270(2)	O'10	0.285(3)	0.234(3)	0.768(2)
O75	0.255(3)	0.000(2)	0.463(2)	O'11	0.775(3)	0.732(3)	0.246(2)
O76	0.763(3)	0.495(2)	0.475(2)	O'12	0.770(3)	0.736(3)	0.768(2)
O77	0.187(3)	0.601(3)	0.362(2)	O'13	0.036(3)	0.014(4)	0.016(2)
O78	0.175(3)	0.597(3)	0.872(2)	O'14	0.525(3)	0.508(3)	0.010(2)
O79	0.696(3)	0.104(2)	0.355(2)	O'15	0.047(3)	0.488(3)	-0.003(2)
O80	0.684(3)	0.097(3)	0.866(2)	O'16	0.539(3)	0.010(3)	0.015(2)
O81	0.143(2)	0.163(3)	0.131(2)				
O82	0.132(3)	0.138(2)	0.615(2)				
O83	0.632(3)	0.654(3)	0.118(2)				
O84	0.633(2)	0.656(3)	0.627(2)				
O85	0.179(3)	0.149(3)	-0.004(2)				
O86	0.187(3)	0.150(3)	0.495(2)				
O87	0.690(3)	0.653(2)	-0.004(2)				
O88	0.675(3)	0.643(3)	0.499(2)				
O89	0.131(2)	0.593(3)	0.238(2)				
O90	0.122(3)	0.611(2)	0.751(2)				
O91	0.637(2)	0.105(3)	0.241(2)				
O92	0.645(2)	0.092(3)	0.730(2)				
O93	0.033(2)	0.511(3)	0.341(2)				
O94	0.537(2)	-0.003(3)	0.342(2)				
O95	0.032(3)	0.008(2)	0.153(2)				
O96	0.528(3)	0.500(2)	0.145(2)				

U_{iso} x 100 ($Å^2$): Bi = 0.03(1), Hf = 1.77(6), O = 2.08(6),O' = 2.61(3).

β – Phase (450 °C)

Detailed VT-PXRD experiments showed that, as in the stannate, transformation to a face-centred cubic cell did occur at around 400 °C. No model has yet been described for β-$Bi_2Sn_2O_7$, but it has been indexed on the basis of a large cubic cell with a = 21.4480 Å. This is approximately double that of a standard pyrochlore and $\sqrt{2}a$ times that of the α – phase. Systematic absences suggested a possible space group of $F\bar{4}3c$ for this phase.[10] Indexing and Lebail extractions of short neutron collections and X-ray data (Figure 5.5.3) of $Bi_2Hf_2O_7$ at 450 °C were consistent with these findings. Further high resolution neutron data sets with longer collection times combined with *ab initio* structure determinations would be required to solve fully the structure of this polymorph.

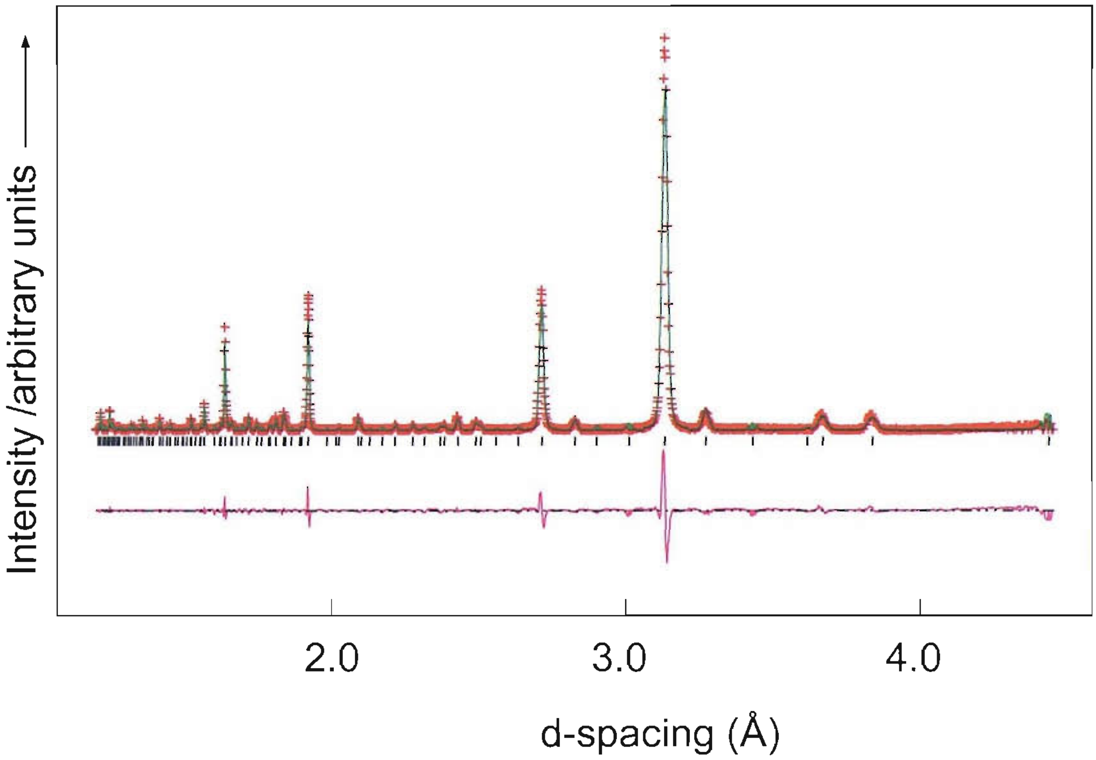

Figure 5.5.3 Fit from Lebail extraction performed on X-ray data collected at 450 °C. Crosses mark the data points, upper continuous line the calculated profile and lower continuous line the difference. Tick marks show the reflection positions.

γ – Phase (600 °C)

Inspection of the data revealed extra reflections and peak splitting consistent with a distortion of the unit cell away from the ideal cubic pyrochlore. Model independent refinements were carried out using space groups from the $Fd\bar{3}m$ subgrouping as described by Hiroi in work on symmetry-lowering structural transitions of $Cd_2Re_2O_7$ (Figure 5.5.4).[20]

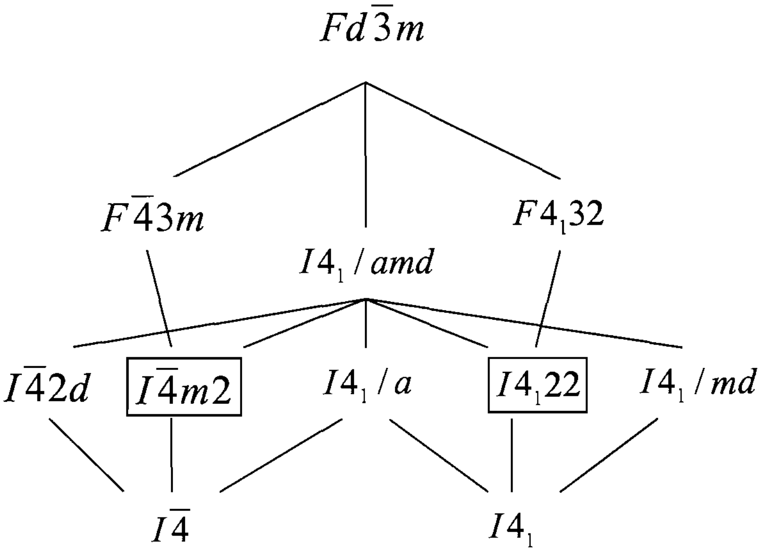

Figure 5.5.4 Group-subgroup relations of symmetry reductions for the maximum subgroups stemming from the standard pyrochlore space group.

The subgrouping follows reductions in the pyrochlore symmetry from a face-centred to a body-centred lattice. It became clear that the phase was tetragonal as the difference between the *a* and *c* parameters was significantly greater than the statistical error (($\sqrt{2}$a)/c = 1.002). The space group $I4_1/amd$ could also be ruled out as it did not allow the reflection at d= 1.51 Å to be modelled. The remaining possibilities all had similar fit statistics from Lebail extractions. Examination of the literature revealed two models (space groups $I\bar{4}m2$ and $I4_122$) which could be used for comparative Rietveld refinement of the data. Table 5.5.3 shows the atomic positions for the two models. The postion of the Bi and Hf sites are described by 8 fold sites in both space groups. For $I4_122$ the O postions are described by three 8-fold sites and a 4-fold O' site. The lower symmetry $I\bar{4}m2$ model requires two 2-fold

O' sites with two 8-fold and two 4-fold positions to describe O. In a translation from $I4_122$ to $I\bar{4}m2$ a two-fold axis is removed and a mirror plane added. Both models gave a reasonable fit to the data but the fit statistics were slightly better for the $I4_122$ model than the $I\bar{4}m2$ (R_p = 4.63 and 4.82 % respectively). As the extra oxygen positions did not improve the description of the structure, the lower symmetry $I\bar{4}m2$ model was discounted.

Table 5.5.3 The two possible pyrochlore models for γ-$Bi_2Hf_2O_7$.

$I4_122$ (no. 98)					$I\bar{4}m2$ (no. 119)				
Bi	8*f*	$^{1}/_{4}$	$\bar{x}+{}^{1}/_{2}\approx 0$	$^{3}/_{8}$	Bi	8*i*	$x\approx{}^{1}/_{4}$	0	$z\approx{}^{3}/_{8}$
Hf	8*f*	$^{1}/_{4}$	$x\approx 0$	$^{7}/_{8}$	Hf	8*i*	$x\approx{}^{1}/_{4}$	0	$z\approx{}^{7}/_{8}$
O	8*d*	x	x	0	O	8*g*	x	x	0
	8*e*	$\bar{x}$	x	0		8*h*	x	$x+{}^{1}/_{2}$	$^{1}/_{4}$
	8*c*	0	0	z		4*e*	0	0	z
O'	4*b*	0	0	$^{1}/_{2}$		4*f*	0	$^{1}/_{2}$	z'
					O'	2*b*	0	0	$^{1}/_{2}$
						2*d*	0	$^{1}/_{2}$	$^{3}/_{4}$

Introduction of anisotropy for the thermal displacement of the bismuth atom in the $I4_122$ model resulted in an unusual elongated ellipsoid extending perpendicularly away from the Bi-O' bond. The unusual shape of the Bi ellipsoid suggested that a split Bi position may be required to describe the site more accurately. The only available site with lower symmetry than the 8*f* ($^{1}/_{4}$, $\bar{x}+{}^{1}/_{2}$, $^{3}/_{8}$) is the 16*g* (*x*, *y*, *z*) site. Displacement to this site was tested with an appropriate reduction in the occupancy. The refinement proceeded smoothly and gave a slight improvement in the fit as well as giving more reasonable thermal parameters for Bi (U_{iso}= 0.014 from 0.047 Å^2).

The thermal ellipsoid of the O' was also a large disk shape the edges of which extended towards the side of the puckered ring not occupied by the bismuth suggesting some disorder. A split site was therefore tested, moving O' to an 8*c* (0, 0, *z*) site and halving the occupancy. More reasonable thermal parameters were obtained but the statistical fit was slightly worse than that achieved with an anisotropic 4-fold site (χ^2 = 1.546 *vs.* 1.535). Figure 5.5.5 shows the final fit to the data. Table 5.5.4 and table 5.5.5 show the refined crystallographic parameters and selected bond lengths and angles for γ-$Bi_2Hf_2O_7$.

Table 5.5.4 Refined atomic positions for $Bi_2Hf_2O_7$ at 600 °C (estimated standard deviations in parentheses).

Atom	*x*	*y*	*z*	U_{11} x100 (Å^2)	U_{22} x100 (Å^2)	U_{33} x100 (Å^2)	U_{12} x100 (Å^2)	U_{13} x100 (Å^2)	U_{23} x100 (Å^2)
Bi	0.2213(8)	0.0366(4)	0.3524(3)	3.2(1)	3.21	3.21	0	0	0
Hf	$^{1}/_{4}$	-0.0022(3)	$^{7}/_{8}$	3.7(2)	0.0(1)	1.9(2)	0	1.3(1)	0
O1	0.1997(4)	0.1997(4)	0	4.8(2)	4.8(2)	4.8(4)	1.7(2)	3.2(2)	-3.2(2)
O2	-0.1964(4)	0.1964(4)	0	4.1(2)	4.1(2)	5.0(5)	2.3(2)	-1.1(2)	-1.1(2)
O3	0	0	0.1999(3)	6.1(4)	5.3(4)	5.0(3)	-3.7(3)	0	0
O'	0	0	$^{1}/_{2}$	3.8(2)	3.8(2)	11.5(5)	-3.4(4)	0	0

Space group $I4_122$; *a* = 7.68966(3) Å, *c* = 10.85169(8) Å;

R_{wp} = 4.85 %, R_p = 4.12 %, χ^2 = 1.54.

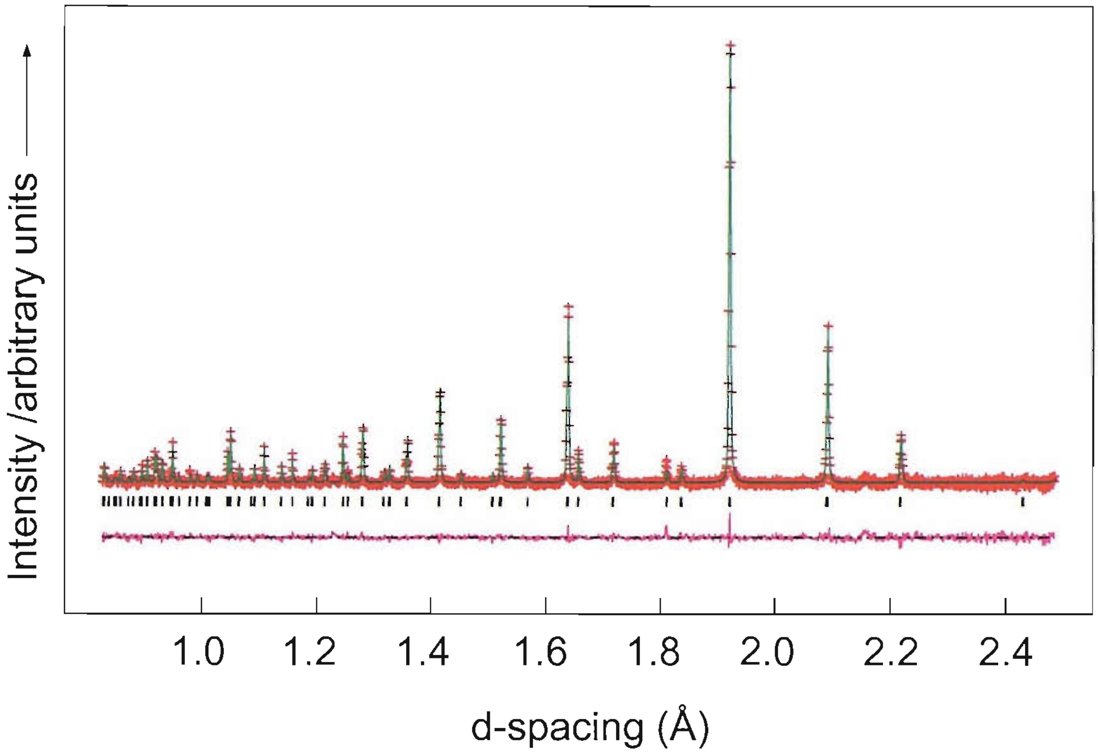

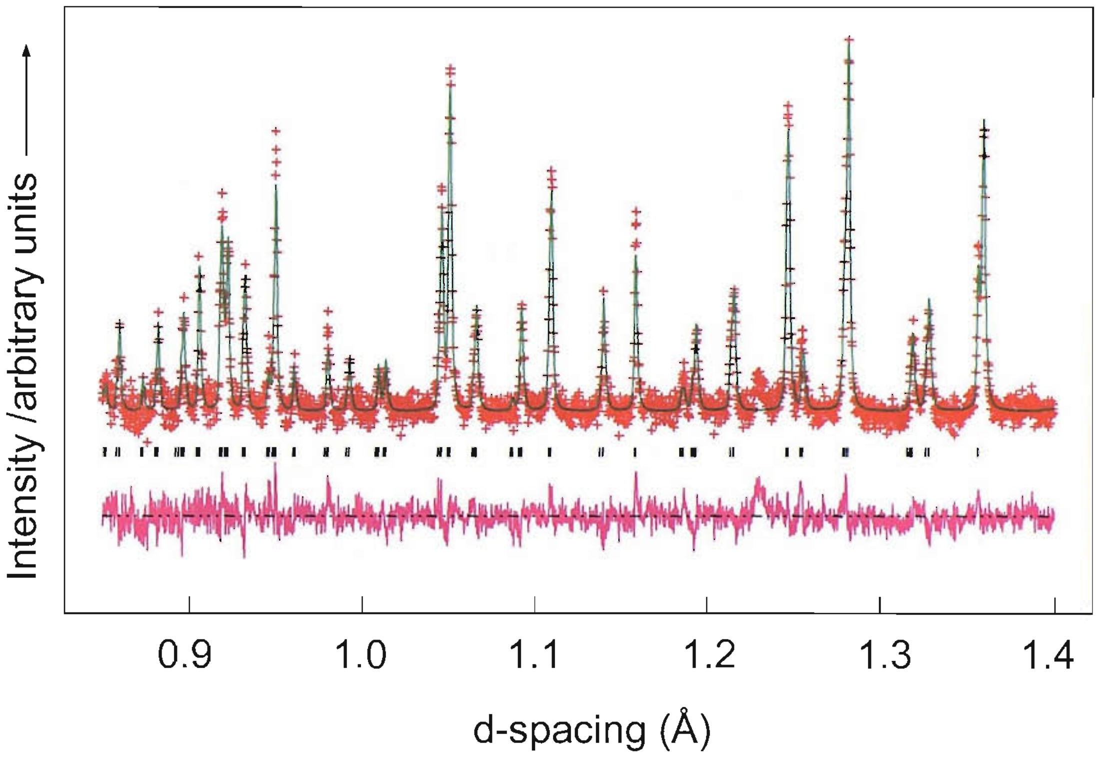

Figure 5.5.5 Final fit to the data collected at 600 °C. Crosses mark the data points, upper continuous line the calculated profile and lower continuous line the difference. Tick marks show the reflection positions. Reflections at 2.15, 1.51 and 1.23 Å are from vanadium.

Table 5.5.5 Selected bond distances (Å) and angles (°) for $Bi_2Hf_2O_7$ at 600 °C (estimated standard deviations in parentheses).

Bond	Length	Angle	Angle (°)
Bi-O1	2.655(4)	O'-Bi-O'	159.19(9)
	2.318(4)		
Bi-O2	3.132(4)	Hf-O1-Hf	133.7(2)
	2.848(4)		
Bi-O3	2.390(5)	Hf-O2-Hf	136.4(2)
	3.045(4)		
Bi-O'	2.354(6)	Hf-O3-Hf	134.1(2)
	2.430(6)		
Hf-O1 (x2)	2.098(2)		
Hf-O2 (x2)	2.059(2)		
Hf-O3 (x2)	2.087(1)		

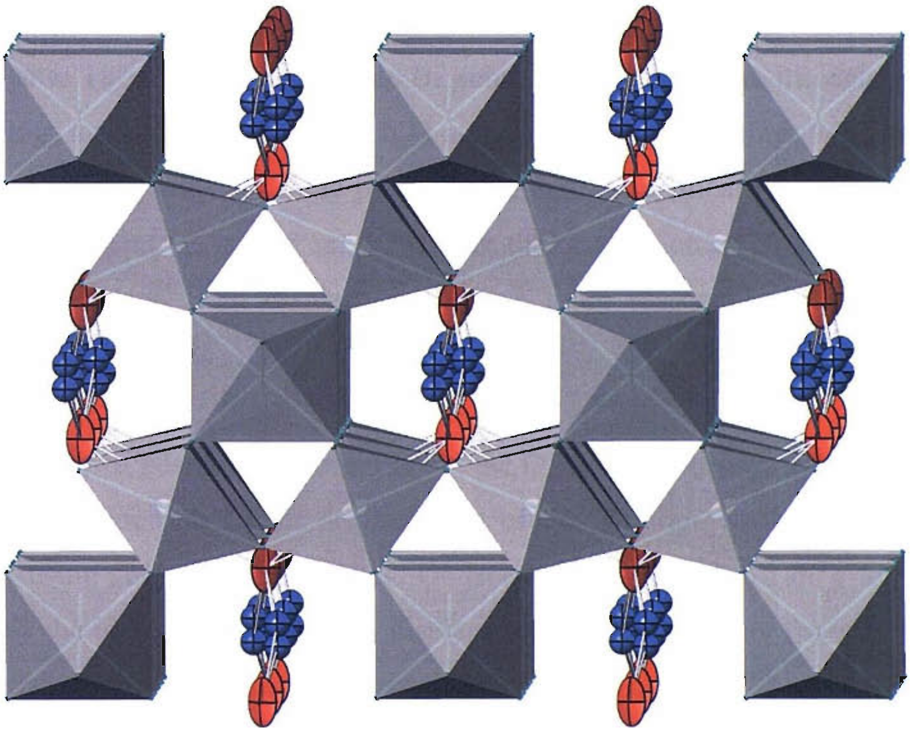

Figure 5.5.6 The structure of $Bi_2Hf_2O_7$ at 600 °C. Bi in blue, O' in red and HfO_6 octahedra in grey.

δ – Phase (900 °C)

Preliminary refinements were carried out using the ideal pyrochlore structure (Bi (0,0,0), Hf ($^1/_2$, $^1/_2$, $^1/_2$), O (x, $^1/_8$, $^1/_8$) and O' ($^1/_8$, $^1/_8$, $^1/_8$)) in the $Fd\bar{3}m$ space group, with isotropic temperature factors on all atoms except O. A minor HfO_2 impurity was included in the refinement using the monoclinic model appropriate for this temperature.[21] The formation of this phase may be due to decomposition occuring at the surface of the sample. The remaining weak reflections at 2.15, 1.51 and 1.23 Å were attributed to the vanadium sample holder. A reasonable fit to the data was obtained but with very high thermal parameters on the Bi and O' (U_{iso} = 0.1074 and 0.0814 Å^2). Anisotropic refinement of the Bi thermal parameter improved the fit further (R_p = 5.35 *vs.* 5.14 %) and gave intensity to the previously zero intensity 442 reflection (d = 1.813 Å). Broadening of the Bi thermal ellipsoid perpendicular to the [111] axis, toward the puckered ring of O atoms occurred. This indicated that a static displacement of the Bi to a 96*g* (x, x, z) or 96*h* (0, y, $\bar{y}$) site as in $Bi_{1.74}Ti_2O_{6.62}$,[8] $Bi_2Ti_2O_7$[9] and γ-$Bi_2Sn_2O_7$[13] could be a better structural representation. These sites both correspond approximately to a ring of scattering density around the central bismuth site. The displacement of the Bi being toward the centre of each pair of O atoms (96*g*; model 1) or toward each O atom in the puckered ring (96*h*; model 2). Refinements using either of these positions resulted in identical fit statistics, with a slight improvement (χ^2 = 1.13 *vs.* 1.23) over the description of Bi with anisotropic thermal parameters. Both displacements gave more reasonable bismuth thermal parameters (U_{iso} = 0.025 Å^2).

The possibility of positional disorder about the O' site was then tested as its thermal parameter remained high after displacement of the Bi atom. Such disorder can be achieved using several possible sites. O' is located at the centre of a tetrahedron formed by the ideal bismuth sites. A displacement toward or away from each vertex of the tetrahedron can be described using the 32*e* (x, x, x) site.[2,10] The 48*f* (x, $^1/_8$, $^1/_8$) site displaces O' toward the centre of each edge of the tetrahedron. The 96*g* and 96*h* sites will displace O' roughly toward half of the bismuth sites as described by the 96*g* Bi displacement.[5] Refinements were carried out with the O' displaced to each of these sites with both possible Bi positions. Initially a reduced thermal parameter was found in all cases but refinement of the atom position tended towards the central site with a very high thermal parameter. Modelling the O' with a combination of the 8*a* and 32*e* site as described for $Bi_2Ti_2O_7$[9] also resulted in no improvement in the fit and refinements were unstable. Exploration of the O' site using δF_{hkl} Fourier maps indicated that the nuclear density around the site is purely spherical. Therefore it can be assumed that the large thermal parameter is due to thermal disorder at the high measurement temperature and not to any static displacement of O'. Refined crystallographic parameters and selected bond distances and angles are shown in Tables 5.5.6 and 5.5.7. The final fits achieved to the data are shown in Figure 5.5.7.

Table 5.5.6 Refined atomic positions for $Bi_2Hf_2O_7$ at 900 °C. Upper values are for model 1, lower values for model 2 (estimated standard deviations in parentheses).

Atom	*x*	*y*	*z*	*Occupancy*	U_{iso}/U_{11} x100 (Å^2)
Bi	-0.0166(9) 0	-0.0166(9) 0.0268(2)	0.0300(8) -0.0268(2)	$^1/_6$	2.5(2) 2.6(2)
Hf	$^1/_2$	$^1/_2$	$^1/_2$	1	2.2(1) 2.2(1)
O	0.4246(2) 0.4246(2)	$^1/_4$	$^1/_4$	1	5.7(2)* 5.6(2)*
O'	$^1/_4$	$^1/_4$	$^1/_4$	1	8.4(2) 8.3(2)

U_{22} x100 (Å^2)	U_{33} x100 (Å^2)	U_{12} x100 (Å^2)	U_{13} x100 (Å^2)	U_{23} x100 (Å^2)
*4.4(1)	4.4(1)	0	0	-2.39(8)
*4.4(1)	4.4(1)	0	0	-2.38(8)

Space group $Fd\bar{3}m$; a = 10.87791(3) Å(model 1), 10.87791(3) Å(model 2);
R_{wp} = 5.80 %, R_p = 5.10 %, χ^2 = 1.13 (Both models).

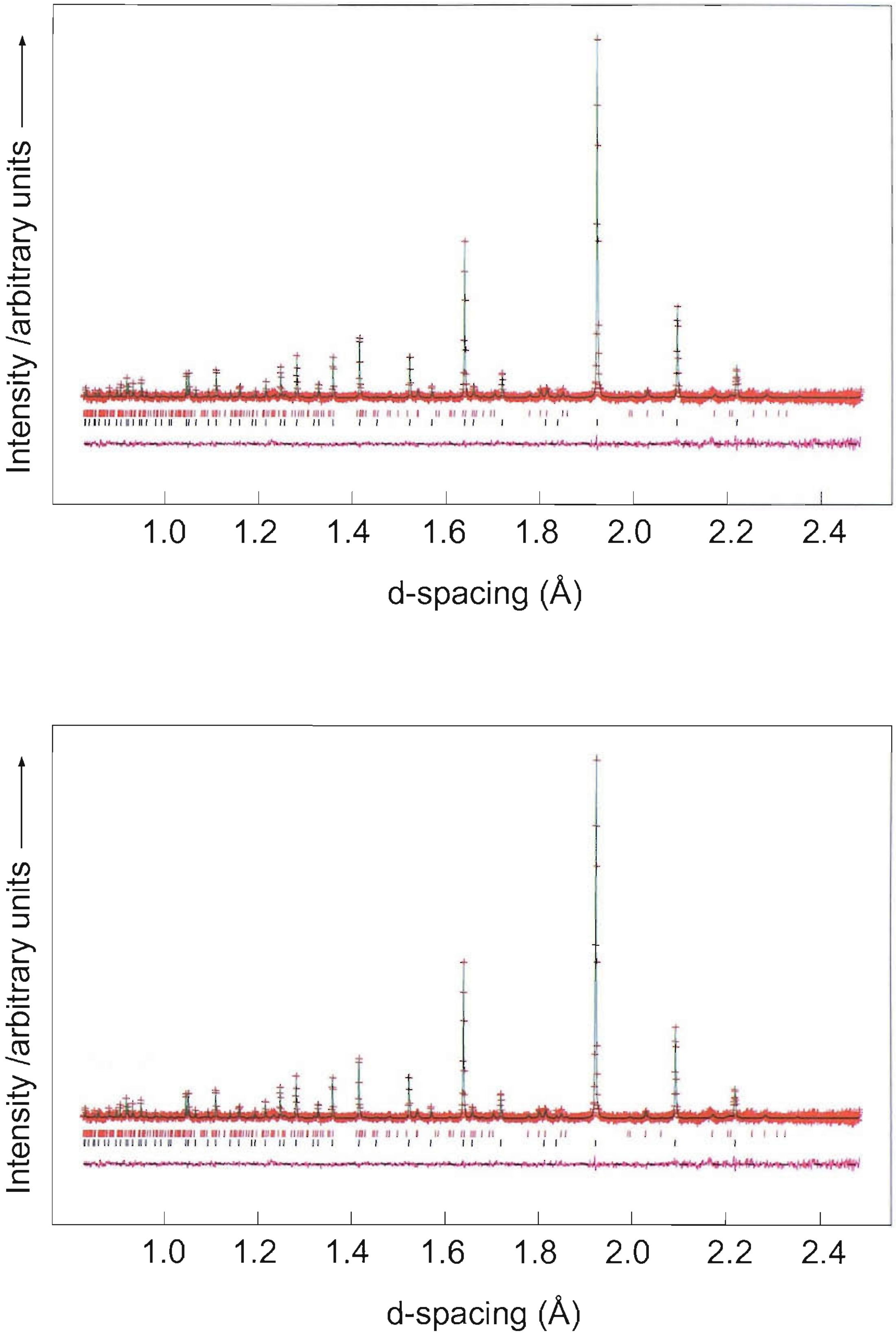

Figure 5.5.7 Final fits to the data collected at 900 °C (model 1 top, model 2 bottom). Crosses mark the data points, upper continuous line the calculated profile and lower continuous line the difference. Black tick marks indicate the main phase, red tick marks the HfO_2 impurity

Table 5.5.7 Selected bond distances (Å) and angles (°) for $Bi_2Hf_2O_7$ at 900 °C (estimated standard deviations in parentheses).

Bond	Length (Å)		Angle	Angle (°)	
	Model 1	Model 2		Model 1	Model 2
Bi-O	2.926(3) (x2) 2.529(3) (x2) 2.293(5) 3.114(4)	2.361(2) (x2) 2.734(1) (x2) 3.062(2) (x2)	O'-Bi-O'	160.1(1)	160.2(1)
Bi-O'	2.41(2) 2.37(2)	2.3909(4) (x2)	Hf-O-Hf	133.81(8)	133.79(8)
Hf-O	2.0905(6) (x6)	2.0906(6)	O-Hf-O	84.99(6) 95.01(6)	84.99(5) 95.01(5)

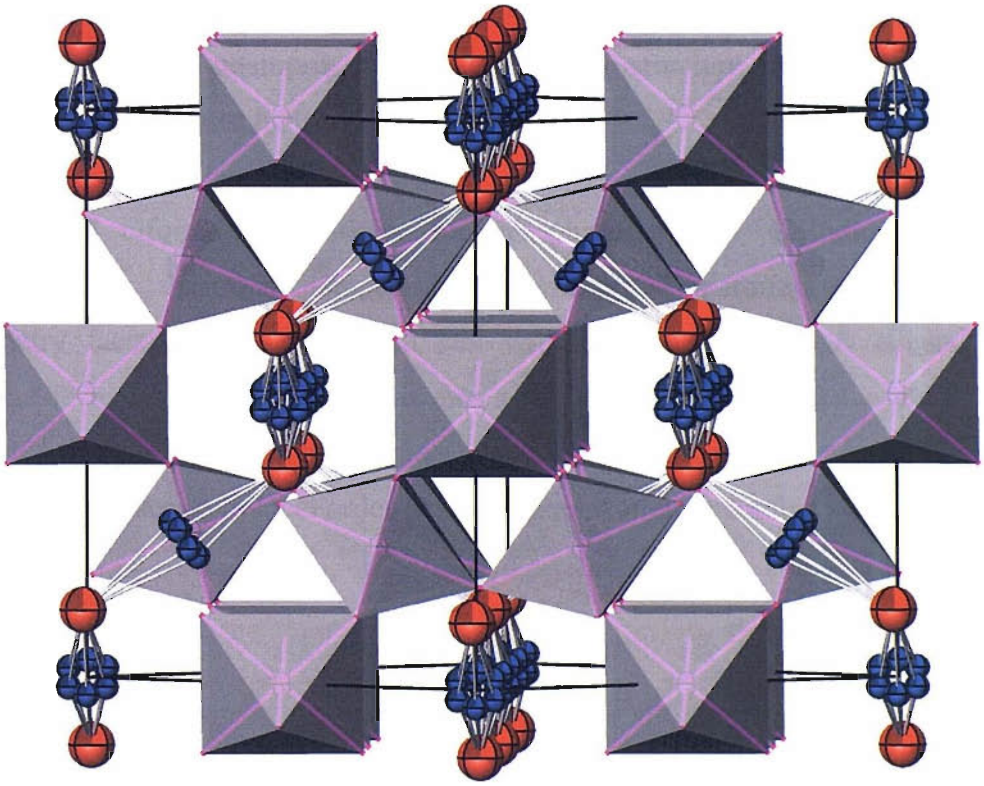

Figure 5.5.8 The structure of $Bi_2Hf_2O_7$ at 900 °C. Bi in blue, O' in red and HfO_6 octahedra in grey.

5.6 Discussion

At room temperature $Bi_2Hf_2O_7$ has unit cell parameters of a = 15.3536(4) Å, b = 15.3320(4) Å, c = 21.8253(3) Å and β = 90.051(5) ° consistent with the α-$Bi_2Sn_2O_7$ structure. The static displacements of Bi and O' lead to zig-zag Bi-O' chains with one short (min.= 2.20 Å, max.= 2.29 Å, avg.= 2.24 Å) and one long (min.= 2.57 Å, max.= 2.68 Å, avg.= 2.63 Å) Bi-O' bond. The O'-Bi-O' bond angle, which in an idealised pyrochlore is 180 °, varies from 132.7 to 177.3 °. Figure 5.6.1 shows the distribution of O'-Bi-O' bond angles with respect to their deviation from 180 °. The displacement of Bi is more pronounced perpendicular to the O'-O' axis. This was noted for α- $Bi_2Sn_2O_7$ where displacement in this plane was on average four times that in the direction of the O'-O' axis.[16] The Hf-O subnetwork is distorted to a lesser extent than that of the Bi-O'. The average Hf-O linkage is 2.09 Å with a range from 2.07- 2.11 Å. The Hf-O-Hf angles range from 120.0 to 145.6 ° with an average of 134.0 °. The large variation in the Hf-O-Hf and O'-Bi-O' angles may be a result of the quality of the data. The structural model provides a good fit to the data but resolving the atom positions of such a complex structure from powder data is ambitious and this must be taken into account.

The limited information available for the phase at 450 °C indicates a close relationship to the room temperature polymorph. Transformation to a higher symmetry face-centered cubic unit cell with a = 21.7326(18) Å occurs. It is reasonable to expect that this phase has a higher disorder than the α-phase. This probably includes split bismuth sites, as seen at higher temperatures, with the consequent reduction in local order facilitating relaxation into cubic symmetry.

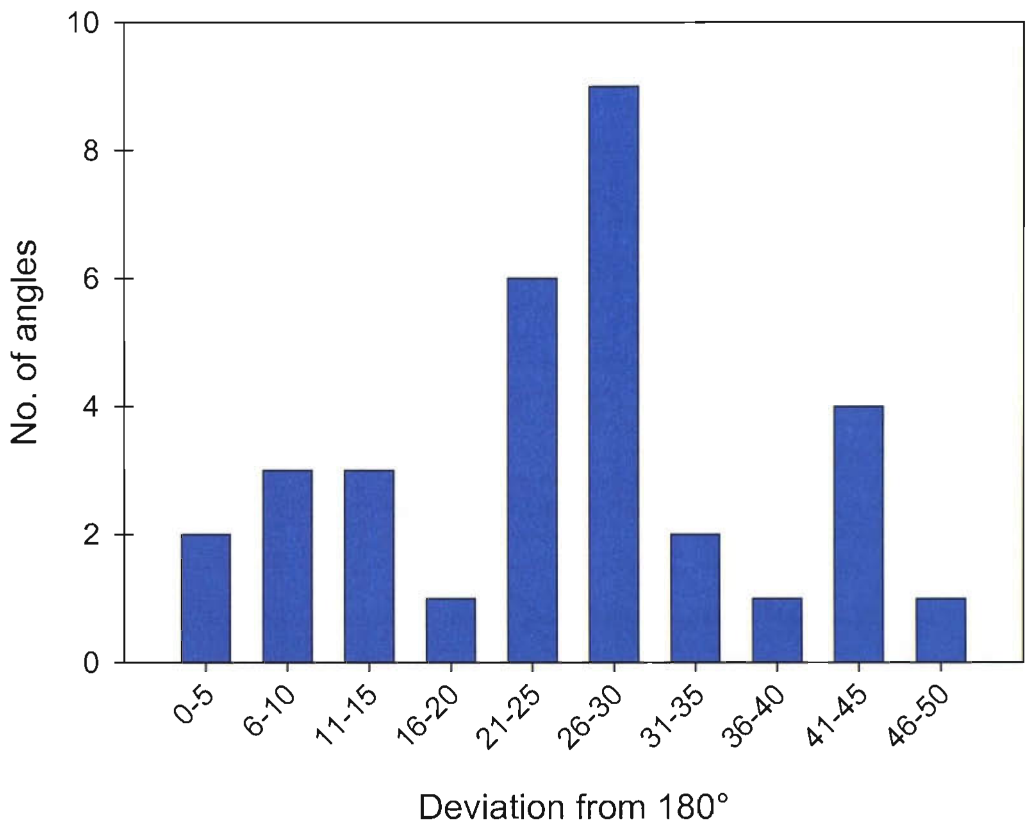

Figure 5.6.1 The variation in O'-Bi-O' bond angles for α-$Bi_2Hf_2O_7$ with respect to the value expected for an idealised pyrochlore (180 °).

The compound transforms to a tetragonal unit cell at 600 °C with smaller cell parameters of a = 7.68966(3) and c = 10.85170(8) Å, again reflecting a reduction in the degree of Bi-O' ordering. This phase has not been identified in $Bi_2Sn_2O_7$ but offers an insight into the possible mechanism of the phase change behaviour of both compounds. Figure 5.6.2 shows VT-PXRD data collected for $Bi_2Sn_2O_7$ (prepared by annealing an intimately ground mixture of Bi_2O_3 and SnO_2 at 1000 °C for 16 hours) using identical conditions to those for the $Bi_2Hf_2O_7$ sample. These data are consistent with the literature in that no intermediate tetragonal phase (analogous to the γ-phase from this work) is seen between β-$Bi_2Sn_2O_7$ and γ-$Bi_2Sn_2O_7$.

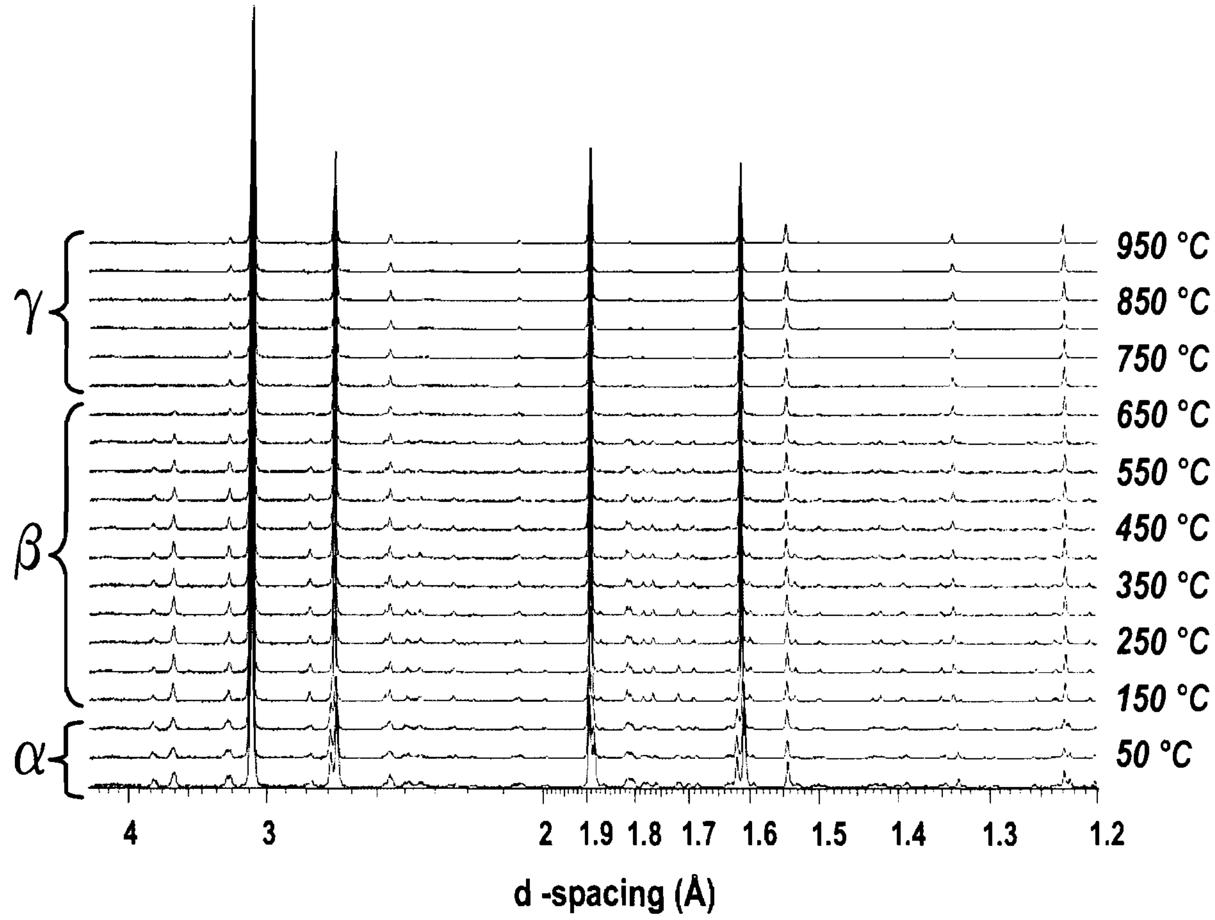

Figure 5.6.2 Variable temperature PXRD data for $Bi_2Sn_2O_7$ from 25 °C to 950 °C.

In the γ-$Bi_2Hf_2O_7$ structure hafnium is bonded to six oxygens with contacts of 2.059, 2.087 and 2.098 Å to form a distorted octahedron. The network of these HfO_6 octahedra is close to that of an ideal pyrochlore with the familiar puckered O ring, which has Hf-O-Hf bond angles of 133.7, 136.4 and 134.1 °. The scattering density of Bi is positioned toward one half of this ring, with the next bismuth ion in the Bi-O' chain being located toward the opposing half of the next O ring. This gives a Bi-O' chain which appears to follow a cork-screw formation as it oscillates in both the x and z directions. Where each of the split bismuth sites is associated with one side of the O ring there are two Bi-O contacts to the closest edge (2.318 and 2.655 Å), two to the apical oxygens (2.390 and 3.045 Å) and two to the furthest edge (2.848 and 3.132 Å) (Figure 5.6.3). The lone pair is likely to be positioned in the void created by this arrangement.

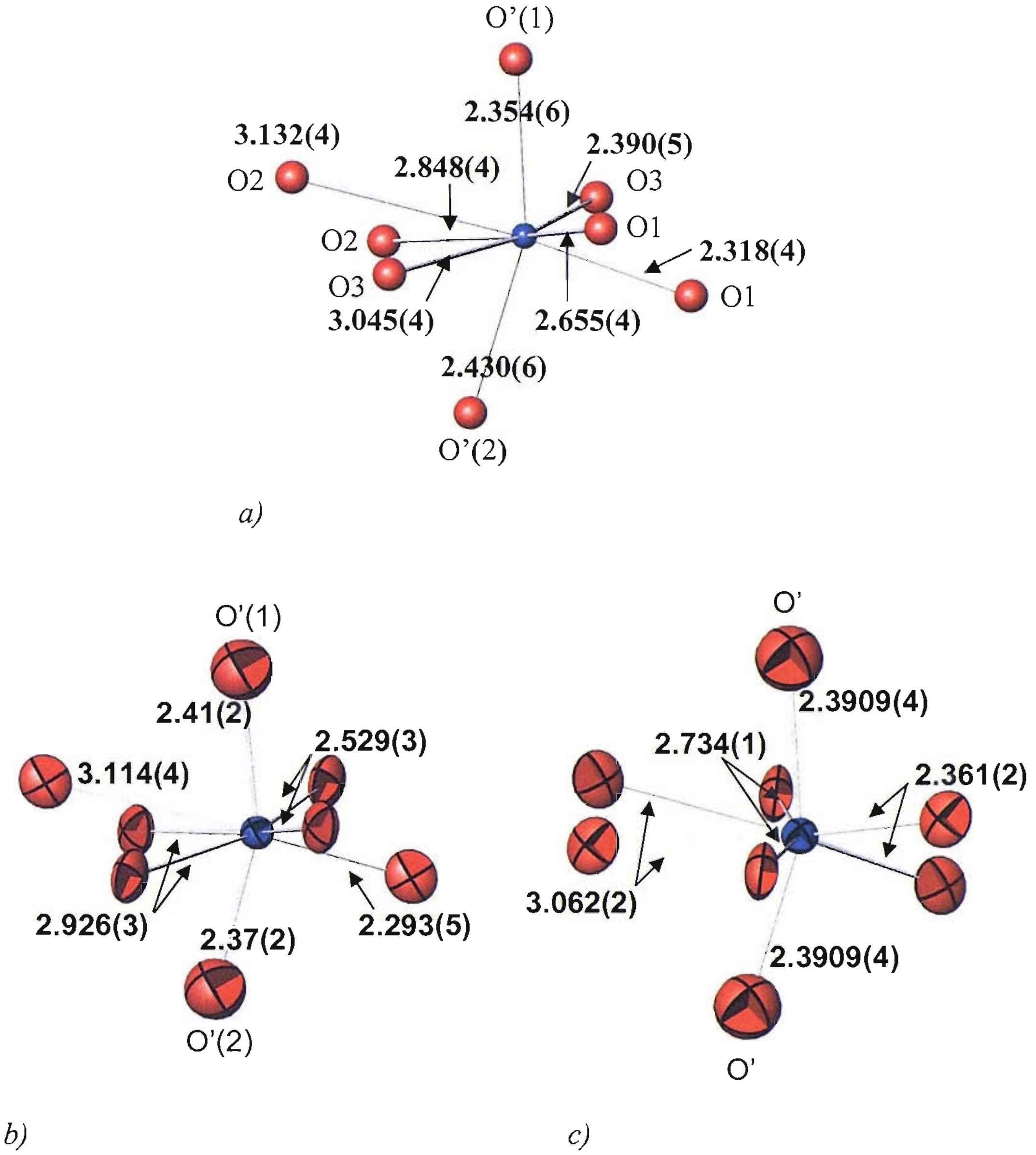

Figure 5.6.3 The coordination environment about bismuth at 600 °C (a) and 900 °C (b = model 1; c = model 2). Bi is blue and O is red; bond lengths are given in Å (estimated standard deviations in parentheses).

At 900 °C $Bi_2Hf_2O_7$ adopts a more standard cubic pyrochlore unit cell with a = 10.87791(2) Å. For both possible models the hafnium is surrounded by six O atoms on 48*f* sites (x = 0.4246). Anisotropic thermal parameters for these oxygens are consistent with local tilting of the HfO_6 octahedra giving a Hf-O-Hf bond angle of 133.8 °. The Hf-O contacts (2.091 Å) are in good agreement with those observed in $La_2Hf_2O_7$ (2.10 Å).[22] The bismuth is displaced away from the $\bar{3}m$ centre of symmetry, normally occupied by *A* cations in ideal pyrochlores, due to the sterically active lone pair. The coordination sphere of bismuth is different depending whether the 96*g* or 96*h* model is used (Figure 5.6.3). Both however result in the lone pair of electrons being directed towards a vacant site in the bismuth coordination polyhedron which may be explained by mixing of the s and p orbitals on the metal ion.[23] In the 96*g* model there is one short Bi-O contact of 2.293 Å, two of 2.529 Å, two longer contacts of 2.926 Å and one very long contact of 3.114 Å. The lone pair then is likely to lie along the direction of this longest distance. The 96*h* model has two contacts of 2.361 Å, two of 2.734 Å and two of 3.061 Å. The lone pair in this case adopts a position between the two longest Bi-O contacts. The site occupied also affects the Bi-O' bonding. The 96*g* model leads to bond lengths of 2.372 Å and 2.410 Å with a O'-Bi-O' angle of 160.09 °, whereas in the 96*h* model, all contacts are at 2.391 Å with a O'-Bi-O' angle of 160.15 °. These differences were also noted for γ-$Bi_2Sn_2O_7$ where, as in this study, it was not possible to distinguish between the two models on the basis of chemical plausibility.

The crystallographic models obtained from the neutron refinements were used to analyse the ambient and variable temperature PXRD data. Initially the background, zero point and lattice parameters were refined followed by profile coefficients and thermal parameters. The fit obtained to the data collected at ambient temperature using the Siemens D5000 is shown in Figure 5.6.4.

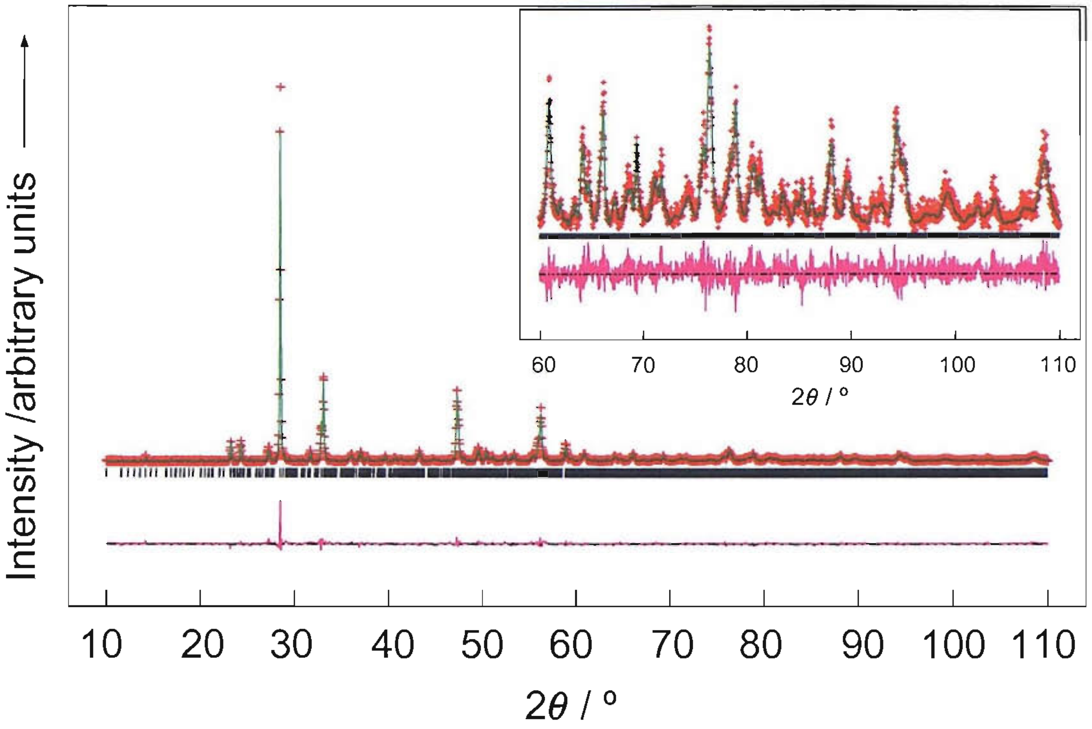

Figure 5.6.4 Final fit to the room temperature PXRD data. Crosses mark the data points, upper continuous line the calculated profile and lower continuous line the difference. (Space group Pc; χ^2 = 2.81; a = 15.3567(12) Å, b = 15.3408(13) Å, c = 21.8486(11) Å, β = 90.044(12) °).

Figure 5.6.5 shows the variation in lattice parameter with increasing temperature with the values for each phase normalised to be consistent with the room temperature unit cell. The plot demonstrates the gradual increase in both the *a* and *b* parameters accompanied by a linear decrease in the *c* parameter of α-$Bi_2Hf_2O_7$ between 25 and 350 °C. The transition to the doubled cubic cell occurs as *a* and *b* converge and the *c* value approaches $\sqrt{2}$ times that of *a* and *b* at 400 °C. The transition to the γ phase is seen as a drop in the *c* parameter at 500 °C while the *a* value continues to increase. The lattice parameters increase until *c* again becomes equal to $\sqrt{2}\times a$ at 900 °C and the structure adopts a cubic cell.

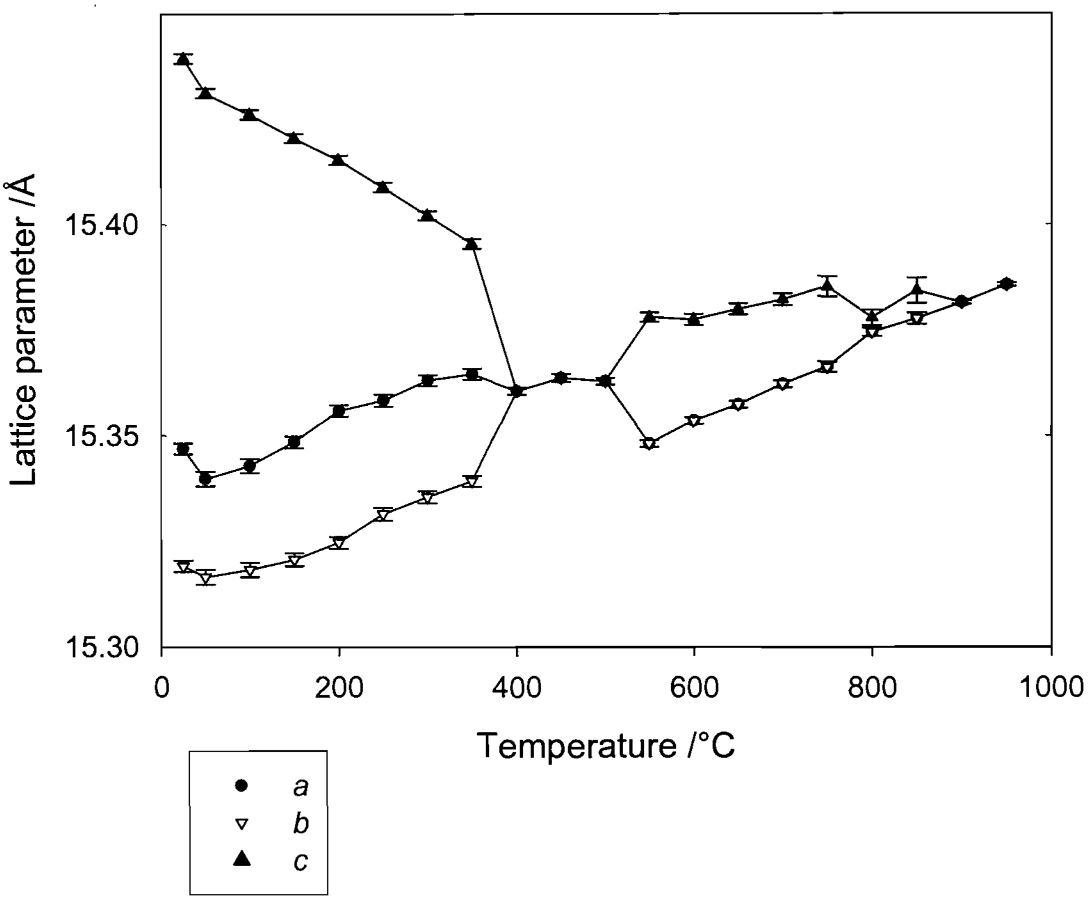

Figure 5.6.5 Variation in lattice parameter from VT-PXRD (Values normalised to be consistent with a parameter of room temperature phase).

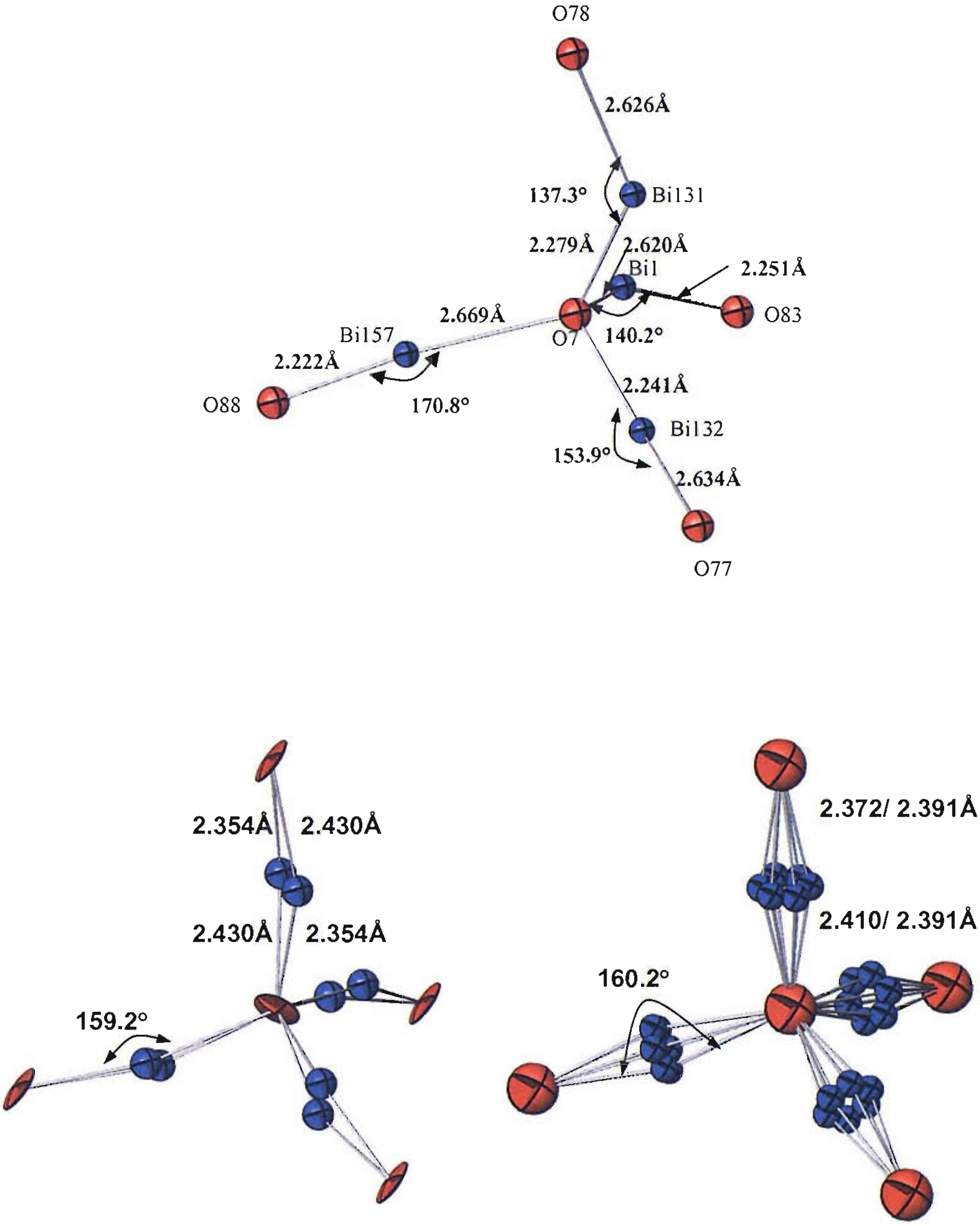

Figure 5.6.6 The coordination environment about O' at 22 °C (top), 600 °C (left) and 900 °C (right). Bi is in blue and O' is in red.

The most interesting feature for comparison between each of the phases is that of the Bi-O' network. Figure 5.6.6 shows the variation in coordination environment about O'. At room temperature the bismuth and oxygen adopt specific sites resulting in a variety of bond lengths and angles but always with one long and one short contact from Bi to O'. In the γ-phase displacements again result in a distortion of the O'-O' tetrahedron. The distortion is however less ordered than that of the α-phase, due to the increasing thermal energy of the system. In this case each of the twofold bismuth sites has bonds of 2.354 and 2.430 Å to O'. Thus the overall bismuth scattering density occupies a position approximately equidistant from the neighbouring oxygens. The accommodation of the bismuth lone pair leads to a O'-Bi-O' angle of 159.2 °. At 900 °C the dynamic displacement of the bismuth to form a ring of scattering density allows the lone pair to be accommodated whilst maintaining a tetrahedral geometry in the O'-O' network. The O'-Bi-O' angle of 160.2 ° to each individual site is close to that of the γ-phase, but is 180 ° if taken through the centre of scattering density. These changes represent the gradual increase in symmetry and disorder with increasing temperature.

The changes in the Bi-O' sublattice are accommodated by more subtle variations in the Hf-O network. The corner-sharing HfO_6 octahedra become less distorted with increasing temperature as the atoms move to increasingly higher symmetry positions (Figure 5.6.7). At room temperature the Hf and O adopt specific sites leading to a variety of bond lengths and angles (Hf-O-Hf = 120.0 – 145.6 °). In the γ-phase the three oxygen sites result in Hf-O-Hf angles of 133.7, 136.4 and 134.1 ° while at 900 °C the value is 133.8 °. Despite these changes the average of the Hf-O-Hf bond angles remains reasonably consistent; 134.0 ° at 22 °C, 134.7 ° at 600 °C and 133.8 ° at 900 °C. This reflects the flexibility afforded by the HfO_6 network to accommodate the stereochemically active bismuth lone pair whilst retaining the pyrochlore structure. It is interesting to note that the zirconium analogue, $Bi_2Zr_2O_7$, is not known.[17] In this case the larger Zr^{4+} (Sn = 69 pm , Hf = 71 pm and Zr = 72 pm)[24] ion may be unable to maintain the coordination environment required to stabilise the pyrochlore structure.

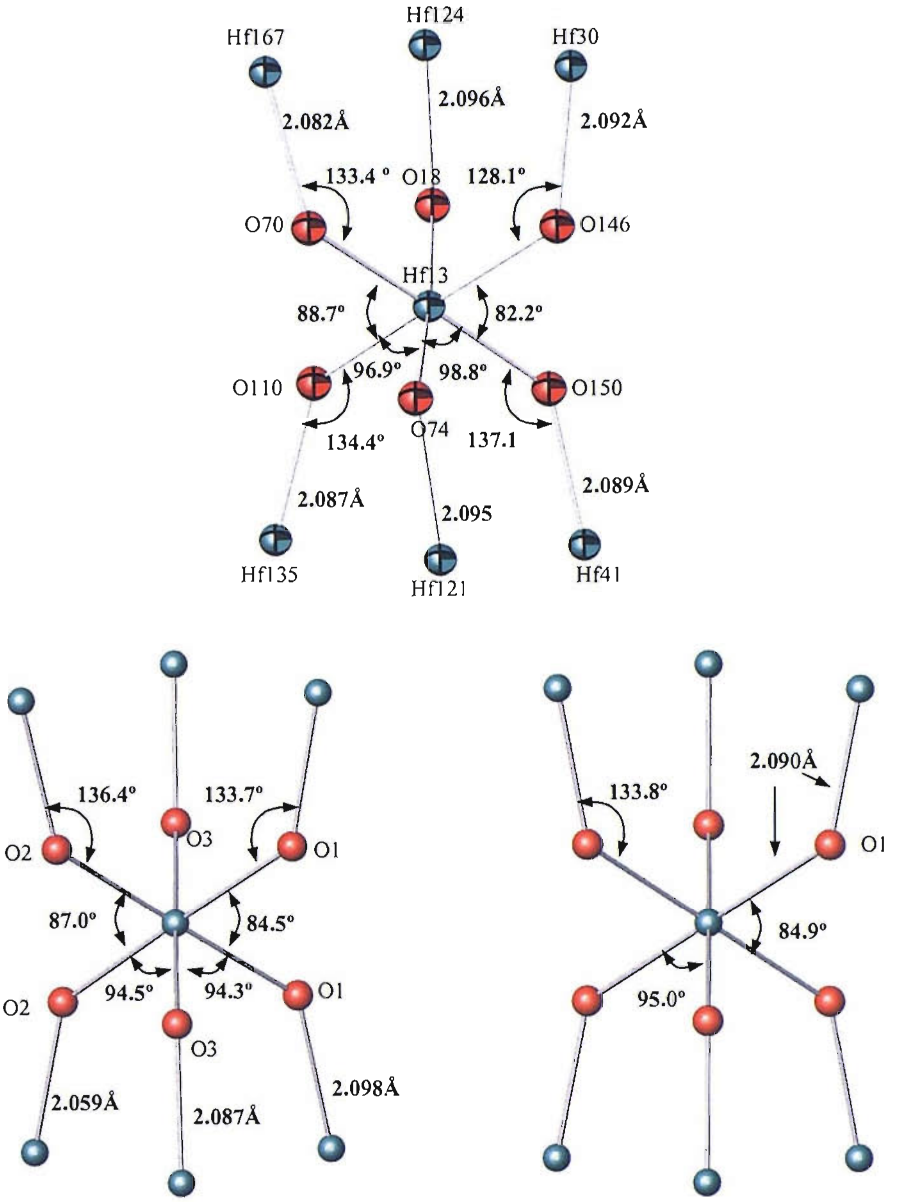

Figure 5.6.7 The coordination environment about hafnium at 22 °C (top; Hf13), 600 °C (left) and 900 °C (right). Hf is green and O is red.

5.7 Conclusions

The structural behaviour of the pyrochlore $Bi_2Hf_2O_7$ with varying temperature has been determined by powder neutron and X-ray diffraction. The unit cell transforms from monoclinic (a = 15.3536(4) Å, b = 15.3320(4) Å, c = 21.8253(3) Å and β = 90.051(5)°) at room temperature to cubic (a = 21.7326(18) Å) at 400 °C then to tetragonal (a = 7.68964(3), c = 10.85171(9) Å) at 550 °C and finally to cubic (a = 10.87791(2) Å) at 900 °C. The transformations represent a gradual increase in disorder and symmetry with temperature. The driving force for these changes is the need to accommodate the active bismuth lone pair. The structural variation of the Bi_2O' and HfO_6 sublattices have been described and compared with the behaviour of $Bi_2Sn_2O_7$.

5.8 References

[1] M. A. Subramanian, G. Aravamudan and G. V. Subba Rao, *Prog. Solid State Chem.* **15** 55 (1983).

[2] M. Avdeev, M. K. Haas, J. D. Jorgensen and R. J. Cava, *J. Solid State Chem.* **169** 24 (2002).

[3] T. Birchall and A. W. Sleight, *J. Solid State Chem.* **13** 118 (1975)

[4] J. C. Nino, M. T. Lanagan, C. A. Randall and S. Kamba, Appl. *Phys. Lett.* **81** 4404 (2002).

[5] I. Levin, T. G. Amos, J. C. Nino, T. A. Vanderah, C. A. Randall and M. T. Lanagan, *J. Solid State Chem.* **168** 69 (2002).

[6] J. Lu and S. Stremmer, *Appl. Phys. Lett.* **83** 2411 (2003).

[7] J. Lu, D. O. Klenov and S. Stremmer, *Appl. Phys. Lett.* **84** 957 (2004).

[8] I. Radosavljevic, J. S. O. Evans and A. W. Sleight, *J. Solid State Chem.* **136**, 63 (1998).

[9] A. L. Hector and S. B. Wiggin, *J. Solid State Chem.* **177** 139 (2004).

[10] B. J. Kennedy, Ismunandar and M. M. Elcombe, *Mater. Sci. Forum* **278** 762 (1998).

[11] R. D. Shannon, J. D. Bierlein, J. L. Gillson, G. A. Jones and A. W. Sleight, *J. Phys. Chem. Solids* **41** 117 (1980).

[12] R. H. Jones, K. S. Knight, J. *Chem. Soc. Dalton Trans.* 2551 (1997).

[13] J. D. Bernal and R. H. Fowler, *J. Chem. Phys.* **1** 515 (1933).

[14] L. Pauling, *J. Am. Chem. Soc.* **57** 2680 (1935).

[15] R. Seshadri, *Los Alamos National Laboratory, Preprint Archive, Condensed Matter* **arXiv:cond-mat/0507634** 1 (2005).

[16] I. Radosavljevic Evans, J. A. K. Howard and J. S. O. Evans, *J. Mater. Chem.* **13** 2098 (2003).

[17] S. L. Sorokina and A. W. Sleight, *Mater. Res. Bull.* **33** 1077 (1998).

[18] C. Favotto, M. Mansori and L.Tortet, *Ann. Chem. Sci. Mat.* **26** 71 (2001).

[19] R. B. Von Dreele and A. C. Larson, GSAS general structure analysis system, Neutron Scattering Centre, MS-H805, Los Alamos National Laboratory, NM (2004).

[20] J. I. Yamaura and Z. Hiroi, *J. Phys. Soc. Jpn.* **71** 2598 (2002).

[21] R. E. Hann, P. R. Suitch and J. L. Pentecost, *Phase Transition* **38** 127 (1992).

[22] A.W. Sleight, *Inorg. Chem.* **7** 1704 (1968).

[23] L. E. Orgel, *J. Chem. Soc.* 3815 (1959).

[24] R. D Shannon, *Acta. Cryst.* **A32** 751 (1976).

Chapter 6

Synthesis, Structure and Physical Properties of the Pyrochlore Series, $Bi_2Hf_{2-x}Ti_xO_7$.

6.1 Introduction

Dielectric ceramics are widely used in microelectronic and microwave communication technologies.[1] Materials with high dielectric constants are particularly important in reducing the size of microelectronic circuits, where high permittivity and low dielectric loss are required for many applications.[2] Bismuth based pyrochlore compounds are attractive candidates for capacitor and high-frequency filter applications in multilayer structures co-fired with silver electrodes.[3] Ternary oxides in the Bi_2O_3-ZnO-Nb_2O_5 system have received intensive attention as they exhibit high dielectric constants (ϵ = 80-150), low dielectric losses and chemically tuneable temperature coefficients of capacitance (τ_c).[4,5] The properties of these pyrochlore type compounds are further enhanced by their low sintering temperatures (less than 950 °C).[6]

Various work has been undertaken to improve these properties further, especially enhancing permittivity and reducing dielectric loss. For example, titanium substitution of bismuth zinc niobate (BZN) resulted a significant increase in dielectric constant with increasing titanium content.[1] The dielectric constant of compounds in the $Bi_2Sn_{2-x}Ti_xO_7$ ($0 \leq x \leq 1.4$) system were also found to increase almost linearly with increasing substitution of Ti^{4+}.[7] This solid solution series was prepared from co-precipitated precursors fired at temperatures of up to 1100 °C and pressures up to 100 MPa and analysed by X-ray diffraction and Raman spectroscopy.

In light of the investigations in this, work on $Bi_2Hf_2O_7$ (Chapter 5) and previous work within the group studying $Bi_2Ti_2O_7$,[8] the logical progression was to produce a solid solution series between these pyrochlore compounds. Comparison of the dielectric properties of the series $Bi_2Hf_{2-x}Ti_xO_7$ ($0 \leq x \leq 2$) with structural and compositional variance should lead to improved understanding of the factors influencing these properties and provide potential alternatives to BZN compounds.

6.2 Synthesis

$Bi_2Hf_{2-x}Ti_xO_7$ ($0 \leq x \leq 2$) samples were prepared by co-precipitation of a basic titanium solution with an acidic bismuth/hafnium solution in the appropriate stoichiometric ratio. Titanium metal with a particle size of 250 μm was added to a mixture of hydrogen peroxide (28 %, 40 ml) and ammonia solution (35 %, 14 ml). The stirred mixture was maintained at just below room temperature using a water bath and the titanium dissolved over a period of 3–4 h, resulting in a bright yellow solution. This was added quickly to a stirred solution of bismuth nitrate pentahydrate and hafnium oxynitrate hydrate in 1.2 mol dm^{-3} HNO_3 (50 cm^3). Initially a dark orange solution formed with vigorous evolution of gas. With continued stirring a pale cream precipitate soon formed, this was stirred for 30 min to agglomerate the particles and ensure complete precipitation. After filtering and washing with dilute (10 %) ammonia the cream-coloured solid was dried at 50 °C. In order to minimise loss of bismuth through volatilisation, samples were calcined as pressed disks. These were stacked in a closed alumina crucible before firing at temperatures between 470 °C and 700 °C for 16 hrs.

6.3 Characterisation

Initial phase identification was carried out on all samples using the Siemens D5000 diffractometer. Scans were run in the range 20 - 60 ° in 2θ over a 30 minute period. Further data were collected for structural refinement in the range 10 - 110 ° in 2θ for a period of 15 hours. Data were refined using the GSAS package.[9] The samples were analysed by EDAX using a JEOL JSM-5910 with an Oxford Inca 300 detector. The compositional analysis results from area scans of each sample are shown in Table 6.3.1.

Raman spectra were obtained from pelletised samples by Dr. O. Shebanova (UCL) using a high-throughput optical system based on an Acton Research spectrometer equipped with a liquid-N_2 cooled back-illuminated silicon CCD detector (Princeton Instruments) and Kaiser® SuperNotch filters to reject the incident laser line. Raman spectra were excited by the 514.5 nm line of air-cooled Ar+ laser and collected in a backscattering geometry, using a 50x Mitutoyo objective.

Table 6.3.1 Elemental analysis results for the $Bi_2Hf_{2-x}Ti_xO_7$ series (atomic %).

x value	Bismuth		Hafnium		Titanium	
	expected	recorded	expected	recorded	expected	recorded
0	50	49.51	50	50.49	0	0.00
0.2	50	49.86	45	45.37	5	4.76
0.4	50	49.21	40	40.19	10	10.61
0.6	50	49.71	35	34.71	15	15.58
0.8*	50	-	30	-	20	-
1	50	49.20	25	25.11	25	25.69
1.2	50	48.97	20	18.81	30	32.22
1.4	50	47.85	15	16.28	35	35.87
1.6	50	49.21	10	10.27	40	40.51
1.8	50	50.26	5	5.32	45	44.42
2.0	50	48.98	0	0.00	50	51.02

* Data not available

6.4 Results and Discussion

6.4.1 X-ray Diffraction Data

Pyrochlore bismuth hafnate undergoes three phase transitions between room temperature and 950 °C. These polymorphs (described in Chapter 5) represent a gradual increase in disorder and symmetry with temperature. Phase identification of the $Bi_2Hf_{2-x}Ti_xO_7$ ($0 \leq x \leq 2$) series revealed that this trend also occurred with compositional variation. As the titanium content is increased the structure changes from a large monoclinic cell to a tetragonal phase and finally to a cubic unit cell

(Table 6.4.1). These phases are directly analogous to the α, γ and δ polymorphs of $Bi_2Hf_2O_7$. It is interesting to note that the temperature at which these phases crystallise also varies with composition. Bismuth titanate has previously been shown to form only at 470 °C,[8] while bismuth hafnate can be prepared between 700 and 875 °C (Section 5.2). The synthesis temperature for the intermediate phases decreases as the titanium content increases. Samples with higher hafnium (x = 0 - 1.6) content were prepared at their minimum temperature (700 °C) to avoid discrepancies in analysis due to particle size effects.

From inspection of both the short and longer PXD scans it was not clear whether the samples $0.8 \leq x \leq 1.8$ crystallised with a tetragonal or cubic unit cell. Differentiation between the two models was further complicated by the broad reflections obtained as a result of the low temperature synthesis. To differentiate between these two possibilities detailed scans over the range 32-52 ° in 2θ were collected to confirm the presence of the cluster of reflections (114), (222), and (310). No equivalent reflection is allowed by the cubic pyrochlore model therefore the presence of intensity in this region infers that the tetragonal model is required (Figure 6.4.1). These scans confirmed that all the ambiguous samples do crystallise with tetragonal symmetry. Table 6.4.1 shows the phase identification for the samples in the series.

This structural trend was not seen in the study of $Bi_2Sn_{2-x}Ti_xO_7$ ($0 \leq x \leq 1.4$).[7] However, it must be noted that accurate structures of $Bi_2Sn_2O_7$[10] and $Bi_2Ti_2O_7$[8] were not known at the time of publication and the synthesis methods involved high temperature and pressure. Instead a transition from the α-$Bi_2Sn_2O_7$ structure (described as tetragonal) to the large cubic cell β-$Bi_2Sn_2O_7$ phase was observed at x = 0.6. Further investigation of the Sn-Ti system using lower temperature, chloride free synthesis methods may provide a closer comparison to the Hf-Ti system in this work.

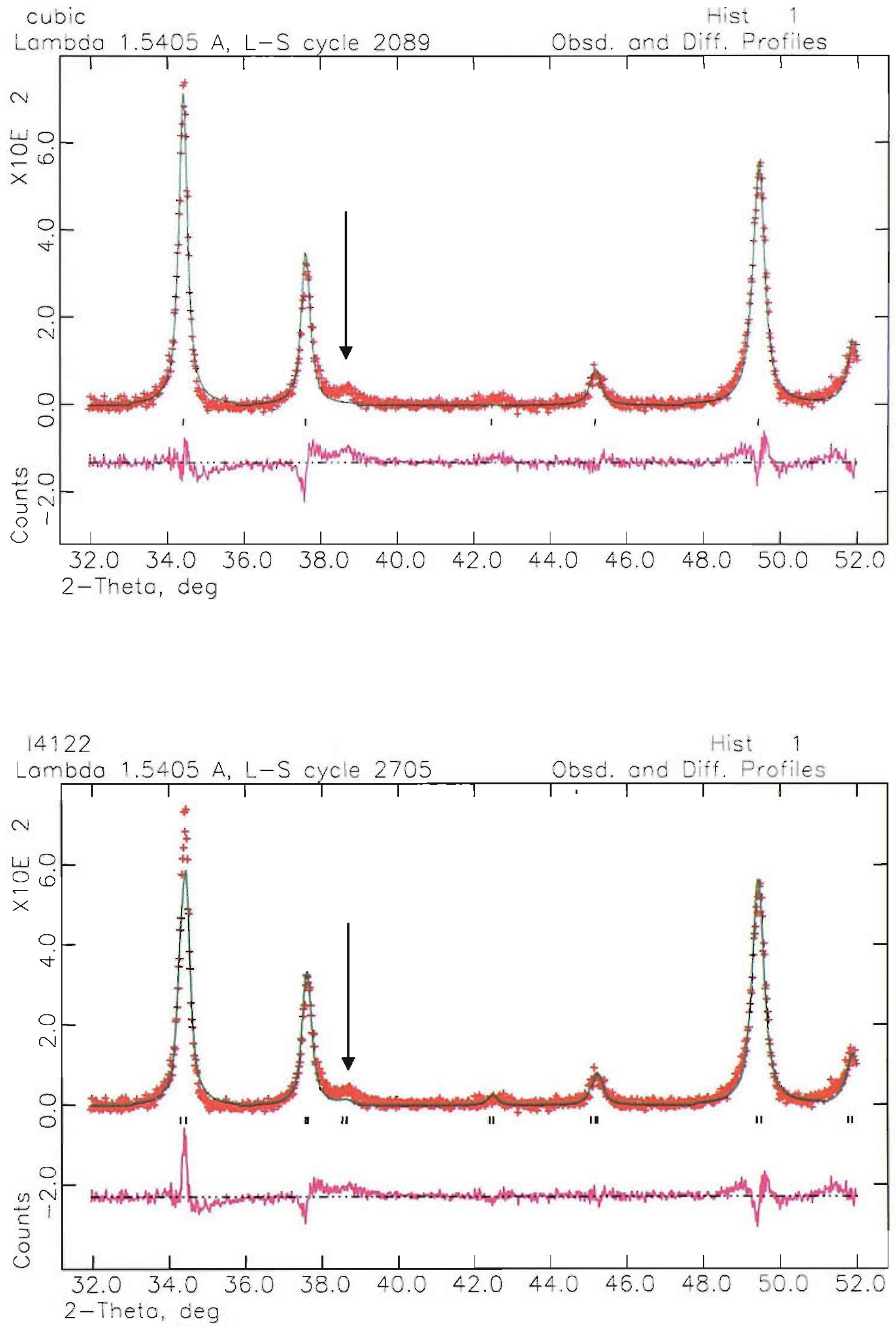

Figure 6.4.1 PXD data for $Bi_2Hf_{0.2}Ti_{1.8}O_7$ refined using the cubic (top) and tetragonal (bottom) pyrochlore models. The arrow indicates the position of the overlapping (114), (222), and (310) reflections.

Table 6.4.1 Phase identification of samples in the in the $Bi_2Hf_{2\text{-}x}Ti_xO_7$ series.

x value	Synthesis temperature / °C	Cell symmetry	Polymorph of $Bi_2Hf_2O_7$
0	700	monoclinic	α
0.2	700	monoclinic	α
0.4	700	monoclinic	α
0.6	600	tetragonal	γ
0.8	600	tetragonal	γ
1	600	tetragonal	γ
1.2	600	tetragonal	γ
1.4	600	tetragonal	γ
1.6	550	tetragonal	γ
1.8	500	tetragonal	γ
2.0	470	cubic	δ

Full Rietveld refinements were undertaken for each sample using the GSAS[9] suite of programs. The refined structures obtained from the variable temperature PND study of $Bi_2Hf_2O_7$ (Chapter 5) were used as starting models for the appropriate phases. A uniform approach to the structure refinement was undertaken for each of the data sets in turn to ensure consistent results. Each data set was refined using a shifted Chebyschev background function (GSAS type 1) with twelve terms. Zero point, cell parameters, peak shape profile and isotropic thermal parameters were sequentially added to the refinement. Atomic positions were varied where appropriate. Thermal parameters were constrained to be equal for the Ti/Hf sites and the oxygen sites were set at U_{iso} = 0.025 Å due to their poor scattering of X-rays. The refinements converged smoothly to give good fits to the data and acceptable *R*-factors. Accurate cell parameters were determined for each composition from the refinement along with derived bond lengths and bond angles, which can be found in Tables 6.4.2 and 6.4.3. Examples of the fits for each structure type are shown in Figure 6.4.2.

Table 6.4.2 Refined structural parameters for $Bi_2Hf_{2-x}Ti_xO_7$ ($0 \le x \le 2$) series (estimated standard deviations in parentheses).

x	Space group	χ^2	*a* (Å)	*b* (Å)	*c* (Å)	β (°)	Molar volume (Å^3)
0	*Pc*	4.51	15.357(1)	15.341(1)	21.849(1)	90.04(1)	643.4(1)
0.2	*Pc*	2.52	15.283(2)	15.255(2)	21.681(2)	90.03(2)	631.9(1)
0.4	*Pc*	3.43	15.191(3)	15.159(3)	21.560(4)	89.72(1)	620.3(2)
0.6	$I4_122$	1.96	7.5487(7)	7.5487(7)	10.716(2)	90	610.6(1)
0.8	$I4_122$	1.20	7.473(2)	7.473(2)	10.622(6)	90	593.2(4)
1	$I4_122$	1.22	7.469(2)	7.469(2)	10.606(4)	90	591.6(3)
1.2	$I4_122$	1.40	7.434(2)	7.434(2)	10.577(4)	90	584.5(3)
1.4	$I4_122$	1.37	7.422(1)	7.422(1)	10.558(3)	90	581.6(2)
1.6	$I4_122$	3.54	7.3897(9)	7.3897(9)	10.532(2)	90	575.1(2)
1.8	$I4_122$	2.18	7.3555(6)	7.3555(6)	10.446(1)	90	565.2(1)
2.0	$Fd\bar{3}m$	1.52	10.382(1)	10.382(1)	10.382(1)	90	559.5(2)

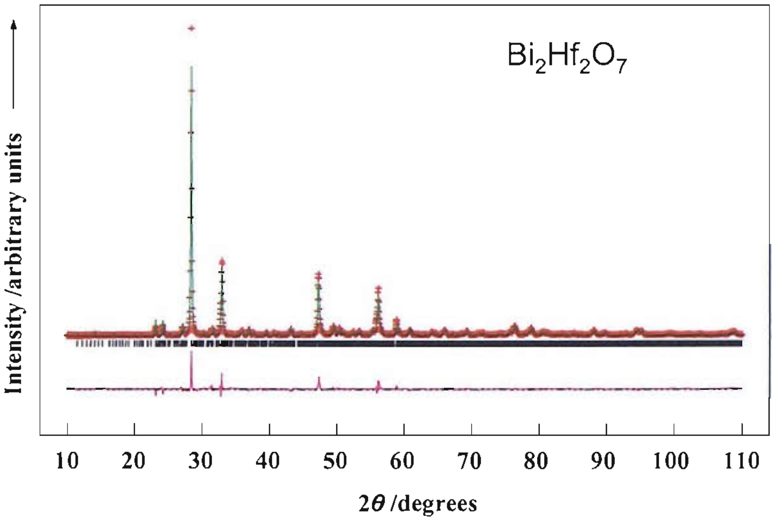

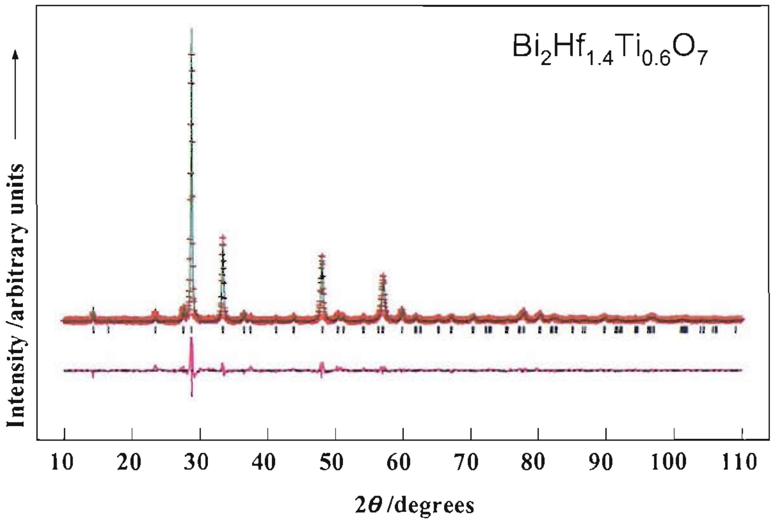

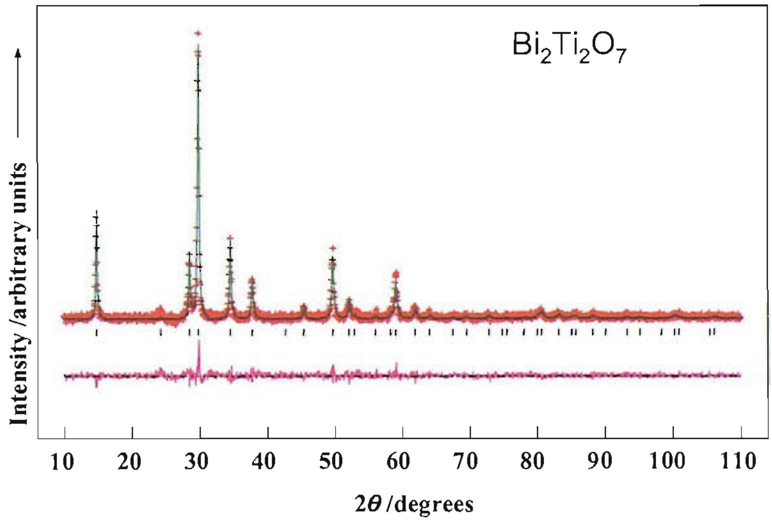

Figure 6.4.2 Final fits to the data for selected samples showing the three different structures. Crosses mark the data points, upper continuous line the calculated profile and lower continuous line the difference. Tick marks show the reflection positions.

Table 6.4.3 Selected bond distances (Å) for the $Bi_2Hf_{2-x}Ti_xO_7$ ($0 \le x \le 2$) series (estimated standard deviations in parentheses).

x	Bi-O’ i)	Bi-O’ ii)	Hf/Ti-O
0	*(Avg.)* 2.6323 *(Min.)* 2.5715(4) *(Max.)*2.6807(3)	2.2472 2.2016(3) 2.2924(3)	2.0952 2.0709(4) 2.1121(4)
0.2	*(Avg.)* 2.6147 *(Min.)* 2.5552(3) *(Max.)* 2.6631(3)	2.2261 2.1838(3) 2.2733(3)	2.0792 2.0621(3) 2.0958(3)
0.4	*(Avg.)* 2.5994 *(Min.)* 2.5448(4) *(Max.)* 2.6427(3)	2.2124 2.1697(3) 2.2599(3)	2.0667 2.0468(3) 2.0871(3)
0.6	2.42(1)	2.29(1)	(-*O1*) 1.979(3) (-*O2*) 2.109(4) (-*O3*) 2.0493(3)
0.8	2.368(6)	2.254(6)	(-*O1*) 2.052(6) (-*O2*) 1.995(6) (-*O3*) 2.0281(5)
1	2.42(2)	2.22(2)	(-*O1*) 1.984(7) (-*O2*) 2.060(7) (-*O3*) 2.0266(5)
1.2	2.39(2)	2.22(3)	(-*O1*) 2.03(2) (-*O2*) 1.99(2) (-*O3*) 2.0174(6)
1.4	2.42(2)	2.20(2)	(-*O1*) 2.04(2) (-*O2*) 1.96(2) (-*O3*) 2.013(1)
1.6	2.38(1)	2.23(1)	(-*O1*) 1.960(7) (-*O2*) 2.047(8) (-*O3*) 2.0064(3)
1.8	2.37(1)	2.21(1)	(-*O1*) 1.915(8) (-*O2*) 2.070(9) (-*O3*) 1.9978(6)
2.0	2.294(1)	-	1.950(5)

Table 6.4.3 Selected bond angles (°) for the $Bi_2Hf_{2-x}Ti_xO_7$ ($0 \le x \le 2$) series (estimated standard deviations in parentheses).

x	O'-Bi-O'	(Hf/Ti)-O-(Hf/Ti)
0	*(Avg.)* 154.69 *(Min.)* 132.7(2) *(Max.)* 177.3(3)	134.037 120.320(2) 145.580(2)
0.2	*(Avg.)* 154.68 *(Min.)* 132.5(2) *(Max.)* 177.4(2)	134.0369 120.088(2) 145.605(2)
0.4	*(Avg.)* 154.7 *(Min.)* 132.9(2) *(Max.)* 177.3(2)	134.0379 120.173(2) 145.580(2)
0.6	158.7(2)	(-*O1*-) 138.5(1) (-*O2*-) 132.7(1) (-*O3*-) 134.365(8)
0.8	165.4(1)	(-*O1*-) 135.05(1) (-*O2*-) 136.03(1) (-*O3*-) 134.29(2)
1	160.9(4)	(-*O1*-) 137.5(3) (-*O2*-) 133.6(2) (-*O3*-) 134.33(2)
1.2	162.8(6)	(-*O1*-) 135.6(7) (-*O2*-) 135.5(7) (-*O3*-) 134.24(2)
1.4	160.3(3)	(-*O1*-)137.4(3) (-*O2*-) 133.8(3) (-*O3*-)134.25(2)
1.6	159.7(2)	(-*O1*-) 137.8(3) (-*O2*-)133.5(3) (-*O3*-)134.18(1)
1.8	159.5(2)	(-*O1*-) 139.1(4) (-*O2*-) 132.3(3) (-*O3*-) 134.37(2)
2.0	156.9(2)	140.5(8)

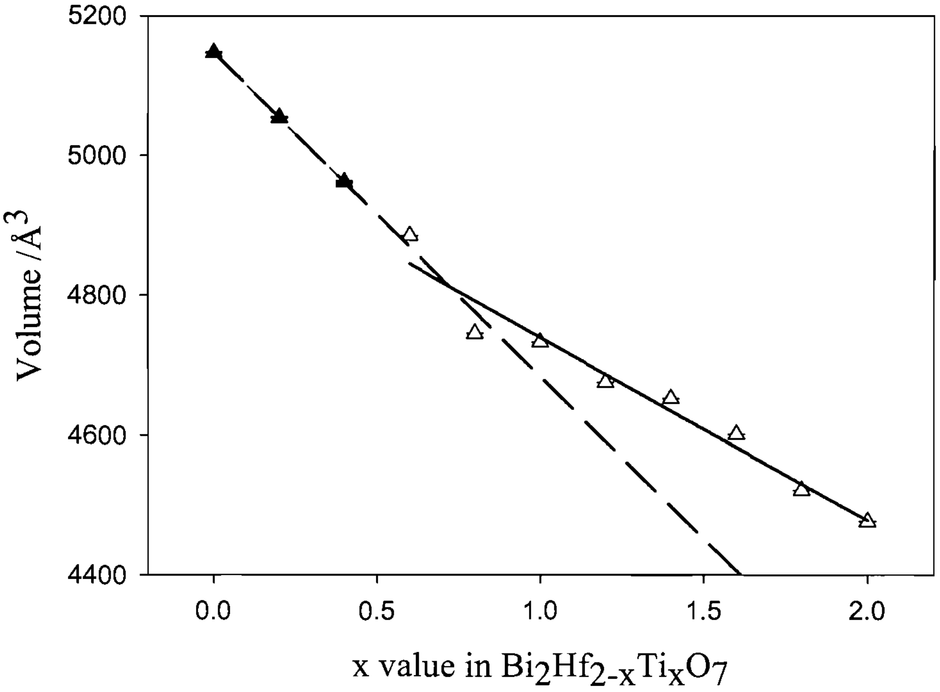

Figure 6.4.3 Cell volumes for the $Bi_2Hf_{2-x}Ti_xO_7$ series, normalised to α-$Bi_2Hf_2O_7$ for clarity. Black triangles = monoclinic phase; white triangles = tetragonal phase. (Error bars within point size).

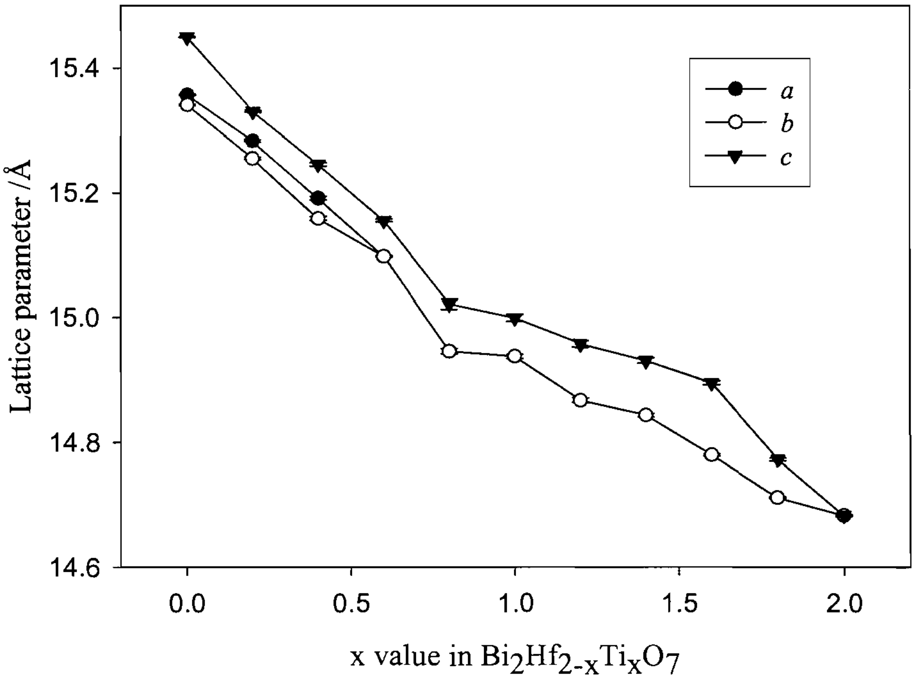

Figure 6.4.4 Variation of the lattice parameters for the $Bi_2Hf_{2-x}Ti_xO_7$ series. Lengths are normalised to the a parameter of α-$Bi_2Hf_2O_7$. (Error bars within point size).

The incorporation of titanium into the hafnium sub-lattice leads to a unit cell contraction (where the values are normalised to those of α-$Bi_2Hf_2O_7$). This is explained by simple steric considerations in view of the smaller ionic size of Ti^{4+} (60.5 pm) compared to Hf^{4+} (71 pm).[11] This can be observed by viewing plots of the normalised cell volume as a function of composition (Figure 6.4.3).

Figure 6.4.4 shows the variation in lattice parameter with composition, again normalised to be consistent with the α-$Bi_2Hf_2O_7$ unit cell. The plot demonstrates the gradual decrease in the *a*, *b* and *c* lattice parameters from x = 0 to 0.4. The transition to a tetragonal cell occurs as *a* and *b* converge at x = 0.6. The *a* and *c* parameters continue to decrease concurrently up to the x = 1.8 sample. The values then converge again at the transition to cubic $Bi_2Ti_2O_7$.

The most interesting feature of these pyrochlore systems is the Bi-O' sub-network. Figure 6.4.5 shows the variation in Bi-O' bond length with composition. The graph depicts a gradual convergence of the long and short Bi-O' contacts with increasing titanium content. This occurs as the decrease in cell volume leads to increasing disorder about the bismuth site in order to accommodate the lone pair of electrons. The Hf/Ti-O contacts decrease in length as expected as the level of substitution of the smaller Ti^{4+} cation increases (Figure 6.4.6).

Figure 6.4.7 demonstrates the variation in the Bi-O' network in relation to the network of HfO_6 octahedra. In the phases with a monoclinic structure the bismuth and oxygen adopt specific sites resulting in a variety of bond lengths and angles but always with one long and one short contact from Bi to O'. In the tetragonal phases, displacements again result in a distortion of the O'-O' tetrahedron. The distortion is however less ordered than that of the monoclinic phase. In this case each of the twofold bismuth sites has one longer and one shorter bond to O'. Thus the overall bismuth scattering density occupies a position approximately equidistant from the neighbouring oxygens. In the cubic $Bi_2Ti_2O_7$ the displacement of the bismuth to form a ring of scattering density allows the lone pair to be accommodated whilst maintaining a tetrahedral geometry in the O'-O' network. The O'-Bi-O' angle of 156.9 ° to each individual site is close to that of the tetragonal phase, but is 180 ° if taken through the centre of scattering density. These changes represent the gradual increase in symmetry and disorder with decreasing cell volume. The changes in the Bi-O' sublattice are accommodated by more subtle variations in the Hf/Ti-O network. The corner-sharing Hf/TiO$_6$ octahedra become less distorted with increasing titanium content as the atoms adopt increasingly higher symmetry positions.

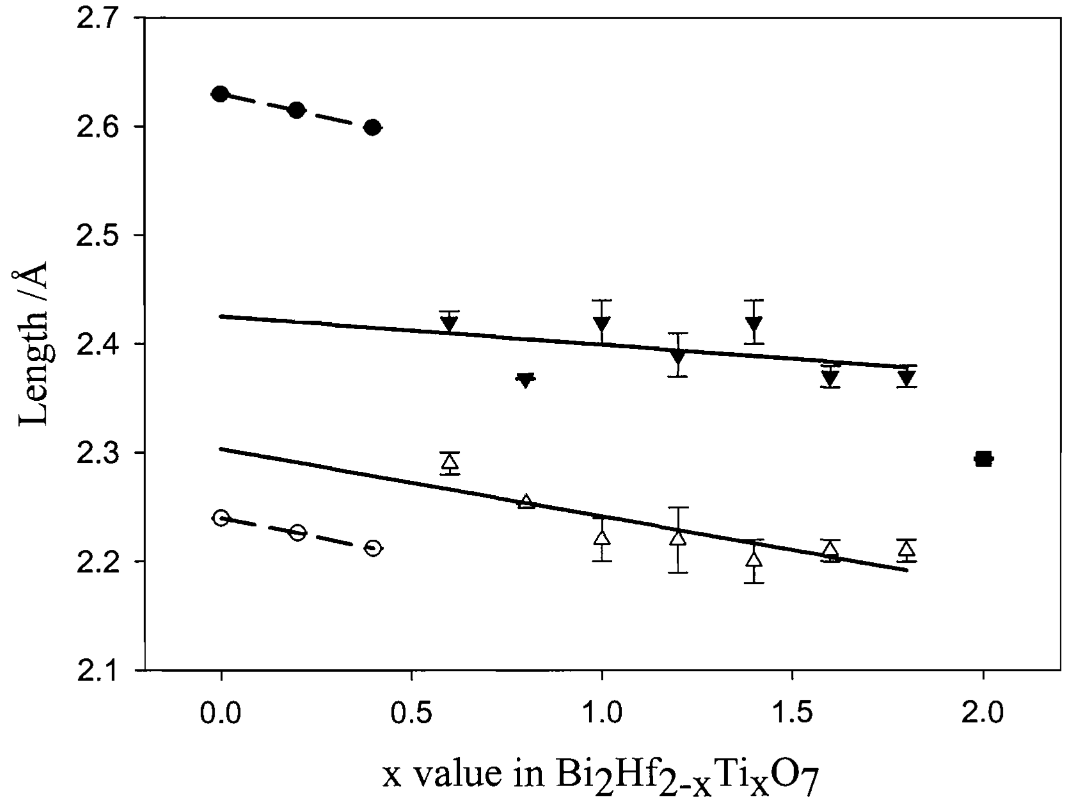

Figure 6.4.5 Variation of the Bi-O' bond lengths for the $Bi_2Hf_{2-x}Ti_xO_7$ series. Black symbols represent Bi-O'(i); white symbols Bi-O'(ii). (Average values are shown for $x = 0 - 0.4$).

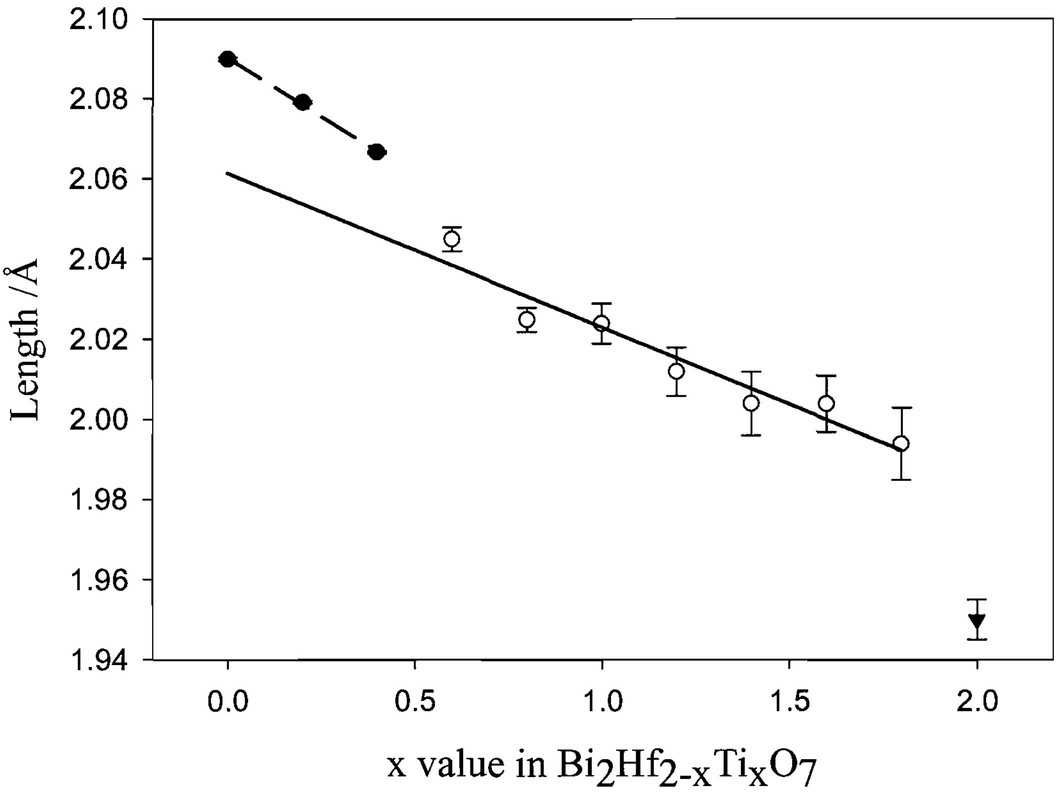

Figure 6.4.6 Variation of the average Hf/Ti-O bond lengths for $Bi_2Hf_{2-x}Ti_xO_7$. Black circles = α-phase, white circles = γ-phase and black triangles = δ-phase.

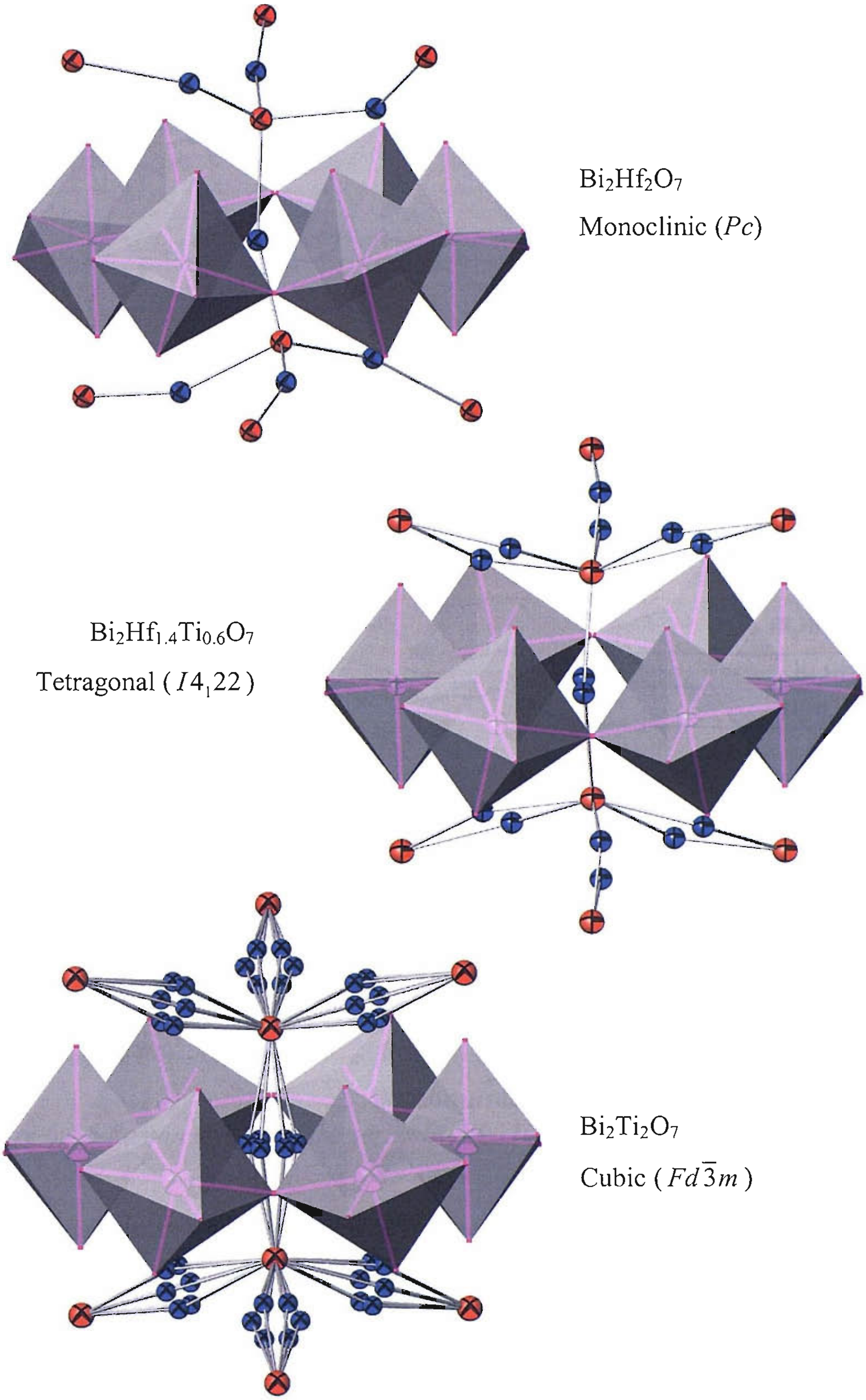

Figure 6.4.7 Schematic structures showing the relationship between the varying Bi (blue) -O' (red) network and the puckered ring created by the HfO_6 octahdra (grey).

6.4.2 Raman Spectroscopy

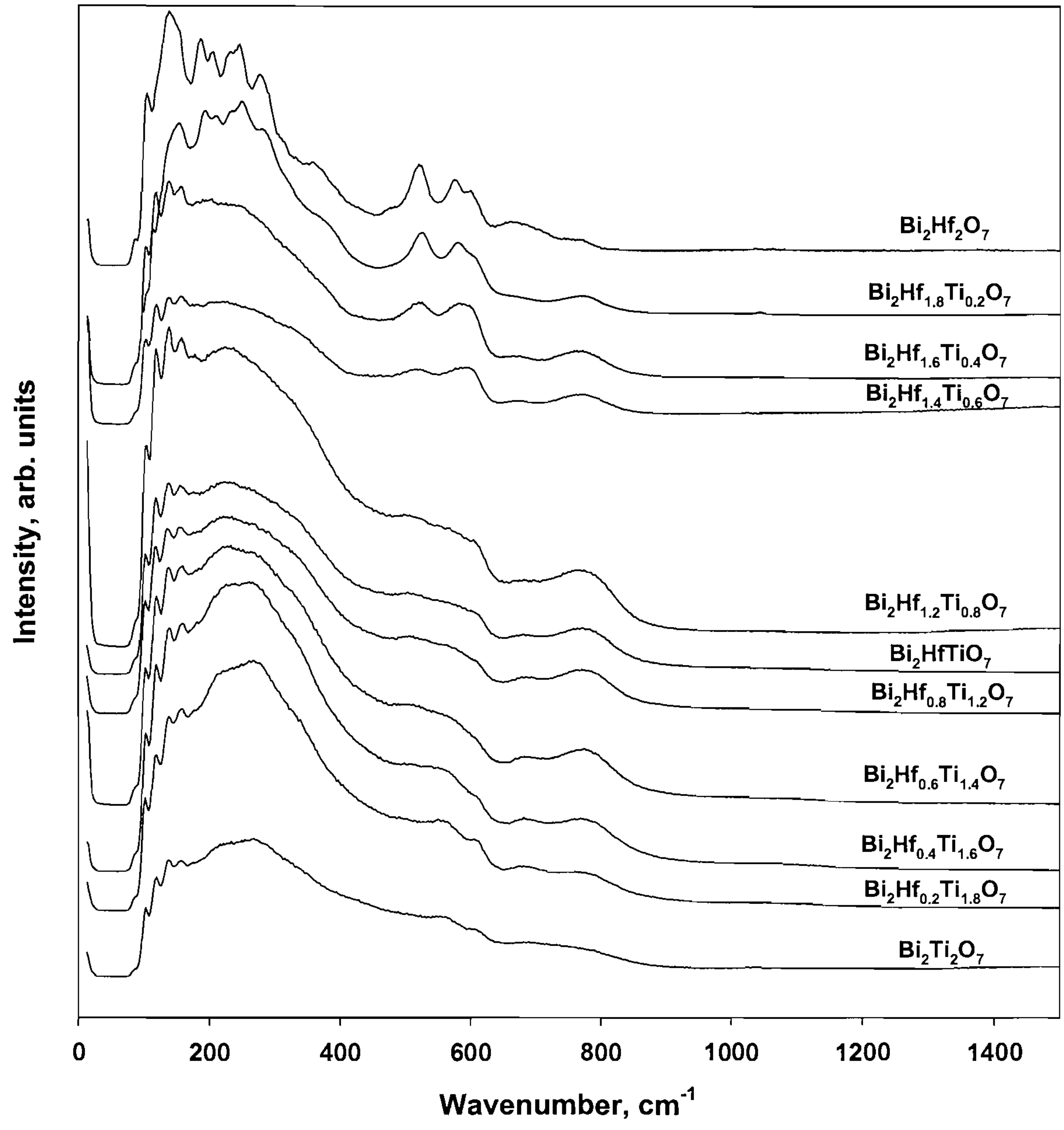

Figure 6.4.8 Raman spectra of the series $Bi_2Hf_{2-x}Ti_xO_7$.

The Raman spectra for the solid solution series display features in the region 90-800 cm^{-1} (Figure 6.4.8), comparable to those reported for the tin-titanium analogues.[7] It is clear that the number of discrete peaks decreases with increasing titanium content. This is consistent with a decrease in crystal symmetry and supports the findings of the diffraction experiments. Variable temperature Raman experiments for $Bi_2Hf_2O_7$ and $Bi_2Sn_2O_7$ would be of interest for comparison to the spectra reported here. These are in progress but the results were not available at the time of writing.

6.5 Conclusions

A series of compounds with the formula $Bi_2Hf_{2-x}Ti_xO_7$ ($0 \leq x \leq 2$) have been prepared from co-precipitated precursors. The compounds were shown to follow a variation in structure with composition similar to that seen with variable temperature studies of $Bi_2Hf_2O_7$, as described in Chapter 5. The monoclinic α-$Bi_2Hf_2O_7$ structure is adopted by samples in the range $0 \leq x \leq 0.4$, those in the range $0.6 \leq x \leq 1.8$ crystallise in the tetragonal γ-$Bi_2Hf_2O_7$ structure, while $Bi_2Ti_2O_7$ is isostructural to cubic δ-$Bi_2Hf_2O_7$. The transformations represent a gradual increase in disorder and symmetry with increasing titanium content. This is driven by the need to accommodate the active bismuth lone pair within the decreasing channel size created by the Hf/TiO_6 sub-network. This decrease in structural symmetry is also supported by Raman spectroscopy which shows a gradual decrease in the number of peaks with increasing Ti^{4+} content.

Results from dielectric measurements of the samples in this series were unavailable at the time of writing but will be reported at a later date. However, it can be expected that the dielectric constant increases with increasing titanium content as in the Sn-Ti series.[7]

Further work in this area may include similar structural and physical property studies of other bismuth pyrochlore series, such as $Bi_2Hf_{2-x}Zr_xO_7$, $Bi_2Sn_{2-x}Zr_xO_7$ or $Bi_2Zr_{2-x}Ti_xO_7$. These systems would be of particular interest in light of the fact that $Bi_2Zr_2O_7$ is not known.[12] A solid solution series could provide an indication of the stability limit for the pyrochlore structure with regard to the B cation radius.

6.6 References

[1] H. Du and X. Yao, Mater. Res. Bull., **40** 1527 (2005).

[2] H. C. Ling, M. F. Yan and W. W. Rhodes, *J. Mater. Res.* **5** 1752 (1990).

[3] I. Levin, T. G. Amos, J. C. Nino, T. A. Vanderah, C. A. Randall and M. T. Lanagan, *J. Solid State Chem.* **168** 69 (2002).

[4] H. Kagata, T. Inoue, J. Kato and I. Kameyama, *Jpn. J. Appl. Phys.* **31** 3152 (1992).

[5] A. Mergen and W. E. Lee, *Mater. Res. Bull.* **32** 175 (1997).

[6] S. M. Zanetti, S.A. da Silva and G. P. Thim, *J. Solid State Chem.* **177** 4546 (2004).

[7] J. Takahashi, M. Takatsu, T. Ota and I. Yamai, *J. Ceram. Soc. Jap.* **98** 786 (1990).

[8] A. L. Hector and S. B. Wiggin, *J. Solid State Chem.* **177** 139 (2004).

[9] R. B. Von Dreele, A. C. Larson, GSAS General Structure Analysis System, Neutron Scattering Centre, MS-H805, Los Alamos National Laboratory, Los Alamos, NM, USA (2003).

[10] I. Radosavljevic Evans, J. A. K. Howard and J. S. O. Evans, *J. Mater. Chem.* **13** 2098 (2003).

[11] R. D. Shannon, *Acta. Cryst.* **A32** 751 (1976).

[12] S. L. Sorokina and A. W. Sleight, *Mater. Res. Bull.* **33** 1077 (1998).

Chapter 7

Structural and Compositional Variations in Ta_3N_5 Produced by Ammonolysis of Tantalum Oxide

7.1 Introduction

Tantalum (V) nitride has an optical band gap of 2.08 eV[1] making it a useful red pigment.[2] Pearlescent effect pigments can be produced by coating silica flakes with Ta_3N_5 using fluidized bed apparatus.[3] The compound has been shown to be an active photocatalyst in the visible region of the electromagnetic spectrum, including a quantum efficiency of *ca.* 10 % for overall water splitting and good hydrolytic stability.[4] Inverse opal thin films of Ta_3N_5 show promise as optical wavelength photonic structures[5] and it has also been investigated for use as a capacitor dielectric,[6] a gas sensor material for propanal[7] and an anti-reflective coating in photolithography.[8]

Ta_3N_5 is composed of irregular TaN_6 octahedra with both three and four coordinate nitrogen atoms and has the pseudobrookite (Fe_2TiO_5) structure, as shown in Figure 7.7.1. The structure has been determined[9] using powder neutron diffraction (PND) on samples prepared by ammonolysis of $TaCl_5$; a route originally reported by Hamblet.[10] However, some diffraction studies on Ta_3N_5 have been based on material derived from the reaction of Ta_2O_5 with ammonia[11] and this is a common preparative method in the more recent applications-based studies.[1-5,7] Where elemental analysis has been undertaken in these investigations, some oxide is always found and the nitride content fails to reach that of stoichiometric Ta_3N_5.[4,12-14] Often this is attributed to air oxidation causing an unrepresentative result in surface-based methods or to combustion analysis giving a low nitrogen content on a refractory material. Domen nitrided a Ta_2O_5 film at 850 °C in the X-ray photoelectron spectrometer antichamber with various flow rates and reaction times.[15] Even under these conditions, with no air exposure, the surface composition did not become richer in nitrogen than $Ta_3N_{4.8}O_{0.3}$. Questions therefore remain about whether residual oxide is located only on the surface or in the bulk of the material.

The band gap of a material can be varied by altering the electronegativity difference between the cationic and anionic elements.[16] Nitrogen has a lower electronegativity than oxygen and the presence of O^{2-} in the anionic framework will act to increase the band gap, altering the compound's optical properties. Thus Ta_3N_5 is red (E_g = 2.08 eV) whereas TaON is yellow (2.5 eV). Electronic structure calculations for Ta_3N_5

predict a smaller band gap than that observed experimentally;[1] this is also in line with some oxide content in the measured materials.

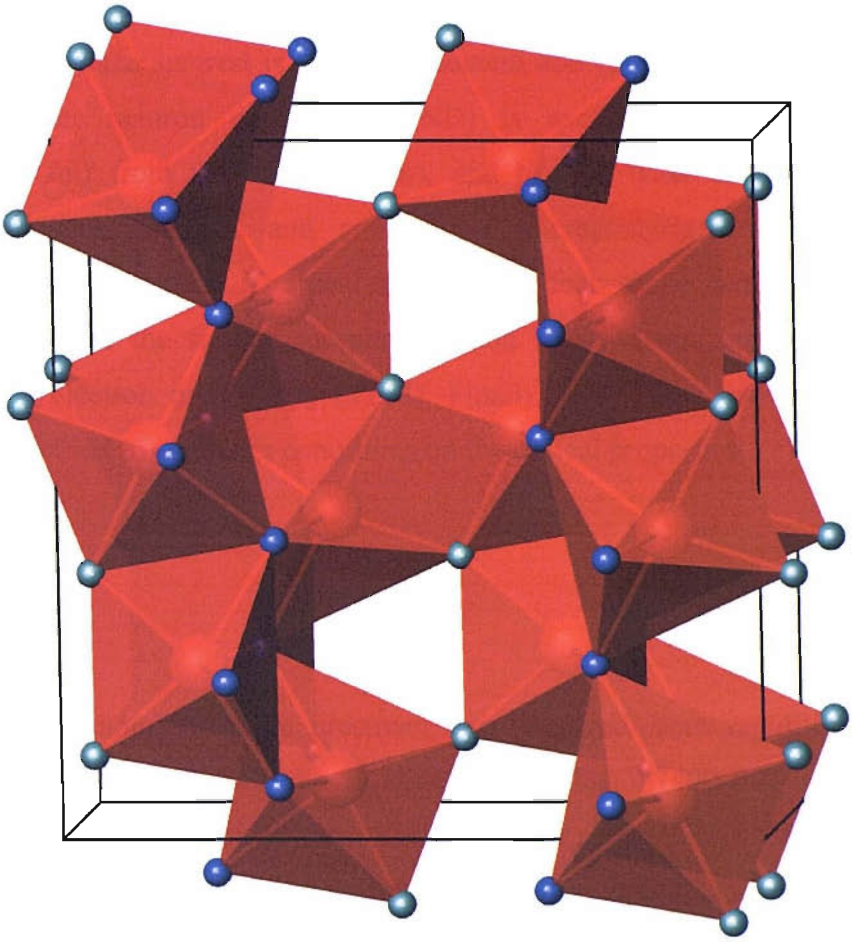

Figure 7.1.1 The structure of Ta_3N_5 highlighting the TaN_6 octahedra (red) linked by three (green) and four (blue) coordinate nitrogens.

Other aspects of the synthesis of Ta_3N_5 from Ta_2O_5 are intriguing; for example, at 850 °C this route can lead to porous crystallites[17] and the resulting increase in surface area may improve the catalytic properties. The colour and catalytic properties of materials are also dependent on crystallite size and morphology as well as the surface composition and band gap. Many properties are likely to depend on an interplay between the composition (harsher conditions resulting in higher nitrogen content and smaller band gap) and microstructure (harsher conditions closing up pores and annealing particles).

In view of the many applications envisaged for oxide derived Ta_3N_5, a re-evaluation of how its composition, structure and properties vary with synthesis conditions is timely. Of particular interest is the oxide content and its location within the Ta_3N_5 lattice. Powder neutron diffraction (PND) is useful in distinguishing oxide ($B_{coh} = 5.80$ fm) from nitride (9.36 fm), and here is used in conjunction with thermogravimetric analysis and combustion microanalysis to obtain detailed compositional information. The analysis of PND peak shape can also give useful information about the sample morphology and these results are combined with transmission electron microscopy (TEM). Finally, UV-visible spectra are used to examine the effect of synthesis conditions on the optical properties.

7.2 Synthesis

An amorphous tantalum oxide precursor was prepared from rapidly hydrolysed tantalum ethoxide. $TaCl_5$ (40 g) was stirred with ethanol (400 ml) under flowing ammonia gas for two hours to form $Ta(OEt)_5$. The mixture was then poured into dilute aqueous ammonia (1 L, ~2 moldm^{-3}). The white precipitate was collected by filtration, washed with water and dried at 100 °C. The precursor (~1 g) was placed in an alumina boat inside a silica tube and nitrided under flowing ammonia gas (Air Products, technical grade anhydrous, 99.9 %) with a flow rate of 2 Lmin^{-1} at a series of temperatures (680, 700, 750, 800 and 900 °C) and times (2, 4, 8, 24 and 120 h).

7.3 Characterisation

Samples were characterised by powder X-ray diffraction using a Bruker D8 diffractometer with Cu-$K_{\alpha 1}$ radiation. Phases present were identified by comparison with the PDF2 database.[18] Thermogravimetric analyses were carried out on a Mettler Toledo TGA/SDTA851e under flowing oxygen from 25-1000 °C; complete decomposition to Ta_2O_5 occurs at around 700 °C (Figure 7.3.1). Transmission electron microscopy (TEM) was performed on a Jeol JEM-3010 microscope at 300 kV accelerating voltage. Samples were prepared by ultrasound dispersal in toluene followed by deposition on carbon coated grids. Diffuse reflectance UV-Vis. spectra were obtained using a Perkin Elmer Lambda 35 spectrometer with an integrating sphere, in the range 380-780 nm.

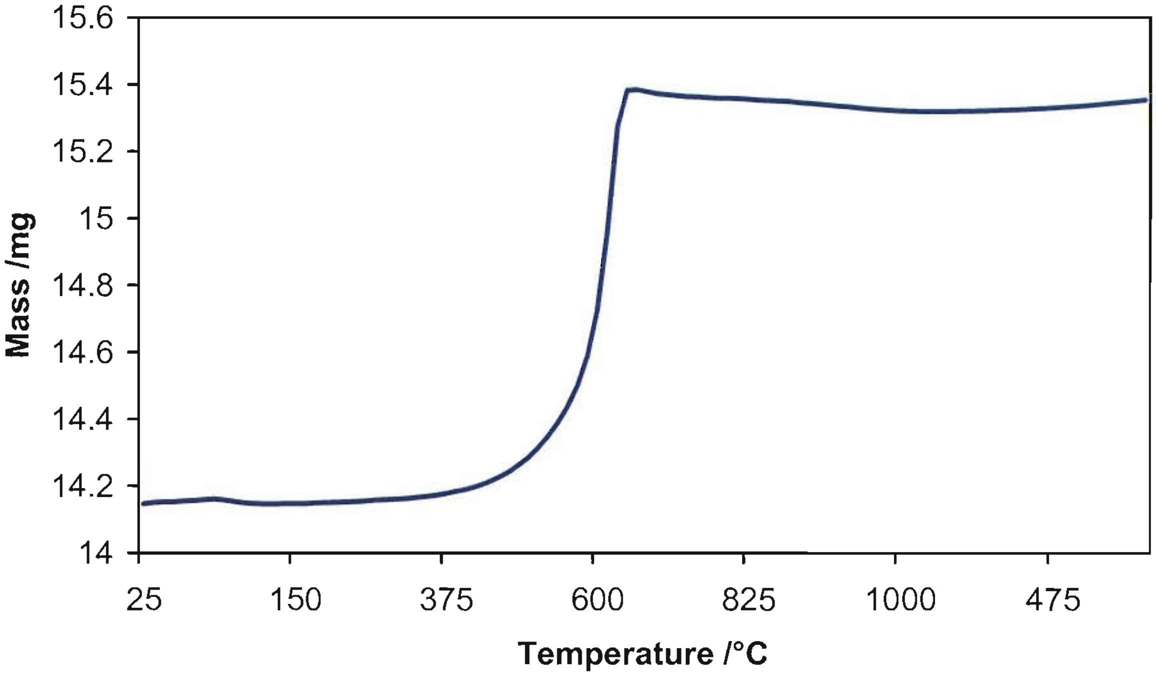

Figure 7.3.1 TGA trace for the Ta_3N_5 sample heated for 120 hrs at 900 °C.

Powder neutron diffraction data were collected at ambient temperature in 6 mm vanadium cans using the medium resolution, high intensity time-of-flight POLARIS diffractometer at the ISIS facility. Data from the backscattered bank ($2\theta = 145$ °) with a time-of-flight range of 2–19 μs ($d = 0.324$–3.084 Å, 3993 reflections) were used for structural refinement with the GSAS suite of programs.[19] Scale factor, lattice parameters and 10 background terms in a cosine Fourier series (GSAS function no. 2) were refined, followed by a linear absorption correction, atom positions, isotropic temperature factors and peak shape (GSAS profile type 3). Finally anisotropic temperature factors were used and the anion sites were refined as mixed O/N with total occupancy fixed at 1; these sites were set as nitrogen if a small negative or zero O occupancy resulted.

7.4 Results and Discussion

Ta_3N_5 is red in colour, so visual impression is a good indication of its phase purity. Sample colours and the phases observed by PXD are shown in Table 7.4.1. Generally, samples, which have an orange or brown colouration, contain amorphous material or TaON. All samples heated for 2 or 4 h were impure with the sample size used, hence the work focused on samples heated for 8 h or longer. With smaller sample sizes (~ 100 mg) than we needed for the PND studies, phase pure Ta_3N_5 can be obtained in much shorter time periods.

Table 7.4.1 Colour and PXD phase identification with various heating times and temperatures.

	680 °C	700 °C	750 °C	800 °C	900 °C
2 h	yellow, amorphous	yellow-brown, amorphous	orange-brown, Ta_3N_5 plus amorphous	orange, Ta_3N_5 plus TaON	orange-red, Ta_3N_5 plus TaON
4 h	yellow-brown, amorphous	brown, amorphous	orange-brown, Ta_3N_5 plus a little amorphous	orange-red, Ta_3N_5 plus TaON	red, Ta_3N_5 plus TaON
8 h	brown, Ta_3N_5 plus amorphous	orange-brown, Ta_3N_5 plus a little amorphous	orange-red, Ta_3N_5	Red, Ta_3N_5	Red, Ta_3N_5
24 h	orange-red, Ta_3N_5	Red, Ta_3N_5	Red, Ta_3N_5	Red, Ta_3N_5	Red, Ta_3N_5
120 h	Red, Ta_3N_5	Red, Ta_3N_5	Red, Ta_3N_5	Red, Ta_3N_5	Red, Ta_3N_5

The composition of samples, Table 7.4.2, was obtained using a combination of combustion microanalysis (% C, H, N) and TGA (% Ta). Oxygen content was inferred by difference. Carbon and hydrogen content was typically 0.1 % or less except in the sample annealed at 680 °C for 8 h, where 0.24 % H was found. The general trend is for nitrogen content to increase and oxygen to decrease with increasing synthesis temperature or time. Samples made at 680 °C were found to be anion rich, from $Ta_3N_{3.99}O_{3.36}$ after 8 h (though amorphous material was observed in the PXD and H was found in the microanalysis) to $Ta_3N_{4.76}O_{0.56}$ after 120 h. Samples were not found to be oxide free even after heating at 900 °C, where the composition was $Ta_3N_{4.76}O_{0.25}$ after 8 h, $Ta_3N_{4.73}O_{0.21}$ after 24 h and $Ta_3N_{4.67}O_{0.23}$ after 120 h. Anion deficient samples were obtained after 24 h at 900 °C and after 120 h at 800 or 900 °C. Note that at 900 °C the nitrogen content was reduced with longer heating time, at all other temperatures the nitrogen content increased with heating time. In nitrogen Ta_3N_5 starts to lose mass and decompose to TaN at around 800 °C, the ammonia atmosphere has stabilised the Ta_3N_5 phase to 900 °C but the reducing N content shows that it is close to its decomposition temperature.

Table 7.4.2 Variation in composition of Ta_3N_5 samples with preparation conditions as obtained by (top) microanalysis and TGA or by (bottom) PND.

	680 °C	700 °C	750 °C	800 °C	900 °C
8 h	$Ta_3N_{3.99}O_{3.36}$ -	$Ta_3N_{4.28}O_{1.68}$ $Ta_3N_{4.43}O_{0.57}$	$Ta_3N_{4.62}O_{0.64}$ $Ta_3N_{4.63}O_{0.37}$	$Ta_3N_{4.61}O_{0.51}$ $Ta_3N_{4.68}O_{0.32}$	$Ta_3N_{4.76}O_{0.25}$ $Ta_3N_{4.77}O_{0.23}$
24 h	$Ta_3N_{4.59}O_{0.96}$ $Ta_3N_{4.56}O_{0.44}$	$Ta_3N_{4.67}O_{0.74}$ $Ta_3N_{4.66}O_{0.34}$	$Ta_3N_{4.68}O_{0.38}$ $Ta_3N_{4.68}O_{0.32}$	$Ta_3N_{4.72}O_{0.40}$ $Ta_3N_{4.67}O_{0.33}$	$Ta_3N_{4.73}O_{0.21}$ $Ta_3N_{4.74}O_{0.26}$
120 h	$Ta_3N_{4.76}O_{0.56}$ $Ta_3N_{4.71}O_{0.29}$	$Ta_3N_{4.75}O_{0.61}$ $Ta_3N_{4.65}O_{0.35}$	$Ta_3N_{4.85}O_{0.27}$ $Ta_3N_{4.71}O_{0.29}$	$Ta_3N_{4.80}O_{0.13}$ $Ta_3N_{4.78}O_{0.22}$	$Ta_3N_{4.67}O_{0.23}$ $Ta_3N_{4.80}O_{0.20}$

7.4.1 Neutron Diffraction Data

PND data were collected in order to refine the anion occupancies and yield compositional information on the crystalline Ta_3N_5 material directly. This is complementary to the analytical data, which gives the composition of the material as a whole and can be affected by amorphous material or differences at particle surfaces. The structure of Ta_3N_5 consists of irregular TaN_6 octahedra sharing edges and corners (Figure 7.1.1). Of particular interest here are the anion sites, of which there are three, N(3) and N(5) are 4-coordinate whereas N(4) is 3-coordinate. The starting model used for refinement is given in Table 7.4.3.

Table 7.4.3 Starting model for Ta_3N_5 refinements.[9] *(Anion sites mixed N and O with total occupancy = 1)*

Atom	site	*x*	*y*	*z*	
Ta(1)	4*c*	0	0.20	¼	(6-coordinate)
Ta(2)	8*f*	0	0.13	0.56	(6-coordinate)
N(3) / O(6)	4*c*	0	0.76	¼	(4-coordinate)
N(4) / O(7)	8*f*	0	0.05	0.12	(3-coordinate)
N(5) / O(8)	8*f*	0	0.31	0.07	(4-coordinate)

Space group *Cmcm;*
$a = 3.89$ Å, $b = 10.22$ Å, $c = 10.28$ Å.

Initial refinements with a stoichiometric Ta_3N_5 model yielded reasonable fits, though with slightly high extracted thermal displacement parameters on N(3) and N(4). Use of anisotropic thermal displacement parameters and mixed occupancy (O,N) on these sites yielded much improved fits, typically with $R_{wp} < 2$ % and $R_p < 4$ %. The O content of the N(5) site refined to a slightly negative value (within e.s.d. of zero), indicating full occupancy with N, and was set at zero. This was also true of N(3). The 3-coordinate N(4) site was always, however, refined to a noteworthy oxide content. A typical fit is shown in Figure 7.4.1 and the associated crystallographic parameters given in Table 7.4.4. Variations in the derived lattice parameters are displayed in Figure 7.4.2. Only a small variation is observed between samples in *a* or *c*, whereas *b* is much more sensitive to heating time and temperature.

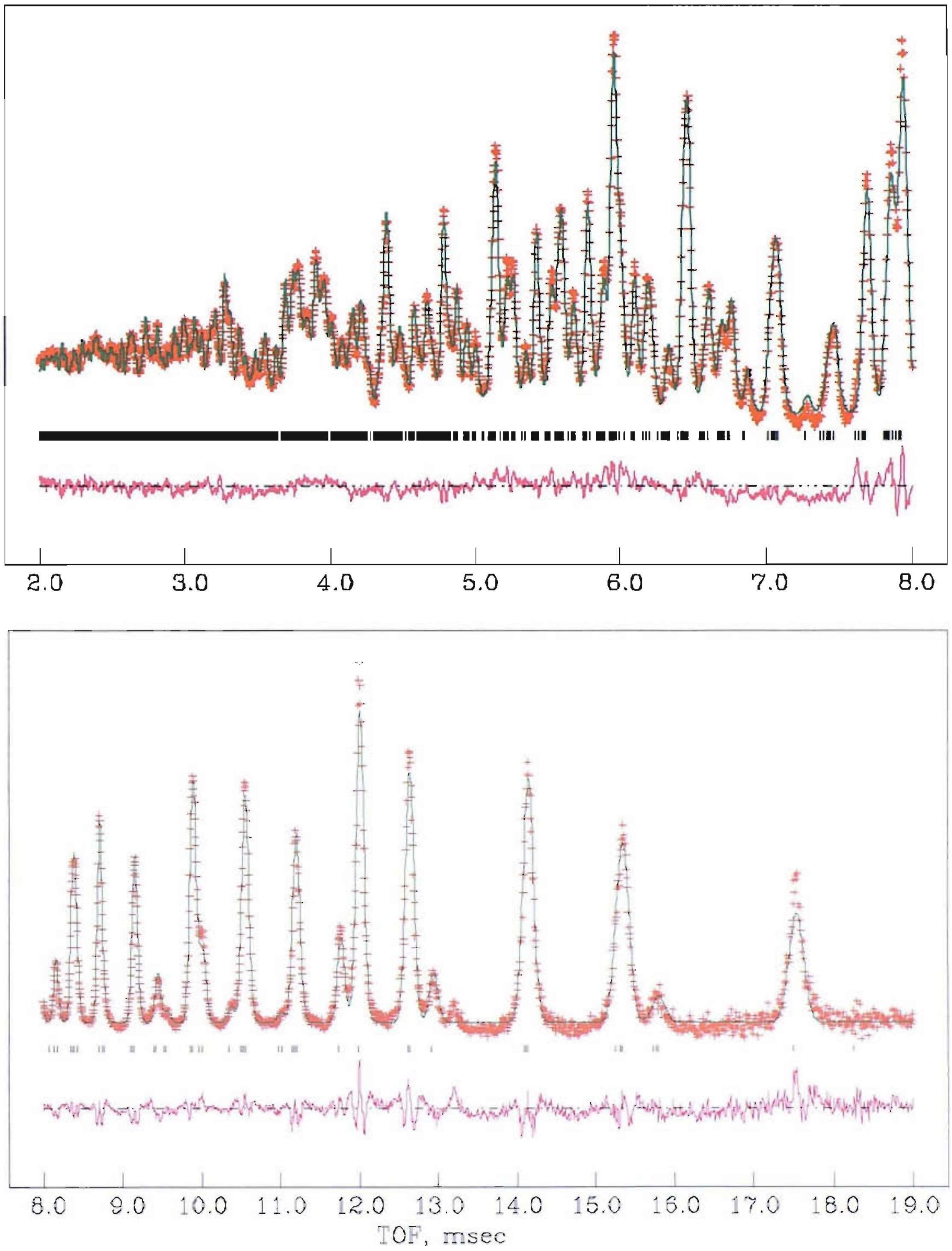

Figure 7.4.1 Fit to the PND pattern of Ta_3N_5 produced at 750 °C with a heating time of 120 h. Crosses mark the data points, upper continuous line the calculated profile and lower continuous line the difference, tick marks are the positions of allowed reflections.

Table 7.4.4 Refined crystallographic parameters for Ta_3N_5 produced at 750 °C with a heating time of 120 h (Thermal parameters multiplied by 100).

Name	X	Y	z	U_{iso}/U_e (Å^2)	Fraction
Ta1	0.0000	0.1980(2)	0.2500	0.27*	1.0000
Ta2	0.0000	0.1345(1)	0.5596(1)	0.28*	1.0000
N3	0.0000	0.7627(1)	0.2500	0.47*	0.95(2)
N4	0.0000	0.0470(1)	0.1197(1)	0.56*	0.88(2)
N5	0.0000	0.3086(1)	0.0738(1)	0.45*	1.0000
O6	0.0000	0.7627(1)	0.2500	0.47*	0.05(2)
O7	0.0000	0.0470(1)	0.1197(1)	0.56*	0.12(2)
O8	0.0000	0.3086(1)	0.0738(1)	0.45*	0.0000

Name	U_{11}	U_{22}	U_{33}	U_{12}	U_{13}	U_{23}
Ta1	0.19(5)	0.39(5)	0.23(5)	0.00	0.00	0.00
Ta2	0.14(3)	0.35(4)	0.35(4)	0.00	0.00	-0.02(3)
N3	0.25(5)	0.78(5)	0.37(5)	0.00	0.00	0.00
N4	1.26(4)	0.15(3)	0.28(3)	0.00	0.00	-0.01(2)
N5	0.15(2)	0.55(3)	0.64(3)	0.00	0.00	0.07(3)
O6	0.25(5)	0.78(5)	0.37(5)	0.00	0.00	0.00
O7	1.26(4)	0.15(3)	0.28(3)	0.00	0.00	-0.01(2)
O8	0.15(2)	0.55(3)	0.64(3)	0.00	0.00	0.07(3)

a = 3.89046(9), b = 10.2171(2), c = 10.2712(3) Å,

Cell volume = 408.27(2) Å^3,

$\chi^2 = 1.92$, R_{wp} = 1.81 %, R_p = 3.82 %,

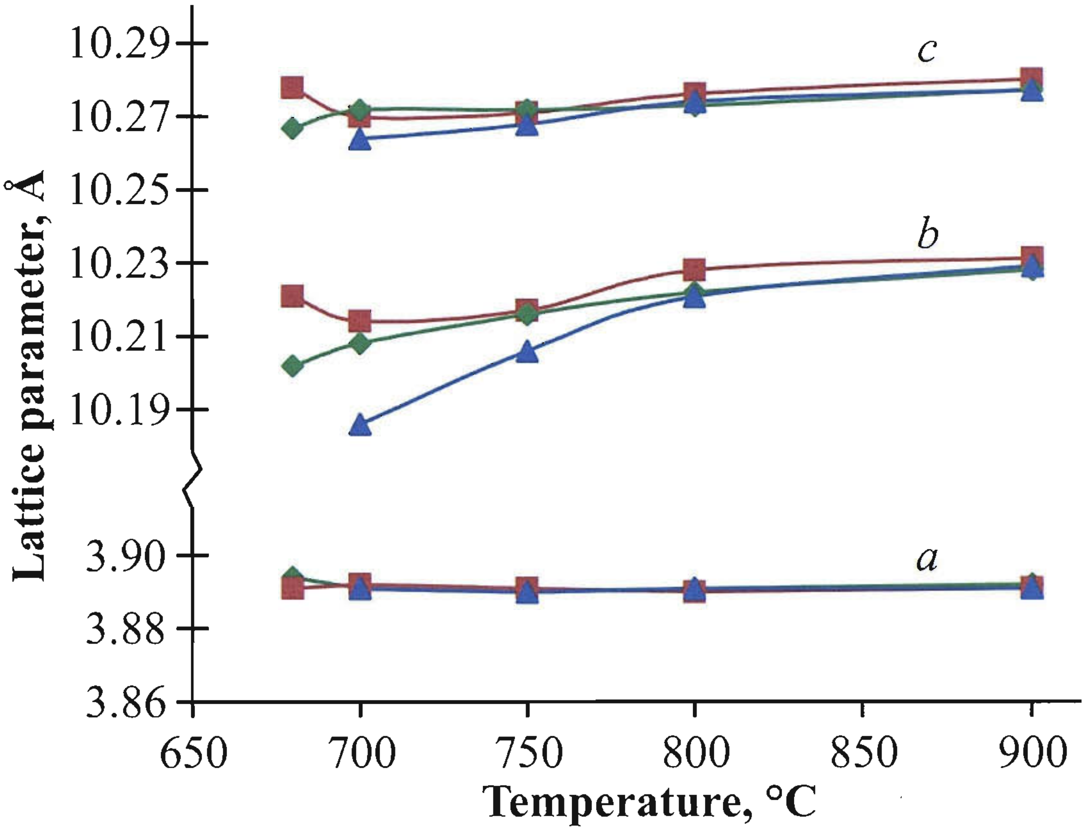

Figure 7.4.2 Variation of lattice parameters of Ta_3N_5 with synthesis conditions. Squares indicate samples heated for 120 h, diamonds for 24 h and triangles for 8 h.

The compositions of samples derived by PND as described above are shown in Table 7.4.2. Any anion site could be occupied by N, O or a vacancy whereas PND can only gauge the total scattering from the site and cannot deconvolute these three parameters. Hence the sites were assumed to be fully occupied with the scattering described by:

$$\text{Scattering} = (9.36 \times \text{N occupancy}) + (5.80 \times (1\text{-N occupancy}))$$

A more accurate description would be:

$$\text{Scattering} = (9.36 \times \text{N occupancy}) + (5.80 \times \text{O occupancy}) + (0 \times \square\ \text{occupancy})$$

where 9.36 and 5.80 are the coherent scattering lengths in fm of N and O respectively. Comparison of the analytical and PND-derived compositions in Table 7.4.2 reveals three scenarios:

1) In samples heated at 700 °C and below, also those heated for 8 h at 750 and 800 °C, the O-content in the analysis is markedly higher than that from the PND data. This can be attributed either to some amorphous oxide or oxide nitride, or to a crystalline but anion rich/cation deficient Ta_3N_5-type phase. In the latter case the stoichiometric model employed in the PND refinements would result in a low modelled anion content, which would be compensated by an increase in the proportion of the stronger: weaker anion content, i.e. the proportion of N:O suggested by the PND would be too high. The lack of diffraction evidence for amorphous material combined with the varying lattice parameters would suggest that the latter explanation applies to most of these samples. It would seem likely that both scenarios apply to the samples heated for 8 h at 680 and 700 °C, where amorphous material was observed by PXD.

2) The samples in the shaded region of Table 7.4.2 have similar analytical and PND compositions, suggesting roughly stoichiometric materials. Note that in all cases the oxide content is significant.

3) Samples heated for 24 h at 900 °C or for 120 h at 800 or 900 °C were found to be anion deficient, this is consistent with the observation that Ta_3N_5 starts to lose mass at around 900 °C in flowing N_2. In these samples the proportion of N:O would be underestimated by PND. However, the analysis still shows that oxide is present to a significant extent.

PND peak shape analysis (as described in Section 2.5.3) shows that for a given annealing time crystallite size stays relatively constant up to 800 °C (Figure 7.4.3), before increasing more rapidly between 800 and 900 °C as diffusion becomes more significant. Strain decreases steadily with annealing time and temperature. A small decrease in the crystallite size is observed between 680 and 750 °C in the samples annealed for 24 h.

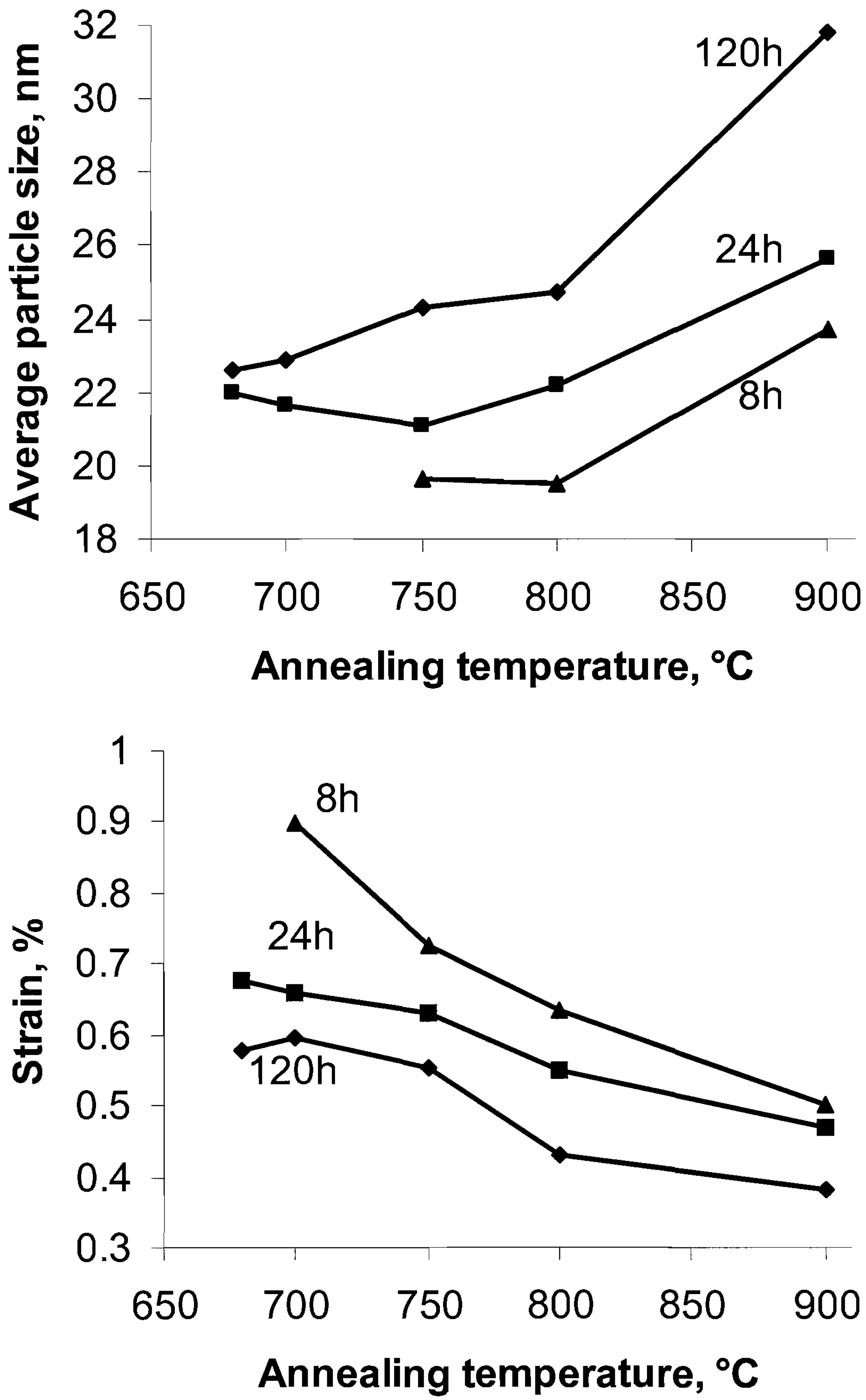

Figure 7.4.3 Variation in particle size and strain obtained by analysis of the PND peak shape.

TEM (Figure 7.4.4) shows that porous, quite complex, single crystalline shapes are present at 680 °C. By 800 °C these have annealed into more rounded, solid crystallites. It appears that the sintering process is mainly intraparticular up until 800 °C, then interparticle reactions begin to occur to a significant extent.

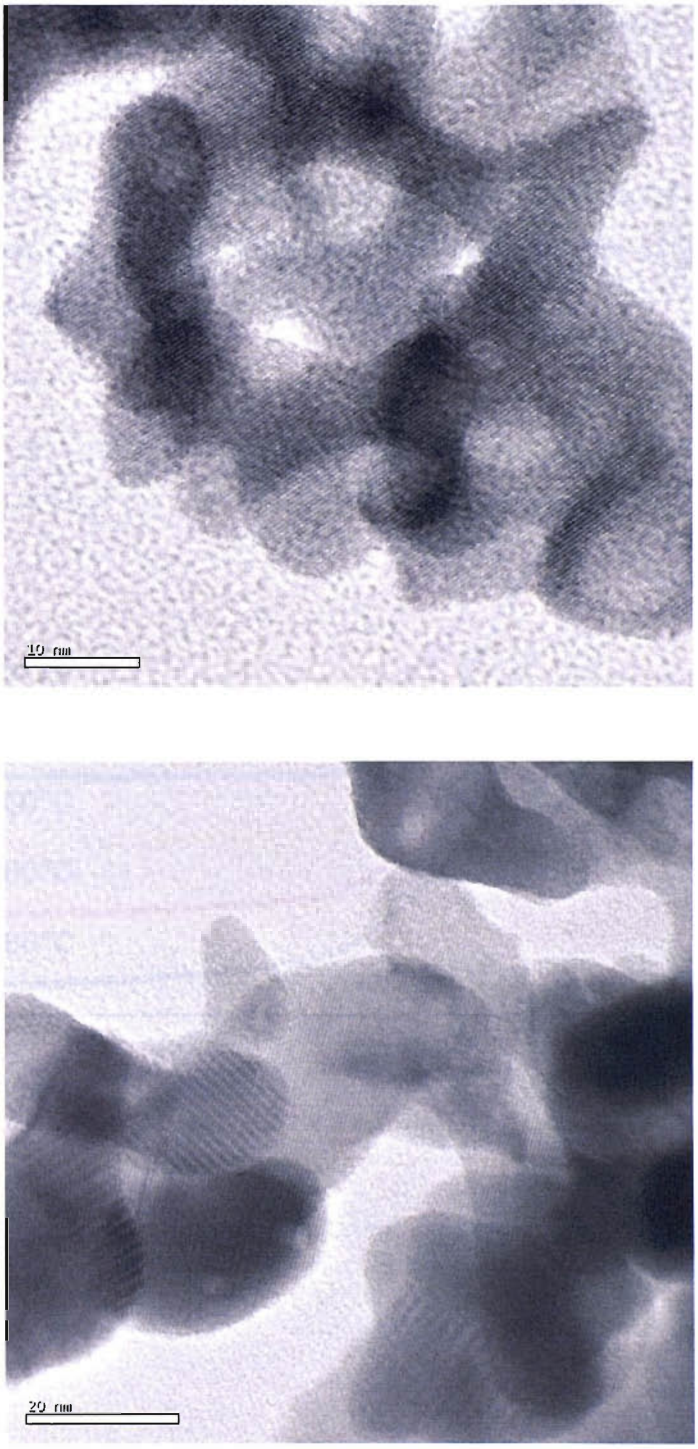

Figure 7.4.4 Transmission electron micrographs of samples fired for 24 h at 680 °C (top) and 800 °C (bottom).

7.4.2 Effect of composition on optical properties

UV-Vis spectra show a step in the absorbance at around 600 nm (Figure 7.4.5), corresponding to the band gap of Ta_3N_5. Optical band gap data for samples produced in this study are shown in Figure 7.4.6. Generally the band gap decreases with increasing nitrogen content and as the anion surplus and oxygen content fall. The values obtained herein are slightly lower for most samples than the published value of 2.08 eV.[1] It is noteworthy that the samples heated at 800 and 900 °C for 120 h have a larger bandgap than those heated at the same temperatures for 24 h. These samples are anion deficient and some reduction in population of the valence band could be responsible for this effect.

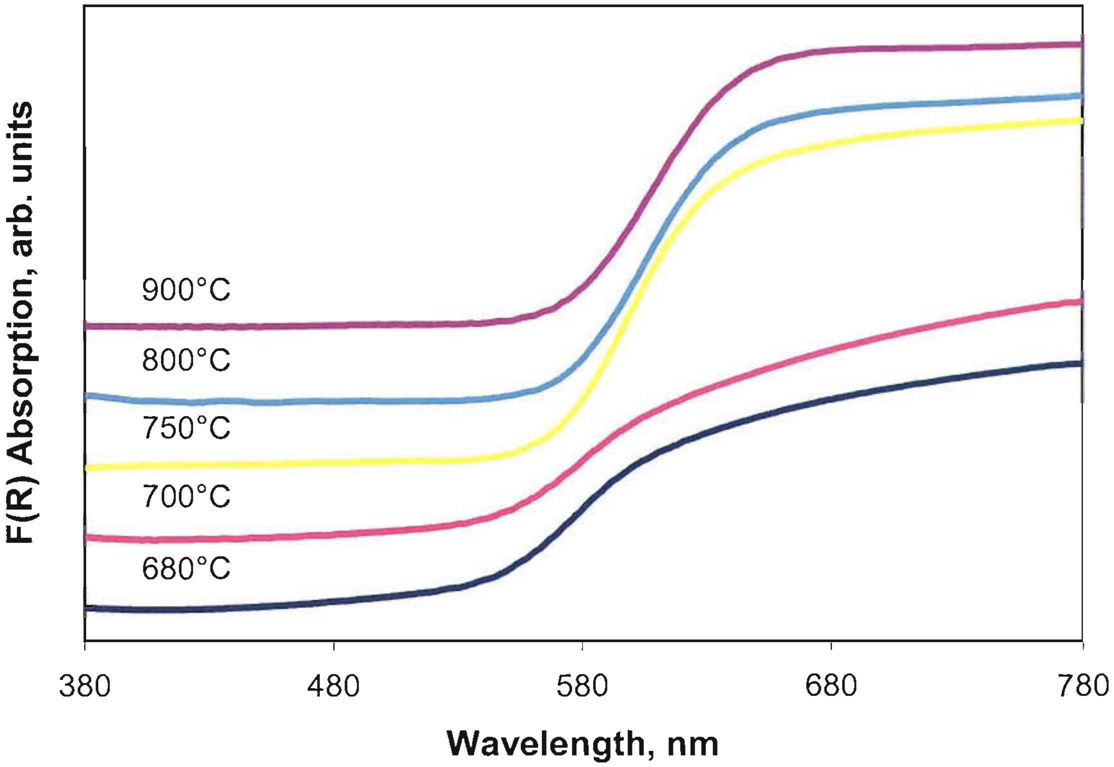

Figure 7.4.5 UV-Visible spectra for samples heated for 8 hours at various temperatures.

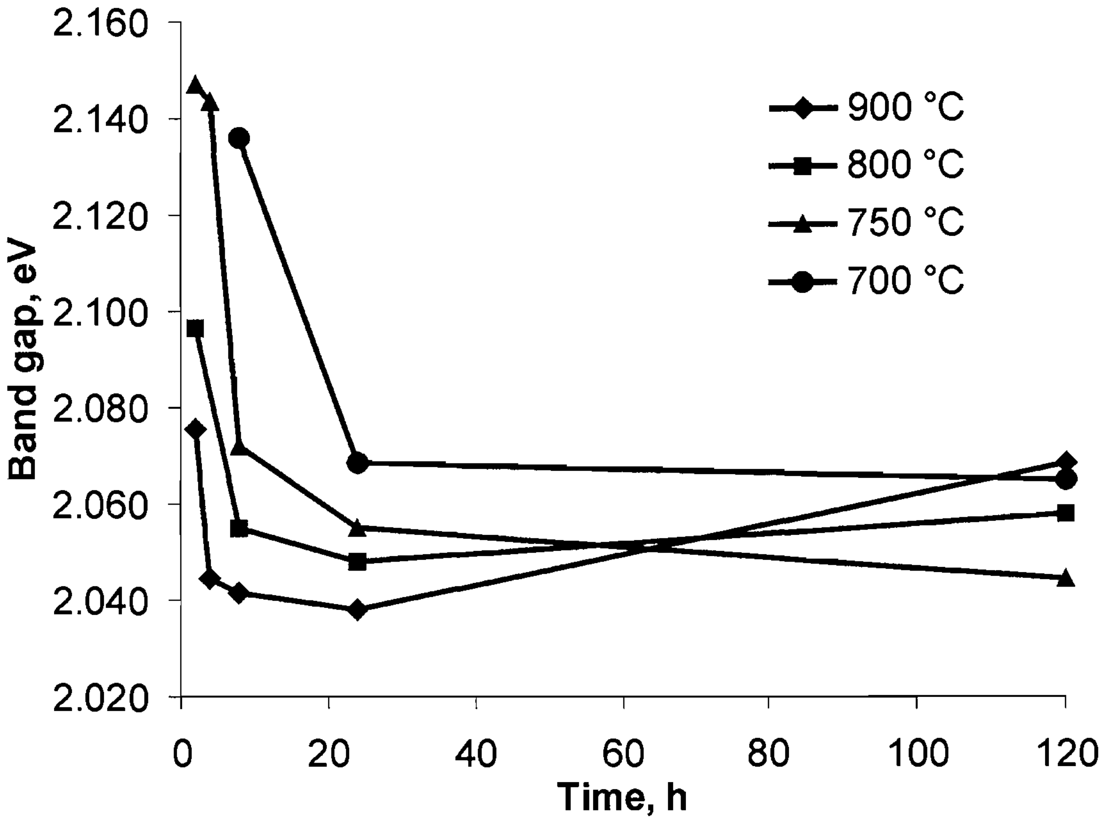

Figure 7.4.6 Variation of optical band gap with synthesis conditions.

7.5 Conclusions

Significant amounts of oxide ions remain in Ta_3N_5 samples prepared by ammonolysis of Ta_2O_5, even after extended heating periods in anhydrous NH_3. This oxide is located in the three-coordinate anion site in the Ta_3N_5 structure. The optical band gap and lattice parameters of Ta_3N_5 are affected by the oxide content. At higher temperatures, the Ta_3N_5 structure becomes anion deficient and this results in an increase in the optical band gap.

The fact that the band gap alters with the final stoichiometry of the material may be useful for its application as a pigment or photocatalyst. Controlled synthesis conditions could allow fine tuning of the colour or catalytic properties such that the optical band gap is optimised by anion content. This control is important if Ta_3N_5

pigments are to provide the deeper red colour required to replace cadmium compounds. The colour of any red compound must be matched to those of Cd(S,Se) and HgS, a poor alternative is not an appropriate substitute despite the associated reduction in toxicity.

7.6 References

[1] C. M. Fang, E. Orhan, G. A. de Wijs, H. T. Hintzen, R. A. de Groot, R. Marchand, J. Y. Saillard and G. J. de With, *J. Mater. Chem.* **11** 1248 (2001).
[2] M. Jansen, E. Guenther and H. P. Letschert, German Patent 199 07 618.9 (1999).
[3] S. Bertaux, P. Reynders, J. M. Heintz and M. Lerch, *Mater. Sci. Eng. B* **121** 137 (2005).
[4] G. Hitoki, A. Ishikawa, T. Takata, J. N. Kondo, M. Hara and K. Domen, *Chem. Lett.* **7** 736 (2002); M. Hara, G. Hitoki, T. Takata, J. N. Kondo, H. Kobayashi and K. Domen, *Catal. Today* **78** 555 (2003).
[5] A. Rugge, J. S. Park, R. G. Gordon and S. H. Tolbert, *J. Phys. Chem. B* **109** 3764 (2005).
[6] K. J. Lee and H. S. Yang, Japanese Patent 2001237399 (2001).
[7] O. Merdrignac-Conanec, M. Kerlau, M. Guilloux-Viry, R. Marchand, N. Barsan and U. Weimar, *Silicates Industriels* **69** 141 (2004).
[8] A. Jain and K. Lucas, US patent 5741626 (1998).
[9] N. E. Brese, F. J. Disalvo, M. O'Keeffe and P. Rauch, *Acta Cryst.* **C47** 2291 (1991).
[10] H. Moureu and C. H. Hamblett, *J. Amer. Chem. Soc.* **59** 33 (1937).
[11] G. Brauer and J. R. Weidlein, *Angew. Chem.* **77** 218 (1965).
[12] Q. Zhang and L. Gao, *Langmuir* **20** 9821 (2004).
[13] V. G. Brauer, J. Weidlein and J. Strähle, *Z. Anorg. Allg. Chem.* **348** 298 (1966).
[14] J. H. Swisher and M. H. Read, *Metall. Trans.* **3** 489 (1972).
[15] M. Hara, E. Chiba, A. Ishikawa, T. Takata, J. N. Kondo and K. Domen, *J. Phys. Chem. B* **107** 13441 (2003).
[16] E. Günther and M. Jansen, *Mater. Res. Bull.* **36** 1399 (2001).
[17] D. Lu, G. Hitoki, E. Katou, J. N. Kondo, M. Hara and K. Domen, *Chem. Mater.* **16** 1603 (2004).

[18] Powder Diffraction File, version 2.4, International Centre for Diffraction Data, Swarthmore, PA 19073, USA (2004).

[19] R. B. Von Dreele and A. C. Larson, *Generalized Structure Analysis System*, Los Alamos National Laboratory, NM87545, USA (December 2002 release).

Chapter 8

Conclusions

8.1 High Throughput Method Development

High throughput methods have received increasing interest over the past decade due to the need for cost effective discovery of novel functional materials. This project has focussed on the development of generic high throughput methods that may be used to investigate a wide range of material types. These techniques have been used for the synthesis and preliminary characterisation of optically functional ceramic oxide and oxide-nitride materials on an alumina substrate. Gel routes have been investigated for their viability when used with a Teflon masking system. Three different systems and deposition methodologies have been studied. The first system uses a polymer complex method based on citric acid and ethylene glycol in aqueous media to create arrays of the formula $Ca_{1-x}Sr_xZr_{1-y}Cr_yO_3$ ($0 \leq x \leq 1$; $0 \leq y \leq 0.24$). A metal alkoxide sol-gel method using an acetic acid, acetic anhydride solvent has been employed to produce arrays of oxides and oxide-nitrides with the general formulae $SrZr_{1-x}Ta_xO_3$ and $SrZr_{1-x}Ta_xO_{2+x}N_{1-x}$ ($0 \leq x \leq 1$). Co-evaporation from aqueous solutions of metal salts has also been utilised to prepare compounds with the spinel structure in the series $Cu_{1-x}Zn_xAl_{2-y}Cr_yO_4$ ($0 \leq x \leq 1$, $0 \leq y \leq 2$) at a range of temperatures.

Potential phosphor materials have also been studied using this system. Arrays of europium doped lanthanum phosphate have been prepared and have revealed that the maximum intensity of the $^5D_0 \rightarrow {}^7F_2$ red transition is achieved at a composition of $(La_{0.8}Eu_{0.2})PO_4$. However, the increase in europium also reduces the ratio of red:orange luminescence, reducing the usefulness of the material as a red phosphor. The compound $(Gd_{0.75}Tb_{0.25})P_{1.14}O_\delta$ was found to be the best green phosphor material from arrays replicating previous studies, where the optimum composition from slightly different synthetic conditions was $(Gd_{0.83}Tb_{0.17})P_{1.14}O_\delta$.

Sol–gel techniques when used in association with robotics and a suitable masking system for the generation of arrays allows high throughput techniques to be applied to the formation of complex metal oxide and oxide nitride materials. Undertaking such chemistry requires a detailed understanding of the sol-gel chemistry to be developed and optimised for the particular system under study. Once this has been completed then the chemistry may be widely used for generating arrays of complex mixed metal systems with ease.

It has been demonstrated that analysis of these arrays can be undertaken by powder X-ray diffraction to investigate the nature of the phases present and determine lattice parameters. Basic colour measurement and UV-Visible spectroscopy have been successfully used to determine absorbance of the complex oxides/nitrides as a function of wavelength and thus measure key physical properties such as colour for pigmentary systems. Fluorescence spectroscopy can also be used to study luminescent materials. However, application of these characterisation methods can be problematic for materials deposited in arrays on tiles using sol-gel methods. While simple properties, such as phase identification and colour, can be readily assessed, extraction of more complex information, such as accurate lattice parameters and exact visible region absorbencies, which rely on having samples in idealised geometries, can be problematic.

Further high throughput work on these systems should enable new, optimised materials to be developed. One advantage of using sol-gel methods for preparing these materials is that the technique can be rapidly transferred to the synthesis of a bulk or coated material once a new optimal composition has been identified. For ceramic materials this represents a distinct improvement on chemical or physical vapour deposition based high throughput methods.

8.2 Bismuth Pyrochlores

Insulating pyrochlores containing polarisable A-cations provoke extensive interest as electroceramic materials for capacitor and high-frequency filter applications. Bismuth zinc niobate (BZN) in particular has received attention for its dielectric capabilities, which are also tuneable with composition.[1] This interest is further enhanced by the increasing pressure to reduce dependence upon high toxicity ceramics such as lead zirconate titanate (PZT).

This study investigated the structural behaviour of pyrochlore bismuth hafnate and its titanium substituted derivatives. The most interesting aspect of the structural chemistry of $Bi_2Hf_2O_7$ is the Bi-O' network, which is highly ordered at room temperature and becomes progressively more disordered as the temperature increases, with displacements allowing accommodation of the Bi^{3+} lone pair. The α-phase resemble the ice I_h structure in that the O' atoms each have two long and two short Bi-O' bonds, each Bi having a long and a short bond to O'. The β-phase was not solved but can be expected to have a lower level of order in the Bi-O' network, increasing still further in the γ-phase with a statistical distribution of longer and shorter bonds. The δ-phase is highly disordered and only a ring of scattering density around the O'-O' bond is observed.

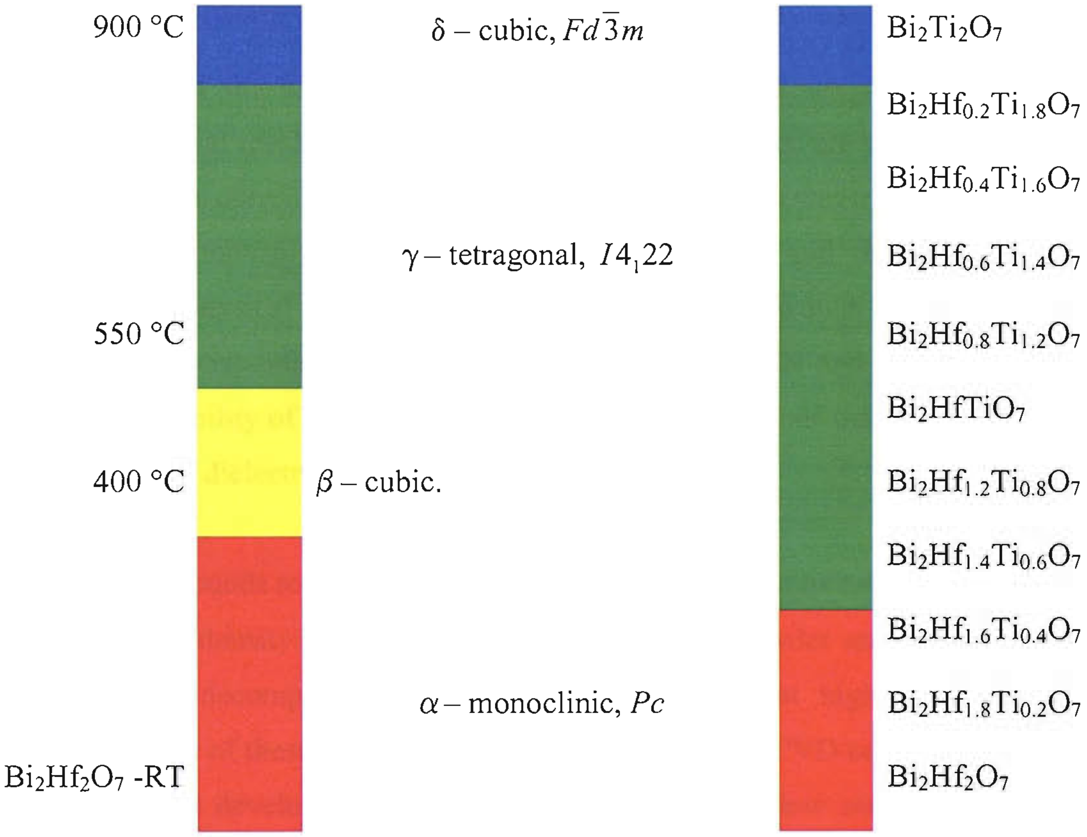

Figure 8.2.1 Graphical representation of the relationship between the phase behaviour of $Bi_2Hf_2O_7$ with temperature and compositional variance.

An analogous structural variation was observed with compositional change. Increasing substitution of titanium for hafnium on the B site of the pyrochlore structure also results in an increasing disorder. Figure 8.2.1 graphically illustrates the comparative phase behaviour of these materials.

It is interesting to note that the beta phase could not be identified in the solid solution series. This phase is likely to be isostructural to the as yet unsolved β-$Bi_2Sn_2O_7$ phase.[2] Further work in this area may involve preparing a series of samples in the range $Bi_2Hf_{2-x}Ti_xO_7$ ($0.4 \leq x \leq 0.6$) with small increments of x, in order to find the optimum composition to form the β-phase. High resolution neutron diffraction studies of this mixed B-site phase at room temperature would be useful for resolving both the β-stannate and β-hafnate structures and provide a further insight into the behaviour of the bismuth cation.

Measurement of the dielectric properties of these compounds is currently being undertaken. Initial results indicate that the dielectric constants are of the same order of magnitude as current commercial dielectric ceramics. However, further work is required to normalise and extract trends from this data and in turn relate the structural and physical properties of these materials. This would be beneficial not only to the understanding of these compounds but also BZN and related materials where the possibility of tuning the displacement of bismuth ions may be important to their efficacy as dielectrics.

For these compounds to be of use as electroceramics it would be necessary to anneal them to a high density. This may be problematic from powder samples due to the relatively low decomposition temperatures, particularly at higher levels of Ti content. If films of these compounds could be produced by CVD or if a suitable sol-gel method was developed, these could provide attractive low cost electroceramic materials with only moderate toxicity.

8.3 Tantalum Nitride Red Pigment

In recent times, concern about the use of heavy metals such as cadmium and lead in materials has resulted in tighter health and safety regulations.[3] Many pigment systems in current commercial use contain such metals, *i.e.* cadmium sulfoselenide ($CdS_{1-x}Se_x$) and lead chromate ($PbCrO_4$), thus there is an increased effort in industry to synthesise inorganic pigments with less toxic elements. Unfortunately, the replacement of certain colour systems, particularly red pigments, has been difficult to achieve.

One potential alternative red material is tantalum (V) nitride.[4] Typically Ta_3N_5 for commercial applications is prepared by the ammonolysis of Ta_2O_5. However, the final optical and physical properties of the material are particularly sensitive to the synthetic conditions. This project aimed to investigate how preparative variables, namely heating time and temperature, affect the stoichiometry, structure and colour of Ta_3N_5.

It has bee found that stoichiometric Ta_3N_5 is not produced under any of the chosen conditions. Oxide ions remain within the structure even after extended periods of heating under anhydrous, high purity ammonia gas. The oxide ions appear to reside in the three-coordinate anion site and influence both the optical band gap and the lattice parameters of the compound, the *b* parameter being particularly anion sensitive. Heating at higher temperatures results in an anion deficient material and an increase in the band gap. This control of the band gap may be important for the application of Ta_3N_5 as a pigment or photocatalyst.

Further work in this area may include attempts to alter the colour through the addition of other metals. Small variations in the electronegativity difference between the anions and cations can allow fine tuning of the optical band gap. For example, the electronegativities for Ta and Nb are 1.5 and 1.6 on the Pauling scale respectively, hence substituting niobium for tantalum would give an overall reduction in electronegativity difference, narrowing the band gap. A compound with a small band gap has the ability to absorb more wavelengths of visible light resulting in a darker appearance. Therefore a combination of substituting Ta(V) for Nb(V) to give compounds of the type $Ta_{3-x}Nb_xN_5$, and control of the anion content by synthetic conditions could produce materials, which compare more favourably to cadmium red for commercial application.

8.4 References

[1] I. Levin, T. G. Amos, J. C. Nino, T. A. Vanderah, C. A. Randall and M. T. Lanagan, *J. Solid State Chem.* **168** 69 (2002).

[2] I. Radosavljevic Evans, J. A. K. Howard and J. S. O. Evans, *J. Mater. Chem.* **13** 2098 (2003).

[3] European Economic Guideline No. 91 / 338 / EWG (1991).

[4] M. Jansen, E. Guenther and H. P. Letschert, German Patent 199 07 618.9 (1999).